

Gold based Nanorods

Tuning the Structure for Catalysis and Sensing

On the cover: Electron microscopy images of gold-, gold-platinum, gold-silver nanorods and a gold nanorod supraparticle

PhD thesis, Utrecht University, the Netherlands, May 2019.

ISBN: 978-90-393-7141-1

Printed by proefschriftmaken.nl

The work described in this thesis was performed in the Soft Condensed Matter and Biophysics group and Inorganic Chemistry and Catalysis group, which are part of the Debye Institute for Nanomaterials Science, at Utrecht University.

Gold based Nanorods: Tuning the Structure for Catalysis and Sensing

Gouden nanostaafjes: het afstemmen van de structurele
eigenschappen voor katalyse en spectroscopie

(met een samenvatting in het Nederlands)

Proefschrift

ter verkrijging van de graad van doctor aan de Universiteit Utrecht op gezag van de rector
magnificus, prof. dr. H.R.B.M. Kummeling ingevolge het besluit van het college voor promoties
in het openbaar te verdedigen op woensdag 12 Juni 2019 des middags te 12.45 uur

door

Jessi E.S. van der Hoeven

geboren op 25 Juli 1991 te Haarlem.

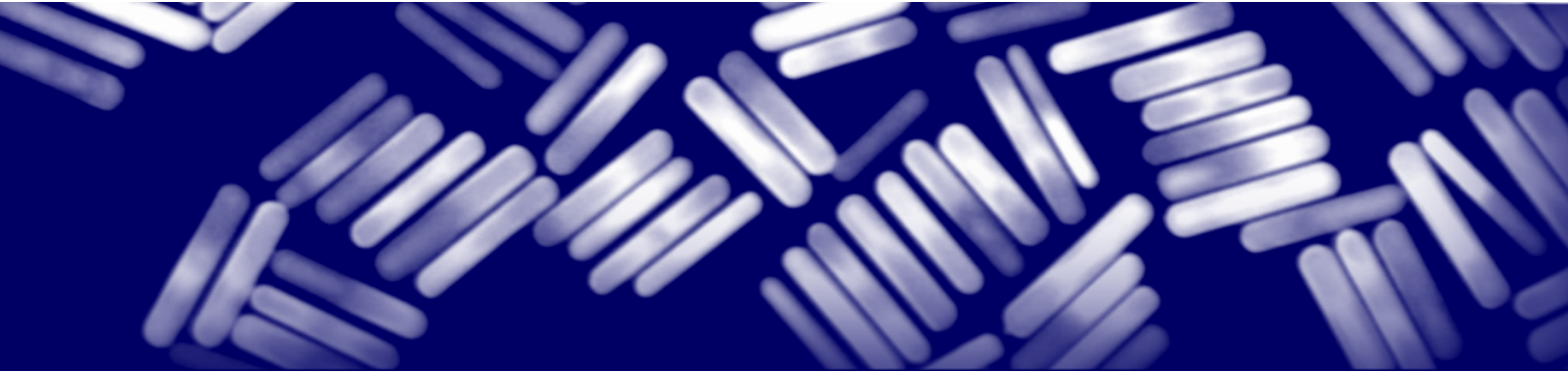
Promotors: Prof. dr. P.E. de Jongh, Prof. dr. A. van Blaaderen

This research was supported by the European Research Council (ERC) under the European Union's Horizon 2020 research and innovation programme, the ERC under the European Unions Seventh Framework Programme, and the Debye Graduate Program financed by the Dutch Organisation for Scientific Research (NWO).

Contents

1	Introduction	1
1.1	Metal nanoparticles: small is different	2
1.2	Synthesis of colloidal gold nanoparticles	4
1.3	Optical properties of gold nanoparticles	7
1.4	Catalytic properties of gold based nanoparticles	11
1.5	Scope of the thesis	14
2	Synthesis and thermal stability of silica coated gold nanorods	17
2.1	Introduction	18
2.2	Experimental	19
2.3	Results and Discussion	22
2.4	Conclusions	34
3	Synthesis of bimetallic core-shell nanorods	37
3.1	Introduction	38
3.2	Experimental	39
3.3	Results	44
3.4	Discussion	55
3.5	Conclusions	58
4	Alloyed metal nanorods with tunable properties	61
4.1	Introduction	62
4.2	Experimental	63
4.3	Results and Discussion	67
4.4	Conclusions	75
5	<i>In situ</i> observation of atomic redistribution in alloying gold-silver nanorods	77
5.1	Introduction	78
5.2	Experimental	79
5.3	Results and Discussion	84
5.4	Conclusions	96
6	Tuning the metal distribution of gold-palladium catalysts for bimetallic synergy in the selective hydrogenation of butadiene	97
6.1	Introduction	98
6.2	Experimental	99

6.3	Results	104
6.4	Discussion	114
6.5	Conclusions	117
7	3D real-space characterization of colloidal assemblies	119
7.1	Introduction	120
7.2	Experimental	122
7.3	Results	126
7.4	Discussion	133
7.5	Conclusions	137
8	Gold nanorod supraparticles for surface enhanced Raman spectroscopy	139
8.1	Introduction	140
8.2	Experimental	141
8.3	Results	144
8.4	Discussion	154
8.5	Conclusions	157
	References	159
	Summary	180
	Samenvatting voor iedereen	184
	Acknowledgements	190
	List of publications	194
	Oral and poster presentations	196
	About the author	197



Introduction

1



1.1 Metal nanoparticles: small is different

In this thesis we discuss the thermal, catalytic and optical properties of tiny metal nanoparticles. These nanoparticles typically have dimensions of 1 - 100 nanometres (nm). For comparison, a nanometer is approximately 100 000 times smaller than the width of a human hair ($\sim 100 \mu\text{m}$). Nanoparticles are exciting to work with as their properties deviate from those of their bulk counterparts [1]. Gold is a nice example of a metal where the bulk properties are greatly altered at the nanoscale [2]. Bulk gold is a noble metal, which means that it does not have the tendency to react with molecules in its surroundings, e.g. oxygen molecules from the air. Its non-reactive nature makes gold a desirable material in the fabrication of jewellery for which a long-term chemical stability is required. However, because of its chemical inertness, gold was incorrectly assumed to be unsuitable for catalysis. Herein, a catalyst is a compound that can accelerate a chemical reaction by lowering the activation energy of the reaction without being consumed itself. In 1989 Haruta was one of the first to show that gold can catalyse chemical reactions, when using sufficiently small particles [3]. Gold nanoparticles with a diameter below 10 nm dispersed on a metal oxide support, showed remarkably high catalytic activities in the oxidation of hydrogen and CO, even at temperatures as low as $-70 \text{ }^\circ\text{C}$. This finding formed the starting point for many gold-based catalysis studies. Nowadays, the number of publications on gold catalysis is approaching 2000 papers per year, showing the great interests in- and potential of gold nanoparticles in catalysis.

Not only the catalytic properties of metal particles change when working at the nanoscale, also other physiochemical properties start to deviate significantly from bulk behavior. For instance the rather high melting point of bulk gold ($1064 \text{ }^\circ\text{C}$) shifts to temperatures below $300 \text{ }^\circ\text{C}$ as the particle size is decreased to a few nanometers [4, 5]. Such deviations in physiochemical properties arise due to size-dependent effects. Herein, roughly two classes of size-dependent effects can be distinguished: surface- and quantum size related effects [1]. Surface effects arise due to an increased number of surface atoms which are less stable than bulk atoms due to a lower number of neighbouring atoms and therefore more reactive. Surface effects typically scale with the surface to volume ratio of the nanoparticles. Quantum size effects are related to changes in the electronic structure of the metal nanoparticles as a function of their size. For example, the optical properties of semiconductor nanoparticles vary as a function of the particle size due to quantum size effects [6].

Apart from the particle size, there are several other parameters influencing the physiochemical properties of metal nanoparticles. Also the shape and exact composition of the particles are crucial. For example, the colour of gold nanoparticles strongly depends on the particle shape. In Figure 1.1 dispersions of single-crystalline gold nanorods with different aspect ratios (length/diameter) in ethanol are shown. As the gold nanorods become more elongated the colour of the dispersion changes from purple, blue, green to brown. Understanding and designing the physiochemical properties of nanoparticles becomes more complicated when introducing a second metal. In the resulting bimetallic nanoparticles, not only the overall metal composition, but also the distribution of the metals within the nanoparticles becomes crucial (e.g. core-shell versus alloyed) as we will

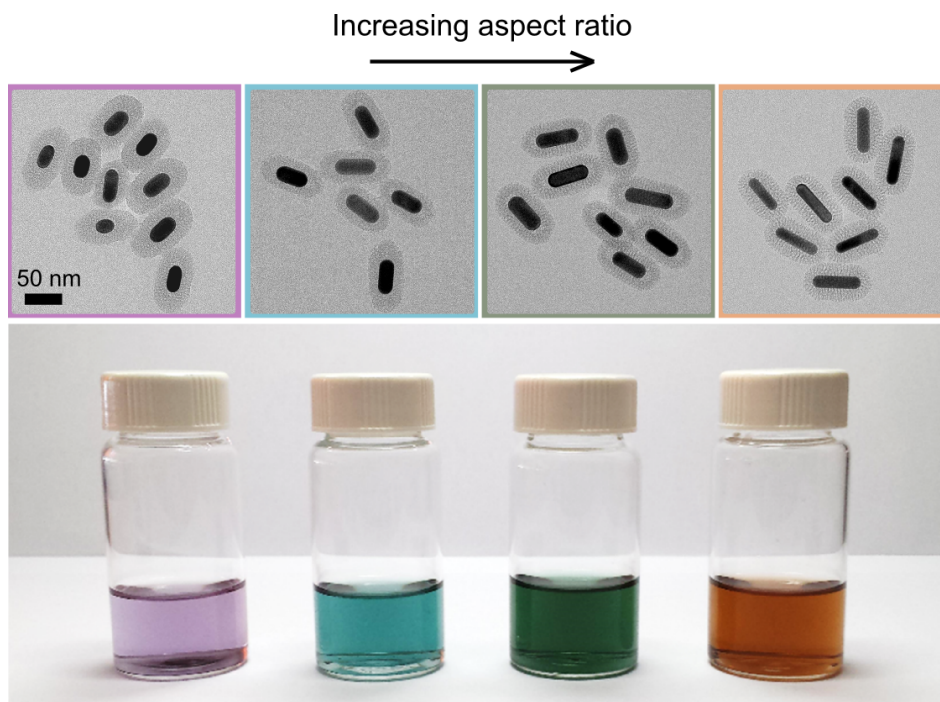


Figure 1.1: The colour of gold nanoparticles is shape dependent. Electron microscopy images of (silica coated) gold nanorods with aspect ratio (length/diameter) 1.7 (purple), 2.2 (blue), 2.7 (green) and 4.5 (brown), and digital photograph of the corresponding coloured dispersions.

see in Chapter 4 and 6, where we discuss the optical and catalytic properties of differently structured bimetallic nanoparticles.

When nanoparticles are dispersed in a liquid, like the gold nanorods in ethanol, we can also refer to the particles as "colloids". A colloid is a particle with dimensions between 1 nm and 1 μm [7]. Particles in this size range are on one hand much larger than the molecules of the medium that they are suspended in. On the other hand, they are small enough to experience Brownian motion and not directly sediment to the bottom due to gravity, such as sand grains in water. Brownian motion is a phenomenon named after Robert Brown and refers to the diffusive motion of a colloid caused by the collisions of the surrounding solvent molecules with the colloid [8–10]. The resulting diffusive motion, or "random-walk", of the colloids makes that particles can homogeneously distribute themselves in a medium without any external assistance. However, if there are attractions between the colloidal particles they can start to stick together and aggregate, which makes that the colloidal suspension becomes unstable. To prevent aggregation, colloidal particles are typically stabilized with ligands, e.g. large polymer molecules adsorbed on the colloid surface, or via surface charges.

Colloidal particles are of interest to both industry and fundamental science. In food industry and in cosmetics colloidal systems are present in many products such as mayonnaise, milk, toothpaste, creams and paint. As colloidal particles experience Brownian motion, they are also suitable model systems to study the phase behavior of atoms and molecules. With phase behavior we mean the different phase transitions that can occur

such as melting, freezing, nucleation, crystallization etc. Since colloidal particles are much larger than molecules and atoms, and diffuse much slower, it is easier to study these phase transitions with microscopy techniques. The organization of colloidal particles into larger structures is called self-assembly and can be used to build functional materials with new optical, catalytic or magnetic properties [11], as we will see in Chapter 8.

Our continuously advancing ability to control the particle size, shape and metal composition of nanoparticles and their assemblies has enabled a wide variety of applications in the fields of biology, health care, physics and chemistry. In this introductory chapter we will restrict ourselves to gold based nanoparticles. First, we will discuss wet chemistry based colloid synthesis as a suitable route to well-defined gold based particles of which the size, shape and composition can be tuned precisely. Next, we will discuss the optical properties of gold based nanoparticles and explain how the plasmonic properties of these particles can be used in Raman spectroscopy. Thereafter, the catalytic properties of gold based mono- and bimetallic particles will be discussed. Finally, we will finish the introduction with an outline of the work and the corresponding chapters described in this thesis.

1.2 Synthesis of colloidal gold nanoparticles

In this thesis we will make use of wet chemistry based colloid synthesis methods to make gold nanorods with a controllable shape and size, and a well-defined crystal structure. In wet colloid synthesis, metal nanoparticles are grown in solution. Generally, the growth mixture contains metal ions and ligands, which are for instance organic molecules. By adding a reducing agent the metal ions are reduced to the metallic state and small metal particles are formed. During this process the ligands form a protective layer around the metal particles and prevent the particles from clustering together. Apart from their stabilizing function, ligands can also act as shape directing agents and induce specific particle shapes. When the ligands bind more strongly to a specific surface facet of the metal nanoparticles, additional metal growth will predominately occur at the less shielded, more accessible facets. This can lead to the formation of non-spherical particles such as cubes [12], rods [13] or triangles [14]. Many colloid syntheses rely on a seeded growth approach. In this, the nucleation of small metal nanoparticles, called seeds, and subsequent growth of these seeds to larger particles are separated in two processes. By separating the nucleation and growth stage more monodisperse metal nanoparticles can be formed [15].

Synthesis of gold nanorods

Nowadays, monodisperse gold nanorods of the same size and shape can be synthesized, and the rod length and diameter can controllably be tuned between ~ 40 -120 nm and ~ 10 -40 nm. Although there are many reports of robust synthesis protocols for gold nanorods, only limited methods have been reported for the synthesis of nanorods composed of different metals [16, 17]. A reason for the specific interest in gold nanorods, compared to e.g. Ag and Pd nanorods, is possibly the good chemical stability of the gold combined with excellent plasmonic properties.

The synthesis of gold nanorods is relatively new and originates from the first report by Jana *et al.* in 2001 [18]. In this protocol, a seed mediated growth method was employed in which citrate capped gold seeds were grown, which were then added to an aqueous growth solution containing cetyltrimethylammonium bromide (CTAB) molecules as ligands. The CTAB molecules bind more strongly to the specific surface facets, in this case the $\{100\}$ and $\{110\}$ facets, leading to symmetry breaking and the formation of rods instead of spheres. The resulting rods had face centred cubic crystals (FCC) and were pentatwinned, meaning that they have a five-fold symmetry along the long axis of the rod (Figure 1.2a).

Two years later, the first report appeared in which CTAB capped instead of citrate capped seeds were used [20]. Important advantages of using CTAB capped seeds are that single-crystalline [21] (FCC) instead of pentatwinned rods are formed and that a higher yield of rods can be obtained. The difference in crystal structure of the nanorods is caused by a difference in crystallinity of the gold seeds. CTAB capped seeds are single-crystalline, whereas citrate capped seeds often have a pentatwinned structure [19, 21]. In 2017, the group of Liz-Marzán demonstrated that the quality of the seeds determines the quality of the final gold nanorods [19]. The conventional citrate method typically leads to a relatively large shape polydispersity, but this can be significantly improved by improving the quality of the Au-seeds via thermal treatment.

In Figure 1.2a and b examples of rods synthesized with citrate and CTAB capped seeds are shown, respectively. Note that the contrast of the pentatwinned and single-crystalline rods is not the same in the transmission electron microscopy (TEM) images. The single-crystalline rods have an inhomogeneous contrast within one rod and some rods

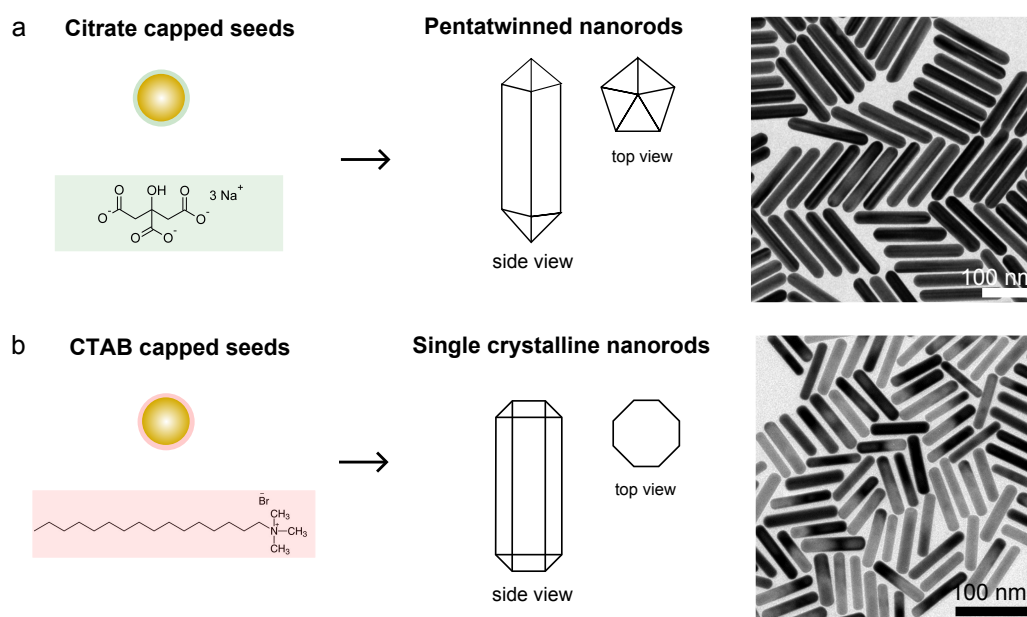


Figure 1.2: Schematic representation of the two main routes to synthesize gold nanorods. a) Citrate capped gold seeds lead to the formation of pentatwinned nanorods. The TEM image was taken from ref [19]. b) CTAB capped gold seeds lead to the formation of single-crystalline rods. Both types of nanorods have an FCC crystal structure.

appear more dark than others. This is due to the diffraction of the electron beam by the nanorods and is called diffraction contrast. When the crystal planes of the nanorod are in the correct orientation to diffract the electron beam, the number of transmitted electrons going to the detector is diminished and the rods will appear dark. If the rod is not diffracting the electron beam, the contrast in the TEM image is only based absorption of the electrons, resulting in more bright nanorods. Thus, the contrast of the single-crystalline rods depends on the orientation of the rods with respect to the electron beam. Contrarily, the contrast of the pentatwinned nanorods is not sensitive to the orientation of the rods due to the polycrystalline structure of the nanorods.

In 2013 a significant improvement of the CTAB-seeded nanorod synthesis was made by the Murray group, who synthesized very monodisperse nanorods (polydispersity below 10%) with almost no shape impurities by making use of a growth solution containing a binary surfactant mixture consisting of CTAB and sodium oleate. [13] This method enabled the synthesis of gold nanorods with aspect ratios from about 2 to 8 and particle volumes between $1 \times 10^4 \text{ nm}^3$ and $\sim 2 \times 10^5 \text{ nm}^3$. The good reproducibility and large control over the nanorod size formed the main reasons for using the method of Murray *et al.* for synthesizing the gold nanorods described in this thesis.

It is important to mention that in the CTAB seeded syntheses silver nitride is added to the growth mixture. The presence of silver ions is crucial in forming rod shaped particles, where higher silver to gold precursor ratios typically lead to higher aspect ratio rods [13, 22, 23]. Why and how silver plays a role in the synthesis is still a matter of debate. The silver content in CTAB-capped gold nanorods is between 1-4 atm% and increases with the aspect ratio and surface-to-volume ratio of the nanorods [23]. 3D electron microscopy measurements revealed that the silver is probably located at the particle surface [24]. There are two main mechanisms that would coincide with these findings and explain the role of the silver in the rod growth. The first mechanism is based on the underpotential deposition of Ag at the high index surface facets of the nanorods, leading to the stabilization of more open surface facets along the sides of the rods [25]. Alternatively, the silver ions were reported to form a complex with CTAB molecules which preferentially attach to the facets at the long sides of the rods. The existence of CTA-AgBr complexes has been verified with nuclear magnetic resonance measurements (NMR) [26].

It is good to realize that the gold nanorods have an out-of-equilibrium shape, meaning that they have a shape which is not the thermodynamically most favourable one for a given particle volume. The equilibrium shape for bulk crystals is given by the Wulff theorem, which states that the equilibrium structure is the crystal with minimal surface Gibbs free energy [27]. For FCC crystals the Wulff equilibrium shape is a truncated octahedron with $\{100\}$ and $\{111\}$ facets [28]. At the nanoscale the equilibrium shape will deviate from the Wulff structure and start to depend on the size of the nanocrystal [29, 30]. In any case, a rod-like particle shape is not the equilibrium structure as a rod has a higher fraction of surface atoms compared to a sphere of the same volume. Nanorods therefore have the tendency to deform to a more spherical shape when they are heated. Such deformations can already occur at temperatures as low as 200 °C, as we will see in Chapter 2.

1.3 Optical properties of gold nanoparticles

The dispersions in Figure 1 show that colloidal gold particles can give beautiful colours. Unknowingly, the Romans already used gold nanoparticles to make coloured glass, an art which was rediscovered in the 16th century during the Renaissance. In particular, colloidal Au, Ag and Cu nanoparticles and their alloys dispersed in glass are suitable metals in making glass with intense colours. Red coloured Gold Ruby glass is a well-known example of this. Although metal particles were being applied as colourants, the origin of the strong interaction between the metal and visible light was not known. In 1857 Faraday ascribed the colour to a "finely divided metallic state" [31]. About 50 years later, Mie was the first to quantitatively describe the interaction between light and spherical metal nanoparticles [32].

Herein, the colour of metal nanoparticles originates from the interaction between the electromagnetic waves of the incident light and the free electrons in the metal particle. Light induces collective oscillations of these free electrons, called plasmons. Bulk- and surface plasmons exist in bulk metals and at the interface between a metal and dielectric, respectively. For metal nanoparticles, the particle size is often smaller than the wavelength of the light that excites a surface plasmon, which gives rise to so-called localized surface plasmon resonances (LSPR). For Au, Ag, Cu the LSPR lies in the visible range of the electromagnetic spectrum resulting in visible colours [33].

When the particle size is smaller than the wavelength of the incident light, the extinction cross section (C_{ext}) of a spherical particle can be described by the following relation:

$$C_{ext} = \frac{24\pi^2 r^3 \epsilon_m^{3/2}}{\lambda_{inc}} \frac{\epsilon_i}{(\epsilon_r + 2\epsilon_m)^2 + \epsilon_i^2} \quad (1.1)$$

where r is the radius of the particle, ϵ_m is the dielectric constant of the surrounding medium, ϵ_i and ϵ_r the imaginary and real part of the particle's dielectric constant and λ_{inc} the wavelength of the incident light. From this relationship it follows that the particle size, the dielectric constant of the metal nanoparticles and the dielectric constant of the surrounding medium determine the extinction cross section as a function of λ_{inc} , and thus the position and intensity of the LSPR peak. The LSPR position of monometallic, spherical particles can relatively easily be calculated since the dielectric constants of bulk metals are well known [34, 35] and also hold for nanoparticles. Only for particle sizes below ~ 10 nm the bulk dielectric constants can no longer be used [36].

Predicting the optical response of plasmonic nanoparticles becomes more complicated when considering anisotropic nanoparticles. Nowadays, many different particle shapes can be synthesized. Here, we will restrict ourselves to rod shaped particles since nanorods are the main focus of this thesis. Due to their anisotropy, gold nanorods have two LSPR modes: one along the long axis of the nanorods and one along the width of the rods. This results in a longitudinal and transverse LSPR, respectively (Figure 1.3a). A theoretical description of the plasmonic properties of rod-like particles was first reported by Gans in 1915 [37]. He extended the Mie theory to ellipsoidal particles, where the particle's anisotropy is taken into account via shape factors $L_{x,y,z}$ with the x -axis running along the longest dimension of the ellipsoid. The extinction cross-section of such particles can be calculated as follows:

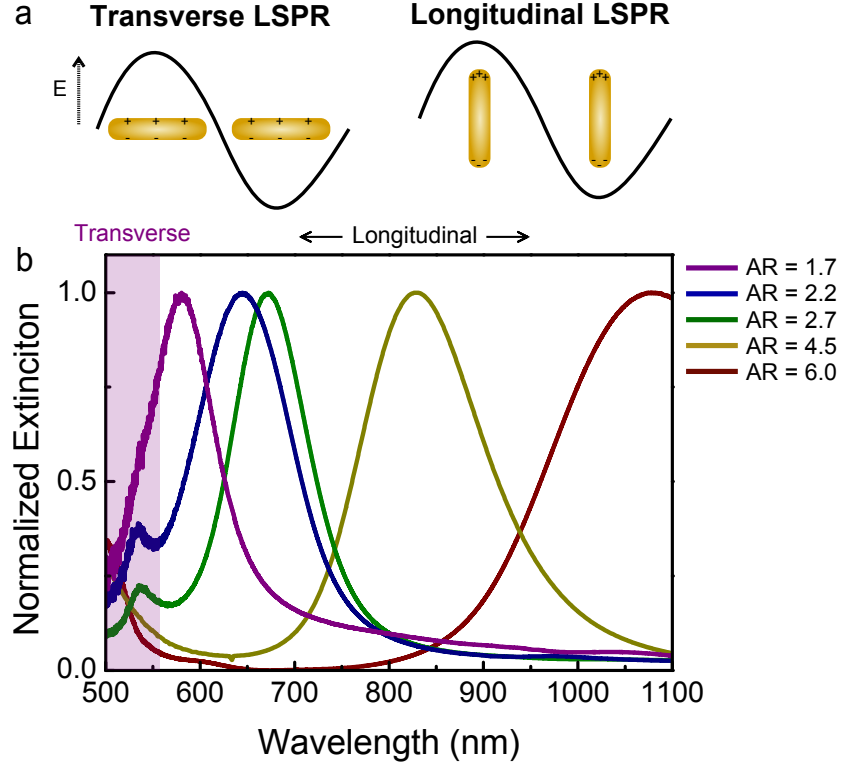


Figure 1.3: Gold nanorods have a transverse and longitudinal plasmon resonance mode (a). The longitudinal plasmon peak can be tuned via the aspect ratio of the nanorods. b) The purple, blue, green, golden and brown lines show the extinction spectra of gold nanorods with aspect ratio (length/diameter) 1.7, 2.2, 2.7, 4.5 and 6.0 in ethanol, respectively.

$$C_{ext} = \frac{2\pi V \epsilon_m^{3/2}}{3\lambda_{inc}} \sum_J \frac{(1/L_J^2)\epsilon_i}{(\epsilon_r + [(1-L_J)/L_J]\epsilon_m)^2 + \epsilon_i^2} \quad (1.2)$$

where V is the particle volume and the shape factors L_J with $J = x, y, z$ can be derived from equation 1.3 and 1.4:

$$L_x = \frac{1 - e^2}{e^2} \left(\frac{1}{2e} \ln \left(\frac{1+e}{1-e} \right) - 1 \right) \quad (1.3)$$

$$L_y = L_z = \frac{1 - L_x}{2} \quad (1.4)$$

$L_{x,y,z}$ depend on the aspect ratio (AR) of the rod via $e = \sqrt{1 - AR^2}$. L_y and L_z are equal, since nanorods are rotationally symmetric along the long the x axis. From these equations it follows that especially the longitudinal LSPR mode, which depends on L_x is sensitive to the aspect ratio of the rods. This is in accordance with experiments where the longitudinal LSPR can indeed easily be tuned via the aspect ratio from the visible into the infrared. To demonstrate this we show the extinction spectra of the nanorod dispersions from Figure 1.1 in Figure 1.3b.

The exact plasmonic response of non-ellipsoidal rods and more complex nanoparticle shapes can only be computed numerically. Since the computation of plasmonic properties

is not the focus of this thesis, we refer to a review by Myroshnychenko *et al.*, which gives a good overview of the different numerical methods to compute the plasmonic properties of variously shaped nanoparticles [38].

Surface enhanced Raman spectroscopy

In Chapter 8 of this thesis we describe how one can make use of the plasmonic properties of gold nanorods in Raman spectroscopy. This spectroscopic technique is named after its inventor Raman. In 1928 Raman and Krishnan were the first to report Raman scattering, which is the inelastic scattering of light by molecules [39]. We schematically explain Raman spectroscopy in Figure 1.4. When irradiating a molecule with laser light most of the light is scattered elastically, which is called Rayleigh scattering. A small fraction of the light is scattered inelastically, meaning that the scattered light has an different energy compared to the incident light. When the scattered light has an energy smaller than the incident light, it is called Stokes Raman Scattering. Alternatively, in the case of Anti-Stokes Raman scattering, the scattered laser light has an energy higher than the incident laser light. In most Raman spectroscopy measurements only Stokes scattering is considered, since Anti-Stokes scattering would require the molecules to be in an excited vibrational state. At room temperature most molecules are in the ground state and Anti-Stokes scattering is thus less likely to occur.

The intensity of the Raman signal depends on the type of molecule that is being probed. Herein, the Raman signal scales with the polarizability of a molecule. The ease with which a molecule is polarized depends on the response of its electron cloud to an electric field. Easily polarizable molecules, e.g. with conjugated π -systems such as benzene, are generally strong Raman scatterers while small inorganic molecules with single bonds tend to be weak Raman scatterers. Typical Raman probe molecules therefore contain one or more benzene rings. A nice overview of suitable Raman probe molecules is given in ref. [40].

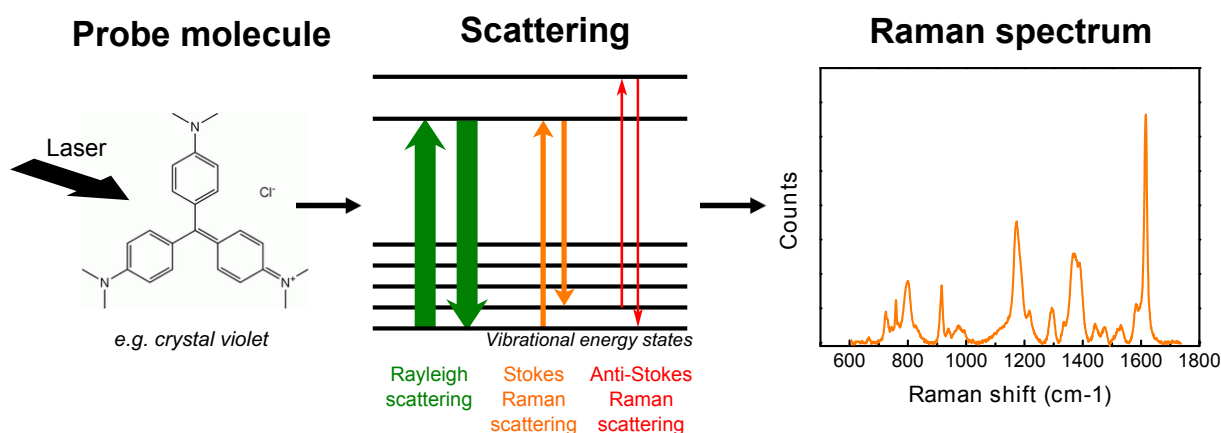


Figure 1.4: Schematic representation of Raman spectroscopy: a probe molecule is irradiated with laser light, which is scattered elastically (Rayleigh scattering) or inelastically (Anti- and Stokes Raman scattering). The inelastic scattering is used to obtain a Raman spectrum.

The Raman signal of most molecules is generally very weak (about 1 out of 10^4 scattered photons is Raman active) [41], but can significantly be enhanced when a molecule is brought to a metal surface. In the 1970s anomalously high ($\sim 10^5$ - $10^6 \times$ enhanced) Raman signals were reported for molecules close to rough silver surfaces [42–44]. This finding formed the starting point of a technique which we now know as Surface Enhanced Raman spectroscopy (SERS). When a metal particle is irradiated with light, ideally of a wavelength close to the plasmon resonance frequency of the particle, strong local electromagnetic fields are induced at the particle surface. This local electromagnetic field leads to an enhancement in the intensity of the Raman scattering of molecules close to the metal surface. In turn, the Raman scattered light excites the localized surface plasmon and generates an enhanced field at the Raman Stokes frequency. The total field enhancement G_{SERS} is given in equation 1.5 and is proportional to the square of the product of the local field $E_{loc}(\omega_{exc})$ at the incident frequency ω_{exc} and the local field $E_{loc}(\omega_{RS})$ at the scattered Raman Stokes frequency ω_{RS} [45–47]:

$$G_{SERS} \propto |E_{loc}(\omega_{exc})E_{loc}(\omega_{RS})|^2 \quad (1.5)$$

Equation 1.5 is often approximated with $G_{SERS} \propto |E_{loc}(\omega_{exc})|^4$, when assuming that $E_{loc}(\omega_{exc})$ and $E_{loc}(\omega_{RS})$ are the same. Thus, the Raman signal scales with about the fourth power of the local electromagnetic field. A small increase in the electromagnetic field can therefore lead to a strong enhancement in Raman scattering.

There are several approaches to obtain high local field enhancements with plasmonic nanoparticles. One can change the particles' morphology, where especially particles with sharp metal tips can lead to high enhancements [48, 49]. Alternatively, one can synthesize bimetallic nanoparticles. In particular particles containing silver are desirable here [49–53], as silver has superior plasmonic properties compared to e.g. Au [54–57]. Finally, one can also assemble plasmonic nanoparticles into larger super-structures such as colloidal crystals. When the distance between the particles is small, the surface plasmons of the individual particles will couple and larger field enhancements can be induced in between the particles, leading to so-called plasmonic hotspots. The intensity of these hotspots depends on the interparticle spacing, the geometric arrangement and number of particles in the assembly [46, 58, 59]. Recent publications on this topic have shown that large enhancements can be obtained when assembling gold nanorods in large particle assemblies [53, 59–62]. Those reports formed an important motivation for the work presented in Chapter 8 of this thesis, where we performed SERS measurements with spherical assemblies of gold nanorods. In general, such spherical assemblies are called supraparticles and can be composed out of many different building blocks leading to a wide variety of functional properties [63].

To date, the development of suitable SERS substrates has enabled the detection of trace amounts of molecules, which is useful in a wide variety of applications such as single-molecule spectroscopy [64], *in situ* monitoring of chemical reactions [65], biomedical applications [64], forensic research [41] and even art history [66].

1.4 Catalytic properties of gold based nanoparticles

Gold nanoparticles fall in the class of heterogeneous catalysts, where reactants from the gas or liquid phase adsorb on the metal surface, are converted into products, and desorb into the gas or liquid phase again. The rate of these adsorption and desorption processes depends on the adsorption energies of the reactants and products on the catalysts. In 1911 Sabatier postulated a relationship between the reaction rate in a catalytic process and the adsorption energies of the molecules involved [67]. A more precise relation between the catalytic activity and the adsorption energies was given by Balandin in 1969, who plotted the catalytic activity as function of the heat of adsorption, revealing a volcano like plot [68]. Herein, the catalytic activity is maximized for a binding energy where the adsorption of the molecules involved is not too strong nor too weak. The adsorption energies can be measured experimentally on single-crystalline metal or metaloxide surfaces with calorimetry measurements [69] or computed theoretically with Density Functional Theory (DFT) calculations [70, 71].

The adsorption energy of a molecule on a metal nanoparticles depends on many factors such as the type of metal, the exposed surface facets and coordination numbers of the individual surface atoms. These factors are mainly determined by size, shape and metal composition of the nanoparticles. It is good to realize here that the coordination number of the surface atoms varies within a particle, i.e. atoms at steps and kinks have a lower coordination number than atoms at facets. This means that each metal nanoparticle has different surface sites with different adsorption energies [72, 73]. The surface site which exhibits the highest catalytic activity, is often referred to as the "active site". In literature many observations of size dependent and/or facet dependent catalysis have been reported [74–78], indicating importance of controlling the size, shape of- and number of defects in the metal particles precisely.

To obtain stable catalysts, metal nanoparticles are typically supported on metaloxide or carbon supports. These supports prevent the nanoparticles from sintering at elevated temperatures and/or under reaction conditions, as the high support surface area provides anchoring sites for the metal particles and allows for large spacings in between the nanoparticles. In addition, the support material can be used to alter the catalytic activity of the metal nanoparticles [79], especially when using reducible supports [80, 81]. The exact metal-support contact area is therefore an important parameter and the catalyst activity can be directly related to metal-support interface [82, 83]. The influence of the support can be ascribed to indirect effects such as charge transfer to the metal [79], but also to direct effects where the support plays an active role in the catalytic process [84, 85].

To properly understand the catalytic behavior of metal nanoparticles, well-defined model systems are indispensable, where not only the particle size and morphology but also the contact area with the support can be controlled precisely. Via colloid synthesis routes such a high control over the catalysts design is feasible. Herein, metal particles with narrow size distributions, fixed particle shapes, well-defined crystal structures and bimetallics with controlled metal compositions can be obtained [15, 86]. Moreover, a particularly elegant way of achieving control over the exact metal-support contact area is via the self-assembly of colloidal metal and support particles into binary superstructures [11, 83, 87, 88].

Nowadays, beautiful colloidal particles and particle assemblies can be synthesized, but an important challenge is freeing the metal surface from the ligands, which were used in the colloid synthesis. An easy way to do this is via a thermal treatment in an oxygen rich environment, where the carbon-containing ligands are simply burned off. However, relatively high temperatures above 300 °C are required to completely remove the ligands [89]. Such temperatures often lead to loss of the initial particle shape and can lead to sintering of the metal particles, resulting in a less-defined system. An innovative way to prevent these processes from happening is by protecting each colloidal particle with a porous coating [89–91]. Such coatings significantly increase the nanoparticles stability, as we will demonstrate in Chapter 2 of this thesis. Alternatives for thermal ligand removal for research purposes are more mild washing approaches. The catalysts can be washed with solvents in which the ligands are well-solvable and/or make use of additives which (temporarily) remove the ligands from the surface such that they can be washed away [92, 93]. The advantage of these washing approaches is that they can be carried out at room temperature. In this thesis we will use a combination of washing and low temperature thermal pretreatment before catalysis.

Bimetallic catalysts

To date, many different types of supported gold nanoparticles are being applied as catalysts in a wide range of chemical reactions [2, 94]. Although gold tends to be less active than e.g. Pt or Pd based catalysts, it can outperform these metals in terms of selectivity towards the desired product. This characteristic has resulted in the investigation of gold catalysts for chemical reactions varying from selective hydrogenation and oxidation reactions to the water-gas shift reaction and hydro-chlorination reactions [2, 93–97].

The catalytic properties of gold nanoparticles can be tuned and optimized further by introducing a second metal. When bringing two metals together at the nanoscale, enhanced and even completely new catalytic properties can arise. So-called synergistic effects occur when the catalytic properties of the bimetallic nanoparticles exceed those of the single components. This is for example the case in CO oxidation, where gold-silver particles are more active than their monometallic counterparts [98]. Generally, two metals are brought together to combine specific properties of each metal. For instance, Pd tends to be a very active hydrogenation catalyst, whereas gold is considerably less active but more selective to the desired product(s) [99]. Ideally, a combination of these metals leads to a catalyst in which the best of both metals are retained.

In bimetallic nanoparticles the composition and the distribution of the metal atoms are crucial [97, 100–103]. Herein, colloid synthesis does not only offer control over the metal composition, but also on the arrangement of the metal atoms. As we will shown in Chapter 4 and 5, the initial arrangement of the atoms can be altered when going to elevated temperatures and under catalytic reaction conditions [97, 100–105]. Such metal redistribution alters the metal surface composition and therefore the catalytic activity of the bimetallic nanoparticles.

Although it is generally assumed that the atoms at the particle surface govern the catalytic behavior of metal nanoparticles, the influence of the sub-surface layers should not be neglected [76, 86]. The effect of the sub-surface layer on the reactivity of the surface

atoms is best investigated by making use of core-shell particles of which the number of atomic shell layers can be controlled. Herein, a non negligible influence of the core-metal is expected up to at least 6 atomic shell layers [86]. For higher shell thickness the catalytic properties will start to mainly be governed by the shell metal. The influence of the sub-surface layers can be of a geometric and/or electronic nature. An example of a geometric effect is the strain induced in the lattice of the shell metal when it has a different lattice constant than the underlying core-metal. Electronic effects occur when the core and shell metal have different electronegativities. The subsurface layers can change the position of d-band center of the shell metal and therefore alter the adsorption energy of the reactants/products, and thus the catalytic activity [106]. A detailed investigation of the effect of the sub-surface layers on the catalytic properties is given in Chapter 6.

Finally, both mono- and bimetallic, gold-containing nanoparticles are being used for light enhanced catalysis. Herein, one irradiates the nanoparticles at the surface plasmon resonance and uses the resulting "hot electrons" to participate in the catalysis [107]. Although this is an interesting and novel field of research, it is not within the scope of this thesis. For good reviews we refer to [108, 109].

1.5 Scope of the thesis

In Figure 1.5 we present a graphical abstract of this thesis. We start off with monometallic gold nanorods. In **Chapter 2** the synthesis of gold nanorods with different volumes and aspect ratios, and the coating of gold nanorods with a protective mesoporous silica shell is described. We investigated the thermal stability of these mesoporous silica coated gold nanorods and show that both the particle volume and aspect ratio play an important role in the thermally induced deformation of the gold nanorods to a more spherical shape. In **Chapter 3** the gold nanorod synthesis is extended to bimetallic nanorods. We describe a stepwise approach for the synthesis of well-defined core-shell nanorods in which Ag, Pd and Pt shells of controllable thickness and morphology were grown around the Au nanorods. In **Chapter 4** these core-shell nanorods were used as a starting material for the formation of alloyed bimetallic nanorods, which was successfully done via thermal treatment. Herein, the mesoporous silica shell was crucial in preserving the anisotropic rod shape at the high temperatures required for the alloying process. In **Chapter 5** the alloying of Au-Ag core-shell nanorods is described in more detail. We employed advanced characterization techniques such as *in situ* heating electron microscopy and *in situ* X-ray spectroscopy to study the alloying process *in situ* on a single particle and ensemble averaged level. We found that the particle composition and volume strongly influenced the alloying process and developed a theoretical model that successfully predicts the alloying temperatures of bimetallic nanoparticles. For the work presented in **Chapter 6** we used the knowledge of the previous chapters and synthesized differently structured Au-Pd nanorods, which were used as catalysts in the selective hydrogenation of butadiene. We precisely correlated the structure and catalytic properties of the bimetallic nanorods and showed that their catalytic behavior critically depends on both the metal distribution and Pd-shell thickness. Uniquely, our relatively large Au-core Pd-shell nanorods outperformed conventional Pd and Au-Pd catalysts which contain much smaller nanoparticles. In **Chapter 7** we move to spherical assemblies of gold nanorods and their characterization in 3D. We show that FIB-SEM tomography is ideal for the analysis of particle ensembles too large for electron microscopy containing particles too small to be resolved with confocal microscopy. By making use of advanced tracking algorithms both the positions and orientations of the individual nanoparticles in the assemblies were obtained. In **Chapter 8** we describe the usage of gold nanorod ensembles for surface enhanced Raman spectroscopy. By assembling gold nanorods with a thick and thin silica shell, structures with and without plasmonic hotspots between the nanorods were obtained, respectively. Structures with plasmonic hotspots in between the particles exhibited large enhancements of the Raman signal, if the porosity of the ensemble was sufficient for the probe molecules to diffuse into the structure.

All together this thesis shows that well-defined gold-based nanorods are valuable model systems to precisely correlate structural and functional properties of mono- and bimetallic nanoparticles and their assemblies.

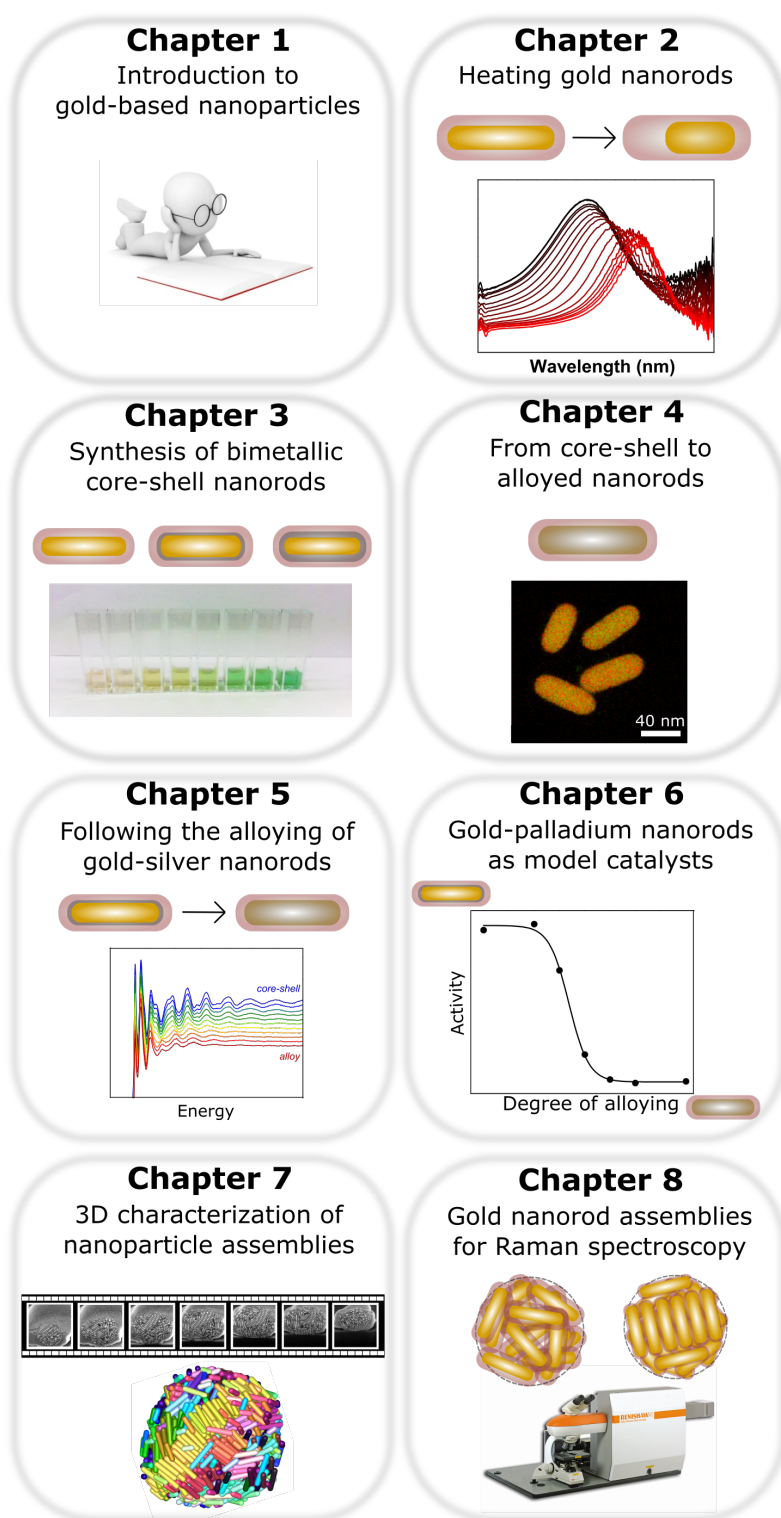


Figure 1.5: Graphical outline of the chapters in this thesis.
The image for Chapter 1 was taken from shutterstock.com

Synthesis and thermal stability of silica coated gold nanorods

2

Abstract

Gold nanorods have successfully been applied in many light based applications ranging from photo-thermal cancer treatment to plasmon enhanced catalysis and optical data storage. These applications all make use of the plasmonic properties of the gold nanorods, which largely depend on the shape and in particular the aspect ratio (length over diameter) of the rod. However, at elevated temperatures the out of equilibrium rod shape has the tendency to deform to a thermodynamically more favourable, spherical shape. In this chapter, we investigated the parameters influencing the synthesis and deformation of mesoporous silica coated, single-crystalline gold nanorods (Au@SiO₂ NRs). In particular, we studied the relationship between the deformation behaviour and the particle volume ($V = 3 - 60 \times 10^3 \text{ nm}^3$) and aspect ratio ($AR = 2.8 - 6.0$) of the nanorods. By changing the seed concentration and the reaction rate in the seed mediated rod synthesis, the particle volume and aspect ratio of the nanorods were adjusted, respectively. Next, we employed a multi-technique approach comprising *ex situ* transmission electron microscopy (TEM), *in situ* and *ex situ* Fourier transform visible infrared (VIS-IR) spectroscopy to monitor the thermal stability of the differently sized Au@SiO₂ NRs in a temperature range from 100 to 500 °C. The deformation of all Au@SiO₂ NRs occurred well below the melting point of bulk gold and the deformation behavior depended on both the particle volume and aspect ratio, where lower particle volumes and higher aspect ratios led to more severe deformation, already at temperatures below 200 °C. At higher temperatures ($\geq 300 \text{ °C}$) the particle deformation was slowed down for all sizes studied, possibly due to restrictions imposed by the silica shell.

2.1 Introduction

Gold nanorods have well-defined plasmonic properties, which can be adjusted by tuning the particle shape as described in Chapter 1. In particular the longitudinal surface plasmon (LSPR) is highly particle shape dependent and can easily be changed via the aspect ratio (AR) of the NRs [13, 110]; low and high AR rods have resonance frequencies in the visible and near-infrared region of the spectrum, respectively. Generally, gold nanorods have superior plasmonic properties, i.e. higher extinction cross sections and higher local electric field enhancements, compared to spheres. These properties, in combination with a good chemical stability, make gold nanorods suitable materials for optical applications such as optical data storage [111–113], biomedical applications [114–116] and plasmon enhanced catalysis [117, 118].

However, during oven- [91, 119–121] or laser induced heating [119, 122, 123], the out-of-equilibrium rod-shape becomes unstable and deformation to a more spherical shape can occur, leading to a blue shift and lower intensity of the LSPR. Some applications make use of this deformation and altered optical properties to store information [111–113], but in most cases thermally induced deformation is undesirable.

There are several parameters influencing the deformation behaviour of AuNRs. Firstly, the aspect ratio has a large impact on the thermal stability. High AR rods deform more severely and at lower temperatures/laser powers compared to low AR rods [91, 112, 122]. Secondly, the presence of a coating around the nanorods strongly influences the deformation behaviour. Inorganic coatings such as thin carbon shells [121, 124], silica coatings [91, 120, 125] and zirconia matrices [126] can stabilize the nanorod shape to hundreds of degrees higher temperatures compared to uncoated NRs, which already deform fully below 200 °C [119, 121, 127, 128]. Coating induced stabilization has been observed both in laser induced heating [112, 125] and oven heating [91, 120, 125]. The stabilizing effect of the surface coatings is probably a combination of a kinetic effect originating from retardation of the Au atom surface migration, and a thermodynamic effect coming from the lowering of the surface energy of the AuNRs when applying a surface coating. For many applications, porous coatings are usually favoured over closed shells as the porosity keeps the Au surface accessible, which is crucial in e.g. catalysis [129, 130]. Thirdly, the crystallinity and the type of surface facets are expected to affect the deformation behaviour of AuNRs as well, as was demonstrated in computational studies [131, 132], although rarely studied in experiments [133] as far as we are aware of. The orientation of the FCC lattice planes and surface facets of the AuNR generally depend on the colloid synthesis method and can be tuned by varying the type of surfactant; e.g. use of citrate, CTAB and gemini surfactants results in pentatwinned $\{100\}$ [19, 134], single-crystalline $\{110\}$ and $\{100\}$ [21], and single-crystalline $\{520\}$, $\{110\}$ and $\{100\}$ surface faceted AuNRs [21], respectively.

Although many studies have been carried out to understand the key parameters governing the deformation of AuNRs better, there are unstudied parameters left. As mentioned above, the influence of the surface facets and crystallinity on the deformation of AuNRs has not been investigated experimentally. More surprisingly, the influence of the particle volume has rarely been studied [135]. It is well known that the physicochemical properties of gold nanoparticles (AuNPs) strongly depend on the particle size [4, 5, 136].

For instance, the melting temperature of AuNPs changes drastically from 900 to 300 °C when decreasing the particle diameter from 20 to 1.5 nm. Recently, the thermal stability of small gold nanorods embedded in polymer matrices was indeed found to be size dependent, where small ($V = 10 \times 10^3 \text{ nm}^3$) NRs deformed more severely than large ($V = 18 \times 10^3 \text{ nm}^3$) NRs when heated at 120-220 °C. Finally, the influence of the aspect ratio on thermally induced deformation of silica coated AuNRs was only studied for silica coated AuNRs with a relatively small variation in aspect ratio ($AR = 2.5 - 4.3$) and small, non-equal particle volumes ($V = 1.7 - 3.8 \times 10^3 \text{ nm}^3$) [91], or only for low temperatures ($\leq 220 \text{ °C}$) [135]. However, studying purely the volume and aspect ratio dependency while keeping all other parameters the same is not trivial since this would require simultaneous control over the AR and particle volume in the colloidal synthesis.

In this chapter we systematically studied the particle volume and aspect ratio dependency on the thermal stability of mesoporous silica coated gold nanorods (Au@SiO₂NRs) over a large temperature range from 100 to 500°C. We synthesized two series of well-defined, CTAB stabilized AuNRs, coated with a $\sim 18 \text{ nm}$ thick mesoporous silica coating. The AuNRs had either a varying particle volume and fixed aspect ratio ($V = 0.2 - 6 \times 10^4 \text{ nm}^3$, $AR = 4$), or a varying aspect ratio but fixed particle volume ($AR = 2.8 - 6.0$, $V = 1.0 \times 10^4 \text{ nm}^3$). All NRs had the same single-crystalline structure with predominantly $\{110\}$ and $\{100\}$ FCC surface facets [21]. We studied the thermally induced deformation of these rods *ex-* and *in situ*, both on a single particle and ensemble averaged level by using TEM imaging and VIS-IR spectroscopy, respectively. We specifically chose to investigate silica coated AuNRs because the deformation of the AuNRs is slowed down compared to uncoated AuNRs, which makes it easier to compare the thermal stability of different samples and because plasmonic coupling between the AuNRs is prevented which enables studying of the deformation of the rods with VIS-IR spectroscopy. Our thermal stability studies show that the particle volume indeed had a large impact on the deformation behaviour of Au@SiO₂NRs, where smaller particle volumes led to more severe deformation. In line with previous reports, we also find a clear dependency on the aspect ratio of the NRs, where higher aspect ratios ($AR = 6$) led to more severe deformation, occurring at temperatures as low as 200 °C. The results described in this chapter contribute to the fundamental understanding of the deformation behaviour of AuNRs and will help to improve AuNR based (photo)thermal applications.

2.2 Experimental

Chemicals

All chemicals were used as received without further purification. Hexadecyltrimethylammonium bromide (cetyltrimethylammonium bromide, CTAB, >98.0%) and sodium oleate (NaOL, >97.0%) were purchased from TCI America. Hydrogen tetrachloroaurate trihydrate (HAuCl₄·3H₂O), sodium hydroxide (98%), and polyvinylpyrrolidone (PVP, average molecular weight 58 kg/mol, K29-32) were purchased from Acros Organics. L-Ascorbic Acid (BioXtra, $\geq 99\%$), silver nitrate (AgNO₃, $\geq 99\%$), sodium borohydride (NaBH₄, 99%), hydrochloric acid (HCl, 37 wt% in water, 12.1 M) and tetraethyl orthosilicate (TEOS, 98%) were purchased from Sigma-Aldrich. Ultrapure water (Millipore Milli-Q grade)

with a resistivity of $18.2\text{ M}\Omega$ was used in all of the experiments. All glassware for the AuNR synthesis was cleaned with fresh aqua regia (HCl/HNO_3 in a 3:1 volume ratio), rinsed with large amounts of water and dried at $100\text{ }^\circ\text{C}$ before usage.

Synthesis of AuNRs of varying particle volume

To obtain smaller AuNRs, we modified the seed mediated growth protocol of Ye *et al.* and increased the Au-seed concentration to decrease the nanorod particle volume. Here, we varied the seed concentration over a larger range than described in the original protocol. To exclude any other differences in the synthesis mixture apart from the seed concentration, we prepared one 125 mL growth solution, which we split up in 5×25 mL batches, just before adding the seeds. To each 25 mL growth solution 4.0, 8.0, 40, 200 or 400 μL seed solution was added.

For the rods presented in Figure 2.1 we first prepared an aqueous solution containing 1.75 g CTAB, 0.307 g NaOL and 62.5 mL MQ H_2O , which was stirred at 350 rpm for 30 min in a $50\text{ }^\circ\text{C}$ waterbath. Next, the waterbath was cooled to $30\text{ }^\circ\text{C}$, and 2.40 mL 10 mM AgNO_3 was added. After 30 s 62.5 mL 1.0 mM HAuCl_4 was added and the mixture was left for 90 min while stirring at 350 rpm (revolutions per minute). Meanwhile, a seed solution containing 10 mL 0.10 M CTAB and 51 μL 50 mM HAuCl_4 was prepared. By adding 1.00 mL 6.0 mM icecold NaBH_4 , while vigorously stirring for 2 min, small Au-seeds were formed. After 90 minutes, 1.05 mL concentrated HCl (37 wt%, 12.1 M) was added to the growth solution, followed by the addition of 0.313 mL 0.064 M ascorbic acid 15 min later. Thereafter the growth mixture was divided in 5 separate batches of 25 mL. To each batch 4.0, 8.0, 40, 200 or 400 μL seed solution was added. After ~ 2 min of stirring, the growth mixtures were left unstirred at $30\text{ }^\circ\text{C}$ overnight. The next morning, extinction spectra were recorded of the AuNRs before washing the rods (Figure 2.1e). To this end, 250 μL rod dispersion was diluted with 750 μL H_2O . The rods grown with 4.0, 8.0 and 40 μL seeds were washed using centrifugation at 7000 rcf (relative centrifugal force) for 40 min (Rotina 380R Hettich centrifuge). The rods grown with 200 or 400 μL seeds were washed using centrifugation at 12000 rcf for 60 min. All rods were washed once with 10 mL of MQ H_2O and stored in 10 mL 5.0 mM CTAB H_2O .

Preparation of the AuNRs for the thermal stability measurements

For the synthesis of the AuNRs with different volumes but similar aspect ratio, and for the AuNRs with a different aspect ratio but similar volume, the method by Ye *et al.* was used, as described above. Generally, the synthesis was performed on a 500 mL scale with a growth solution containing 7.0 g CTAB, 1.24 g NaOL, 25 mL MQ H_2O and 250 mL 1.00 mM HAuCl_4 , x mL AgNO_3 (10 mM), y mL concentrated HCl (12.1 M), 64 mM ascorbic acid and z mL seed solution. The x , y , z values are given in Table 2.1. The seeds were prepared from a 10 mL 0.10 M CTAB, 51 μL HAuCl_4 and 1.0 mL NaBH_4 . The subsequent rod growth was performed under static conditions in a $30\text{ }^\circ\text{C}$ water bath overnight. Thereafter, the rods were centrifuged at 8000 rcf for 30 min, washed with H_2O and redispersed in 5.0 mM CTAB H_2O .

Table 2.1: Synthesis parameters of the Au@SiO₂ NRs used for the particle volume dependent thermal stability measurements. The concentration of the AgNO₃ solution and HCl were 10 mM and 12.1 M, respectively.

Volume ($\times 10^3$ nm ³)	AgNO ₃ (mL)	HCl (mL)	Seeds (mL)
2.7 ± 1.5	9.60	2.10	4.00
10 ± 3.7	9.60	2.50	1.60
21 ± 6.4	9.60	2.10	0.80
60 ± 30	9.60	3.0	0.40

Table 2.2: Synthesis parameters of the Au@SiO₂ NRs used for the aspect ratio dependent thermal stability measurements.

Aspect ratio	AgNO ₃ (mL)	HCl (mL)	Seeds (mL)
2.8 ± 0.45	7.20	2.10	2.40
3.8 ± 0.51	7.20	2.10	2.40
4.1 ± 0.56	9.60	2.10	1.0
6.0 ± 1.0	9.60	4.20	0.80

Silica coating

The CTAB stabilized AuNRs were coated with a 18 nm mesoporous silica shell *via* the method of Gorelikov *et al.* [90]. The coating was performed in 1.5 mM CTAB aqueous solution containing 1.0 mM NaOH and an AuNR concentration corresponding to an extinction maximum of 1.0 when diluting 10 \times in H₂O. To 100 mL reaction mixture 3 times 300 μ L of a 0.90 M TEOS in EtOH was added with a 30 min time interval in between the additions, while magnetically stirring at 300 rpm in a 30 °C water bath. The Au@SiO₂ NRs were centrifuged at 8000 ref for 30 min, washed with water and ethanol, and stored in ethanol.

Electron microscopy

The Au@SiO₂ NR samples before and after thermal treatment were imaged with a Tecnai12 microscope operating at 120 keV and a Tecnai20FEG microscope operating at 200 keV. Prior to the transmission electron microscopy (TEM) measurements the Au@SiO₂ NRs were dispersed in EtOH and dropcasted on a copper TEM grid (200 mesh copper (100), Formvar/carbon film).

Thermal stability experiments

The thermal stability experiments were carried out in a Linkam temperature stage, mounted on a Bruker Hyperion 2000 IR microscope connected to a Bruker Vertex 70 FTIR/VIS spectrophotometer. All measurements were carried out in N₂ flow. For the thermal stability experiments, the AuNRs were first dropcasted on a circular glass slide. In the *in situ* measurements the temperature was increased with 1 °C/min from 20 to 500 °C. Every 25 °C an extinction spectrum was recorded. For the *ex situ* heating experiments

the sample was heated with 30 °C/min to 100, 200, 300, 400 or 500 °C and kept at this temperature for 2 h. After the sample had cooled down to room temperature a drop of 85 wt% glycerol in water (refractive index $n_D^{21} = 1.45$)[137] was put on top to refractive index match the silica shell and an extinction spectrum was recorded.

Nitrogen physisorption

The pore size distribution of the mesoporous shells around the AuNRs was determined with nitrogen physisorption. The analysis was performed on only one Au@SiO₂ NR sample since a relatively large amount of sample was needed (13.7 mg dried sample, $L_{Au} = 83$ nm, $D_{Au} = 27$ nm, $D_{SiO_2} = 17$ nm). Prior to the measurements the CTAB was removed by washing the NRs with a 0.10 M HCl in EtOH solution [49]. Thereafter the rods were dried from 15 mL EtOH dispersion at 100°C in static air overnight. The nitrogen physisorption measurements were done at -196 °C (77 K) (Micromeritics, TriStar 3000). Before the measurement an additional drying step at 200 °C in N₂ was performed overnight.

2.3 Results and Discussion

Controlling the particle volume of CTAB stabilized AuNRs

In Figure 2.1 the transmission electron microscopy (TEM) images and corresponding optical spectra of the AuNRs grown with 4.0, 40 and 400 μ L are shown (Figure 2.1a,b,c). The TEM images are displayed at the same magnification to clearly show the decrease in particle volume with increasing seed concentration. From these TEM images we determined the full set of size parameters (volume, length, diameter, aspect ratio) per particle. The average size parameters and corresponding standard deviations are given in Table 2.3. In Figure 2.1d we plot the particle volume versus the amount of seed solution added during the synthesis. The corresponding extinction spectra of the AuNRs, 4 \times diluted in water compared to the original synthesis mixture, are shown in Figure 2.1e.

The TEM images and corresponding analysis in Figure 2.1a-d clearly show that the amount of seed solution (4.0-400 μ L) added to the same volume of growth solution (25 mL) influenced the particle volume. As expected the AuNRs grown in the solution with the lowest amount of seeds were much larger. When adding 4.0 μ L seeds the particle volume was 8.8×10^4 nm³, whereas the addition of 400 μ L seed solution led to a 40 times smaller particle volume of 2.2×10^3 nm³. Thus, by increasing the amount of seeds the particle volume was successfully decreased and the particle diameter decreased below 10 nm.

We noticed that when using higher seed concentrations the polydispersity of the resulting NRs increased and more non-rod like particles were formed such as cubes and spheres, as can be seen in Figure 2.1c. An increase in polydispersity is most clearly visible from the VIS-IR spectra (Figure 2.1e), where the width of the LSPR peak is increased, which is related to the polydispersity in the aspect ratio of the NRs. From the TEM size measurements we determined the polydispersity in size for all the different batches of nanorods. The polydispersity in length and diameter was only 6% for the rods with the largest volume ($V = 8.8 \times 10^4$ nm³), whereas it exceeded 16% for the sample containing

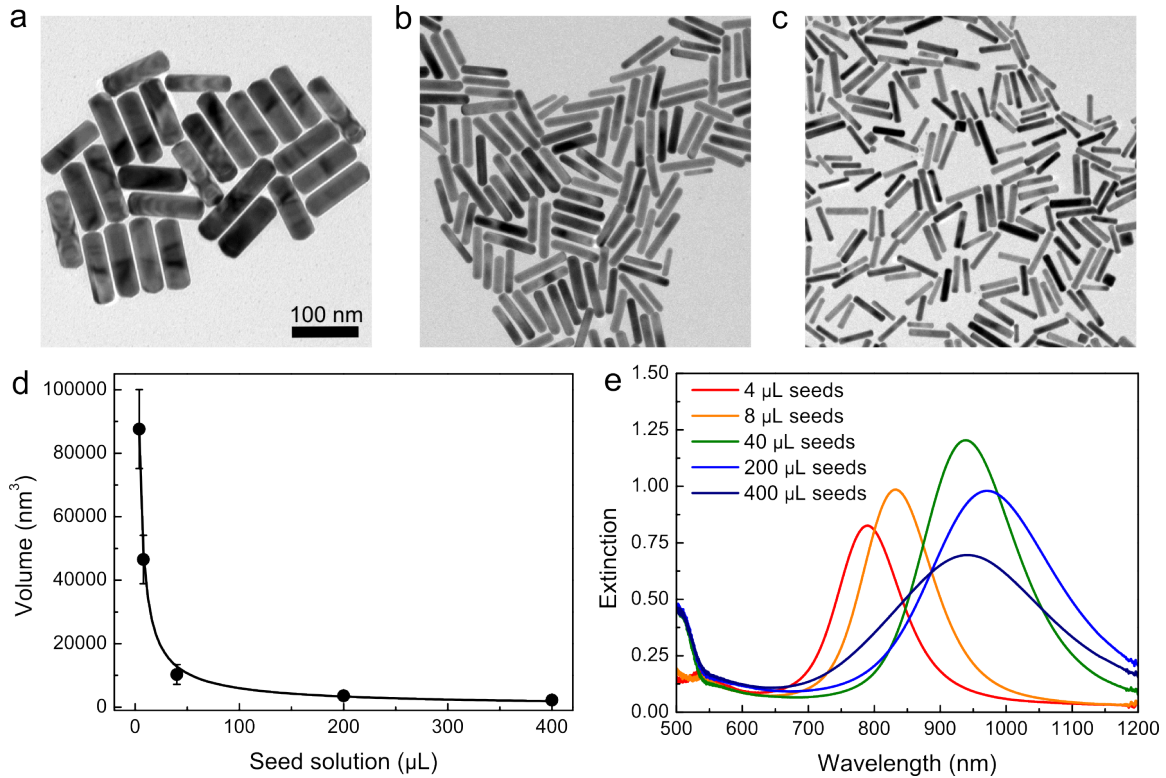


Figure 2.1: CTAB stabilized AuNR with different particle volumes, synthesized by adding different amounts of seed solution. TEM images of AuNRs grown in a 25 mL growth solution to which 4.0 (a), 40 (b) and 400 μL (c) was added, resulting $V = 2.22, 10.3$ and $87.6 \times 10^3 \text{ nm}^3$, respectively. d) Plot of the particle volume determined from TEM versus the amount of seed solution added. The line is an exponential fit to the experimental data. e) Extinction spectra of the AuNRs recorded directly after synthesis, $4\times$ diluted in water.

the smallest NRs ($V = 2.2 \times 10^3 \text{ nm}^3$). In addition it should be noted that not only the particle volume changed upon increasing the amount of seeds, but also the aspect ratio of the rods. When decreasing the particle volume from $8.8 \times 10^4 \text{ nm}^3$ to $2.2 \times 10^3 \text{ nm}^3$, the aspect ratio of the rods increased from 3.3 to 5.1. Thus, the synthesis of rods

Table 2.3: Dimensions of CTAB stabilized AuNRs synthesized with different seed concentrations. The AuNRs were synthesized on a 25 mL scale to which $x \mu\text{L}$ seed solution was added. The particle sizes were determined from TEM analysis. The volume length, diameter and aspect ratio were determined per particle and then averaged over 80 particles. The \pm -values are the corresponding standard deviations.

Seeds (μL)	Volume ($\times 10^3 \text{ nm}^3$)	Length (nm)	Diameter (nm)	Aspect ratio
4.0	87.6 ± 12.4	110 ± 9.5	33.5 ± 2.1	3.30 ± 0.36
8.0	46.5 ± 7.60	98.6 ± 6.8	25.6 ± 2.0	3.88 ± 0.42
40	10.3 ± 3.1	71.4 ± 8.7	13.8 ± 1.5	5.19 ± 0.60
200	3.56 ± 1.3	50.4 ± 8.66	9.61 ± 1.2	5.25 ± 0.70
400	2.22 ± 0.73	42.4 ± 6.83	8.31 ± 0.86	5.11 ± 0.70

with different particle volumes but the same aspect ratio requires adjustment of multiple parameters in the synthesis.

The plot in Figure 2.1d shows that the particle volume as a function of the amount of seeds flattens around $2 \times 10^3 \text{ nm}^3$, meaning that lower particle volumes can not be achieved via this method. So far, only *via* seedless synthesis methods one can go to particle volumes below $1 \times 10^3 \text{ nm}^3$ and obtain rods with a particle diameter as small as 2.5 nm [138]. However, these seedless growth methods are known to be very sensitive to the exact synthesis conditions, such as the pH [138] and the AgNO_3 concentration [139], but also the stirring rate and stirring time [140], making seedless syntheses more difficult to reproduce. We therefore preferred adjusting the seed mediated growth of *Ye et al.* to synthesize the differently sized Au@SiO_2 NRs used for the thermal stability measurements described in the remainder of this chapter.

Tuning the dimensions of mesoporous silica coated gold nanorods

For the thermal stability measurements we synthesized two series of four batches of mesoporous silica coated AuNRs (see Table 2.5 and 2.4). Within a series the Au@SiO_2 NRs had either a fixed aspect ratio and varying particle volume or a fixed particle volume and varying aspect ratio. To achieve this, we first synthesized uncoated, CTAB stabilized AuNRs and modified 3 parameters in the synthesis: the AgNO_3 , HCl and seed concentration. As described in the previous section the seed concentration can be used to vary the particle volume. The AgNO_3 and HCl concentration are important in modifying the aspect ratio of the rods [13]. Both a higher HCl and AgNO_3 concentration lead to higher aspect ratio rods. As discussed in the introduction of this thesis, the role of the Ag^+ ions in the gold nanorod synthesis is rather complex and largely debated. It is therefore not clear as to why higher silver concentrations are needed to obtain higher AR rods, but it

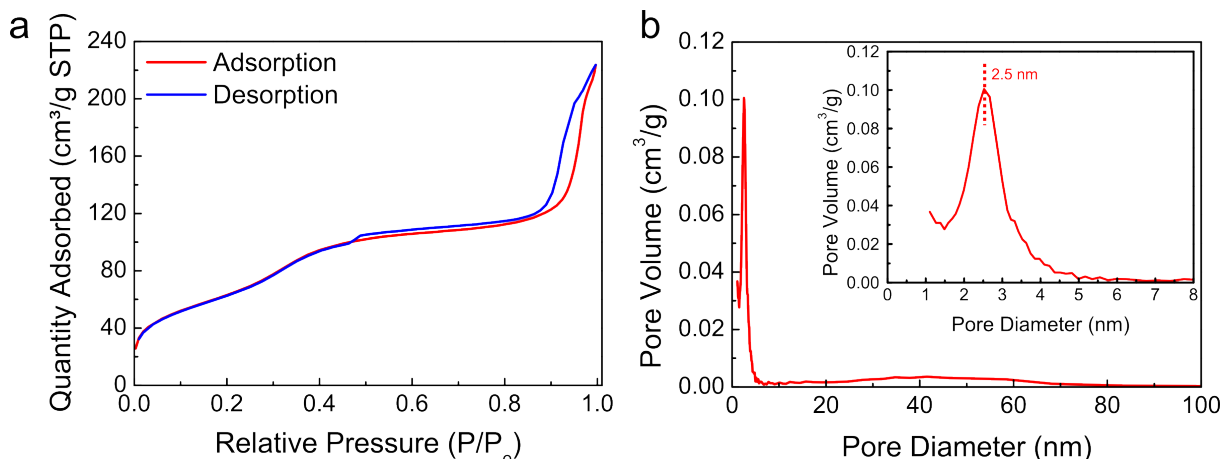


Figure 2.2: Nitrogen physisorption analysis of mesoporous silica coated Au NRs ($L_{\text{Au}} = 83 \text{ nm}$, $D_{\text{Au}} = 27 \text{ nm}$, $D_{\text{SiO}_2} = 17 \text{ nm}$). a) Adsorption (red) and desorption (blue) isotherms where the amount of adsorbed N_2 is plotted against the relative pressure with p_0 as the standard pressure. b) Plot of the pore diameter versus the pore volume, derived from the adsorption isotherm in a. CTAB was removed from the mesopores prior to the measurement (see Experimental section).

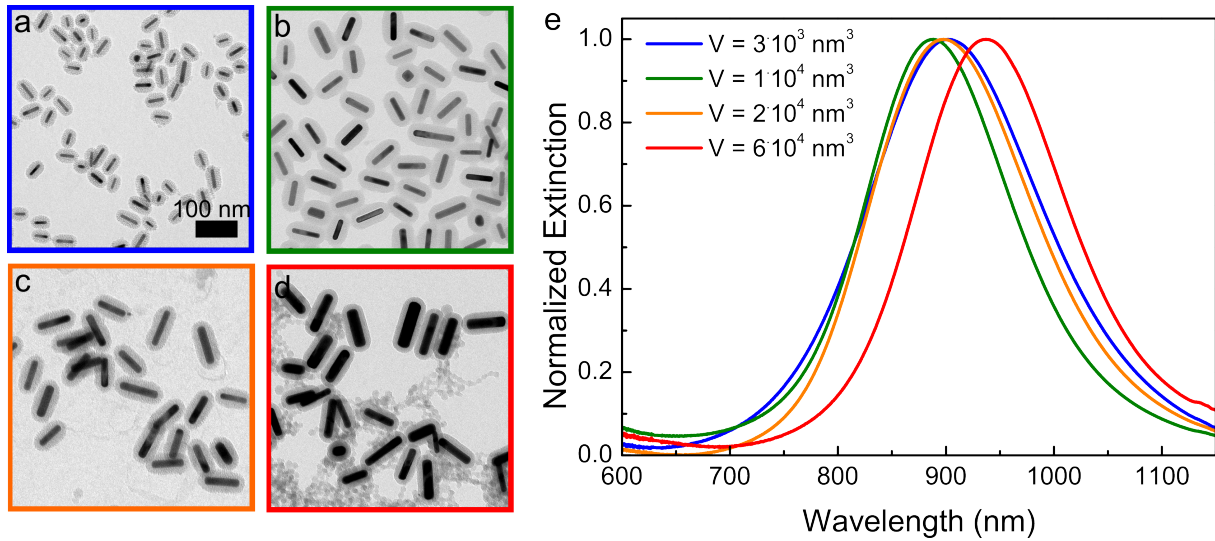


Figure 2.3: TEM images and optical extinction spectra of the samples used for the particle volume thermal stability measurements. a-d) Au@SiO₂ NRs with the same aspect ratio but increasing particle volume: a) $V = 2.7 \times 10^3 \text{ nm}^3$ / $AR = 4.1$, b) $1.0 \times 10^4 \text{ nm}^3$ / $AR = 4.0$, c) $2.1 \times 10^4 \text{ nm}^3$ / $AR = 4.2$, d) $6.0 \times 10^4 \text{ nm}^3$ / $AR = 4.1$. e) Corresponding normalized extinction spectra of the Au@SiO₂ NRs with $V = 2.7 \times 10^3$ (blue), 1.0×10^4 (green), 2.0×10^4 (orange), $6.0 \times 10^4 \text{ nm}^3$ (red) recorded in EtOH. The full set of particle dimensions are given in Table 2.4.

could be related to the blockage of surface facets along the length of the rods leading to preferential growth of the tips. By adding HCl the pH of the growth solution is lowered and the fraction of reactive, deprotonated ascorbic acid molecules is reduced (see Chapter 3), leading to a slower nanorod growth and more elongated nanorods. The synthesis details such as the seed, AgNO₃ and HCl concentration that we used to obtain differently sized AuNRs can be found in Table 2.1 and 2.2 in the Experimental section.

After the rod synthesis, the AuNRs were coated with a $\sim 18 \text{ nm}$ mesoporous silica coating [90]. The silica coating was grown in an aqueous, basic solution ($\text{pH} \sim 11$) containing CTAB micelles, which served as a template for the formation of a MCM-41 like mesoporous structure [141]. We analysed the pore size of the mesopores in the silica shells with nitrogen physisorption. In Figure 2.2a and b the nitrogen physisorption isotherm upon adsorption (red) and desorption (blue), and the pore volume versus the pore diameter derived from the adsorption isotherm are shown, respectively. The plot in Figure 2.2b shows that the pore diameter distribution was bimodal with a sharp peak at around a pore diameter of 2.5 nm and a more broad peak around 42 nm, resulting from the pores in and between the mesoporous silica shells, respectively. The BET (Brunauer–Emmett–Teller) surface area was 235 m²/g and the BJH (Barrett, Joyner, and Halenda) cumulative pore volume 0.334 cm³/g for pores with a diameter between 1 and 300 nm (based on the adsorption isotherm).

In Figure 2.3 we show the TEM images of the Au@SiO₂NRs with $V = 2.7 \times 10^3 \text{ nm}^3$ to $6.0 \times 10^4 \text{ nm}^3$ and $AR = 4.0 - 4.2$, and in Figure 2.4 we show the Au@SiO₂NRs with $AR = 2.8$ to 6.0 and $V \sim 1 \times 10^4 \text{ nm}^3$. The full sets of size parameters of the AuNRs are

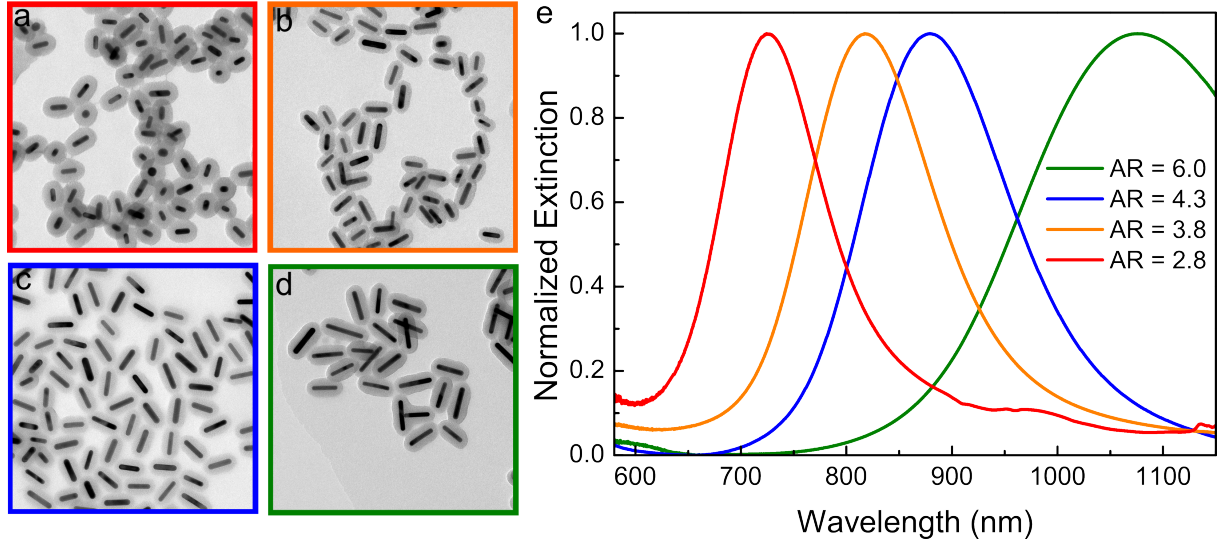


Figure 2.4: TEM images of the samples used for the aspect ratio dependent thermal stability measurements. a-d) Au@SiO₂ NRs with the same particle volume, but increasing aspect ratio: a) $AR=2.8 / V=9.3 \times 10^3 \text{ nm}^3$, b) $AR=3.8 / V=11 \times 10^3 \text{ nm}^3$, c) $AR=4.1 / V=11 \times 10^3 \text{ nm}^3$, d) $AR=6.0 / V=9.5 \times 10^3 \text{ nm}^3$. e) Corresponding extinction spectra of the Au@SiO₂ NRs with $AR=2.8$ (red), 3.8 (orange), 4.3 (blue) and 6.0 (green) recorded in EtOH. The full set of particle dimensions are given in Table 2.5.

listed in Table 2.4 and 2.5. In Figure 2.3e and 2.4e the extinction spectra of the samples with $V=0.27$ to $6.0 \times 10^4 \text{ nm}^3$ and $AR=2.8$ to 6.0 are shown, respectively. The LSPR peaks of the Au@SiO₂ NRs in Figure 2.3e are less than 80 nm apart indicating that the AR of the NRs matched closely, as is also clear from the particle sized derived from the TEM measurements listed in Table 2.4. Only the LSPR peak position of the Au@SiO₂ NRs with the largest particle volume ($V=6.0 \times 10^4 \text{ nm}^3$) is red-shifted, whereas its AR is similar to the other samples according to the TEM measurements. This red-shift is most likely caused by so-called retardation effects which are known to occur at larger particle volumes [142]. The optical spectra in Figure 2.4e show that the LSPR peak positions of the Au@SiO₂ NRs shift from the VIS to IR when increasing the AR from 2.8 to 6.0, as expected.

Table 2.4: Dimensions of the Au@SiO₂ NRs used for the particle volume dependent thermal stability measurements. The average particle sizes and corresponding standard deviations were determined from TEM analysis and are an average of 100 particles. The surface to volume ratio is abbreviated with S/V.

Volume ($\times 10^3 \text{ nm}^3$)	Length (nm)	Diameter (nm)	Aspect ratio	S/V (nm^{-1})
2.7 ± 1.5	40 ± 10	9.4 ± 1.6	4.1 ± 0.88	0.48 ± 0.090
10 ± 3.7	60 ± 12	15 ± 2.0	4.0 ± 0.85	0.30 ± 0.043
21 ± 6.4	79 ± 8.2	19 ± 2.5	4.2 ± 0.61	0.23 ± 0.029
60 ± 30	107 ± 19	27 ± 5.6	4.1 ± 0.67	0.17 ± 0.040

Table 2.5: Dimensions of the Au@SiO₂ NRs used for the aspect ratio dependent thermal stability measurements. The average particle sizes and corresponding standard deviations were determined from TEM analysis and are an average of 100 particles. The surface to volume ratio is abbreviated with S/V.

Aspect ratio	Length (nm)	Diameter (nm)	Volume ($\times 10^3$ nm ³)	S/V (nm ⁻¹)
2.8 ± 0.45	47 ± 9.6	17 ± 1.7	9.3 ± 3.6	0.28 ± 0.031
3.8 ± 0.51	60 ± 10	16 ± 1.8	11 ± 3.9	0.28 ± 0.034
4.1 ± 0.56	64 ± 7.1	15 ± 1.6	11 ± 2.9	0.29 ± 0.030
6.0 ± 1.0	77 ± 13	13 ± 1.5	9.5 ± 3.1	0.34 ± 0.041

Volume dependent thermal stability of mesoporous silica coated AuNRs

First, we investigated the thermal stability of mesoporous silica coated AuNRs as a function of particle volume. The rods were heated at a temperature between 100-500 °C for 2 h in static air on a microscope slide. Next, TEM imaging was used to investigate the degree of deformation in each sample. In Figure 2.5a-d we show the Au@SiO₂ NRs with $V = 2.7 \times 10^3$ nm³ to 6.0×10^4 nm³ after thermal treatment at 100, 300 and 500 °C. From these TEM images the particle dimensions and aspect ratio were obtained. In Figure 2.5e we plot the aspect ratio of the various samples as a function of heating temperature. For all samples the *AR* decreased as a function of heating temperature, but the extent of deformation was different. The smaller the nanorod, the stronger the deformation to a more spherical shape. To show this more clearly, we plot the degree of deformation, expressed in the shift in *AR*, as a function of particle volume for various heating temperatures in Figure 2.5f. Especially when the particle volume was decreased below $V = 2 \times 10^4$ nm³ and the particle diameter below $D = 20$ nm, the influence of particle volume on the thermal stability became more apparent, where significant deformation occurred already between 100 and 200 °C which is many hundreds of degrees below the melting point of bulk Au (1064 °C).

Although the measurement of the particle deformation with *ex situ* TEM measurements is a robust method, it is rather time consuming and does not allow for an *in situ* study of the deformation of a larger amount of rods. Hence, we also used *in situ* visible-infrared spectroscopy measurements (VIS-IR) next to the *ex situ* TEM measurements. In Figure 2.6 we show the *in situ* VIS-IR measurements when heating the same particles as in Figure 2.5 with 1 °C/min in N₂. Extinction spectra were recorded every 25 °C between 25 and 400 °C. In Figure 2.6a and b we show the extinction spectra upon heating for the sample with the lowest and highest particle volume, respectively. The LSPR peak positions of both samples blue shifted for both samples, which indicates deformation of the AuNRs to a more spherical, lower AR shape. The LSPR peak position of the Au@SiO₂ NRs with $V = 2.7 \times 10^3$ nm³ shifted from 890 to 641 nm when heating to 400 °C, whereas the LSPR peak of the Au@SiO₂ NRs with $V = 6.0 \times 10^4$ nm³ shifted only from 922 to 781 nm. This indicates, that similarly to our *ex situ* TEM measurements, smaller Au@SiO₂ NRs deform more strongly. To compare all 4 samples, we plotted the LSPR peak of each sample as a function of heating temperature in Figure 2.6. Despite the fact that the NRs all have a similar AR, the LSPR peak positions do not overlap for the 4 samples

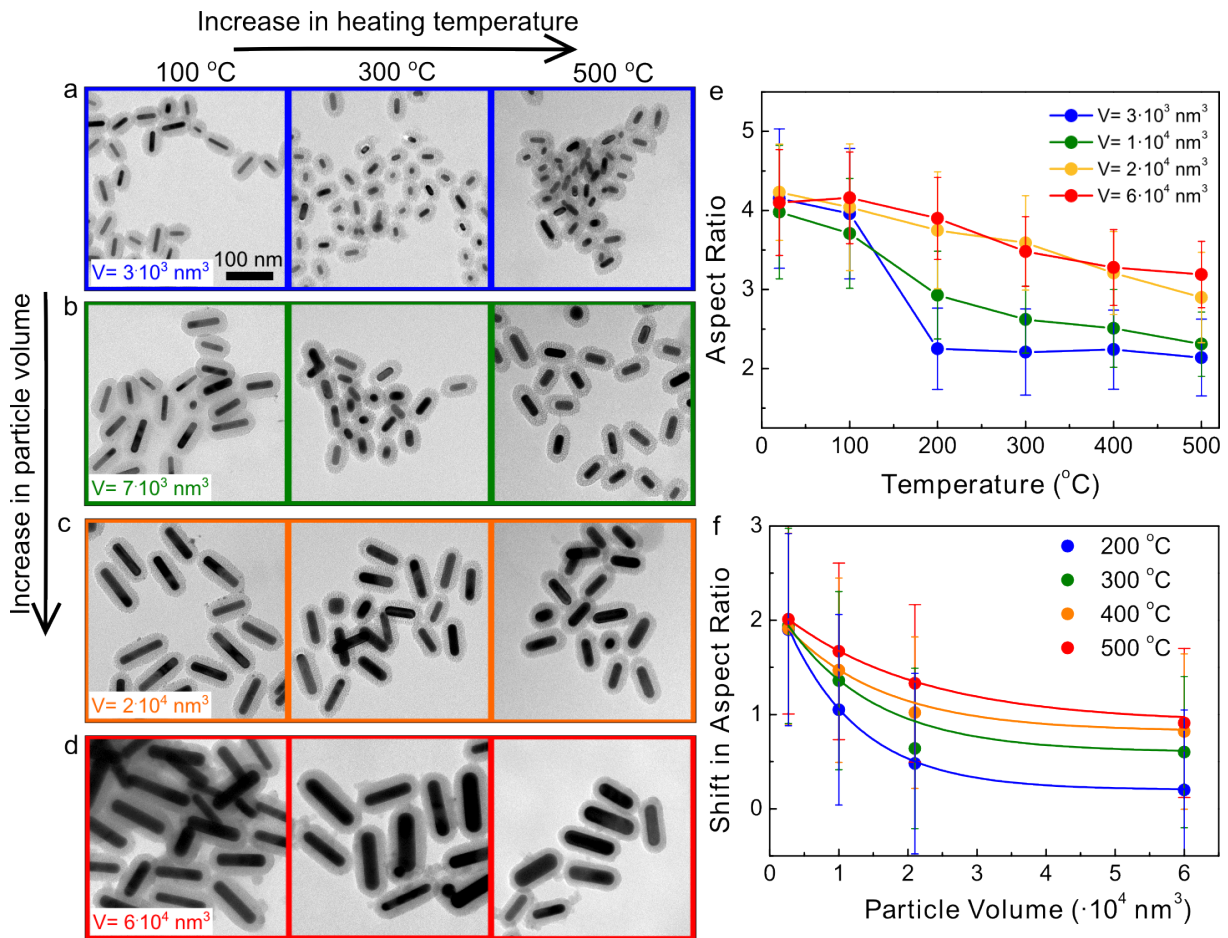


Figure 2.5: Volume dependent thermal stability of mesoporous silica coated AuNRs investigated with *ex situ* TEM measurements. TEM images of Au@SiO₂ NRs with $V = 2.7 \times 10^3 \text{ nm}^3$ (a, blue), $1.0 \times 10^4 \text{ nm}^3$ (b, green), $2.1 \times 10^4 \text{ nm}^3$ (c, orange) and $6.0 \times 10^4 \text{ nm}^3$ (d, red) after thermal treatment at 100 (left), 300 (middle) and 500 °C (right). e) Plot of the aspect ratio (AR) versus the heating temperature. f) Plot of the change in aspect ratio versus the particle volume at 200 (blue), 300 (green), 400 (orange) and 500 (red) °C. The curves in e) are best (exponential) fits to the experimental data. The aspect ratios and particle volumes were determined from TEM and are an average of 100 particles.

before heating. As discussed in the previous section, the red-shift for the larger AuNR samples can be explained by so-called retardation effects which are known to occur at larger particle volumes. In addition, the dielectric constant of the surrounding medium influences the position of the LSPR peak as well. For instance, the dielectric constant of the mesoporous silica shell depends on the degree of condensation of the silica and the amount of physisorbed water in its mesopores. For these reasons, we also plot the relative change in the LSPR peak position as a function of temperature in Figure 2.6d.

We specifically chose not to perform the *in situ* VIS-IR measurements in air since the LSPR peak had the tendency to change with time in air, without heating the sample. In Figure 2.7a the extinction spectra of the same Au@SiO₂ NR sample measured in air directly after drying them on a glass slide and after storage for 2 days at RT are shown

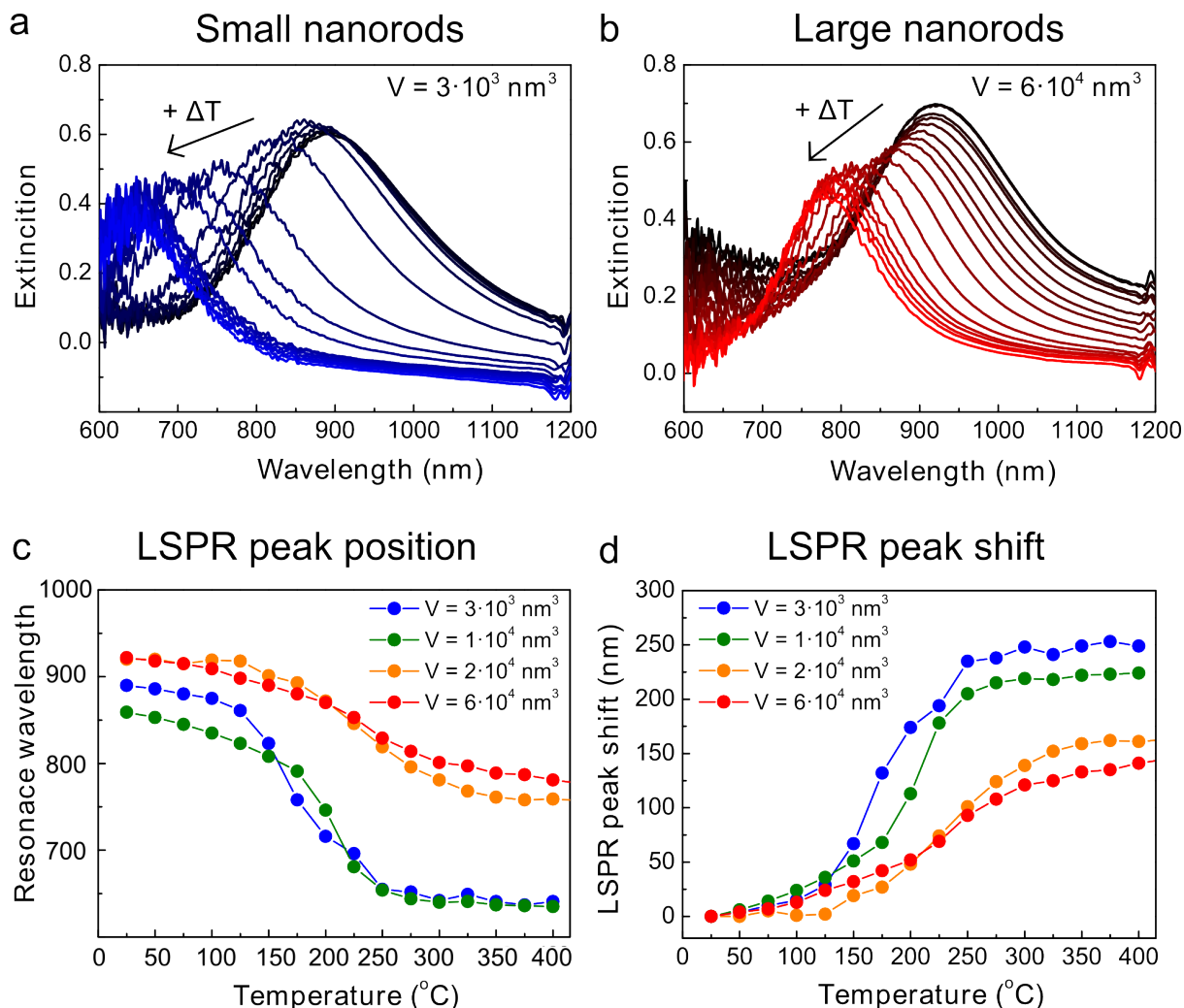


Figure 2.6: *In situ* VIS-IR measurements of thermally induced deformation of differently sized mesoporous silica coated AuNRs. Extinction spectra of Au@SiO₂ NRs with $V = 2.7 \times 10^3$ nm³ (a) and $V = 6.0 \times 10^3$ nm³ (b) acquired every 25 °C from 25 to 400 °. The AR of the rods was similar and varied from 4 to 4.2. c) plot of the LSPR peak position and d) shift in LSPR peak position as a function of heating temperature for particles with $V = 2.7 \times 10^3$ nm³ (blue), 1.0×10^4 nm³ (green), 2.1×10^4 nm³ (orange) and 6.0×10^4 nm³ (red). The heating was carried out under a N₂ flow.

(red curves). The LSPR peak position red-shifted 60 nm in 2 days. Such instabilities in the LSPR peak position were not observed in N₂. The changes in LSPR peak position at RT in air are likely due to an increasing amount of water being physisorbed in the pores of the mesoporous silica shell when exposing the Au@SiO₂ NRs to air. The physisorption of water increases the dielectric constant of the medium around the AuNR and caused a red shift in the LSPR peak position (Figure 2.7b). To test our hypothesis, we diminished the dielectric constant changes in the porous silica shell by adding a drop of glycerol-water (85:15 w%, $n_D^{21} = 1.45$) [137], which is known to refractive index match silica [143]. In Figure 2.7a and b we show that the LSPR peak position indeed stayed considerably more constant when refractive index matching the silica with glycerol-water (blue curves).

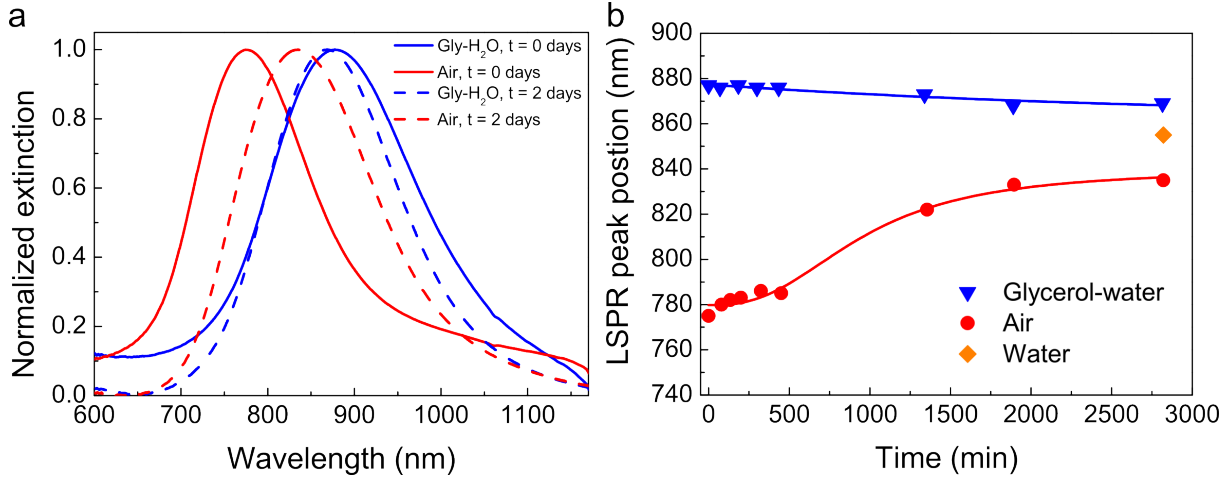


Figure 2.7: Changes in the LSPR peak position of Au@SiO₂ NRs in air at RT. a) Extinction spectra of Au@SiO₂ NRs ($L=72$ nm, $D=19$ nm, $AR=3.8$) dried on glass directly after sample preparation (solid lines) and after storage for 2 days (dotted lines) in air (red) and glycerol-water (blue, 85:15 w%, $n_D^{21} = 1.45$). b) Plot of the LSPR peak position of Au@SiO₂ NRs in air (red), water (orange) and glycerol-water (blue) over time.

To exclude the influence of dielectric constant changes due to variation in the degree of condensation and adsorption of water in the porous silica shell on the LSPR peak position as described above, we also performed *ex situ* VIS-IR measurements. Herein, we heated the Au@SiO₂ NRs at 100-500 °C in a Linkam cell under a N₂ flow. The rods were heated at a constant temperature for 2 h. Afterwards, a drop of glycerol-water was added and the VIS-IR spectra were recorded. From these spectra the LSPR peak position was determined. In Figure 2.8a we plot the LSPR peak position at different heating temperatures for the refractive index matched Au@SiO₂ NRs with $V = 0.27$ to 6.0×10^4 nm³. Clearly, the deformation of the Au@SiO₂ NRs depended on particle volume, where particles with a smaller particle volume deformed more strongly. The *ex situ* VIS-IR measurements were therefore in accordance with the trend measured with *ex situ* TEM and *in situ* VIS-IR.

In Figure 2.8b we compare the thermally induced deformation as measured by the 3 different techniques for Au@SiO₂ with $V = 2.7 \times 10^3$ nm³. The plot shows the LSPR peak position as a function of heating temperature determined via *in/ex situ* VIS-IR (left y-axis) and via *ex situ* TEM (right y-axis). Although there are some absolute differences there is a good qualitative agreement between the 3 techniques. All three techniques show that the rods with $V = 2.7 \times 10^3$ nm³ strongly deform when heating them above 100 °C and did not deform significantly above 300 °C anymore.

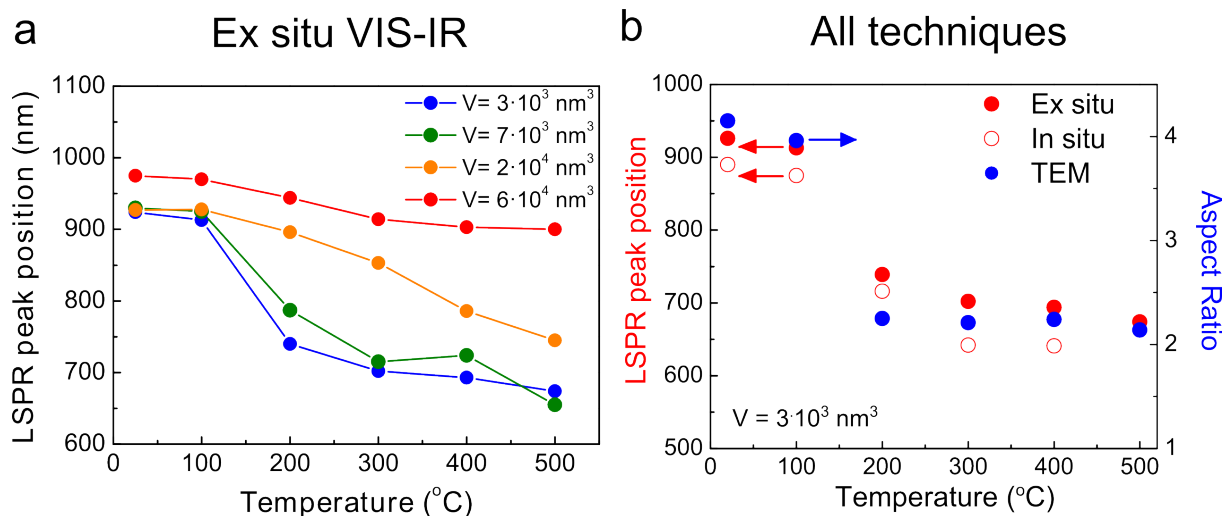


Figure 2.8: Comparison of different techniques to study the thermal stability of Au@SiO₂ NRs. a) *Ex situ* VIS-IR measurements Au@SiO₂ NRs with $V = 2.7 \times 10^3 \text{ nm}^3$ (blue), $1.0 \times 10^4 \text{ nm}^3$ (green), $2.1 \times 10^4 \text{ nm}^3$ (orange) and $6.0 \times 10^4 \text{ nm}^3$ (red). The NRs were heated with $30 \text{ }^\circ\text{C}/\text{min}$ to 100-500 $^\circ\text{C}$ and kept at the desired temperature for 2 h. Afterwards the extinction spectra were acquired in 85 wt % glycerol in water mixture at RT. b) Comparison of the LSPR peak position (red, left axis) and aspect ratio (blue, right axis) as determined with *in/ex situ* VIS-IR spectroscopy and TEM, respectively, for Au@SiO₂NRs with $V = 2.7 \times 10^3 \text{ nm}^3$.

Aspect ratio dependent thermal stability of mesoporous silica coated AuNRs

Apart from the particle volume the aspect ratio is known to be important in the thermal deformation behaviour of Au@SiO₂ NRs [119]. We investigated the influence of the aspect ratio of mesoporous silica coated AuNRs on their thermal stability in a similar way as the volume dependent measurements described above, but now using Au@SiO₂ NRs with the same volume but a different aspect ratio (see Figure 2.4 and Table 2.5). In Figure 2.9 we show the *in situ* and *ex situ* VIS-IR measurements for the Au@SiO₂NRs with $AR = 2.8, 3.8, 4.2$ and 6.0 and $V = 1 \times 10^4 \text{ nm}^3$ in N₂. In the *in situ* measurements, every 25 $^\circ\text{C}$ a spectrum was recorded while heating with $1 \text{ }^\circ\text{C}/\text{min}$ to 400 $^\circ\text{C}$. In Figure 2.9a and Figure 2.9b the resulting *in situ* VIS-IR data for the AuNRs with $AR = 2.8$ and $AR = 6.0$ are shown. The spectra below 800 nm were rather noisy due to the limited sensitivity of the detector in the VIS(-UV) range. For this reason, the spectra obtained via the *in situ* VIS-IR measurements are only shown up to 400 $^\circ\text{C}$. The spectra in Figure 2.9a show that the peak position of the Au@SiO₂ NRs with $AR = 2.8$ shifted only 36 nm from 668 to 632 nm when heating from RT to 400 $^\circ\text{C}$. The LSPR peak of the Au@SiO₂ NRs with $AR = 6.0$ shifted considerably more (Figure 2.4b); 298 nm, from 1069 to 771 nm, indicating a more severe deformation.

In Figure 2.9c and d the LSPR peak positions obtained in N₂ (*in situ* VIS-IR) and in glycerol water (*ex situ* VIS-IR) as a function of the heating temperature are shown. The *in* and *ex situ* measurements are in good agreement and both show that thermally induced deformation becomes more severe when starting with more elongated, higher AR,

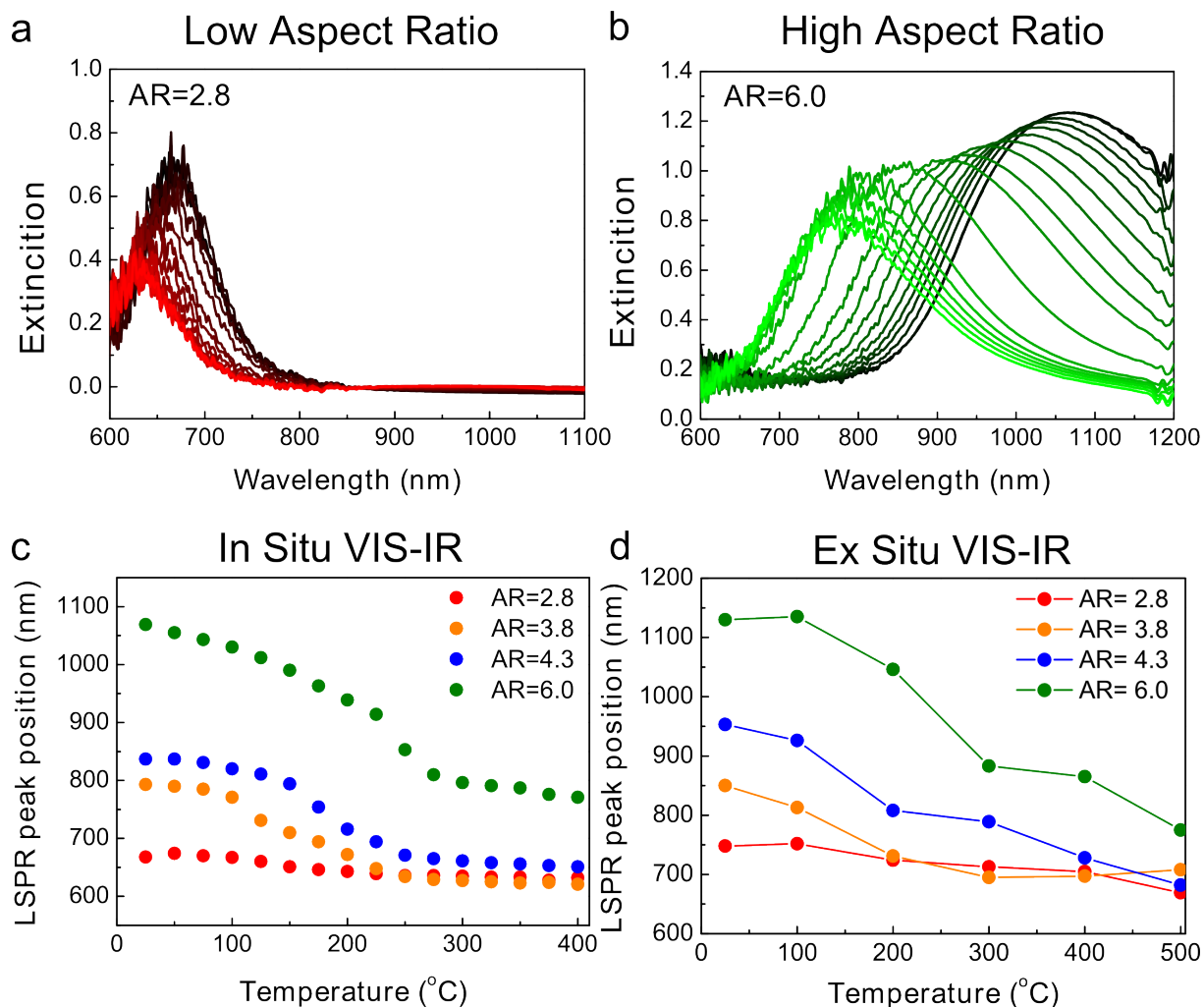


Figure 2.9: Aspect ratio dependent thermal stability of mesoporous silica coated Au NRs investigated with *in situ* VIS-IR spectroscopy. Extinction spectra of Au@SiO₂ NRs with $AR=2.8$, $V=9.5 \times 10^3 \text{ nm}^3$ (a, red) and $AR=6.0$, $V=9.3 \times 10^3 \text{ nm}^3$ (b, green) acquired every 25 °C from 25 to 400 °C. c) Plot of the LSPR peak position of Au@SiO₂ NRs determined with *in situ* and *ex situ* VIS-IR measurements during and after heating from RT to 500 °C, respectively. The *ex situ* extinction spectra were recorded in a 85 wt% glycerol in water mixture at RT after thermal treatment.

nanorods. The rods with $AR=3.8$, 4.3 and 6.0 deform most strongly between 100 and 300 °C after which they stabilize and deform more slowly.

Interpretation of volume and aspect ratio dependent thermal stability

The thermal stability measurements show two clear trends: the deformation of AuNRs increases with decreasing particle volume (1) and increasing aspect ratio (2). In both cases, we observed that the nanorods deformed far below the bulk melting point of gold, which is 1064 °C, pointing at a nanosize effect. The thermodynamic driving force for such deformation is the reduction in the fraction of surface atoms when going from a high surface area, elongated rod to a lower surface area spherical particle, leading to a minimization of the surface free energy.

Regarding the particle volume dependent deformation, we observed that the particle volume became increasingly important at small particle volumes (and high S/V), which is most clearly visualized in the graph in Figure 2.5f. When decreasing V below $2 \times 10^4 \text{ nm}^3$ the thermal stability decreased drastically, whereas an increase of the particle volume to $V = 6 \times 10^4 \text{ nm}^3$ did not lead to any significant changes in the NRs deformation behaviour. Previous studies on particle size dependent melting of silica coated gold nanoparticles showed that the melting temperature of AuNPs started to significantly deviate from the bulk melting point when the particle diameter was decreased below $\sim 15 \text{ nm}$ [4, 5, 136], which is in the same size range as the diameter of the smallest nanorods in this study, being 15 and 9.4 nm for the Au@SiO₂ NRs with $V = 10$ and $2.7 \times 10^3 \text{ nm}^3$. A lowering of the melting point and overall increased atom mobility could therefore (partially) explain the decrease in thermal stability with decreasing nanorod size.

However, a particle size dependent change in melting temperature and overall increase in the mobility of the Au atoms cannot explain the observed aspect ratio dependency in the deformation behaviour. Figure 2.9c and d show that the deformation for the rods with $AR = 2.6 - 6.0$ was very different whereas all NRs had the same particle volume ($V = 10^4 \text{ nm}^3$). This aspect ratio dependency is in line with previous findings by Gergely-Fülöp *et al.* [91]. However, in that study gold nanorods with different aspect ratios ($AR = 2.5 - 4.3$) and non-equal particle volumes ($V = 1.7 - 3.8 \times 10^3 \text{ nm}^3$) were used [91]. Especially, when using such small NRs, deviations in particle volume become increasingly important as we show in Figure 2.5f. To solely study the influence of the aspect ratio on the thermal stability it is therefore preferable to work at larger particle volumes ($\geq 10^4 \text{ nm}^3$) where small deviations in particle volume play a less important role.

Aspect ratio dependent deformation was also observed in laser-induced heating by Taylor *et al.*, where high AR AuNRs deformed more severely compared to low AR rods. Curvature driven surface diffusion was used to explain the observed deformation behaviour. Herein, the deformation of the AuNRs occurs through mobility of surface atoms, which move from the high curvature ends of the rod to lower curvature sides along the length of the NRs. In this model the activation energy of surface atom diffusion decreased from 1.5 to 0.6 eV with an increase in aspect ratio from 2.7 to 5.0, leading to the deformation of high AR NRs at lower temperatures. Note that in our case the curvature of the nanorods does not only change as a function of the aspect ratio, but also when changing the particle volume. Work is in progress to model the volume and aspect ratio dependent deformation of silica coated AuNRs as described in this chapter with the curvature driven surface diffusion model of ref [122].

It is important to stress that not only the particle volume and aspect ratio, but also the degree of encapsulation is an important parameter in the deformation of AuNRs. Uncoated CTAB stabilized NRs already fully deform below ~ 200 °C [119, 121, 127, 128] regardless of their volume and aspect ratio, whereas encapsulation in inorganic coatings can shape stabilize AuNRs up to 600 °C [126]. The stabilizing effect of an inorganic, e.g. silica coating, is most likely a combination of retardation of the Au atomic surface diffusion as well as an increased mechanical stability provided by the surrounding shell acting against deformation of the rods. Retardation of the surface diffusion was for example observed when coating the AuNRs with a thin carbon shell, leading to a strongly increased thermal stability in *in situ* heating electron microscopy measurements [121, 124].

Also the rigidity of the surrounding shell is important in understanding the measurements presented in this chapter. AuNRs coated with a thick zirconia [126] or Stöber silica shell were observed to be more stable than AuNRs coated with a more open and flexible mesoporous silica shell [120]. In our measurements, the stiffness of the silica shell is therefore likely to influence the deformation behaviour as well. In Figure 2.9c and d we observed that after an initial drop in the LSPR peak position, the deformation at higher temperatures slowed down. This could be related to strengthening of the silica shell at higher temperatures since the degree of condensation is known to increase from a mixture of Q3 and Q4 at RT, to predominantly Q4 above 400 °C in MCM-41 like materials [144] and silica microcapsules [145]. Note that the pore structure of the mesoporous silica shell is not expected to change below ~ 750 °C [129, 146], which is also clear from our TEM images in Figure 2.5 where the pore structure is still visible.

2.4 Conclusions

In this chapter we discussed the thermal stability of mesoporous silica coated AuNRs as a function of particle volume and aspect ratio for temperatures between 100-500 °C. First, we described the seed mediated synthesis of small AuNRs and synthesized two well defined series of AuNRs where either the particle volume or the aspect ratio of the rods were changed. We employed a multi technique approach comprising *ex situ* TEM measurements, *in situ* and *ex situ* VIS-IR measurements to study the thermal stability of these particles on a single and ensemble averaged level, respectively. We showed that the deformation of Au@SiO₂NRs is strongly influenced by the particle volume and the aspect ratio, where a lower volume and higher aspect ratio lead to more severe deformation. For all Au@SiO₂NRs the deformation occurred well below the bulk melting point. Curvature driven atomic surface diffusion is a likely mechanism in explaining such low temperature deformation. Moreover, we found that the mesoporous silica shell prevents significant deformations above about 300 °C. Our results on the relationship between particle volume and aspect ratio with respect to the thermal stability are important to many (photo)thermal applications and will be important in the rest of this thesis as well, where we will discuss thermally induced alloying of bimetallic nanorods (Chapter 4 and 5) and gas phase catalysis with mono- and bimetallic nanorods at elevated temperatures (Chapter 6).

Acknowledgements

The work in this chapter was performed in collaboration with Wiebke Albrecht (VIS-NIR measurements). Tian-Song Deng is thanked for preparing the batch of high volume AuNRs ($V = 6.0 \times 10^4 \text{ nm}^3$). Remco Dalebout is acknowledged for performing the N_2 -physisorption measurement.

Synthesis of bimetallic core-shell nanorods

3

Abstract

Bimetallic nanorods are particularly interesting for optical applications and light enhanced catalysis due to their strong and tunable plasmonic resonances. However, synthesizing bimetallic nanorods with good control over composition, morphology and at a large enough scale for self-assembly and/or catalysis, while maintaining their anisotropic, out-of-equilibrium shape is challenging. Here, we present a robust approach for the synthesis of bimetallic core-shell nanorods at a large scale. As a starting material we used mesoporous silica coated gold nanorods and tuned the Au core size precisely via oxidative etching. Subsequent metal overgrowth led to the formation of an Ag, Pt or Pd metal shell around the Au core. We demonstrate that the thickness of the metal shell can be precisely tuned by varying the precursor concentration. The kinetics of the metal overgrowth were controlled via the pH, which allowed scaling up of the synthesis from micro- to milligrams. Furthermore, we demonstrate that the rough morphology of non-epitaxially grown Pd shells can be changed from dendritic to smooth epitaxial shells via thermal treatment without changing the aspect ratio of the nanorods. Our synthesis approach can be extended to different or/and more than two metals, leading to rod-shaped metal particles with tunable material properties, synthesized in the quantities needed for self-assembly, plasmonics and catalysis.

3.1 Introduction

Gold nanorods (AuNRs) exhibit a shape-induced longitudinal Localized Surface Plasmon Resonance (LSPR) in the direction of the length of the rods at low energies, which can easily be tuned by changing the aspect ratio of the rods and extended from visible wavelengths into the near-infrared region of the electromagnetic spectrum [13] (see also Chapter 1, Figure 1.3). This makes AuNRs valuable plasmonic nanoparticles for e.g. biological applications [115, 147], as biological cells and tissues show significantly less absorption in this region of the spectrum. Compared to single-component Au nanorods, bimetallic nanorods offer enhanced physiochemical properties [55, 148]. For example, Ag has superior plasmonic properties with respect to Au, due to less strong damping of the plasmonic resonance [55–57]. Coating the AuNRs with an Ag layer therefore significantly improves their plasmonic properties and their performance in Surface Enhanced Raman Spectroscopy (SERS) [50]. For catalytic applications, the addition of Pd or Pt can be beneficial, since these metals are known to be highly active in catalysis [149, 150]. Coating an Au core with a thin Pd (or Pt) layer can therefore lead to strongly enhanced catalytic properties as we will demonstrate in Chapter 6, while maintaining part of the plasmonic properties [151]. Such bimetallic rods are for example useful for *in situ* monitoring of chemical reactions by using SERS [152, 153], for hydrogen sensing [153, 154] or for plasmon-enhanced catalysis [108, 117, 118, 151, 155, 156].

The exact composition and particle morphology, especially of the surface and sub-surface layers, strongly influence the optical and catalytic properties of bimetallic nanorods [57, 76, 86, 118, 148, 155, 157]. However, precise tuning of the number of atomic shell layers and the shell morphology is challenging. So far, the overgrowth of a second metal is typically performed on bare AuNRs [50, 153, 158, 159]. Herein, the final shell thickness and shape of the bimetallic rods are difficult to tune, and the particle shape can easily transform from a spherocylinder to a brick-like particle [159, 160], which can only be prevented by the addition of shape directing additives [53, 153]. Uncoated AuNRs are also prone to aggregation during the metal overgrowth and secondary nucleation can occur in the presence of the surfactants needed for the stabilization of the AuNRs. In addition, it should be noted that the current syntheses of uncoated core-shell structures are generally performed on a relatively small, mL scale, which yields an insufficient amount of particles for e.g. self-assembly and/or catalysis applications.

Metal deposition is not straightforward for all metals either. The morphology and crystal structure of the metal shell largely depend on the interaction between the core and shell metal, their surface energies and structural characteristics, such as the lattice spacings [86, 158, 161, 162]. Additionally, the reduction potentials of the metals are important for successful core-shell growth, as galvanic replacement can occur when the core material is oxidized upon reduction of the shell metal, resulting in hollow and partially alloyed metal structures [86, 163, 164]. Metal overgrowth with a metal that has a similar crystal structure, lattice constant and lower surface energy such as Ag compared to Au typically results in smooth, epitaxially grown metal shells. Contrarily, the lattice mismatch and high surface energy of Pd and Pt compared to Au, can lead to dendritic, non-epitaxial Pd/Pt shell growth onto Au [54, 157, 158, 165, 166]. Herein, small Pt/Pd nanoparticles form on the surface of AuNRs, resulting in ill-defined surface structures and

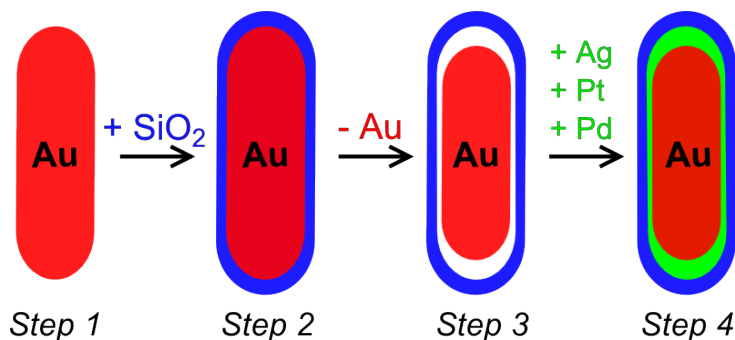


Figure 3.1: Schematic representation of the synthesis steps towards mesoporous silica coated Au core Ag/Pt/Pd shell nanorods. From left to right: 1) Synthesis of surfactant stabilized AuNRs, 2) Mesoporous silica coating of the AuNRs, 3) Removal of part of the Au by oxidative etching, 4) Overgrowth of the Au core with Ag, Pt or Pd.

inhomogenous shell thickness's. This is particularly problematic when using such particles in catalysis, where the exact surface morphology and composition are crucial.

In this chapter, we present a systematic and quantitative study on the synthesis of well-defined bimetallic Au core Ag/Pt/Pd shell nanorods and describe how one can precisely tune the metal composition and surface morphology. To do so, a multiple step synthesis route (Figure 3.1) was used in which colloidal AuNRs are grown (1), protected with a mesoporous silica coating (2), oxidatively etched to tune the size of the Au core (3) and overgrown with a second metal (4). In the metal overgrowth, the mesoporous silica coating was crucial in preventing aggregation and functioned as a shape preserving template to retain the spherocylindrical shape of the nanorods. By varying the metal precursor concentration the metal composition was tuned. The growth kinetics of the metal overgrowth reaction were slowed down by lowering the pH, which allowed for a longer mixing time of the reagents and therefore enabled scaling up of the synthesis. Furthermore, it was possible to change the morphology of non-epitaxially grown Pd shells from dendritic to smooth via a thermal treatment, yielding well-defined, single-crystalline Pd shell Au core nanorods. Finally, the key parameters governing the metal shell growth mechanism and thus the shell morphology and crystal structure are discussed.

3.2 Experimental

Chemicals

All chemicals were used as received without further purification. Hexadecyltrimethylammonium bromide (CTAB, >98.0%) and sodium oleate (NaOL, >97.0%) were purchased from TCI America. Hydrogen tetrachloroaurate trihydrate ($\text{HAuCl}_4 \cdot 3\text{H}_2\text{O}$) and sodium hydroxide (NaOH, 98%) were purchased from Acros Organics. L-Ascorbic Acid (BioX-tra, $\geq 99\%$), hydrogen peroxide (H_2O_2 , 30 wt% in H_2O), hydrochloric acid (HCl, 37 wt% in water), silver nitrate (AgNO_3 , $\geq 99\%$), sodium borohydride (NaBH_4 , 99%), sodium tetrachloropalladate-(II) (Na_2PdCl_4 , 98%), potassium tetrachloroplatinate-(II) (K_2PtCl_4 , 98%) and tetraethyl orthosilicate (TEOS, 98%) were purchased from Sigma-Aldrich. Ul-

trapure water (Millipore Milli-Q grade) with a resistivity of 18.2 M Ω was used in all of the experiments. Methanol was purchased from Interchema ($\geq 99.85\%$.) All glassware for the AuNR synthesis was cleaned with fresh aqua regia (HCl/HNO₃ in a 3:1 volume ratio), rinsed with large amounts of water and dried at 100 °C before usage.

Synthesis of the core-shell nanorods

Step 1: Gold nanorod synthesis

Monodisperse AuNRs were synthesized according to the protocol of Ye *et al.* [13]. The synthesis was performed on a 500 mL scale with a growth solution containing 7.0 g CTAB, 1.24 g NaOL, 250 mL MQ H₂O and 250 mL 1.0 mM HAuCl₄, 7.2 mL AgNO₃, 2.10 mL concentrated HCl (37 wt%, 12.1 M), 64 mM ascorbic acid and 1.0 mL seed solution. The seeds were prepared from a 10 mL 0.10 M CTAB, 51 μ L 50 mM HAuCl₄ and 1.0 mL 6.0 mM NaBH₄. The subsequent rod growth was performed under static conditions in a 30 °C water bath overnight. The resulting AuNR suspensions had a longitudinal LSPR (λ_{LSPR}) of 892 nm and a maximum extinction (Ext) of 1.0 when diluted 4 \times in H₂O. The rods were centrifuged at 8000 rcf (relative centrifugal force) for 30 min (Rotina 380R Hettich centrifuge), washed with H₂O and redispersed in about 40 mL 5.0 mM CTAB H₂O.

Step 2: Mesoporous silica coating

The CTAB stabilized AuNRs were coated with a 18 nm mesoporous silica shell *via* the method of Gorelikov *et al.* [90]. The coating was performed in 170 mL 1.5 mM CTAB aqueous solution containing 1.0 mM NaOH and an AuNR concentration corresponding to an extinction maximum of 1.0 when diluted 10 \times in H₂O. While magnetically stirring at 300 rpm in a 30 °C waterbath, 3 times 0.510 mL 0.90 M TEOS in EtOH was added with a 30 min time interval. The silica coated gold nanorods (Au@SiO₂ NRs) were centrifuged at 8000 rcf for 30 min, washed with water and ethanol.

Step 3: Oxidative etching

200 μ L HCl (37 wt%, 12.1 M) and 200 μ L 50 mM H₂O₂ in MeOH (containing 0.19 M H₂O) were added to 10 mL silica coated AuNRs (λ_{LSPR} = 838 nm, Ext= 1.6 when 2 \times diluted in MeOH) in MeOH, resulting in a final HCl and H₂O₂ concentration of 0.24 M and 1.0 mM, respectively. Thereafter, the reaction was immediately heated in a 60 °C oil bath while magnetically stirring at 400 rpm. After 12 minutes the reaction was quenched with 10 mL fresh MeOH. The longitudinal LSPR peak position of the etched AuNRs in MeOH had shifted to 748 nm. An additional 20 mL fresh MeOH was added and the particles were centrifuged at 8000 rcf for 25 min. Next, the particles were washed with 9 mL MeOH, 9 mL H₂O and redispersed in \sim 7 mL H₂O (λ_{LSPR} = 748 nm, Ext= 2.2).

Step 4: Metal overgrowth

For the metal overgrowth 0.300 mL etched AuNRs@meso-SiO₂ (λ_{LSPR} = 746-748 nm, Ext= 2.2) in H₂O was used, to which AgNO₃, Na₂PdCl₄ or K₂PtCl₄ (1-100 mM, 0.030

mL) was added. Next, ascorbic acid ($4 \times [\text{metal-precursor}]$ mM, 0.030 mL) was added and the mixture was gently shaken for 20 min at room temperature (for Ag and Pd) or overnight (for Pt). The complete set of experimental parameters for the Ag, Pd and Pt overgrowth are listed in Table 3.1, 3.2 and 3.3, respectively. In the tables the concentration and volume of the added metal precursor and ascorbic acid solutions are given and the final metal precursor and ascorbic acid concentration in the reaction mixture. Next, the reaction mixtures were diluted to 1.0 mL H₂O to study their plasmonic properties by recording VIS-IR spectra. Afterwards, the core-shell nanorods were washed with 4 mL H₂O, 2 mL EtOH and redispersed in 1.0 mL absolute EtOH (centrifugation at 7000-9000 rcf for 10-15 min). TEM analysis was used to determine the size of the Ag@Au@SiO₂ NRs. Due to the dendritic nature of the Pd and Pt shell this could not reliably be done for the Au@Pd@SiO₂ and Au@Pt@SiO₂ NRs.

Table 3.1: Ag-overgrowth: reaction conditions used for the Au@Ag@SiO₂ NRs presented in Figure 3.3. For the overgrowth 0.300 mL etched AuNRs@meso-SiO₂ (length (L)= 61.7 nm; diameter (D)= 18.2 nm, λ_{LSPR} = 748 nm, Ext= 2.2) in H₂O were used. Reaction time = 20 min. AgNO₃/Ascorbic acid (added) and AgNO₃/Ascorbic acid (final) refer to the amount and concentration of the AgNO₃/Ascorbic acid solution added to the reaction mixture, and the final AgNO₃/Ascorbic acid concentration in the reaction mixture, respectively.

X_{Ag}	AgNO ₃ (added)	Ascorbic acid (added)	AgNO ₃ (final)	Ascorbic acid (final)
0	0	0	0	0
0.18	0.015 mL 1.0 mM	0.015 mL 4.0 mM	0.045 mM	0.18 mM
0.35	0.030 mL 1.0 mM	0.030 mL 4.0 mM	0.083 mM	0.33 mM
0.41	0.023 mL 2.0 mM	0.023 mL 8.0 mM	0.13 mM	0.53 mM
0.50	0.030 mL 2.0 mM	0.030 mL 8.0 mM	0.17 mM	0.67 mM
0.57	0.019 mL 4.0 mM	0.019 mL 16 mM	0.22 mM	0.90 mM
0.57	0.023 mL 4.0 mM	0.023 mL 16 mM	0.27 mM	1.1 mM
0.61	0.026 mL 4.0 mM	0.026 mL 16 mM	0.30 mM	1.2 mM
0.63	0.030 mL 4.0 mM	0.030 mL 16 mM	0.33 mM	1.3 mM

Table 3.2: Pd-overgrowth: reaction conditions used for the Au@Pd@SiO₂ NRs presented in Figure 3.5. For the overgrowth 0.300 mL etched AuNRs@meso-SiO₂ (L = 60.8 nm, D = 19.5 nm, λ_{LSPR} = 746 nm, Ext= 2.2) in H₂O were used. Reaction time = 20 min. Na₂PdCl₄/Ascorbic acid (added) and Na₂PdCl₄/Ascorbic acid (final) refer to the amount and concentration of the Na₂PdCl₄/Ascorbic acid solution added to the reaction mixture, and the final Na₂PdCl₄/Ascorbic acid concentration in the reaction mixture, respectively.

X_{Pd}	Na ₂ PdCl ₄ (added)	Ascorbic acid (added)	Na ₂ PdCl ₄ (final)	Ascorbic Acid (final)
0	0	0	0	0
0.03	0.030 mL 1.0 mM	0.030 mL 4.0 mM	0.083 mM	0.33 mM
0.14	0.030 mL 2.0 mM	0.030 mL 8.0 mM	0.17 mM	0.67 mM
0.34	0.030 mL 5.0 mM	0.030 mL 20 mM	0.42 mM	1.7 mM
0.39	0.030 mL 10 mM	0.030 mL 40 mM	0.83 mM	3.3 mM

Table 3.3: Pt-overgrowth: reaction conditions used for the Au@Pt@SiO₂ NRs presented in Figure 3.6. For the overgrowth 0.300 mL etched AuNRs@meso-SiO₂ ($L= 61.7$ nm, $D= 18.2$ nm, $\lambda_{LSPR}= 748$ nm, $Ext= 2.2$) in H₂O were used. The reaction mixture was left overnight. K₂PtCl₄/Ascorbic acid (added) and K₂PtCl₄/Ascorbic acid (final) refer to the amount and concentration of the K₂PtCl₄/Ascorbic acid solution added to the reaction mixture, and the final K₂PtCl₄/Ascorbic acid concentration in the reaction mixture, respectively.

X_{Pt}	K ₂ PtCl ₄ (added)	Ascorbic acid (added)	K ₂ PtCl ₄ (final)	Ascorbic acid (final)
0	0	0	0	0
	0.030 mL 1.0 mM	0.030 mL 4.0 mM	0.083 mM	0.33 mM
	0.030 mL 10 mM	0.030 mL 40 mM	0.83 mM	3.3 mM
	0.030 mL 50 mM	0.030 mL 200 mM	4.2 mM	17 mM
	0.030 mL 100 mM	0.030 mL 400 mM	8.3 mM	33 mM

Thermal treatment

Thermal treatment was performed in a tubular oven (Thermolyne 79300 tube furnace) under a constant N₂, H₂ or air flow (~ 100 mL/min). The core-shell NRs were first dried in a glass vial and then heated in a quartz tube oven. The heating rate was 2 °C/min and the particles were heated to 300 °C for 1 h and cooled down under N₂, H₂ or air flow to RT before taking them out of the oven. After heating the NRs were redispersed in 1 mL EtOH. The shell morphology of the rods was analysed in a transmission electron microscope (TEM) and the optical properties by recording extinction spectra (see "Characterization" section for details).

Controlling the growth kinetics

To follow the growth kinetics, *in situ* Fourier transform visible infrared spectroscopy (VIS-IR) measurements were performed (see details below). The Au@SiO₂ cores were dispersed in 1.0 mL H₂O such that $\lambda_{LSPR}= 744$ nm and $Ext= 1.0$. To this solution 20-80 μ L 0.10 M HCl was added. The 0.10 M HCl solution was prepared mixing 83 μ L concentrated HCl (37 wt%, 12.1 M) with 9.92 mL H₂O. Next, 10 μ L 15 mM AgNO₃ was added and an extinction spectrum was recorded before addition of 10 μ L 60 mM ascorbic acid. The final HCl, AgNO₃ and ascorbic acid concentrations in the growth solution were 2-8 mM, 0.15 mM and 0.60 mM, respectively. Every minute for 25 minutes a spectrum was recorded between 400 and 1200 nm with a step size of 1 nm.

Scaling up

For the small and large scale Au@Ag@SiO₂ NR synthesis unetched Au@SiO₂ NRs with $L_{Au}= 107$, $D_{Au}= 35$ nm were used. Prior to the metal overgrowth, the Au@SiO₂ NRs were washed with a 0.10 M HCl in EtOH solution (30 mL absolute EtOH with 246 μ L concentrated HCl (37 wt%, HCl)), followed by 3 \times washing with EtOH and re-dispersion in H₂O ($\lambda_{LSPR}= 819$ nm and $Ext= 2.8$). The HCl washing was performed to remove most of the remaining CTAB molecules from the pores of the mesoporous silica shell (see Chapter 6) [49]. It is necessary to do this step when performing metal overgrowth directly

on unetched Au@SiO₂ NRs. For the etched Au@SiO₂ NRs this step is not required, since (part of) the CTAB is removed during the etching process. The small scale metal overgrowth was carried out in a disposable cuvette containing 1.0 mL Au@SiO₂ NRs in H₂O (λ_{LSPR} = 744 nm and Ext = 1.0), 20 μ L 5.0 mM AgNO₃ and 20 μ L 20 mM ascorbic acid. The large scale metal overgrowth was performed in a 500 mL erlenmeyer with 400 mL Au@SiO₂ NRs in H₂O, 8.0 mL 5.0 mM AgNO₃ and 8.0 mL 20 mM ascorbic acid. The reaction time for both experiments was 30 minutes, during which the large scale reaction mixture was magnetically stirred at 400 rpm. Afterwards, the rods were washed with ethanol twice and re-dispersed in 2 mL (small-scale) and 25 mL (large-scale) EtOH for storage. The λ_{LSPR} for the Au@Ag@SiO₂ NR synthesized at small and large scale was 783 and 794 nm, respectively.

Long-term storage of core-shell NRs

The storage of Au@Ag@SiO₂ NRs in EtOH should *always* be done in the dark and at low temperature to prevent oxidation and subsequent dissolution of the Ag shell. In the fridge (4 °C) the rods can be stored >1 year. We advice to also store the Au@Pd@SiO₂ NRs in the fridge. Storage at RT does not lead to dissolution of the Pd shell, but due to partial oxidation of the Pd shell the plasmonic properties of the Au@Pd@SiO₂ NRs will be lost in time. We observed that the Au@Pt@SiO₂ NRs can be stored well at RT.

Characterization

Extinction spectra were measured using a vertex 70 FTIR Spectrometer (BRUKER) and 1.0 cm cuvettes. The optical spectra were recorded over a spectral range from 400-1200 nm with a step size of 1 nm and averaged over 60 spectra. Bright field transmission electron microscopy images, HAADF-STEM images and EDX maps were recorded with a FEI Talos F200X operated at 200 kV, which is part of the Electron Microscopy facility EM Square at Utrecht University. The particle sizes were measured from TEM images. Per sample the size of 100 particles was determined. The obtained EDX intensity maps were quantified using the Cliff-Lorimer method. The metal compositions determined via EDX are an average of 10 particles.

3.3 Results

Tuning the Au core size with oxidative etching

Tuning of the AuNR size within the mesoporous silica shells was performed by oxidative etching in methanol (MeOH). Employing H_2O_2 as an oxidant instead of O_2 from the air as used previously [54], allows etching in a more reproducible and controlled way. We monitored the etching process by measuring the LSPR peak shift during the etching. In Figure 3.2b we show the extinction spectra of Au@SiO₂ NRs ($L=72$ nm, $D=19$ nm, aspect ratio (AR)= 3.8, $\lambda_{LSPR}=844$ nm) during etching at 60 °C with 50 mM H_2O_2 . Upon etching the LSPR peak position shifted to shorter wavelengths, indicating that the aspect ratio of the NRs was lowered and that etching predominately took place at the tips of the nanorods. The lowering of the LSPR peak intensity is explained by the decrease in AR combined with a loss in particle volume upon etching.

In Figure 3.2c-d and Figure 3.2e-f we show that by varying the H_2O_2 concentration and temperature, the etching rate could be controlled and varied from minutes to hours. We noticed that by increasing the H_2O_2 concentration the etching could also take place at room temperature. However, this makes the etching reaction more difficult to stop at a specific Au core size. It is therefore desirable to make the etching process sufficiently slow at elevated temperatures such that the reaction can easily be quenched at any desired LSPR peak position and Au core dimension. The quenching was typically done by diluting the reaction mixture by a factor 2 with cold (~ 4 °C) methanol. The etching process can be carried out on a millilitre scale, but also on a litre scale.

For the metal overgrowth presented in the rest of this chapter we quenched the etching at $\lambda_{LSPR}=844$ nm, which corresponded to Au@SiO₂ NRs with $L=62$ nm, $D=18$ nm, $AR=3.4$. Compared to the initial Au@SiO₂ NRs, 20% of the particle volume had been removed.

Metal overgrowth

Silver overgrowth

Next, the Au cores were overgrown with an Ag shell by using AgNO_3 as a silver precursor and ascorbic acid as a reducing agent. Figure 3.3 shows the Au@Ag@SiO₂ NRs grown with 0.045-0.33 mM AgNO_3 and 0.18-1.3 mM ascorbic acid in water. Due to the difference in Z-contrast the Ag shell appeared as a light shell around a bright Au core in the HAADF-STEM images. The EDX maps show the Au core, Ag shell, SiO₂ shell in red, green and blue, respectively. Both the HAADF-STEM images in Figure 3.3b as well as the EDX maps in Figure 3.3c-d clearly show that the Ag shell thickness increased with increasing AgNO_3 concentration.

From the electron microscopy images, we analysed the dimensions of the Au@Ag@SiO₂ NRs before and after Ag deposition and listed them in Table 3.4. For the Au@Ag@SiO₂ NRs grown with 0-0.33 mM AgNO_3 the particle volume increased from 1.4 to 4.0×10^3 nm³, which is a factor 2.2 larger than the initial volume of the non-etched Au@SiO₂ NRs. This shows that the silica shell is rather flexible and can accommodate a larger particle volume than that of the initial, unetched Au NR. The flexibility of the SiO₂ shell should

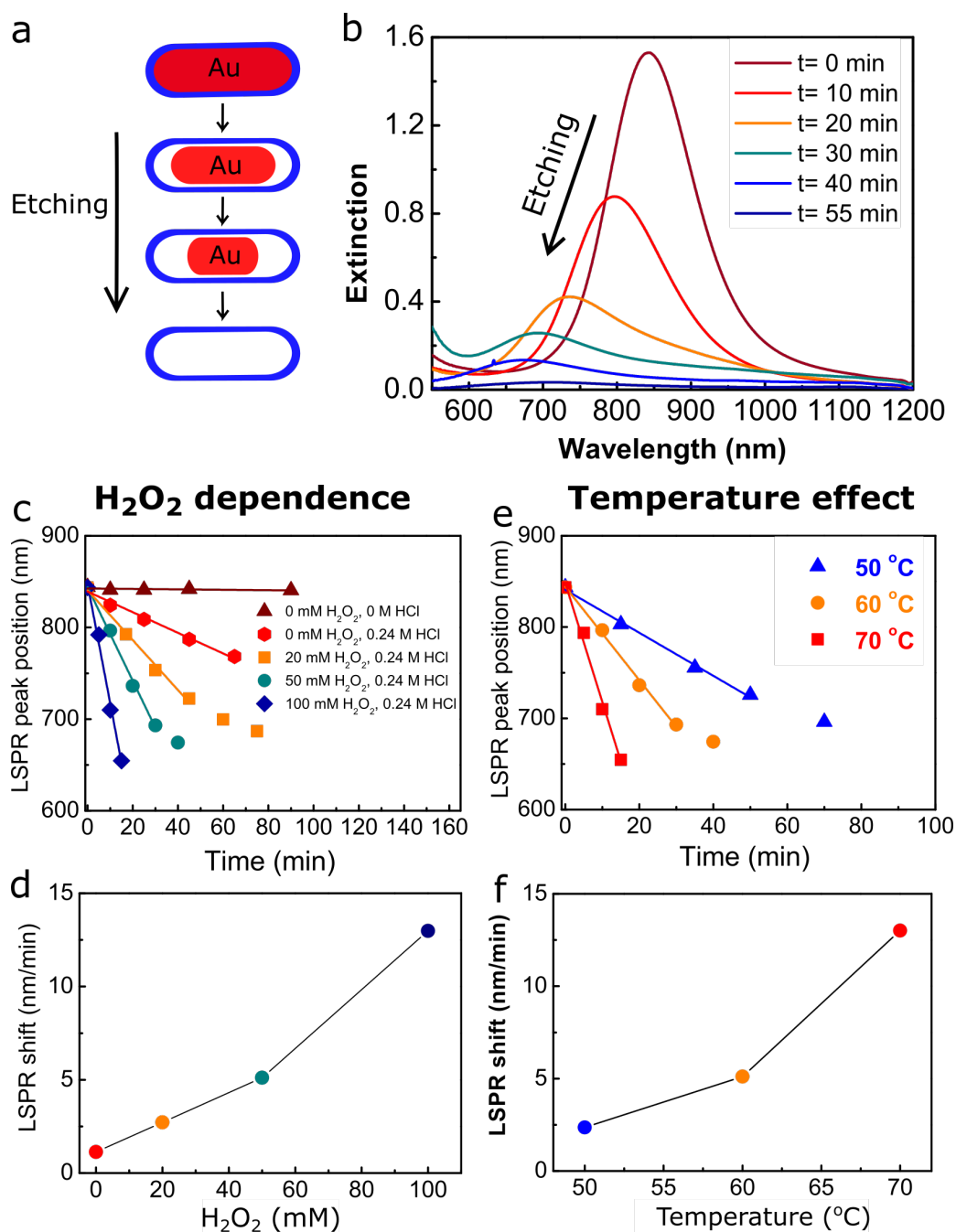


Figure 3.2: Oxidative etching of Au@SiO₂NRs in MeOH. a) Schematic representation of the etching process of the Au@SiO₂NRs. b) Extinction spectra of the Au@SiO₂NRs in MeOH during etching with 50 mM H₂O₂ and 0.24 M HCl. c) LSPR peak shift as a function of etching time when etching with 0 mM HCl and 0 mM H₂O₂ (brown), and 0, 20, 50 and 100 mM H₂O₂ with 0.24 M HCl in MeOH at 60 °C. The lines are best fits to the linear part of the LSPR peak position change in time. d) Same data as in c, but now the LSPR shift is plotted versus the H₂O₂ concentration. e) LSPR peak position vs etching time at 50, 60 and 70 °C with [H₂O₂] = 50 mM. f) Same data as in e, but now the LSPR shift is plotted versus temperature.

Table 3.4: Dimensions of the Au@Ag@SiO₂ NRs. For the overgrowth 0.300 mL etched AuNRs@meso-SiO₂ (L = 61.7 nm, D = 18.2 nm, LSPR = 748 nm, Ext= 2.2) in H₂O were used. The full set of reaction conditions used in the synthesis of the Au@Ag@SiO₂ NRs are presented in Table 3.1.

X_{Ag}	AgNO ₃ (mM)	Length (nm)	Diameter (nm)	AR
0	0	61.7	18.2	3.4
0.18	0.05	64.5	19.7	3.3
0.35	0.08	64.3	22.2	2.9
0.41	0.13	68.4	22.7	3.0
0.50	0.17	72.9	23.9	3.0
0.57	0.22	75.5	25.3	3.0
0.57	0.27	75.6	25.3	3.0
0.61	0.30	76.7	26.6	2.9
0.63	0.33	75.7	27.4	2.8

therefore allow direct growth of Ag on unetched AuNRs. Figure 3.9 illustrates that one can indeed perform direct metal overgrowth on Au@SiO₂ NRs without performing the etching step beforehand.

The size parameters from Table 3.1 and EDX maps from Figure 3.3d were used to quantify the metal composition of the Au@Ag@SiO₂ NRs. The plot in Figure 3.3e shows the atomic Ag-fraction, X_{Ag} , versus the AgNO₃ concentration. X_{Ag} determined from the TEM based size measurements (100 particle average) and EDX quantification (10 particle average) are displayed in red and blue, respectively. X_{Ag} increased with the [AgNO₃] from 0 to 0.62. However, at higher Ag-concentrations the increase in X_{Ag} flattens, which might be due to the limited space in the silica shell and capability of the silica network to stretch. To obtain even higher X_{Ag} fractions smaller Au cores should be used [104].

The increase in X_{Ag} strongly affected the optical properties of the Au@Ag@SiO₂ NRs. In Figure 3.3f we show the extinction spectra corresponding to the Au@Ag@SiO₂ NRs grown with 0-0.33 mM AgNO₃ and X_{Ag} = 0-0.62. The intensity of the LSPR peak increased by a factor 2.4 for the NRs with the largest Ag shell thickness. The enhanced plasmonic properties are due to an increase in Ag-content and particle volume. The LSPR peak also blue shifted from 748 to 710 nm, which is due to a decrease in AR from 3.4 to 2.8.

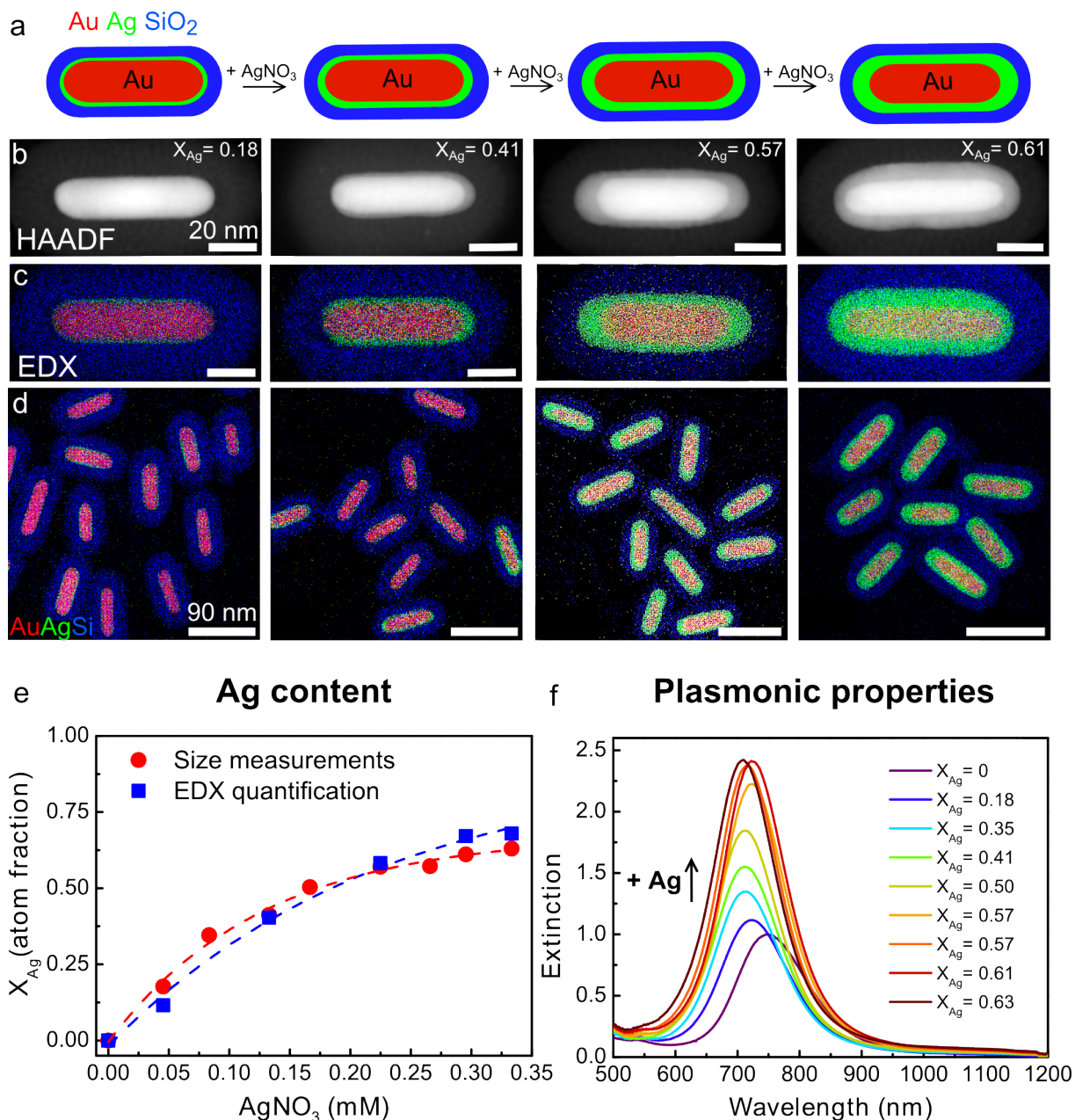


Figure 3.3: Controlled Ag-overgrowth of the Au@SiO₂ cores. a) Schematic representation of the Ag-overgrowth with increasing AgNO₃ concentration, leading to an increased Ag shell thickness. From left to right: b) HAADF-STEM and c) EDX maps of single and d) multiple Au@Ag@SiO₂ core-shell nanorods grown with 0.05, 0.13, 0.22 and 0.30 mM AgNO₃. e) Atomic Ag fraction (X_{Ag}) of the core-shell nanorods synthesized with 0-0.33 mM AgNO₃ as determined from TEM size measurements (red) and EDX quantification (blue). f) Extinction spectra of the Au@Ag@SiO₂ NRs grown with various 0-0.33 mM AgNO₃.

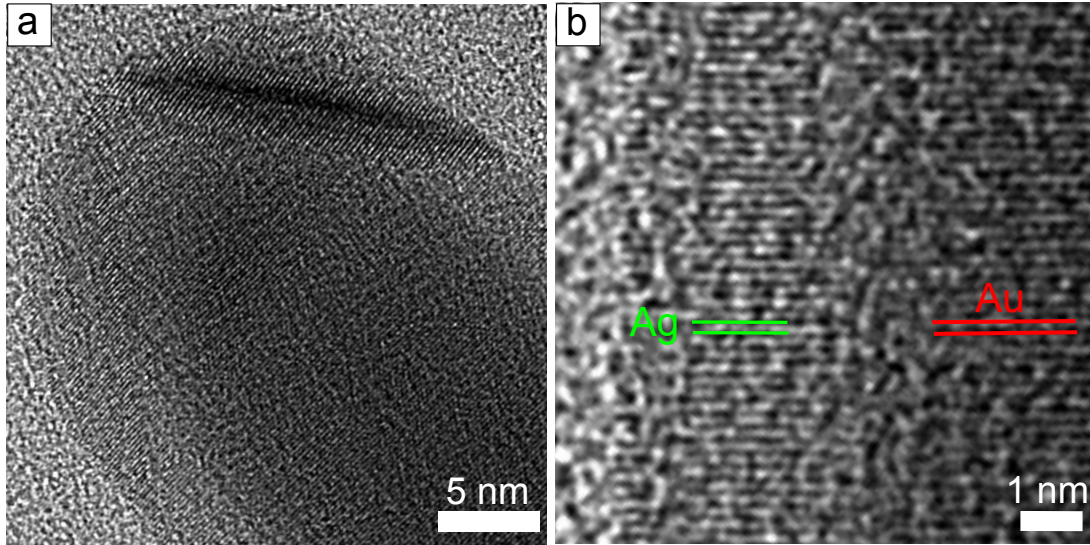


Figure 3.4: High resolution bright field TEM images of Au@Ag@SiO₂ NRs. a) HRTEM image and b) corresponding zoom-in of the Au@Ag@SiO₂ NR with $d_{lattice}^{Au} = d_{lattice}^{Ag} = 0.205$ nm, corresponding to the (200) lattice planes.

To investigate the orientation of the lattice planes in the Ag shell with respect to the Au core, High Resolution Transmission Electron Microscopy (HRTEM) measurements were performed. The resulting bright field images are shown in Figure 3.4. The HRTEM images show that the Ag shell had grown on the AuNR surface with its (200) lattice planes oriented in the same direction as the (200) lattice planes of the Au core.

Palladium overgrowth

For the Pd-overgrowth a similar approach was employed as described for the Ag-overgrowth, but now using Na₂PdCl₄ as a metal precursor. The Au@Pd@SiO₂ NRs were grown with 0.083-0.83 mM Na₂PdCl₄ and 0.33-3.3 mM ascorbic acid in water. In Figure 3.5 a schematic representation, HAADF-STEM images, EDX maps and extinction spectra of the resulting Au@Pd@SiO₂ NRs are shown. In the EDX maps Au, Pd and Si are depicted in red, green and blue, respectively. From the EDX map in Figure 3.5b it can be seen that at low Na₂PdCl₄ concentrations a thin Pd shell was formed on the Au rod surface. With increasing Pd-concentration the shell became more irregular and dendritic, which is most clearly visible in the HAADF-STEM images presented in Figure 3.5d and e.

The atomic Pd fraction (X_{Pd}) was quantified for the different Au@Pd@SiO₂ NRs with EDX, averaged over at least 10 particles. In Figure 3.5f the X_{Pd} is plotted against the Na₂PdCl₄ concentration. The Pd fraction increased with increasing Na₂PdCl₄, from 0.03 to 0.39. The plots of the Ag- and Pd metal content versus metal salt concentration as plotted in Figure 3.3e and Figure 3.5f, show the same trend: the X_{Ag} and X_{Pd} concentration flatten at higher AgNO₃ and Na₂PdCl₄ concentrations, respectively.

In Figure 3.5g the extinction spectra of the Au@Pd@SiO₂ NRs are plotted, showing the change in plasmonic properties upon Pd shell growth. The LSPR peak decreases in intensity and broadens upon adding Pd. These changes can partially be explained by the strong plasmonic damping of Pd compared to Au or Ag. In addition, the increased

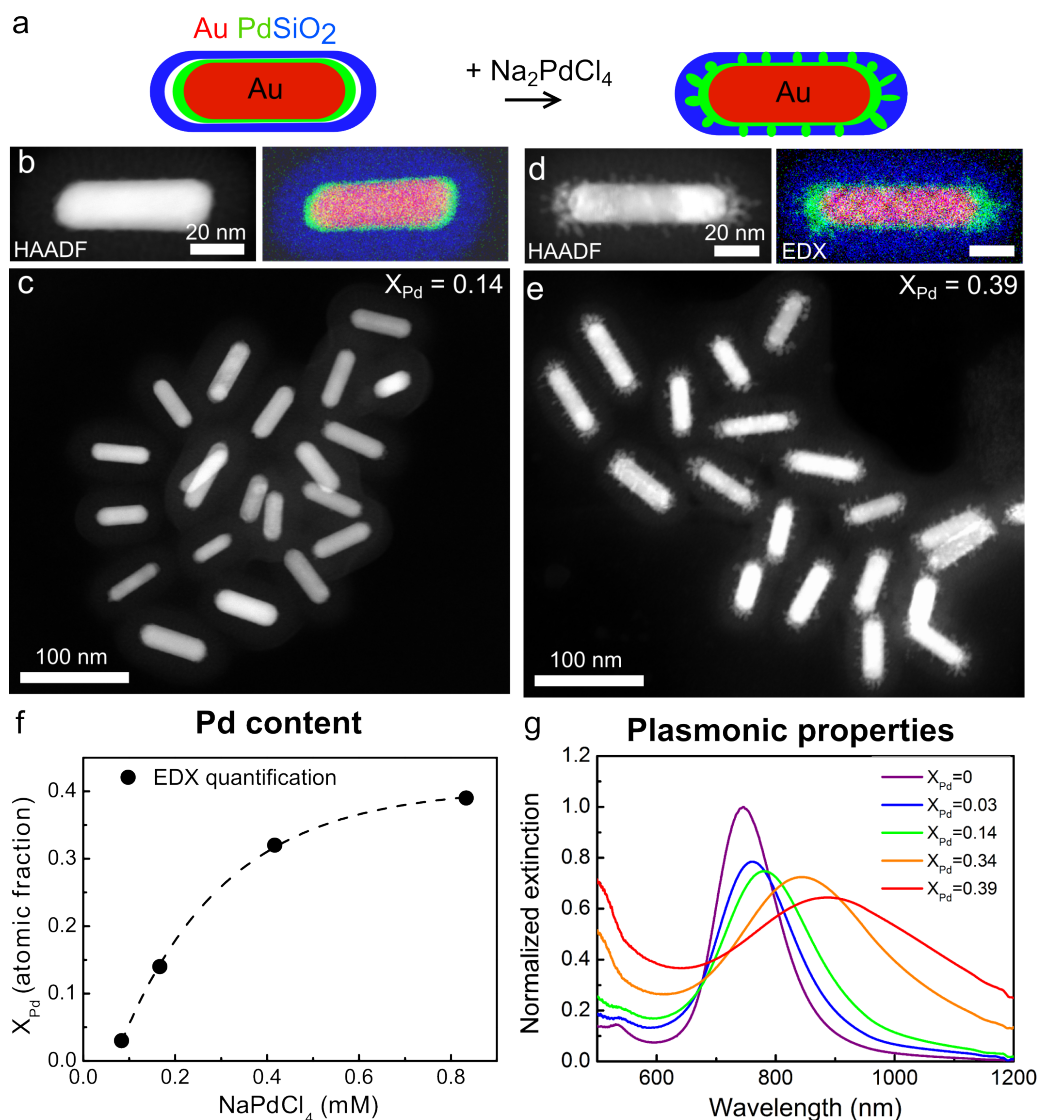


Figure 3.5: Pd-overgrowth: from smooth to spiky Pd shells. a) Schematic representation of the Pd-overgrowth with increasing Na₂PdCl₄ concentration, leading to an increase in roughness of the Pd shell. b-e) HAADF-SEM images and corresponding EDX maps of Au@Pd@SiO₂ NRs grown with 0.18 mM (b,c) and 3.3 mM (d,e). f) Atomic Pd fraction (X_{Pd}) versus the Na₂PdCl₄ concentration. g) Extinction spectra of the Au@Pd@SiO₂ NRs grown with 0-3.3 mM Na₂PdCl₄ and $X_{Pd} = 0-0.39$.

roughness of the Pd shell causes further broadening of the LSPR peak. Optically, this resulted in a black coloured particle dispersion.

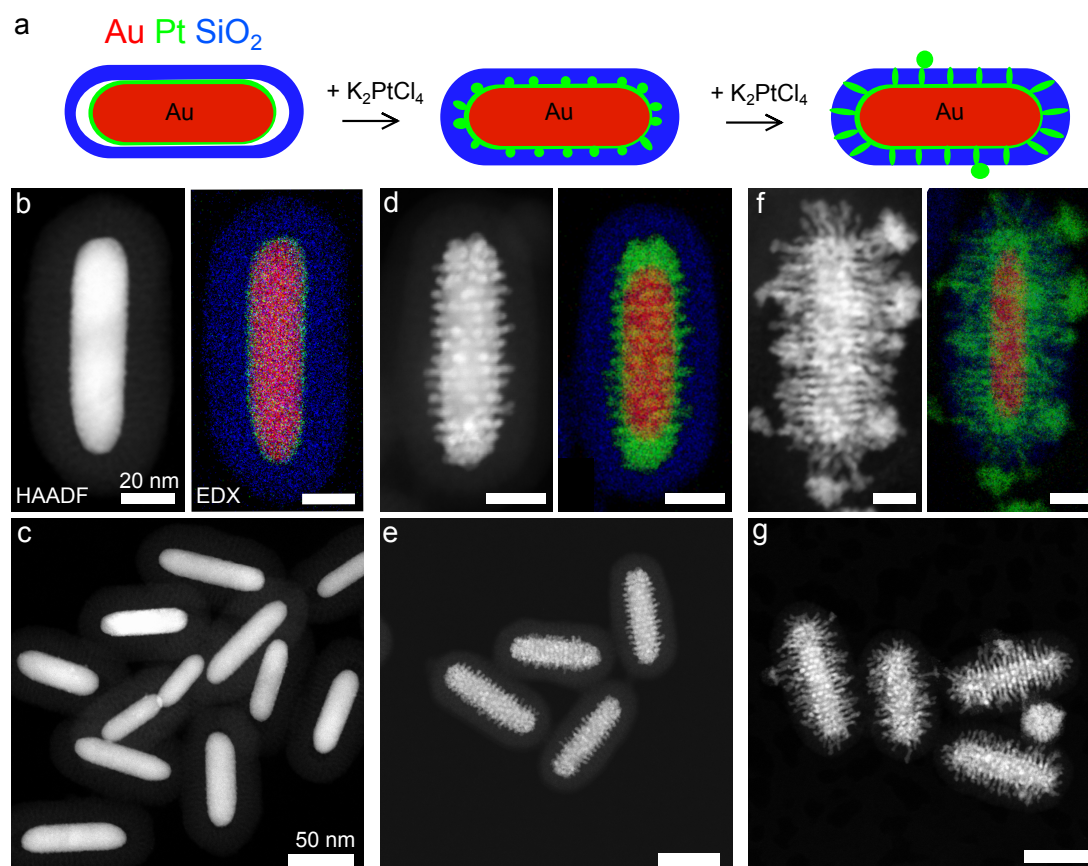


Figure 3.6: Pt-overgrowth of AuNR cores in mesoporous silica shell. a) Schematic representation of the Pt-overgrowth with increasing K_2PtCl_4 concentration, leading to filling of the mesopores of the silica shell. b-g) HAADF-STEM images and corresponding EDX maps of Au@Pt@SiO₂ NRs synthesized with 0.33 (b,c), 3.3 (d,e) and 17 mM (f,g) K_2PtCl_4 .

Platinum overgrowth

For the Pt-overgrowth K_2PtCl_4 was used as a metal precursor. The K_2PtCl_4 concentration of the aqueous solution was varied from 0.083-3.3 mM in a similar way as described above. In Figure 3.6 the HAADF-STEM images and corresponding EDX maps of the resulting Au@Pt@SiO₂ NRs are shown. The EDX maps in Figure 3.6b,d,f display Au, Pt and Si in red, green and blue, respectively. At low Pt concentrations a thin Pt shell had grown around the Au core (Figure 3.6b,c). At higher Pt concentrations, additional Pt spikes started to extend into the pores of the silica coating and revealed the ordered nature of the local pore structure around the AuNRs (Figure 3.6d,e). Once the spikes extended outside the silica shell, the metal structure became more disordered (Figure 3.6f,g). Such dendritic plasmonic nanostructures are very interesting materials for SERS, where especially at the sharp tips high field enhancements can be obtained.

We observed that the growth rate of Pt was much lower than for Ag or Pd. The reaction mixture was therefore left overnight instead of the usual reaction time of 20 min. The Pt content could therefore also be controlled by varying the reaction time. Furthermore we would like to note that the Pt spikes filled the pores of the surrounding

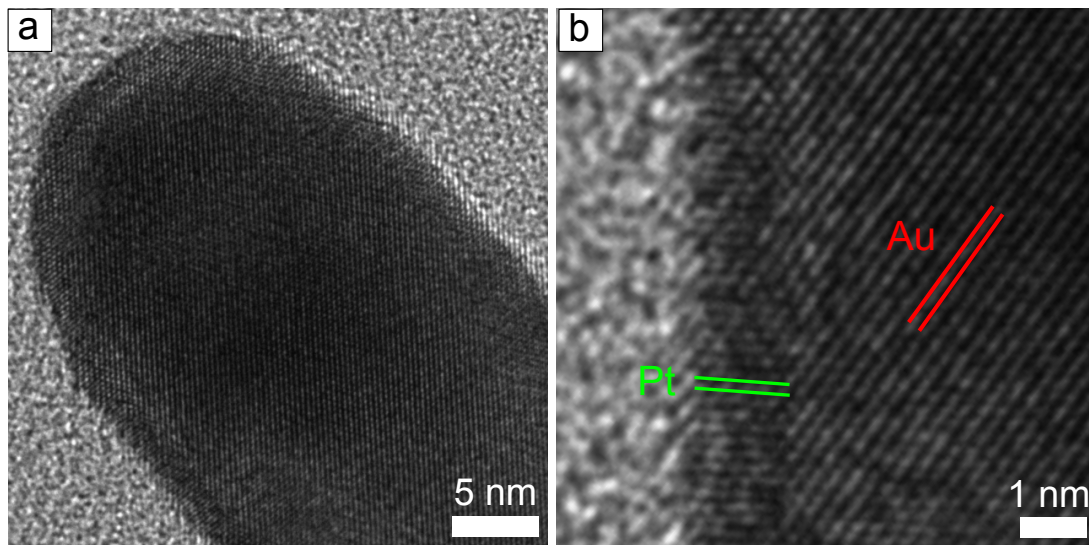


Figure 3.7: High resolution bright field TEM images of Au@Pt@SiO₂ NRs. a) HRTEM image and b) corresponding zoom-in of the Au@Pt@SiO₂ NR with $d_{lattice}^{Au} = 0.237$ nm and $d_{lattice}^{Pt} = 0.22$ nm, corresponding to the (111) lattice planes.

silica shell without destroying it. Contrarily, when growing thick Pd or Ag shells, the silica shell would crack. The Pt spike diameter was approximately 3 nm which is in good correspondence to the pore diameter of MCM-41 like materials [141, 167] (see also Chapter 2). Thus, Pt-overgrowth can successfully be used to visualize the local pore structure around AuNRs.

We also studied the orientation of the lattice planes in the Pt shell with respect to the Au core. In Figure 3.7 a High Resolution Transmission Electron Microscopy (HRTEM) image of Au@Pt@SiO₂ NRs recorded in bright field mode is shown. The HRTEM image shows that a thin crystalline Pt layer had grown on the AuNR surface, but that the (111) lattice planes of the Pt layer were oriented in a different direction compared to the underlying Au (111) lattice planes.

Controlling the growth kinetics

In the small scale reactions, carried out in ultrapure water (Milli-Q), the Ag and Pd metal overgrowth generally took place in less than 10 s. Due to these short reaction times only small scale syntheses with growth solutions below 1 mL resulted in homogeneously coated Au@Ag@SiO₂NRs and Au@Pd@SiO₂NRs without secondary nucleation. To prevent inhomogeneous shell growth and secondary nucleation, the reaction time should be longer than the time needed to fully mix all reagents. To slow down the reaction kinetics we lowered the pH of the reaction mixture by adding HCl. Below a pH of 4.1, part of the ascorbic acid is transformed into its fully protonated, non-reactive form (Figure 3.8a). Via the equilibrium between the deprotonated and protonated ascorbic acid, new deprotonated ascorbic is formed as the metal overgrowth takes place and the reactive, deprotonated ascorbic acid is consumed. Therefore, the kinetics of the metal growth can be tuned via the pH and the reaction time could be varied from seconds to minutes. In Figure 3.8 we

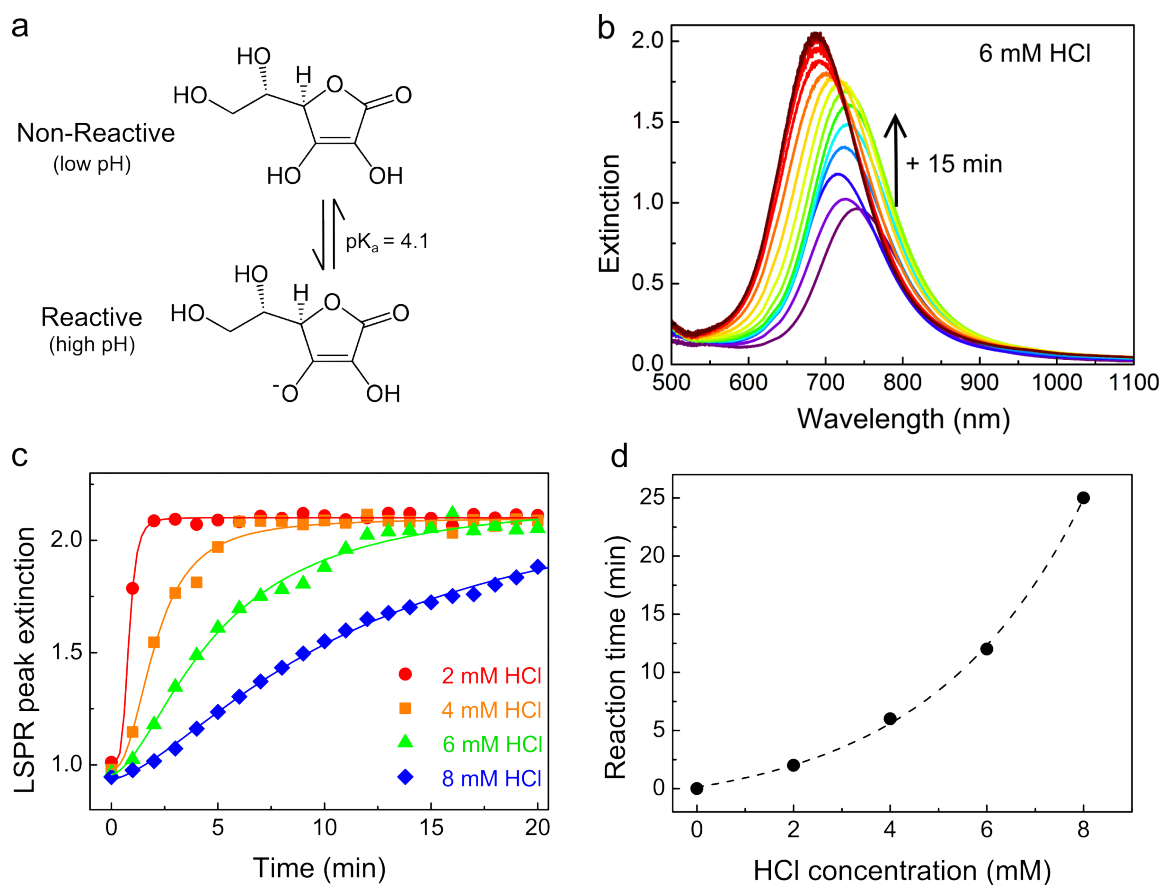


Figure 3.8: Tuning the reaction rate of the Ag metal overgrowth. a) Structural formulas of the non-reactive, fully protonated (top) and reactive, deprotonated form of ascorbic acid (bottom). The pK_a is 4.1. b) The extinction spectra of the Ag-overgrowth performed in an acidified solution with 6 mM HCl, recorded over 15 min with an interval between the spectra of 1 min. c) The LSPR peak intensity vs the reaction time when 2-8 mM HCl was present. d) Plot of the reaction time versus the HCl concentration (mM).

show the influence of the pH on the reaction time, where the latter is defined as the time needed for completion of the Ag-overgrowth. By varying the HCl concentration from 0 to 8 mM the reaction time could be tuned from a few seconds to 25 minutes. TEM analysis of the resulting samples did not show any difference in the structure and composition of the Au@Ag@SiO₂ NRs grown at different pH. Regardless of the reaction kinetics identical Au@Ag@SiO₂ NRs were obtained.

The slow reaction rate at low pH enabled us to scale up the Ag- and Pd-overgrowth drastically. In Figure 3.9a we show the extinction spectra of Au@Ag@SiO₂ NRs synthesized at a 1 mL and 400 mL scale. The spectra match closely; $\lambda_{LSPR}^{smallscale} = 783$ nm and $\lambda_{LSPR}^{largescale} = 794$ nm. The EDX map in Figure 3.9b shows that also at large (400 mL) scale uniform Au@Ag@SiO₂ NRs can be synthesized. The yield of Au@Ag@SiO₂ NRs was 26 mg with a metal loading of 85 wt%. Such large quantities enabled studies of these well defined colloidal particles in e.g. in *in situ* X-ray absorption spectroscopy (Chapter 5), gas phase catalysis (Chapter 6) and self-assembly for Raman spectroscopy (Chapter 8).

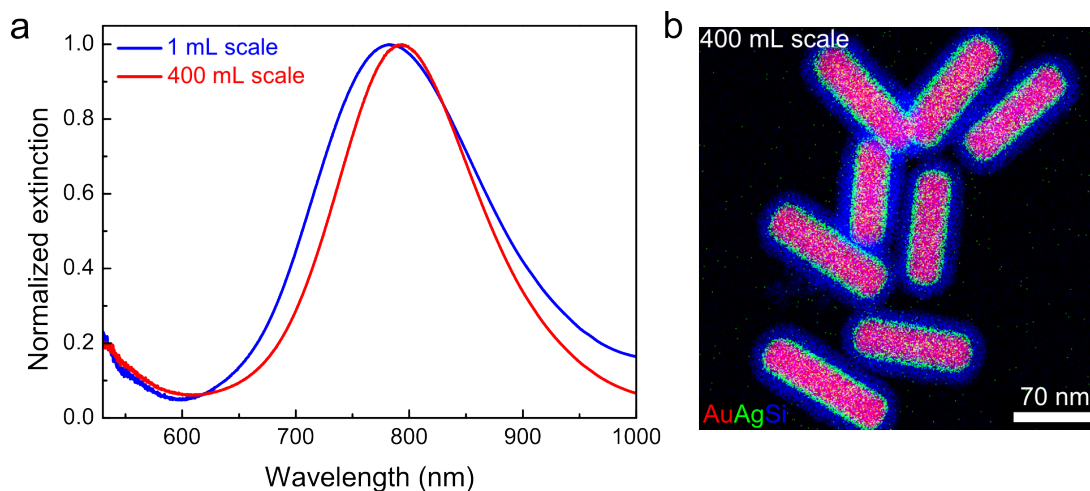


Figure 3.9: Scaling up of the core-shell synthesis. a) Extinction spectra of the Au@Ag@SiO₂ NRs synthesized at a 1 mL (blue) and 400 mL (red) scale. b) EDX map of the Au@Ag@SiO₂ NRs synthesized at a 400 mL scale; $X_{Ag} = 0.24$, sample weight = 26 mg, metal loading = 85 wt%.

Changing the morphology of non-epitaxially grown metal shells

To obtain very thin but smooth Pd shells around the AuNRs, and thus retain the spherocylindrical particle shape with most of the plasmonic properties, we first grew the Pd shells at room temperature. Next, we thermally treated the Au@Pd@SiO₂ NRs in air, N₂ and H₂ for 1 h at 300 °C, which is below the alloying temperature of Au-Pd [57]. Herein, the protective mesoporous silica shell was not only crucial in preventing the NRs from aggregating and in retaining the spherocylindrical shape, but also made it possible to redisperse the Au@Pd@SiO₂ NRs in polar solvents after the thermal treatment. In Figure 3.10 the Au@Pd@SiO₂ as synthesized and after heating to 300 °C are shown. For clarity, we specifically picked Au@Pd@SiO₂ NRs which had a very inhomogeneous Pd shell prior to thermal treatment (Figure 3.5c-d). After heating them to 300 °C the Pd coating was successfully transformed in a smooth, epitaxial shell (Figure 3.5f-h). HRTEM revealed that the as synthesized, polycrystalline Au@Pd@SiO₂ NRs transformed into single-crystalline particles during thermal treatment (Figure 3.10e,h).

Another clear indication for the change in Pd shell morphology, is the change in plasmonic properties upon heat treatment. In Figure 3.10b the extinction spectra of the Au@Pd@SiO₂ NRs before and after thermal treatment in 300 °C in H₂, N₂ and air are shown. The optical properties of the thermally treated Au@Pd@SiO₂ strongly depended on the gas atmosphere in which they were heated. In nitrogen, the LSPR peak only slightly red-shifted and barely broadened, whereas the air and H₂ heated sample blue-shifted. In addition, the LSPR peak of the air treated sample broadened severely. From TEM analysis, the differently treated samples appear to have the same morphology: the surface morphology of all Au@Pd@SiO₂ NRs transformed from dendritic, non-epitaxial to smooth, epitaxial upon thermal treatment. The difference in optical properties is therefore most likely related to a difference in the oxidation state of the Pd-atoms after thermal treatment in air (e.g. partial Pd-oxide formation).

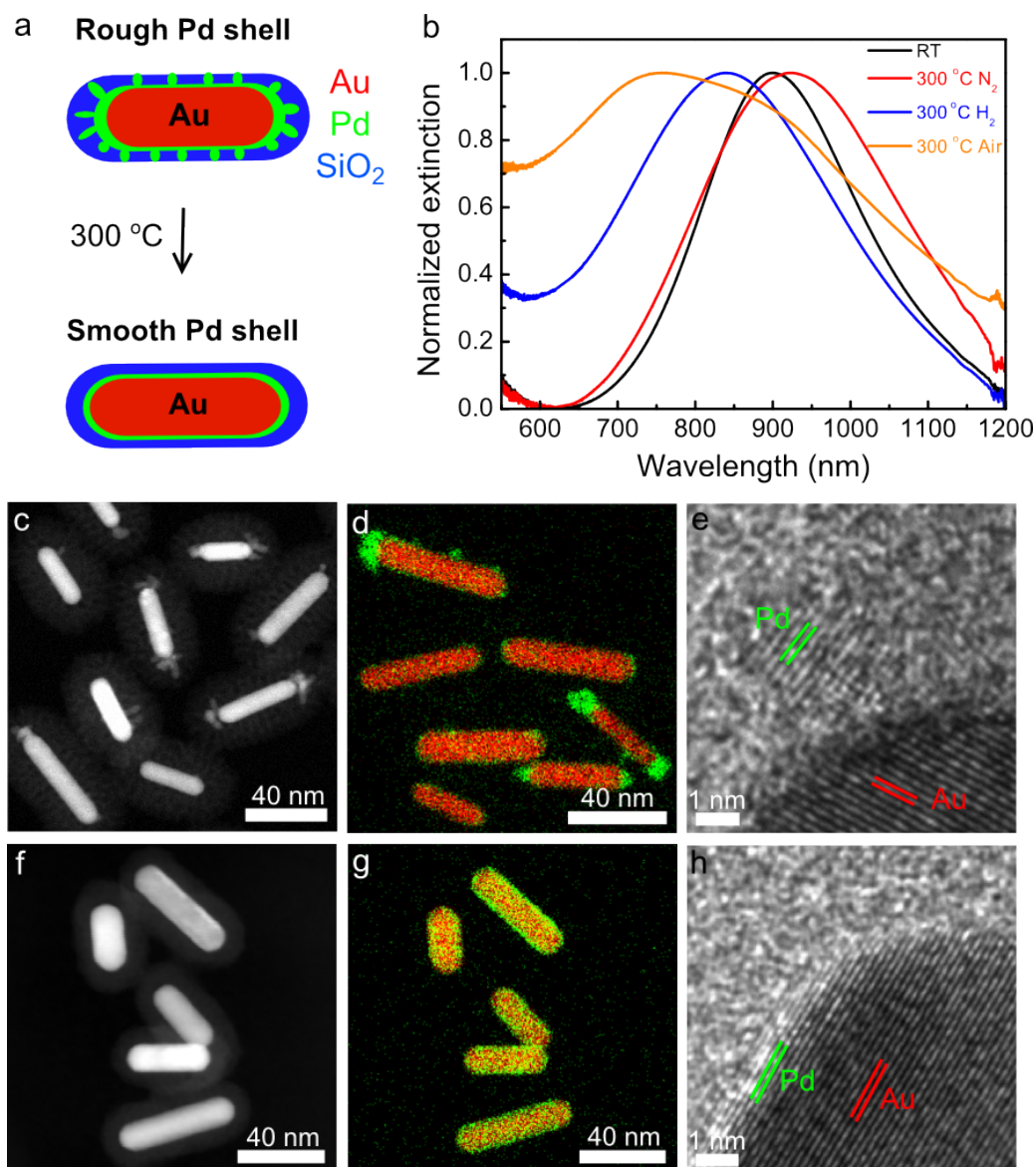


Figure 3.10: Changing the morphology of the Pd shell from dendritic to smooth via thermal treatment. a) Schematic representation of the morphology change of Au@Pd@SiO₂ NRs upon thermal treatment. b) Normalized extinction spectra of the Au@Pd@SiO₂ NRs before (black) and after heating at 300 °C in N₂ (red), H₂ (blue) and air (orange). c) HAADF-STEM, d) EDX map and e) high resolution bright field image of Au@Pd@SiO₂ as synthesized at RT. The Pd shell is inhomogeneous and dendritic. The lattice spacings, $d_{lattice}^{Pd} = 0.228$ nm and $d_{lattice}^{Au} = 0.237$ nm correspond to the (111) lattice planes. f) HAADF-STEM, g) EDX map and h) high resolution bright field image of Au@Pd@SiO₂ with a smooth, homogeneous Pd shell, obtained after heating for 1 h at 300 °C in H₂. The lattice spacing, $d_{lattice}^{AuPd} = 0.202$ nm corresponds to (200) lattice plane.

3.4 Discussion

In the result section we described the overgrowth of Ag, Pd and Pt on Au nanorods. Depending on the type of metal, different shell morphologies, crystal lattice orientations and efficiencies of metal deposition were observed. In this section we will identify the physiochemical properties known for bulk metals that play an important role in the shell growth behavior. Based on these parameters one can predict the metal structures that should form when working under thermodynamic equilibrium conditions. In addition, the role of the mesoporous silica shell in the metal overgrowth process will be discussed.

Different shell morphologies

For the Au@Ag@SiO₂ and Au@Pd@SiO₂/Au@Pt@SiO₂ NRs smooth, continuous and rough, discontinuous shell growth were observed, respectively. The morphology of the metal shell depends on the dominating growth mechanism during the metal deposition. According to crystal growth theory for gas phase deposition, three growth modes can be distinguished: (1) a layered growth mode (Frank van der Merwe, FM), (2) an intermediate growth mode (Stranski Krastanov, SK) and (3) an island growth mode (Volmer Weber, VW) [161, 162]. Herein, FM growth leads to smooth continuous shells, whereas rough, discontinuous shells are being formed in VW growth. Which of the growth modes occurs depends on the surface tensions of- and interactions between the core and shell metal and can be estimated based on Equation 3.1 [162].

$$\Delta\gamma_n = \gamma_{shell_n} + \gamma_{interface} - \gamma_{core} \quad (3.1)$$

where $\Delta\gamma_n$ is the difference in surface tension between a core-shell structure consisting of n atomic shell layers and core particle. γ_{shell_n} , $\gamma_{interface}$ and γ_{core} are the surface tensions of the shell, core-shell interface and core material, respectively. When $\Delta\gamma_n \leq 0$ and > 0 , continuous (FM) and island (VW) growth are expected, respectively. When $\gamma_{shell_n} < \gamma_{core}$, but the $\gamma_{interface}$ increases with the number of layers, SK growth occurs where initially a smooth shell is formed followed by discontinuous growth. This can happen when the strain energy increases with an increasing number of atomic shell layers, for example due to a lattice mismatch between the core and the shell crystal structure.

In Table 3.5 we listed the solid-vapour surface free energy (E_S) for Au, Ag, Pd and Pt (determined at 0 K). When $E_S(\text{shell})$ is smaller than $E_S(\text{core})$, wetting of the core by the shell metal is favourable and continuous growth can occur, given that the interfacial energy is small. As the interfacial surface tensions and energies between the metals are not known we listed the bond dissociation energies between two atoms of the same metal $E_D(\text{M-M})$ and the bond dissociation energies between a metal atom with a Au atom $E_D(\text{Au-M})$ in Table 3.5 as well. These bond dissociation energies indicate whether the interaction between the shell and core materials is favourable compared to the shell-shell interaction. Herein, continuous shell growth is likely when $E_D(\text{Au-M}) > E_D(\text{M-M})$.

From the E_S and E_D values in Table 3.5 it follows that $E_S(\text{Ag}) < E_S(\text{Au})$ and $E_D(\text{Ag-Au}) > E_D(\text{Ag-Ag})$, meaning that continuous growth of a smooth Ag shell around a gold core is thermodynamically favourable. This is in good agreement with our experimental results as presented in Figure 3.3. We observed smooth, continuous Ag shell growth,

Table 3.5: Summary of key parameters of bulk Au, Ag, Pd, and Pt. The FCC lattice constant, solid-vapour surface free energy at 0 K, the bond dissociation energy of the 2 equal metal atoms (M-M) and between Au and a different metal atom (Au-M), and the standard reduction potentials [168–172].

	Au	Ag	Pd	Pt
FCC lattice constant (Å) [168]	4.08	4.09	3.89	3.92
Surface energy (J/m ²) [168, 169]	1.50	1.24	2.00	2.49
Bond dissociation energy (M-M, kJ/mol) [171]	226	160	100	307
Bond dissociation energy (Au-M, kJ/mol) [171]	226	203	155	-
Standard reduction potentials (V) [172]	+1.00 (AuCl ₄ ⁻)	+0.80 (Ag ⁺)	+0.59 (PdCl ₄ ⁻)	+0.76 (PtCl ₄ ⁻)

where we could precisely control the shell thickness and thus the number of atomic layers via the metal precursor concentration (AgNO₃). It should be noted that regardless of the reaction rate, which we varied in Figure 3.8, continuous Ag shell growth was observed. Smooth Ag growth on differently shaped AuNPs has also been observed in literature, both for uncoated and partially coated NPs [49, 54–56, 159, 161, 165]. To the best of our knowledge there are no reports of rough, discontinuous Ag shell growth on Au.

The growth behavior of Pt shells on Au cores, presented in Figure 3.6, can be explained in a similar way. $E_S(\text{Pt}) > E_S(\text{Au})$ and $E_D(\text{Pt-Pt}) > E_D(\text{Au-Au})$, meaning that discontinuous, rough shell growth is indeed expected. Note that $E_D(\text{Au-Pt})$ is not known since Au and Pt do not form an alloy. Our experimental findings are in line with previous reports of metal overgrowth on uncoated and partially coated Au NPs, where always rough shell growth was observed regardless of the presence of a (porous) surface coating [54, 161, 165, 166].

Predicting the type of metal growth for Pd on Au is more complex than for Ag or Pt shell growth. The surface energy of Pd is higher than Au, whereas the bond dissociation energy $E_D(\text{Au-Pd})$ is larger than $E_D(\text{Pd-Pd})$. The latter indicates that continuous Pd shell growth is in principle favourable. However, when overgrowing Au with Pd we observed that Pd, like Pt, tends to grow a rough shell extending into the mesopores of the silica shell. For uncoated Au-Pd NRs both continuous and discontinuous shell growth have been observed [157, 161]. In the case of uncoated AuNRs, the growth behavior could be tuned from continuous to discrete when growing the Pd shell in the presence of Br⁻ and Cl⁻ ions, respectively [157]. This difference in growth behavior is probably due to a variation in the reduction potential and thus in the reduction rate of Pd-ions when adding Br⁻ and Cl⁻ which are known to strongly coordinate with the Pd ions [86, 173]. In our case the growth occurred in the presence of Cl⁻ ions coming from the Na₂PdCl₄ precursor, resulting in discontinuous shell growth. By thermally treating the Au@Pd@SO₂ NRs we could transform the rough Pd shells into a smooth, continuous Pd shells (Figure 3.10). The latter result shows that continuous Pd shell Au core NRs are thermodynamically the most favourable structures.

The role of the silica shell

In general, metal-overgrowth within a mesoporous silica shell has several advantages. By making use of a protective silica shell additional stabilizing surfactants were not needed and/or could be removed, such that secondary nucleation of individual metal NPs was suppressed. The second metal was therefore always preferentially deposited on the Au cores and secondary nucleation of individual was only observed at very high (Pt) precursor concentrations (>3.3 mM). Herein, usage of a relatively mild reducing agent, like ascorbic acid, also contributed to preferential metal-overgrowth on the Au core. In the case of Ag, the silica shell helped to retain the sphereocylindrical rod shape, even when growing thick Ag shells. Ag-overgrowth on uncoated NRs on the other hand, can lead to loss of the sphereocylindrical shape and the formation of nano-"bar" or "brick" like particles [159, 160].

The presence of porous shells, such as the mesoporous silica shell in this study, can alter the growth behavior and lead to the shell morphologies different those grown on uncoated nanoparticles. In the metal overgrowth of mesoporous silica coated AuNRs, spiky Au shells were grown [49], whereas this does not happen when performing the overgrowth on partially, non-porous silica coated [165] or uncoated AuNRs [174]. In our case, the discontinuous Pd shell growth could therefore also be ascribed to the presence of the mesoporous silica template. Rough Pt growth, on the other hand, is not necessarily caused by the presence of the mesoporous silica shell template, as rough shell growth always occurs on Au regardless of type of ligands or shells around the NPs.

We noticed that in particular for Pd, metal growth appeared more clearly at the tips of the NRs (Figure 3.5d and 3.10c). Such preferential coating at the tips rather than the sides of the NRs was also observed in previous reports where bare AuNRs were used [152, 157]. This could be related to the different surface facets at the tips compared to the sides [21], as the surface energy is known to be surface facet dependent [168].

Finally, it should be noted that the silica shell allowed the thermal treatment of the bimetallic rods. The shell prevents the rods from sintering and helps to retain the particle shape. This enabled the synthesis of smooth, epitaxial Pd shell Au core NRs (Figure 3.10), but also allows alloying of the core-shell structures for which thermal treatment at elevated temperatures is needed [57, 104, 175] (see Chapters 4-6).

Crystal orientation of the metal shell

When considering the crystal orientation of the shell material with respect to the core, either epitaxial or non-epitaxial growth can occur. Epitaxial growth means that the second metal forms a crystalline shell with one well-defined orientation with respect to the core crystal structure, whereas non-epitaxial growth indicates the formation of a metal shell having a random orientation with respect to the core, or a completely disordered crystal structure.

Whether epitaxial growth occurs (partially) depends on the lattice parameters of the core and shell metal. In Table 1 we give the lattice constants given for FCC Au, Ag, Pd and Pt crystals. Ag and Au have very similar lattice constants with a discrepancy of only 0.2 %, explaining why we observed epitaxial growth of Ag on Au. The HRTEM images in Figure 3.4 show a crystalline Ag shell had formed and that the lattice planes of the Ag shell adopted the same crystallographic orientation as the underlying Au core. For Pd

and Pt, the lattice mismatch with Au is larger, about 4%. Typically within 5% mismatch, epitaxial growth still possible [176]. The HRTEM image in Figure 3.7 shows that a thin crystalline Pt layer with different orientation to Au was indeed formed. Also for thin Pd such growth can be observed [54, 161]. However, at larger Pd shell thickness's, separate Pd nanocrystals were grown with random orientations compared to the underlying AuNR (Figure 3.10e). In Figure 3.10h we show that these non-epitaxial shells can successfully be transformed into epitaxial Pd shells via thermal treatment.

Efficiency of the metal overgrowth

The amount of metal deposited upon metal overgrowth was not the same for all metals either, meaning that the efficiency of metal overgrowth was different. The EDX quantification in Figure 3.3 and 3.5 show that more Na_2PdCl_4 was needed to increase the X_{Pd} compared to the amount of AgNO_3 to obtain the same increase in X_{Ag} . Thus, a smaller fraction of the PdCl_4^{2-} ions compared to Ag^+ ions was reduced. This could be related to the difference in standard reduction potential of PdCl_4^{2-} and Ag^+ , which is +0.591 and +0.800 V (25 °C, 1 atm), respectively (see Table 3.5). For Pt, it was not possible perform a reliable quantification of X_{Pt} determine well as secondary nucleation occurred at higher Pt concentrations.

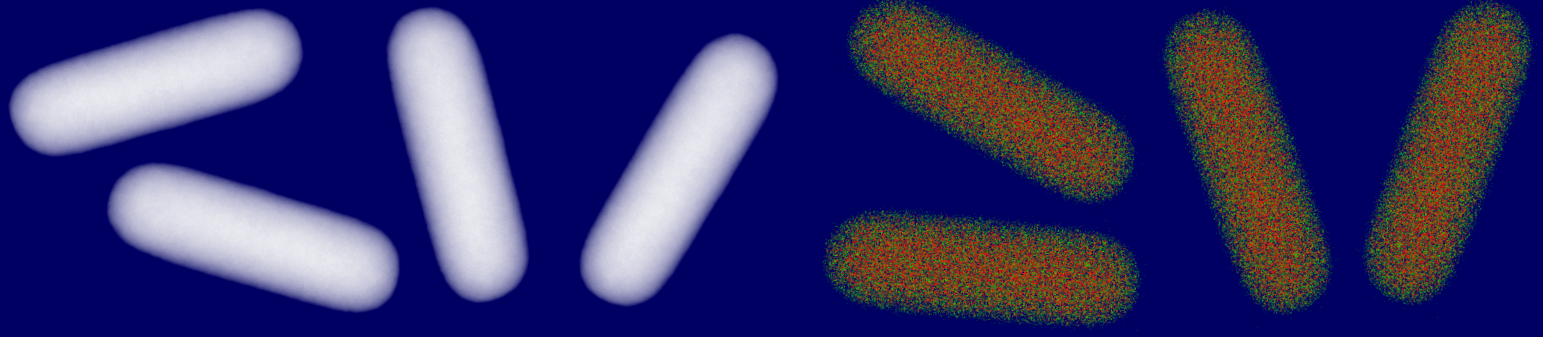
We found that the efficiency of metal overgrowth is also related to the space available in the silica shell. Limited space in- and the flexibility of the silica shell is most likely the reason for the flattening of the X_{Ag} and X_{Pd} at higher metal precursor concentrations. We observed that this flattening occurs at lower Ag contents when performing Ag growth on unetched Au@SiO_2 NRs, where the available space in the silica shell is smaller.

3.5 Conclusions

In this chapter we demonstrated the controlled synthesis of mesoporous silica coated Au core Au/Pd/Pt shell nanorods with precisely adjustable metal compositions and shell-morphologies. First, the Au core size was tuned via oxidative etching with H_2O_2 , which is a more robust method compared to using oxygen from the air that we used previously [54]. In the subsequent metal overgrowth, the metal composition was tuned via the metal precursor, where higher metal precursor concentrations led to thicker Ag- and more dendritic Pt/Pd shells. Next, the growth kinetics of the metal overgrowth were controlled by varying the pH of the reaction mixture. This allowed us to dramatically scale the synthesis up to the quantities needed for e.g. catalysis. Finally, smooth, epitaxial Pd shell Au core NRs were obtained, by thermally treating dendritic Pd shell Au core NRs below the alloying temperature. Such bimetallic core-shell structures are likely to be of great interest for light-based applications such as plasmon enhanced catalysis, self-assembly of the rod-like particles and the *in situ* monitoring of chemical reactions with SERS, allowing interesting comparisons between core-shell versus alloyed nanorods.

Acknowledgements

We are grateful to Dr. Tian-Song Deng for sharing his knowledge on the core-shell synthesis and his pleasant guidance during the project. We thank Dr. Wiebke Albrecht for discussion on the optical properties of the core-shell NRs. Liselotte Olthof and Maarten Bransen are acknowledged for discussion on the synthesis. Hans Meeldijk is acknowledged for his help in performing the electron microscopy measurements.



Alloyed metal nanorods with tunable properties

4

Abstract

In this chapter, we show that alloyed anisotropic nanoparticles can be obtained from core-shell nanorods with complete retention of the particle shape via thermal treatment at temperatures far below the bulk melting temperature. By coating Au-Ag, Au-Pd and Au-Pt core-shell nanorods with a protective mesoporous silica shell the transformation of the rod to a more stable spherical shape was successfully prevented during alloying. The chemical stability of the Au-Ag core-shell nanorods was drastically increased after alloying. From finite-difference time-domain (FDTD) calculations it followed that alloyed AuAg rods also exhibit better plasmonic properties than their spherical counterparts and that their optical properties can be tuned via the metal composition. Finally, the generality of our method is demonstrated by alloying Au-Pd and Au-Pt core-shell NRs, where the AuPd and AuPt alloyed nanorods showed a large increase in thermal stability of several hundred degrees compared to monometallic silica coated Au nanorods.

4.1 Introduction

Gold nanorods (AuNRs) exhibit strong and easily tunable plasmonic properties combined with a good chemical stability [177]. Compared to gold, silver has even better plasmonic properties. In Chapter 3 we showed that by growing a silver shell around AuNRs, the plasmonic properties can be significantly enhanced [54, 56]. However, the applicability of these core-shell NRs is hampered by the relatively poor chemical stability of the Ag-shell, which is prone to oxidation and dissolution. For spherical nanoparticles (NPs) it has been shown that by alloying the chemical stability of Ag-based nanoparticles can significantly be improved [56].

Such alloyed metal NPs are not only interesting for optical applications, but also for heterogeneous catalysis [178, 179], a topic which will be discussed in detail in Chapter 6. By combining two metals in a nanoparticle so-called synergistic effects can arise, where the catalytic properties of the bimetallic catalyst exceed those of the single-component systems [180, 181]. Furthermore, alloying can lead to an increased thermal stability of the NPs [182, 183]. This is relevant in for example thermal, photo- and plasmon enhanced catalysis where heating or light irradiation is used to enhance the catalytic performance of metal catalysts [108, 156].

For many light based applications, rod-shaped alloyed nanoparticles would be ideal since they offer a combination of good plasmonic properties with a high chemical and thermal stability. However, there is no facile way of making rod-shaped alloys while simultaneously controlling their composition and shape. Most studies to date have focused on spherical alloyed NPs only. Few examples were reported on the synthesis of alloyed NRs, such as template-directed electro-chemical or wet-chemical co-deposition and low-temperature decomposition of bimetallic precursors [184–188]. However, these synthesis routes yield NRs with only one fixed composition and/or are highly laborious with small amounts of sample obtained. Alternatively, alloying of spherical core-shell nanoparticles via thermal treatment is a simple and scalable method with precise control over composition and size [56, 189]. Unfortunately, at the elevated temperatures required for alloying, the rod-shape is unstable and the rod deforms to a spherical shape [190]. We showed in Chapter 2 that a protective silica coating can significantly improve the stability during heat treatment. By using a silica coating, spherical Au-Ag NPs could for example successfully be alloyed [56]. However, it has not been shown yet that this method can be extended to anisotropic particles without changing the particle shape after alloying and how an out-of equilibrium NR shape influences this process.

In this chapter, we show that alloyed nanorods can be made via thermal treatment without losing the anisotropic particle shape. To this end, the nanorods were coated with a protective mesoporous-silica layer, which enhances their thermal stability, prevents sintering of NRs during thermal treatment and allows mass transport to the metal surface, which is crucial for catalytic applications. The metal composition of the NRs could be tuned precisely by varying the core-to-shell size ratio [54] (see Chapter 3). We followed the alloying of mesoporous-silica coated Au(core)-Ag(shell) nanorods (Au@Ag@SiO₂ NRs), Au(core)-Pd(shell) nanorods (Au@Pd@SiO₂ NRs) and Au(core)-Pt(shell) nanorods (Au@Pt@SiO₂ NRs) *in situ* with high-angle annular dark field scanning transmission electron microscopy (HAADF-STEM) and energy-dispersive X-ray spectroscopy (EDX). We compared the

experimentally measured extinction spectra of AuAg alloyed NRs to extinction spectra computed with FDTD calculations. The latter showed that alloyed NRs exhibit enhanced plasmonic properties compared to their spherical counterparts. Furthermore, we observed that the thermal stability of the alloyed AuPd and AuPt NRs was greatly improved. The methodology presented in this chapter is not limited to the metals chosen here or to rod-shaped nanoparticles only, but can be applied to different metals and different anisotropic particle shapes as well as long as mixing of the metals is thermodynamically favourable.

4.2 Experimental

Chemicals

All chemicals were used as received without further purification. Hexadecyltrimethylammonium bromide (CTAB, >98.0%) and sodium oleate (NaOL, >97.0%) were purchased from TCI America. Hydrogen tetrachloroaurate trihydrate ($\text{HAuCl}_4 \cdot \text{H}_2\text{O}$), sodium hydroxide (98%), and polyvinylpyrrolidone (PVP, average molecular weight 58 kg/mol, K29-32) were purchased from Acros Organics. L-Ascorbic Acid (BioXtra, $\geq 99\%$), silver nitrate (AgNO_3 , $\geq 99\%$), sodium borohydride (NaBH_4 , 99%), hydrochloric acid (HCl, 37 wt% in water), tetraethyl orthosilicate (TEOS, 98%), ammonium hydroxide solution (≥ 25 wt% in water), sodium tetrachloropalladate-(II) (Na_2PdCl_4 , 98%) and potassium tetrachloroplatinate-(II) (K_2PtCl_4 , 98%) were purchased from Sigma-Aldrich. Ultrapure water (Millipore Milli-Q grade) with a resistivity of $18.2 \text{ M}\Omega$ was used in all of the experiments. All glassware for the AuNR synthesis was cleaned with fresh aqua regia (HCl/ HNO_3 in a 3:1 volume ratio), rinsed with large amounts of water and dried at 100°C before usage.

Synthesis of bimetallic core-shell NRs in a mesoporous silica shell

Synthesis of mesoporous silica coated AuNRs

The synthesis of the uncoated AuNRs was done according to the procedure described by Ye *et al.* [13], making use of a binary surfactant mixture of hexadecyltrimethylammonium bromide (CTAB) and sodium oleate (NaOL). For the silica coating the procedure described by I. Gorelikov and N. Matsuura [90] was followed. Herein, the rods were dispersed in an aqueous solution of 1.5 mM CTAB and 1.0 mM NaOH, to which 3 times 0.33 vol% of a 0.90 M TEOS in ethanol solution was added with a 45 minutes time interval between the additions. After 2 days of ageing at 30°C , while magnetically stirring at 400 rpm, the rods were washed with water and ethanol, and redispersed in methanol (LSPR peak position, $\lambda_{\text{LSPR}}=778 \text{ nm}$, and maximum extinction, $\text{Ext}=1.7$ when diluted $2\times$ in H_2O). In all washing steps we typically used a centrifugation speed of 7000-9000 rcf for 30-10 min. The average silica shell thickness was 18 nm.

Oxidative etching

The oxidative etching of Au@SiO₂ NRs was done with H₂O₂ as oxidizing agent. The H₂O₂ concentration and reaction temperature can be varied to tune the reaction rate of the oxidative etching (see Chapter 3). Here, 12 mL of Au@SiO₂ NRs (λ_{LSPR} = 778 nm, Ext= 3.5) and 240 μ L concentrated HCl (37 vol%, 12.1 M) were mixed in a 40 mL glass vial while magnetically stirring at room temperature. 240 μ L H₂O₂ in MeOH (20 mM) was added and the reaction mixture was placed in a 70 °C oil bath. After 15 min the reaction mixture was removed from the oil bath and cooled down to room temperature by adding 18 mL fresh MeOH. The etched particles were washed with 20 mL and redispersed in 12 mL of a 1.1 wt% PVP (K29-32) in H₂O solution, respectively. The resulting LSPR peak position of the etched Au@SiO₂ NRs in PVP/H₂O was 745 nm with an extinction of 2.2.

Metal overgrowth

The etched Au@SiO₂ NRs were overgrown with Ag, Pd or Pt according to the procedure of Deng *et al.* [54]. 0.30 mL of etched Au@SiO₂ NRs in PVP/H₂O (λ_{LSPR} =745 nm, Ext= 2.2) and 30 μ L 2 mM AgNO₃, 5 mM Na₂PdCl₄ or 10 mM K₂PtCl₄ in water were added to a 4 mL glass vial. Next, 30 μ L of 8, 20 and 40 mM ascorbic acid (AA) were added for the Ag-, Pd- and Pt-shell growth, respectively, and the vial was directly placed into a Vortex Shaker and shaken for 20 min. The samples were washed with H₂O and redispersed in 1.0 mL EtOH (100%).

The dimensions and aspect ratios of the NRs before and after oxidative etching and metal overgrowth were determined by TEM analysis and are summarized in Table 4.1. We used the same batch of silica coated AuNRs for Ag and Pd overgrowth and a comparable batch of AuNRs for Pt overgrowth. The silica shell thickness is the same for the batches in Table 4.1 (~18 nm). It should be noted that an accurate size determination of the Pd and Pt shell is difficult since it exhibits a dendritic structure.

Table 4.1: Dimensions and aspect ratios (AR) of Au@SiO₂ NRs before and after etching, Au@Ag@SiO₂, Au@Pd@SiO₂ and Au@Pt@SiO₂ NRs after metal overgrowth, as determined from TEM analysis.

Sample ID	Length (nm)	Diameter (nm)	AR
Au@SiO ₂ NRs before etching	71	20	3.6
Au@SiO ₂ NRs after etching	61	20	3.1
Au@Ag@SiO ₂ NRs used for <i>in situ</i> heating	74	27	2.7
Au@Ag@SiO ₂ NRs used for N ₂ heating	73	27	2.7
Au@Ag@SiO ₂ NRs used for air heating	73	27	2.7
Au@Pd@SiO ₂ NRs used for <i>in situ</i> heating	73	22	3.3
Au@Pt@SiO ₂ NRs used for <i>in situ</i> heating	57	18	3.2

***In situ* heating experiments**

The *in situ* heating measurements were performed on a FEI Talos F200X operated at 200 kV using a heating holder from DENSsolutions. The Au@Ag@SiO₂ NR solution was dropcasted on a heating chip consisting of several SiN windows. Once a suitable spot was chosen the chip was heated to 600 °C or 800 °C for the Au@Ag@SiO₂ and Au@Pd@SiO₂, Au@Pt@SiO₂ samples, respectively. The temperature was changed in steps of 50 °C and kept for about 5 min. The temperature increase per step was almost instantaneous (<1 s). However, since EDX maps were taken for 15 min the chip was kept at specific temperatures for a longer time. For example, EDX maps were taken of the spot from Figure 1 and a spot on a different window for the Au@Ag@SiO₂ sample at 400 °C (Figure 1). Thus, the sample was effectively heated for 40 min at that temperature. The influence of heating time is further analysed in Figure 4.3.

The Au@Pd@SiO₂ and Au@Pt@SiO₂ NRs were heated in a similar way. EDX measurements were performed at 600 °C, 700 °C and 800 °C and thus at these temperatures the particles were heated for 20 min instead of 5 min. Complete alloying was observed after keeping the temperature at 800 °C for 10 min more, thus 30 min in total. The EDX measurement at 800 °C shown in Figure 4.8 was taken after these 30 min. This was done because 800 °C was the maximal heating temperature. The heating time at 800 °C was therefore increased until alloying was observed.

EDX measurements and analysis

All EDX measurements were performed at a FEI Talos F200X. Each map was taken for 15 min to get a good signal-to-noise ratio. The obtained intensity maps were quantified by using the Cliff-Lorimer method. Only Au and Ag or Pd were used for the quantification while the other elements were used for deconvolution only. For clarity only the Au and Ag or Pd maps are shown and not the Si or O maps although the mesoporous-silica shell is always present. All EDX maps in this chapter are presented in atomic percent except for Figure 4.5, 4.6 and 4.9 which show the intensity maps.

Oven heating experiments

For the oven heating experiments in N₂ and air, the Au@Ag@SiO₂ NRs were dropcasted on microscope glass slides (76×26 mm, Thermo scientific, Menzel-Gläser). The oven heating in N₂ was done in a tube oven (Thermolyne 79300 tube furnace). The sample was placed in a quartz tube and flushed with N₂ for 1 h at room temperature. Thereafter the sample was heated to 300 °C with a rate of 15 °C/min under a constant N₂-flow. After keeping the temperature at 300 °C for 10 min, the sample was heated to 400 °C with a rate of 10 °C/min and kept at 400 °C for 60 min. For the oven heating experiments in air we used a static air oven (Carbolite). After preheating the oven the glass slide was inserted and heated at 400 °C for 30 min. As a control experiment, we also heated the Au@Ag@SiO₂ in air with a similar temperature program as used for the N₂ experiments, but this did not lead to a different result. The extinction spectra before and after heating were measured with Fourier transform visible infrared spectroscopy (VIS-IR) on the particles on a microscope slide in an air environment.

The dimensions of the Au@Ag@SiO₂ NRs before and after heating in N₂ and air are summarized in Table 4.2. It can be seen that the particles heated under N₂ barely changed their aspect ratio, although they seem to slightly have decreased in volume. However, a smaller amount of particles was available for TEM analysis after heating compared to before heating. As the volume and ratio of Au and Ag did not change during the *in situ* measurements, we believe that the apparent volume loss is due to limited statistics. A clear difference can be seen, however, for particles heated in air where a drastic change in volume and aspect ratio occurred. We observed that the porous silica shell structure was preserved during heat treatment at 500 °C in N₂. The mesopores in the silica shell were always still present and are expected to be stable up to ~800°C [191].

Chemical stability experiments

To check the chemical stability, the Au@Ag@SiO₂ core-shell and AuAg@SiO₂ alloyed particles on the microscope slide were exposed to an aqueous mixture of 1.7 vol% H₂O₂ and 0.9 vol% NH₃·H₂O for 15 min and 2 h, respectively. Before and after etching the extinction spectra of the Au@Ag@SiO₂ core-shell and AuAg@SiO₂ alloyed NRs were measured with Fourier transform visible infrared spectroscopy (VIS-IR). This was done on the microscope slide in an air environment.

FDTD calculations

The FDTD calculations were performed with the software package Lumerical FDTD Solutions 8.15. A total field scattered field source was used and the longitudinal localized surface plasmon resonance was monitored at 200 points in a wavelength range from 500 nm to 1200 nm by aligning the polarization with the long axis of the NRs. A three-dimensional non-uniform mesh was used with a grid size of 0.5 nm for the NRs themselves and in their vicinity. The particles were modelled as cylinders using the experimentally determined

Table 4.2: Dimensions and aspect ratios (AR) of Au@Ag@SiO₂, Au@Pd@SiO₂ and Au@Pt@SiO₂ NRs before and after heating *in situ*, in N₂ air at 400 °C of 1 h, as determined from TEM analysis.

Sample ID	Length (nm)	Diameter (nm)	AR
Au@Ag@SiO ₂ NRs before <i>in situ</i> heating	76	25	3.0
Au@Ag@SiO ₂ NRs after <i>in situ</i> heating	74	27	2.7
Au@Ag@SiO ₂ NRs before N ₂ heating	73	27	2.7
Au@Ag@SiO ₂ NRs after N ₂ heating	65	26	2.5
Au@Ag@SiO ₂ NRs before air heating	73	27	2.7
Au@Ag@SiO ₂ NRs after air heating	42	25	1.7
Au@Pd@SiO ₂ NRs before <i>in situ</i> heating	73	22	3.3
Au@Pd@SiO ₂ NRs after <i>in situ</i> heating	71	22	3.2
Au@Pt@SiO ₂ NRs before <i>in situ</i> heating	57	18	3.2
Au@Pt@SiO ₂ NRs after <i>in situ</i> heating	53	18	2.9

sizes as presented in Table 4.2. The atomic Ag silver fraction, X_{Ag} , was varied between 0 and 1 in 0.1 steps.

We took the dielectric functions from an analytical model derived from measurements of the dielectric function of certain alloy compositions which allows for extrapolation of the dielectric function to any composition [192]. It is important to use dielectric functions obtained for alloys as it was demonstrated that measured extinction spectra of spherical AuAg alloyed NPs could not be reproduced by a linear combination of the dielectric functions of Au and Ag, but only by using the dielectric data of alloys [192, 193]. We furthermore size-corrected the dielectric functions to account for the influence of the particle size confinement on the electron mean free path [194].

4.3 Results and Discussion

Alloying Au-core Ag-shell nanorods

To study the thermally induced alloying of nanorods we first synthesized Au@Ag NRs in a mesoporous silica shell [54]. The average length (L) of the Au@Ag rods was 73 nm and the diameter (D) 27 nm, while the Au core length and diameter were 61 nm and 20 nm, respectively. The atomic silver fraction (X_{Ag}) was determined from EDX and was approximately 0.43. In order to find the required heating temperature for alloying, which can deviate substantially from bulk values [189, 195], the core-shell NRs were heated *in situ* in a high-resolution electron microscope operated in HAADF-STEM mode. The temperature was increased in 50 °C steps and kept constant for 5 min at each temperature (Figure 4.1).

Below 400 °C the Au core and Ag shell can clearly be distinguished by the Z-contrast inherent to STEM. At 400 °C this contrast difference became less apparent and vanished at 450 °C indicating that an alloy was formed. The EDX measurements in Figure 4.1b show that alloying started at the Au-Ag interface at 400 °C and confirm the transition of the core-shell structure to a homogeneous alloy at 450 °C. After cooling back to room temperature, the alloyed structure was preserved (Figure 4.1b) and the FCC crystallinity of the rod retained (Figure 4.2), as expected for AuAg alloys. The (111) lattice spacing of a formed AuAg alloy NR was 0.235 nm, which is in good agreement with the known values of 0.2355 nm and 0.2358 nm for Au and Ag FCC crystals, respectively. The particles preserved their anisotropic shape during heat treatment due to the stabilizing silica-shell. The Au-Ag ratio did not change upon alloying.

Next to the heating temperature, the heating time is an important parameter in the alloying process. Figure 4.3a shows the influence of heating time for a temperature of 400 °C. Right after changing the temperature to 400 °C the core-shell structure was still clearly visible (upper left image in Figure 4.3a). After 5 min the shell started to disappear and after 20 min heating at 400 °C the core-shell structure had vanished (lower left image in Figure 4.3a). This was confirmed by EDX measurements of particles lying on a different SiN window shown in Figure 4.3b as most of the particles had formed an alloy. After 40 min no core-shell structure could be seen from the STEM contrast, indicating that the alloying was completed.

To make sure that alloying was not induced by the electron beam, we checked different

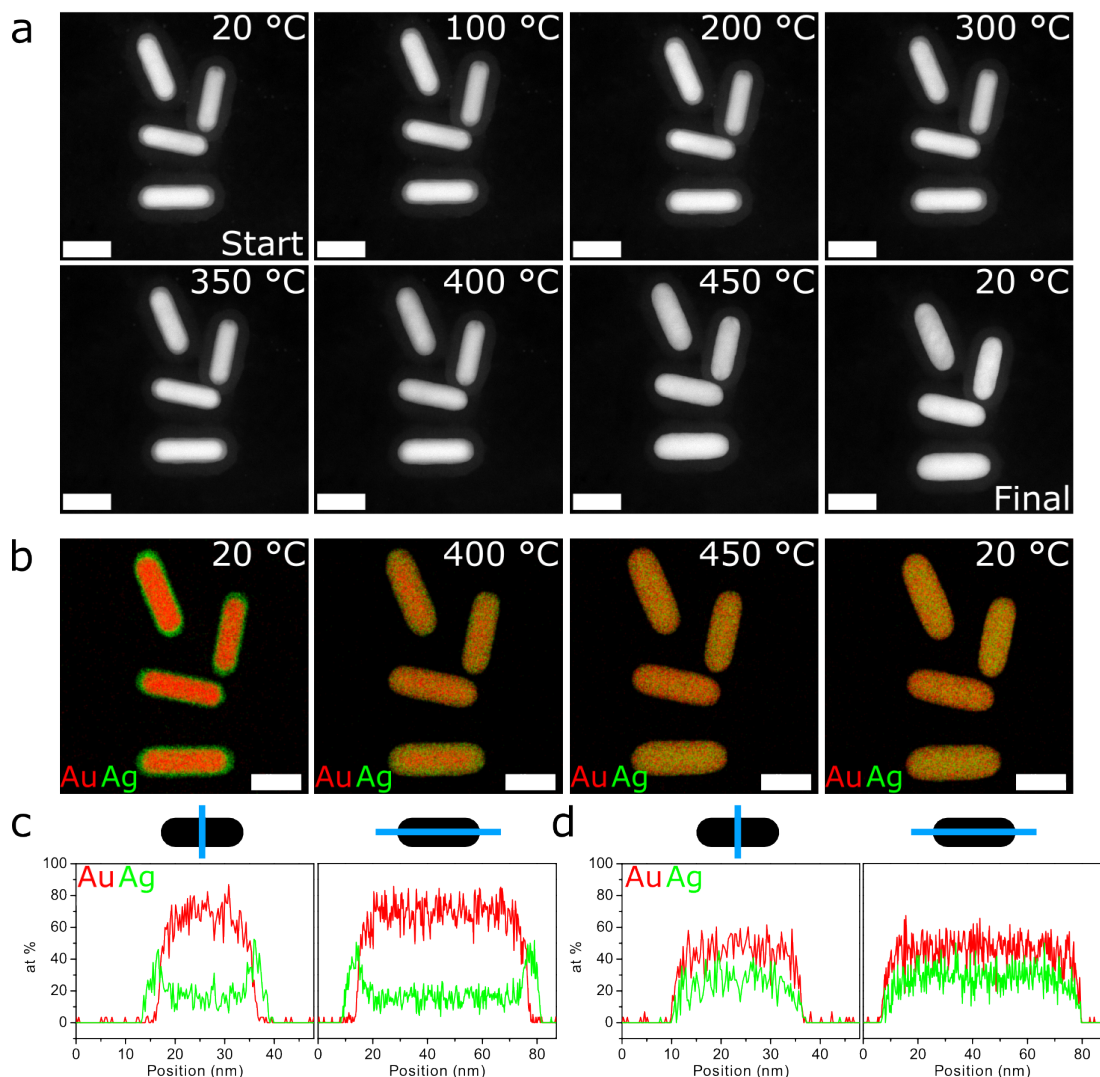


Figure 4.1: *In situ* heating of silica coated Au@Ag core-shell nanorods with $L=73$ nm and $D=27$ nm, $X_{Ag}=0.43$. a) HAADF-STEM images recorded before, during and after heating to 450 °C. The scale bars are 50 nm. b) EDX maps showing the metal distribution of Ag (green) and Au (red) in the core-shell and alloyed metal nanorods before and after heating, respectively. The average aspect ratio (AR) of the four particles shown here changed from 3.0 to 2.7 when heated to 450 °C. All scale bars are 40 nm. c) EDX line scans perpendicular and along the long axis of the top left nanorod at 20 °C and d) 450 °C. It should be mentioned that the SiO_2 shell is always present although the Si or O EDX maps are not shown here and the SiO_2 -STEM contrast is weak compared to the metals.

spots that had not been exposed to the electron beam prior to heating and concluded that the alloying was not modified by the electron beam. The EDX maps in Figure 4.3b confirm that the electron beam had a negligible influence on the alloying process as the particles in 4.3b were not exposed to the electron beam before and still showed the same behaviour as the illuminated spot in Figure 4.1. Figure 4.3c shows STEM images of particles in different SiN windows after the *in situ* heating process without prior electron

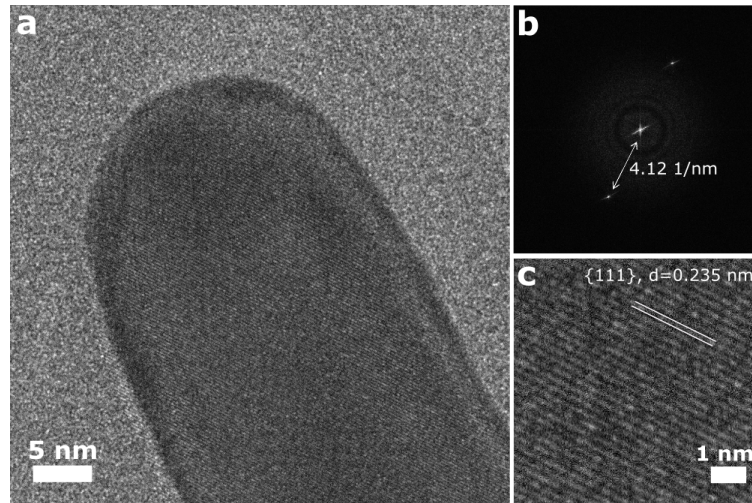


Figure 4.2: High-resolution electron microscopy of an alloyed NR. a) High resolution TEM image, b) the corresponding FFT and c) zoom in of an AuAg@SiO₂ alloyed nanorod ($L=73$ nm, $D=27$ nm, $AR=2.7$) after in situ heating showing the lattice planes in the (111) direction with a lattice spacing of 0.235 nm.

beam exposure. The particles showed a smooth contrast, which indicates that alloying had taken place.

The alloying occurred at temperatures well below the bulk melting temperature of Au and Ag. This is in contrast to the alloying temperatures reported for spherical Au-Ag NPs by Gao *et al.*, which were as high as 930 °C [56]. However, it is to be expected that nanoparticles will alloy below the bulk melting temperature when decreasing their particle size, similar to the volume dependent thermal stability and particle size dependent

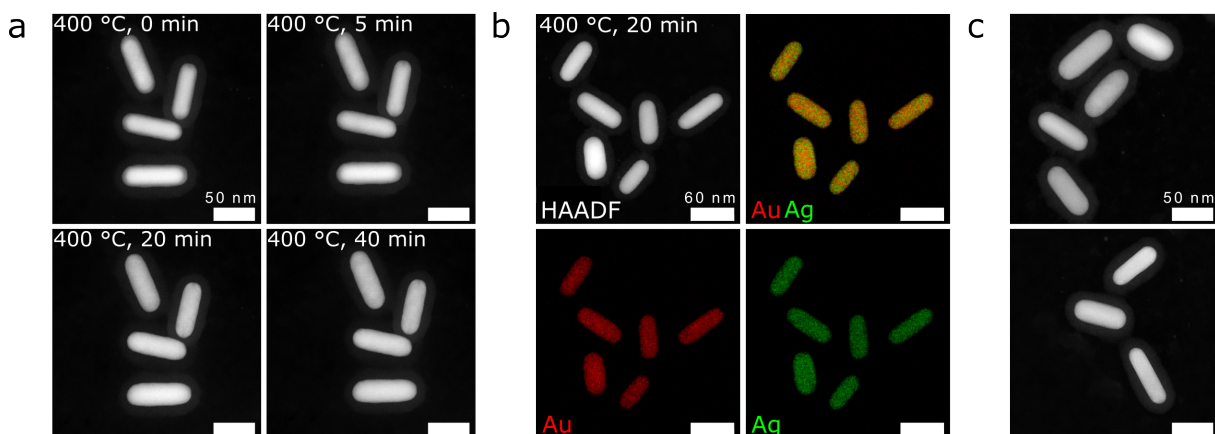


Figure 4.3: Influence of time and electron beam on the *in situ* alloying of Au@Ag@SiO₂ NRs. a) Spot of Figure 1 after different times: directly after changing the temperature to 400 °C (0 min), after 5 min, after 20 min and after 40 min. b) EDX of a different spot on a different SiN window heated at 400 °C for 20 min without prior exposure to the electron beam. c) HAADF-STEM images of different spots on different SiN windows and thus without prior electron beam exposure after the heating process.

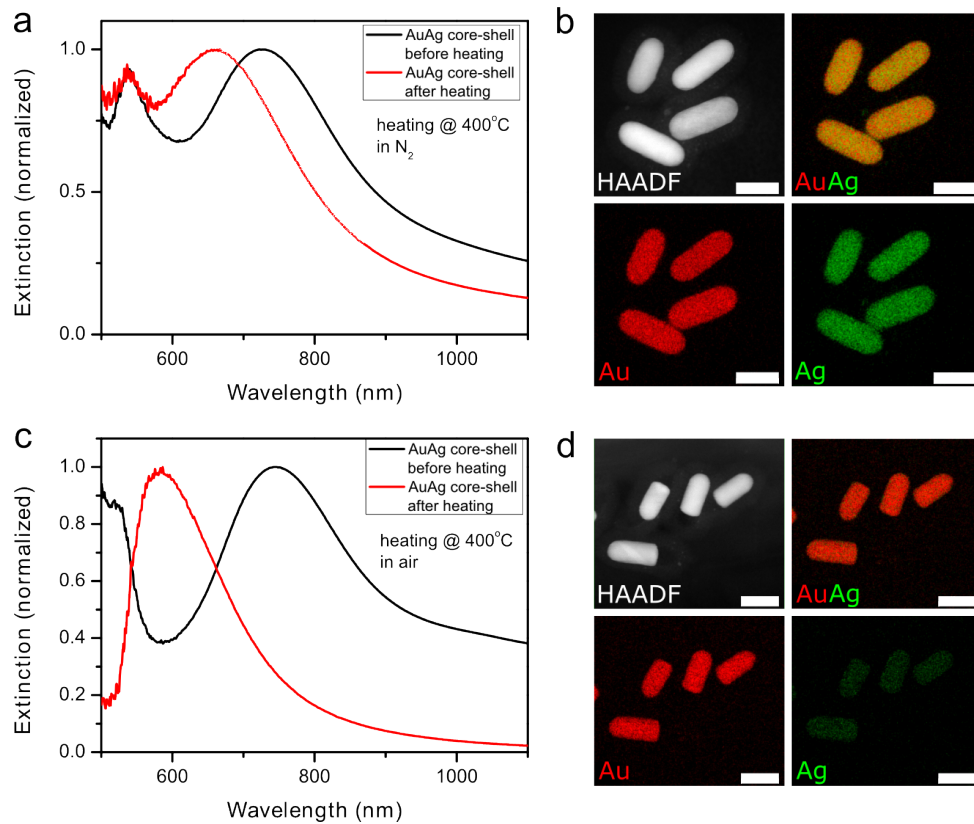


Figure 4.4: Alloying of silica coated Au@Ag core-shell nanorods in different atmospheres. a) Extinction spectra of AuAg nanorods before (black) and after heat treatment (red) in N_2 at 400 °C. The LSPR peak shifted from 740 to 667 nm upon treatment in N_2 . b) HAADF-STEM image and EDX maps of alloyed Au(red)-Ag(green) nanorods after heating in N_2 . c) Extinction spectra of AuAg nanorods before (black) and after (red) heating at 400 °C in air. The LSPR peak shifted from 745 to 586 nm upon thermal treatment in air. The average aspect ratio of the four particles shown in b and d are 2.4 and 2.1, respectively. After heat treatment in N_2 X_{Ag} was 0.44, whereas heating in air caused a loss in Ag; X_{Ag} decreased to 0.21. All scale bars are 40 nm.

melting point of nanoparticles [4, 5, 196–198]. For very small (< 5 nm) Au-Ag particles even spontaneous alloying at room temperature can occur [199]. In Chapter 5 we will investigate the influence of the particle size and composition on the alloying temperature in detail [104].

Alloying of larger quantities of Au@Ag@SiO₂ NRs was successfully achieved outside the electron microscope in an oven. We observed a strong effect of the surrounding atmosphere on the alloying process when heating the NRs to 400 °C. The EDX maps in Figure 4.4a demonstrate that alloyed NRs were formed during heating in nitrogen. The blue-shift in the extinction spectrum after alloying is mainly due to a slight decrease in aspect ratio. Identically to the *in situ* experiments, the particles heated externally kept their rod shape, which would not be possible without the protecting silica shell [123, 190, 200]. We demonstrate this in Figure 4.5 where we show results of heated Au@Ag core-shell NRs ($L = 84$ nm, $D = 24$ nm, $AR = 3.5$) that were not protected by a mesoporous silica

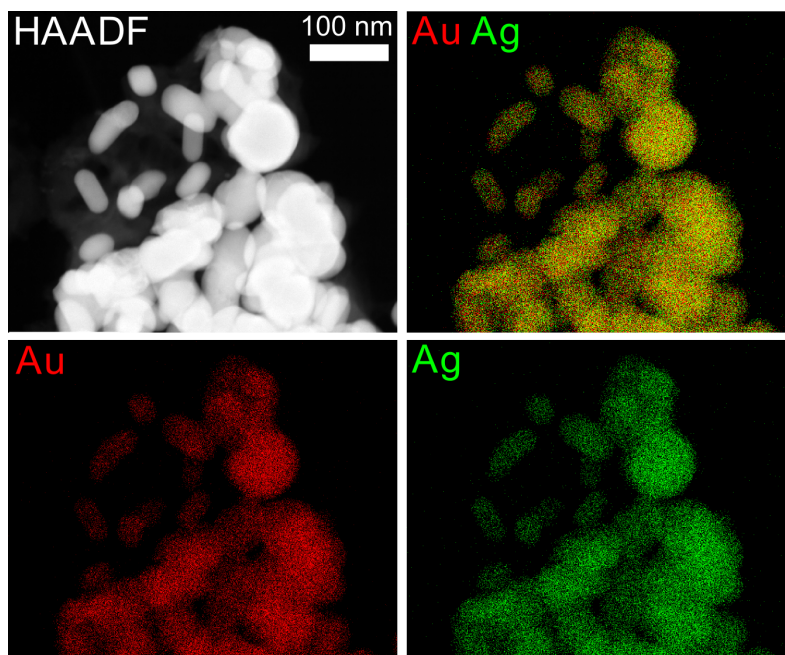


Figure 4.5: Alloying uncoated Au@Ag@SiO₂ NRs: STEM image and EDX intensity maps of initial Au@Ag core-shell NRs without a mesoporous silica shell after heating them for 1 h at 400 °C in N₂.

shell. As expected, the nanorod shape could not be preserved and the particles deformed and sintered together.

The alloying process of Au@Ag@SiO₂ NRs in air is very different from alloying in N₂. The larger blue-shift in the extinction spectrum in Figure 4.4b upon heating, compared to heating under nitrogen flow shows that the rods deformed to a more spherical shape. The EDX and STEM images indeed show that the particles heated in air deformed. The average aspect ratio dropped from 2.7 (73 nm × 27 nm) to 1.7 (42 nm × 25 nm) with an average volume loss of almost 50%. The EDX measurements revealed that most of the Ag vanished after heating which explains the observed volume loss, leaving a void for the Au to deform towards the thermodynamically more stable spherical shape. The difference in the behaviour of the Ag shell during inert and oxygen rich heat treatment is probably linked to the oxidation state of the silver. Heating of Ag NPs on silica supports in air was reported to give similar losses of silver and was ascribed to the dissolution of silver ions in the silica support [201].

We furthermore demonstrate enhanced chemical stability of the obtained alloyed NRs. We exposed both the silica-coated core-shell and alloyed NRs to a mixture of hydrogen peroxide (H₂O₂) and ammonia (NH₃), which is known to oxidize and dissolve Ag [56]. The longitudinal LSPR peak of the core-shell particles dropped to about 40% of the original value and red-shifted after only 15 min (Figure 4.6)a. This indicates that the Ag shell was dissolved as confirmed by our EDX measurements (Figure 4.6)b. Indeed a similar but reverse shift and increase in intensity were observed when Ag was grown onto the Au rod. Contrarily, the peak position and Au-Ag ratio of the alloyed NRs did not change

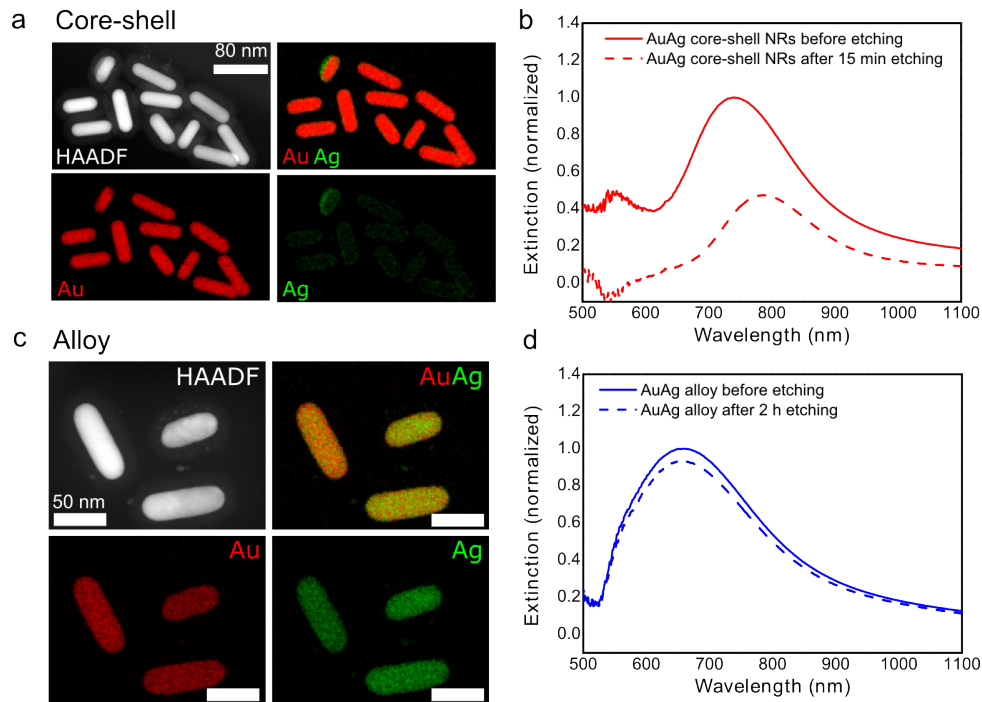


Figure 4.6: Chemical stability of AuAg core-shell and alloyed NRs upon etching. a) EDX map of Au@Ag@SiO₂ NRs after etching. The Ag-shell disappeared after exposing the NRs to an aqueous mixture of 0.9 vol% NH₃ and 1.7 vol% H₂O₂ for 15 min. Here, a not so representative spot was chosen where one particle still contained a small amount of Ag shell to make the difference clear. b) Extinction spectra of core-shell (red) before (solid) and after (dotted) exposure to the etching solution for 15 minutes. c) EDX maps of alloyed nanorods after 2 h of etching. d) Extinction spectra of alloyed nanorods (blue) before (solid) and after (dotted) 2 h of etching.

after keeping the particles in the etch solution for 2 h (Figure 4.6c). This shows that the chemical stability of Au@Ag@SiO₂ NRs was significantly increased upon alloying.

Calculations on the optical properties of Au-Ag nano-alloys

To compare the experimental results to theoretical predictions and to explore a larger parameter space in composition and aspect ratio, we performed FDTD simulations. As displayed in Figure 4.7a, the LSPR can be tuned by changing the composition of the alloyed NR, similarly as for spherical particles. Most compositions show comparable extinction intensities to those of a pure Au NR, although around a Ag composition of $X_{Ag} = 0.5$ the intensities are slightly decreased, caused by the dielectric functions of the alloys exhibiting higher losses close to 50% composition than the pure metals. The plasmonic properties improve when more Ag is added and exceed those of pure gold at $X_{Ag} = 0.7$. As a comparison we added the calculated extinction spectra for alloyed spherical particles of the same volume in Figure 4.7b. Note that the plasmon wavelengths of the pure Ag and Au spherical NP are slightly blue-shifted as known from measurements done in water since our used surrounding medium dielectric constant is lower (1.65) than

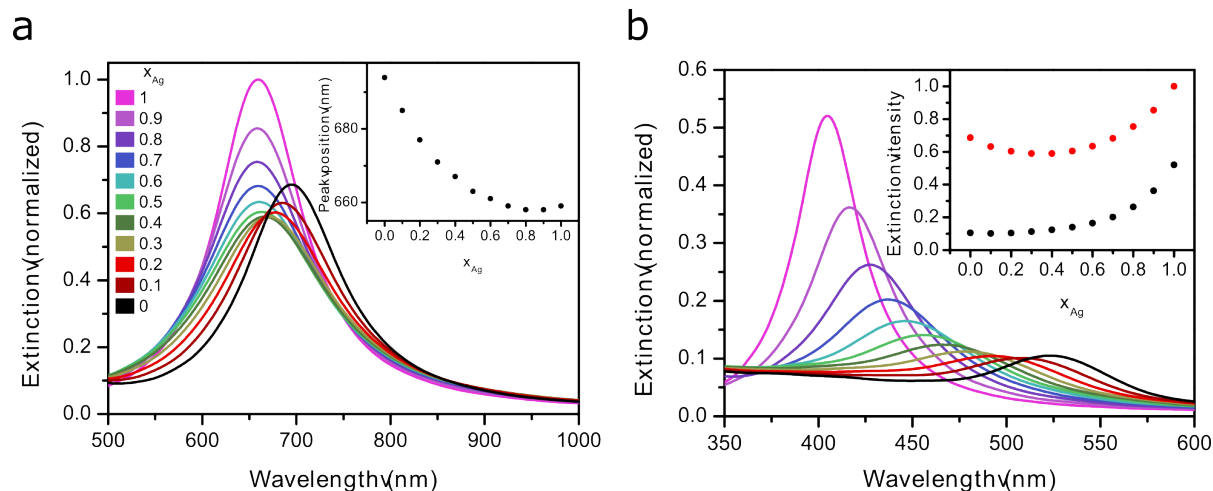


Figure 4.7: Comparison of calculated extinction spectra of AuAg alloyed rods and spheres of the same volume. a) FDTD calculations for AuAg alloyed NRs with a cylindrical shape ($L=65$ nm, $D=26$ nm) and varying composition ($X_{Ag}=0-1$). b) FDTD calculations for spherical AuAg alloyed particles of the same volume as the NRs in a. The inset compares the extinction intensities of the rods (red) with the spheres (black) normalized to the extinction intensity of the Ag NR.

that of water (1.77) to mimic our experimental conditions. The alloyed NRs show improved plasmonic properties compared to spherical particles with up to 9 times higher extinction coefficients. The enhancement can even be increased up to 14 times when increasing the AR to 6. Thus, alloyed AuAg NRs have significantly better plasmonic and hence photothermal properties than their spherical counterparts.

Extending the alloying method to Au-Pd and Au-Pt nanorods

Our method for the alloying of core-shell rods can in principle be applied to any combination of metals that mix in the bulk phase. As a proof of principle *in situ* heating measurements of Au@Pd@SiO₂ NRs with an average length of 73 nm, diameter of 22 nm and atomic Pd fraction (X_{Pd}) of 0.31 (Figure 4.8) and of Au@Pt@SiO₂ NRs with an average length of 57 nm, diameter of 18 nm and atomic Pt fraction (X_{Pt}) of 0.15 (Figure 4.9), were carried out. Figure 4.8 shows that the initially dendritic Pd shell first smoothed around 500 °C, then started to mix with the Au core at 700 °C and finally formed a homogeneous alloy when heated for about 30 min at 800 °C. We found indications that the alloying temperature depends on the metal ratio as for a lower Pd content alloying was achieved at 600 °C. We will study the alloying of lower Pd content Au@Pd@SiO₂ NRs in more detail in Chapter 6. The HAADF-STEM image and EDX intensity maps in Figure 4.9 show the AuPt nanorods before, during and after heating to 800 °C. At 700 °C the core-shell structure vanished and an alloy was formed. In a similar way, AuPt nanorods were heated to 800 °C (Au/Pt=0.85/0.15 and $L=53.3$, $D=18.1$ nm, $AR=2.9$). Like the Au@Ag@SiO₂ NRs the observed alloying temperatures for AuPd and AuPt NRs are far below the bulk melting temperatures of Au, Pd and Pt as well.

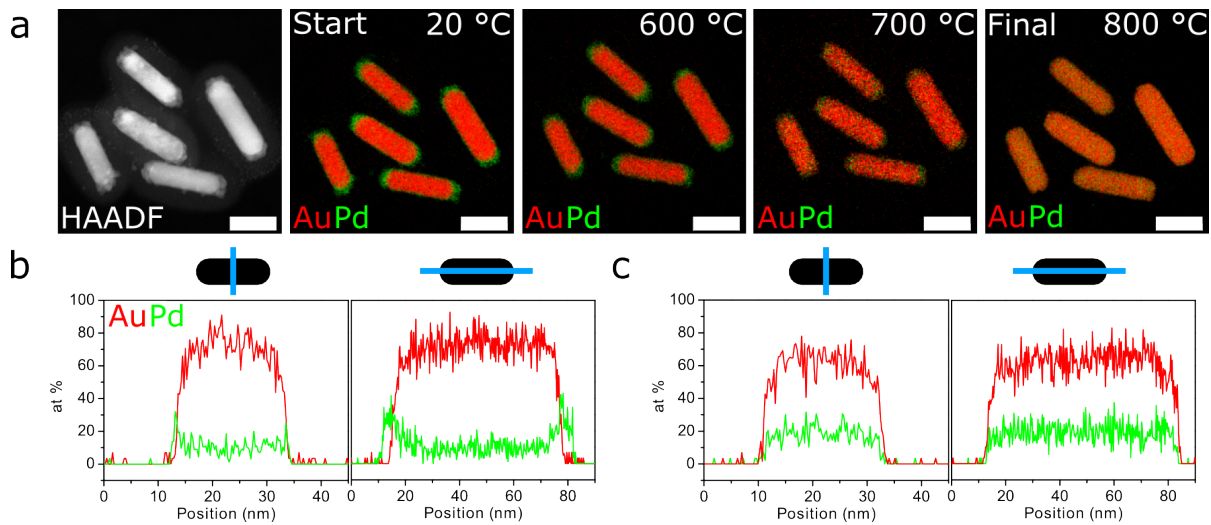


Figure 4.8: *In situ* heating of silica coated Au@Pd core-shell nanorods with $L=73$ nm, $D=22$ nm and $X_{Pd}=0.31$ a) HAADF-STEM image and EDX maps showing the Au (red) and Pd (green) metal distribution before and during heating to 800 °C, respectively. The average aspect ratio of the five particles shown here changed from 3.3 to 3.2 when heating to 800 °C. The scale bars are 40 nm. b) EDX line scan of the most right AuPd nanorod at 20 °C and 800 °C.

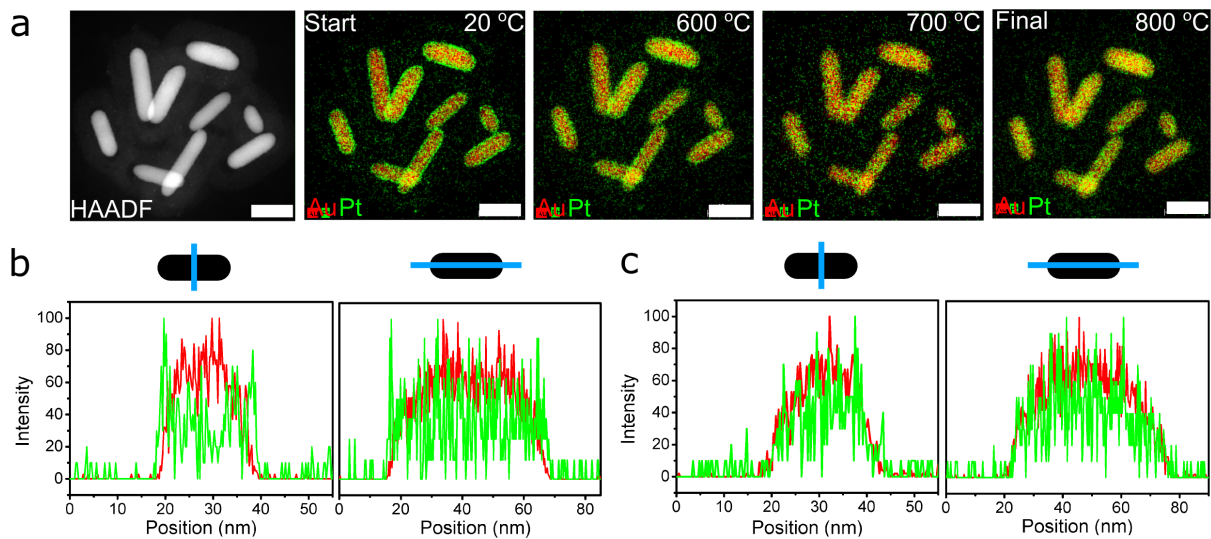


Figure 4.9: *In situ* heating of Au@Pt@SiO₂ core-shell rods with $L=57.2$, $D=17.6$ nm and $X_{Pt}=0.15$. a) HAADF-STEM image and EDX intensity maps showing the Au (red) and Pt (green) metal distribution before, during and after heating to 800 °C. The average aspect ratio of the 9 particles shown here changed from 3.2 to 2.9 when heating to 800 °C. The scale bars are 40 nm. b) EDX line scan of the upper right AuPt nanorod at 20 °C and c) after heating to 800 °C and cooling to room temperature.

The dimensions before and after heating the AuPd and AuPt NRs are listed in Table 4.2. From these size measurements it follows that the NRs did not lose any anisotropy during the heating process. This is in contrast to pure Au NRs, which deform at such high temperatures, even with a silica-coating [200]. Hence, alloying Au with a relatively small

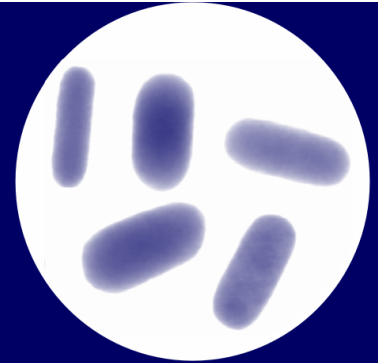
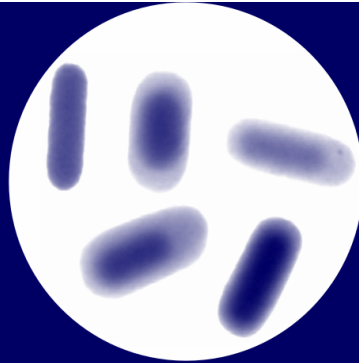
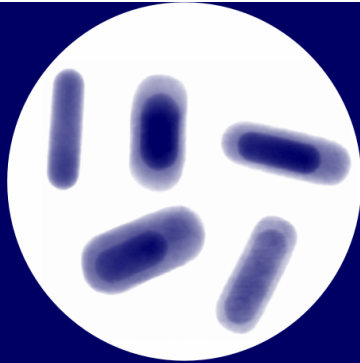
amount of Pd or Pt can drastically increase the thermal stability of the rod. The combination of good optical properties of Au and enhanced thermal and catalytic properties of Pd/Pt make alloyed AuPd/Pt rods interesting materials for e.g. photocatalysis [156, 202], optical laser writing [112] or other applications where the dynamic range is limited by the thermal stability of the NRs [114, 203].

4.4 Conclusions

In conclusion, we introduced a general approach to obtain alloyed metallic NRs in a mesoporous silica shell of which the metal composition and optical properties can be tuned. The silica coating provides both thermal and colloidal stability, whereas its mesoporosity enables mass transport to the NR surface. Alloying was achieved at temperatures considerably lower than the melting point of the metals. We showed that the plasmonic properties of the resulting NRs were enhanced compared to spherical particles of the same volume, and that the thermal stability can be improved by alloying with higher melting point metals. We expect that our method can be employed to any combination of metals that mix in the bulk phase. Furthermore, it is possible to extend the method to more than two metals or to different anisotropic particle shapes. Thus, the method presented here opens the way to a wide variety of anisotropic nano-alloys with variable compositions, tunable properties and different particle shapes which would be difficult to achieve via direct synthesis routes.

Acknowledgements

This chapter was performed in collaboration with Wiebke Albrecht (*in situ* heating TEM and FDTD calculations) and Tian-Song Deng (preliminary alloying experiments). We thank Dr. Marijn A. van Huis for facilitating the *in situ* heating electron microscopy measurements. Tom Welling is acknowledged for discussion on the calculations.



In situ observation of atomic redistribution in alloying gold-silver nanorods

5

Abstract

The catalytic performance and optical properties of bimetallic nanoparticles critically depend on the atomic distribution of the two metals in the nanoparticles. However, at elevated temperatures, during light induced heating or during catalysis atomic redistribution can occur. Measuring such metal redistribution *in situ* is challenging and a single experimental technique does not suffice. Furthermore, the availability of a well-defined nanoparticle system has been an obstacle for a systematic investigation of the key factors governing the atomic redistribution. In this chapter, we continue the work described in Chapter 4 and study in more detail the metal redistribution of in single-crystalline Au-core Ag-shell nanorods *in situ*, both at a single particle and ensemble averaged level, by combining *in situ* TEM with *in situ* EXAFS validated by *ex situ* measurements. We show that the kinetics of atomic redistribution in Au-Ag nanoparticles depend on the metal composition and particle volume, where a higher Ag-content or a larger particle size lead to significantly slower metal redistribution. We developed a simple theoretical model based on Fick's first law which can correctly predict the composition and size dependent alloying behaviour in Au-Ag nanoparticles as observed experimentally.

5.1 Introduction

As explained in Chapter 1, bimetallic nanoparticles (NPs) offer new and enhanced optical and catalytic properties, which can lead to applications in *e.g.* sensing, biomedicine, data storage and catalysis [54, 56, 57, 86, 149, 150, 204–207]. The physicochemical properties of these bimetallic particles can be tuned by varying the metal composition and by changing the atomic distribution of the two metals within the nanoparticles at a fixed composition, for example from core-shell to alloyed NPs [56, 57, 208–212]. The exact atomic distribution of the metals is particularly important in catalysis where the atoms close to the surface play a dominant role in the catalytic performance [97, 102, 103, 150, 213], as we will demonstrate in Chapter 6. Furthermore, when exposing bimetallic nanoparticles to various gas atmospheres and heating them to elevated temperatures atomic redistribution can occur [101–103, 105, 208, 214–218]. This alters the optical [57, 210, 218] and catalytic properties [97, 100–103], and can even lead to severe deactivation of the catalyst. Therefore, understanding atomic restructuring is crucial in the design of new catalytic and optical bimetallic materials.

Various techniques have been employed to follow metal redistribution *in situ*, each providing information on a different length scale [214]. Single-particle studies often make use of *in situ* Transmission Electron Microscopy (TEM). With this technique sub-nanometer or even atomic resolution can be obtained while heating the sample [102, 215, 216]. This technique, however, is limited to samples that are very stable under electron irradiation, in order to avoid electron beam induced artefacts [219–221]. Therefore, to verify the influence of the electron beam, it is important to also perform *ex situ* heating measurements [221]. Alternatively, X-ray based techniques, such as X-ray Photoelectron Spectroscopy (XPS) and X-ray Absorption Fine Structure (XAFS), also offer atomic information, but averaged over a much larger number of particles [103, 217, 222]. XPS allows to specifically study the surface composition of the NPs and it is thus particularly suitable to measure surface segregation effects [101, 102, 105]. On the other hand, XAFS measurements give insight in the degree of mixing and oxidation state of the atoms within the nanoparticles, and can be carried out in different gas atmospheres [103, 217, 222]. Thus, to follow the metal redistribution in bimetallic nanoparticles at multiple length scales - on an atomic, single-particle and ensemble-averaged level - one technique does not suffice and a multi-technique approach is required.

In addition, a systematic, quantitative and reproducible study of atomic restructuring requires a well-defined model system. The use of rather heterogeneous bimetallic catalysts, obtained *via* standard catalyst preparation methods, is especially problematic when using techniques like XAFS and XPS, where the measured signal is an ensemble average. Therefore, the influence of fundamental parameters such as the metal composition and particle volume on the atomic redistribution process in bimetallic nanoparticles are largely unexplored.

In this study, we investigated the thermally driven atomic redistribution in single-crystalline Au-Ag core-shell nanorods *in situ*, both on a single particle and ensemble averaged level. We employed colloiddally synthesized Au-core Ag-shell nanorods of which the composition, size and shape was tuned precisely [54], as demonstrated in Chapter 3. By coating the metal nanorods with a protective mesoporous silica coating [90] preservation

of the particle shape during atomic redistribution was ensured [57] (see also Chapter 4). We specifically chose a Au-Ag based system, since alloy formation is thermodynamically favourable at all compositions and the lattice spacings of Au and Ag closely match [198]. As the nanorods are single-crystalline, this model system is well suited to specifically study the kinetics of metal redistribution during alloying. To this end, we performed both *in situ* TEM and *in situ* EXAFS measurements, yielding sub-nm, single particle and atomic, ensemble averaged information, respectively. In addition, we validated the *in situ* measurements with *ex situ* measurements carried out in the absence of an electron or X-ray beam. In particular, we addressed the influence of the metal composition (Au-Ag ratio) on the alloying temperature of the Au-core Ag-shell nanorods. We unambiguously showed the influence of the metal composition on the kinetics of the alloying process. An increasing Ag-content led to slower metal redistribution, a trend which is opposite to the dependence of the melting temperature on the Au-Ag ratio. In addition, indications for size dependent alloying were found, where a decrease in particle volume led to lower alloying temperatures. We developed a simple theoretical model that correctly predicts the temperatures and time scales for metal redistribution as a function of particle volume and composition. Our study does not only demonstrate a general, multi-scale approach to monitor metal redistribution in bimetallic nanoparticles, but also reveals the influence of fundamental parameters governing metal redistribution which is of importance in bimetallic nanoparticles applications.

5.2 Experimental

Chemicals

All chemicals were used as received without further purification. Hexadecyltrimethylammonium bromide (CTAB, >98.0%) and sodium oleate (NaOL, >97.0%) were purchased from TCI America. Hydrogen tetrachloroaurate trihydrate ($\text{HAuCl}_4 \cdot \text{H}_2\text{O}$) and sodium hydroxide (98%) were purchased from Acros Organics. L-Ascorbic Acid (BioXtra, $\geq 99\%$), silver nitrate (AgNO_3 , $\geq 99\%$), sodium borohydride (NaBH_4 , 99%), hydrochloric acid (HCl, 37 wt% in water), tetraethyl orthosilicate (TEOS, 98%) and ammonium hydroxide solution (≥ 25 wt% in water) were purchased from Sigma-Aldrich. Ultrapure water (Millipore Milli-Q grade) with a resistivity of 18.2 M Ω was used in all of the experiments. All glassware for the AuNR synthesis was cleaned with fresh aqua regia (HCl/ HNO_3 in a 3:1 volume ratio), rinsed with large amounts of water and dried at 100 °C before usage.

Synthesis of the Au-Ag nanorods

Three batches of Au@Ag@SiO₂ NRs with average Ag atomic fractions of 0.20, 0.46 and 0.70 were prepared by changing both the Au core size and the Ag-shell thickness. The synthesis of the AuAg core-shell rods was based on the method described in Chapter 3 and consisted of 4 steps: AuNR synthesis (I), mesoporous silica coating (II), partial etching of AuNRs within their mesoporous silica shells (III) and Ag-shell growth on the etched AuNRs (IV).

In the first step, monodisperse AuNRs were synthesized according to the protocol of Ye *et al.* [13]. Two 500 mL scale syntheses were carried out with growth solutions containing 7.0 g CTAB, 1.24 g NaOL, 25 mL MQ H₂O and 250 mL 1.0 mM HAuCl₄, 7.2 mL AgNO₃, 2.1 mL concentrated HCl, 64 mM ascorbic acid and 1.0 mL seed solution. The seeds were prepared from a 10 mL 0.10 M CTAB, 51 μ L HAuCl₄ and 1.0 mL NaBH₄. The subsequent rod growth was performed under static conditions in a 30 °C water bath overnight. The resulting AuNR suspensions had an extinction maximum (Ext) of 1.0 at LSPR peak position (λ_{LSPR}) of 866 and 853 nm when diluted 4 \times in H₂O. The rods were centrifuged at 8000 rcf for 30 min (Rotina 380R Hettich centrifuge), washed with H₂O and redispersed in 5.0 mM CTAB H₂O.

In the second step, the CTAB stabilized AuNRs were coated with a 18 nm mesoporous silica shell *via* the method of Gorelikov *et al.* [90]. The coating was performed in 350 mL 1.5 mM CTAB aqueous solution containing 1.0 mM NaOH and an AuNR concentration corresponding to an extinction maximum of 1.0 when diluted 10 \times in H₂O. While magnetically stirring at 300 rpm in a 30 °C waterbath, 3 times 1.05 mL 0.90 M TEOS in EtOH were added with a 30 min time interval. The Au@SiO₂ NRs were centrifuged at 8000 rcf for 30 min, washed with water and ethanol.

The third step, oxidative etching of the Au@SiO₂ NRs, was performed by following the procedure described in Chapter 3 with H₂O₂ as an oxidant instead of O₂ from air as in ref. [54]. Different core sizes were obtained by varying the etching time. For the rods with $X_{Ag} = 0.20$, 240 mL AuNRs in MeOH (Ext= 6.0) were heated to 60 °C in an oil bath while magnetically stirring at 400 rpm. 4.8 mL HCl (37 wt%, 12.1 M) and 4.8 mL H₂O₂ (0.2 wt%) were added. The LSPR peak position changed from 838 nm to 822 nm after etching for 10 minutes. The reaction was quenched by putting the mixture in a 4 °C waterbath and diluting it with 200 mL icecold MeOH before centrifugation at 10000 rcf for 20 min. The etched rods were washed with and redispersed in EtOH. For batches with $X_{Ag} = 0.46$ and $X_{Ag} = 0.70$ 210 mL AuNRs in MeOH 4.8 mL HCl (37 wt%, 12.1 M) and 4.8 mL H₂O₂ (0.2 wt%) were added. After 13 and 26 minutes, 100 mL reaction mixture was quenched with 100 mL icecold MeOH and was as described above. The LSPR peak position of the rods were 750 nm and 694 nm.

Finally, the procedure by Deng *et al.* was modified to do the Ag-overgrowth in large reaction volumes ($\gg 1$ mL) (see also Chapter 3). HCl was added to lower the Ag reduction rate by ascorbic acid and allows for a homogeneous shell growth on all particles. The rods with $X_{Ag} = 0.20$ were prepared by adding 2.0 mL 0.1 M HCl, 3.0 mL 5.0 mM AgNO₃ and 3.0 mL 20 mM ascorbic acid were added to 200 mL aqueous AuNR suspension (Ext= 4.5, $\lambda_{LSPR} = 780$ nm) while stirring vigorously. The rods with $X_{Ag} = 0.70$ were prepared in 2 steps. To 120 mL rod suspension, 1.2 mL 0.10 M HCl, 6.6 mL 5.0 mM AgNO₃, 6.6 mL 20 mM ascorbic acid. After washing with MQ H₂O a second Ag-overgrowth step was performed to increase the Ag-content. To 100 mL aqueous Au@Ag@SiO₂ NRs suspension (Ext= 1.2, $\lambda_{LSPR} = 701$ nm), 1.0 mL 0.10 M HCl, 4.0 mL 5.0 mM AgNO₃ and 4.0 mL 20 mM ascorbic acid were added. The $X_{Ag} = 0.46$ sample was prepared on a smaller scale since it was only used for the *ex situ* and *in situ* TEM measurements. To 1.0 mL aqueous Au@SiO₂ NRs suspension (Ext= 2.5, $\lambda_{LSPR} = 745$ nm), 10 μ L 0.1 M HCl, 40 μ L 5.0 mM AgNO₃, 40 μ L 20 mM ascorbic acid were added.

All Au@Ag@SiO₂ NRs were washed with MQ H₂O, ethanol, redispersed in EtOH and stored at 4 °C to prevent oxidation and dissolution of the Ag-shell. The centrifugation speed varied between 6000 and 8000 rcf depending on the volume of the rods. The samples were dried at 60 °C in air. All samples were characterized with VIS-NIR spectroscopy and TEM.

***In situ* TEM**

The *in situ* heating measurements were carried out on a FEI Talos F200X operated at 200 kV using a heating holder from DENSSolutions. A mix of 4 different batches of Au@Ag@SiO₂ NRs was dropcasted on a heating chip (Wildfire Nano-chip) with silicon nitride windows. The overall heating ramp was set to 3 °C/min. EDX maps were acquired at 25, 250, 300, 350 and from 400 to 650 °C with a 25 °C temperature interval. The acquisition time per EDX map was 5 min and the probe current 700 pA. In the intervals between the EDX acquisitions the beam was blanked to minimize the influence of the electron beam on the alloying process. Different SiN windows were checked during heating that where not illuminated prior to heating. No significant differences in alloying kinetics were observed between the illuminated and non-illuminated spots. The SiN chip was plasma cleaned for 10 s in a 20 % O₂ in Ar atmosphere before the TEM experiment.

***In situ* EXAFS**

The *in situ* EXAFS measurements were performed at the ROCK beamline of the SOLEIL synchrotron. At this beamline, continuous switching between the Au L₃-edge (11919 eV) and the Ag K-edge (25514 eV) is possible (time to switch ~1 min) using two Quick-XAS monochromators equipped with Si(111) and Si(220) channel-cut crystals, respectively. The operation parameters of the monochromators were set to record two EXAFS spectra per second. The powdered samples were loaded in a stainless steel sample holder (with a depth of 1 mm) allowing temperature control and gas flow. The $X_{Ag} = 0.20$ and $X_{Ag} = 0.70$ Au@Ag@SiO₂ NRs samples were diluted with boron nitride. The heating was done in a He flow of 25 mL/min and with a heating rate of 3 °C/min. Before and after heating, EXAFS spectra were collected for 500 s at each edge at RT and averaged. During the temperature ramps, alternate measurements at both edges were performed continuously: spectra were collected and averaged for 35 s at the Au edge and 60 to 120 s at the Ag edge, depending on the quality of the Ag-signal. Measurements were done in transmission mode, using ionization chambers as detectors. Energy calibration was ensured by the simultaneous measurement of the absorption spectra of metallic Au and Ag foils.

Spectra analysis was conducted with the IFEFFIT library using the GUI Athena and Artemis [223]. All spectra were energy calibrated to the first inflection point of the Ag or Au foil at 25514 eV and 11919 eV respectively. EXAFS signal was extracted in Athena with a R = 1.0 cut-off and k weight = 2 and Fourier transformed using a Hanning window in k = 3 and dk = 1. EXAFS analysis was conducted in Artemis with the normalized spectra exported from Athena. The amplitude reduction factor (S_0^2) of 0.83 for Ag and 0.79 for Au was obtained by fitting the EXAFS data of the respective metal foils. The

simulation of scattering paths for the bimetallic samples was performed with the ATOMS algorithm with a custom input file created by substituting Au atoms by Ag in the first shell, to obtain the closest rational fraction of atoms. A correction factor was introduced to S_0^2 to obtain the actual sample composition. Structural parameters were determined by multiple k-weight least-square fitting and the quality of fit was determined by observing the reduced χ^2 and R^2 statistical parameters. The full set of fitting parameters is listed in Table 5.1, 5.3, 5.2 and 5.4.

The linear combination fitting was carried out in Athena on the normalized $\mu(E)$ -spectra in the region between -20 eV to 120 eV from the absorption edge.

Table 5.1: EXAFS fitting parameters for the sample $X_{Ag} = 0.20$ before heating

Fitting parameter	Ag K-edge	Au L ₃ -edge
	Ag-Ag path / Ag-Au path	Au-Au path / Au-Ag path
N	10.1 (1.8) / 1.1 (1.3)	11.0 (0.2) / 0.3 (0.2)
R(Å)	2.882 (0.007) / 2.95 (0.08)	2.863 (0.001) / 3.04 (0.06)
$\sigma(\text{Å}^2) \times 10^3$	10.3 (1.8)	8.2 (0.2)
ΔE_0 (eV)	-9.7 (0.8)	4.4 (0.2)
ΔS_0^2 (fixed)	0.83	0.79
Quality of the fit (R^2)	0.022	0.00061
Quality of the fit (red. χ^2)	330	82
Δk (Å ⁻¹)	3.2 - 12.0	3.3 - 14.0
ΔR (Å)	1.7 - 3.3	1.7 - 3.3
E_0 (eV)	25514	11919

Table 5.2: EXAFS fitting parameters for the sample $X_{Ag} = 0.70$ before heating

Fitting parameter	Ag K-edge	Au L ₃ -edge
	Ag-Ag path / Ag-Au path	Au-Au path / Au-Ag path
N	11.0 (0.3) / 0.6 (0.3)	9.8 (0.2) / 0.3 (0.2)
R(Å)	2.871 (0.001) / 2.88 (0.03)	2.865 (0.001) / 3.01 (0.04)
$\sigma(\text{Å}^2) \times 10^3$	9.6 (0.3)	8.2 (0.1)
ΔE_0 (eV)	2.3 (0.2)	3.9 (0.2)
ΔS_0^2 (fixed)	0.83	0.79
Quality of the fit (R^2)	0.00061	0.00061
Quality of the fit (red. χ^2)	92	56
Δk (Å ⁻¹)	3.2 - 12	3.3 - 14.0
ΔR (Å)	1.7 - 3.3	1.7 - 3.3
E_0 (eV)	25514	11919

***Ex situ* heating**

The *ex situ* heating experiments were performed in a tubular oven (Thermolyne 79300 tube furnace) under a constant N₂ flow. The three different samples were each dropcasted on a copper TEM grid (200 mesh copper (100), Formvar/carbon film) and heated in a ceramic cup placed in a quartz oven tube. The heating rate was always 3 °C/min and the particles were heated to 250, 300, 325, 350, 375 and 400 °C and cooled down under N₂ to RT before taking them out of the oven. After heating all samples were analysed

Table 5.3: EXAFS fitting parameters for the sample $X_{Ag} = 0.20$ after heating

Fitting parameter	Ag K-edge	Au L ₃ -edge
	Ag-Ag path / Ag-Au path	Au-Au path / Au-Ag path
N	2.5 (0.6) / 6.8 (1.6)	9.6 (0.2) / 1.8 (0.1)
R(Å)	2.90 (0.03) / 2.892 (0.007)	2.863 (0.001) / 2.862 (0.004)
$\sigma(\text{Å}^2) \times 10^3$	7.2 (2.5)	8.4 (0.2)
ΔE_0 (eV)	-9.7 (0.8)	4.4 (0.2)
ΔS_0^2 (fixed)	0.83	0.79
Quality of the fit (R ²)	0.023	0.00065
Quality of the fit (red. χ^2)	338	105
Δk (Å ⁻¹)	3.2 - 12	3.3 - 14.0
ΔR (Å)	1.7 - 3.3	1.7 - 3.3
E ₀ (eV)	25514	11919

Table 5.4: EXAFS fitting parameters for the sample $X_{Ag} = 0.70$ after heating

Fitting parameter	Ag K-edge	Au L ₃ -edge
	Ag-Ag path / Ag-Au path	Au-Au path / Au-Ag path
N	7.7 (0.4) / 3.5 (0.2)	3.1 (0.3) / 8.3 (0.5)
R(Å)	2.873 (0.002) / 2.875 (0.006)	2.862 (0.006) / 2.862 (0.002)
$\sigma(\text{Å}^2) \times 10^3$	9.1 (0.5)	8.2 (0.4)
ΔE_0 (eV)	2.3 (0.2)	3.9 (0.2)
ΔS_0^2 (fixed)	0.83	0.79
Quality of the fit (R ²)	0.0014	0.0028
Quality of the fit (red. χ^2)	135	187
Δk (Å ⁻¹)	3.2 - 12	3.3 - 14.0
ΔR (Å)	1.7 - 3.3	1.7 - 3.3
E ₀ (eV)	25514	11919

with HAADF and EDX on a FEI Talos F200X, operated under the same conditions as described above.

Diffusion model

To predict the rate of alloying in Au-Ag nanoparticles, we numerically calculated Fick's first law. The number of Au n_{Au} and Ag atoms n_{Ag} diffusing through the static Au-Ag interface per time step was calculated with equation 5.4. After each step the Au-Ag ratio of the core and the shell was updated, affecting D_0 , Q , C_{core} and C_{shell} in Equation 5.4. The values for D_0 and Q for silver and gold diffusing into various Au-Ag compositions were taken from the work of Mallard *et al.* [224]. These bulk values of D_0 and Q were corrected for NP size effects according to the model of Guisbiers [225, 226], in which the change in activation energy for a NP compared to the activation energy in the bulk can be described as

$$\frac{Q_{NP}}{Q_{bulk}} = 1 - \frac{\alpha_{shape}}{D} \quad (5.1)$$

where the shape factor α_{shape} is given by [225]

$$\alpha_{shape} = \frac{D(\gamma_s - \gamma_l)}{\Delta H_{m,\infty}} \times \frac{S}{V} \quad (5.2)$$

Here, D is the diameter of the NP, $\gamma_{s,l}$ are the surface energies in the solid and liquid phase, respectively, S the surface area of the NP, V the volume of the NP and $\Delta H_{m,\infty}$ the bulk melting enthalpy.

Lastly, the temperature was updated every time step according to the temperature ramp used in the experiments. Usually one time step was one second, which ensured small changes in the Au-Ag content per time step for the temperatures used in this work. Subsequent time steps were evaluated until the core and shell consist of the same Au-Ag composition, when a full alloy composition is reached. Only geometric input parameters determined from TEM such as the core-shell volume, the interface surface area and the radius of the NP were needed for the calculations.

5.3 Results and Discussion

Preparation of core-shell nanorods

Mesoporous silica coated Au-core Ag-shell nanorods (Au@Ag@SiO₂ NRs) with similar volumes, but with 3 different Au-Ag ratios were colloiddally synthesized. The colloidal synthesis was performed on a relatively large, milligram scale in order to obtain the required amount of sample needed for the EXAFS measurements. To this end, the Ag-shell growth as described by Deng *et al.*, comprising the reduction of Ag⁺ ions on the Au nanorods by ascorbic acid, was performed in an acidified, instead of neutral, aqueous solution [54] (see Chapter 3). The presence of H⁺ ions slowed the Ag-shell growth down considerably (from seconds to minutes), resulting in sufficiently long mixing times for the reagents and homogeneous Ag-shell growth. To limit the variation in particle volume when changing the Au-Ag ratios of the particles, both the core and the shell size of the Au-core and Ag-shell were varied. In this way, 3 batches of mesoporous silica coated Au-core Ag-shell NRs with an average atomic Ag fraction X_{Ag} of 0.20, 0.46 and 0.70 and an average particle volume V of 2.2, 4.1 and 5.6·10⁴ nm³ were obtained, respectively. To also investigate the influence of the particle volume on the atomic redistribution, a batch of considerably smaller Au@Ag@SiO₂ NRs with average $X_{Ag} = 0.46$ and $V = 0.7 \cdot 10^4$ nm³ was prepared.

In Table 5.5 we report a summary of the sample details and in Figure 5.1 we show the corresponding High Annular Dark-Field Scanning Transmission Electron Microscopy

Table 5.5: Sample details for the Au@Ag@SiO₂ NRs depicted in Figure 5.1. The average and corresponding standard deviations of the atomic Ag fraction, length, diameter and volume are indicated with X_{Ag} , L , D and V , respectively. The values were based on 50 measurements per sample.

X_{Ag}	L (nm)	D (nm)	V ($\cdot 10^4$ nm ³)
0.20	67±10	21±2.1	2.2±0.58
0.46	74±8.7	28±1.9	4.1±0.77
0.70	80±9.2	32±3.8	5.6±1.6
0.46	48±9.2	14±1.8	0.7±0.3

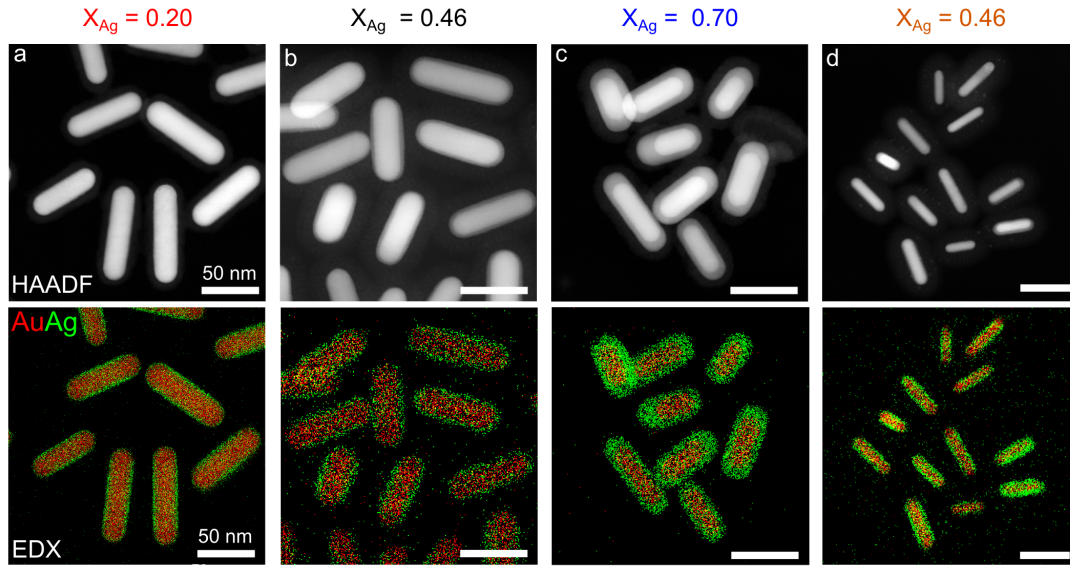


Figure 5.1: Electron microscopy images of mesoporous silica coated Au-core Ag-shell nanorods (Au@Ag@SiO_2 NRs) with different X_{Ag} ratios and particle volumes. Top: HAADF-STEM images. Bottom: EDX maps with Au and Ag in red and green, respectively. Au@Ag@SiO_2 NRs with $X_{\text{Ag}} = 0.20$; $V = 2.2 \cdot 10^4 \text{ nm}^3$ (a, red), $X_{\text{Ag}} = 0.46$; $V = 4.1 \cdot 10^4 \text{ nm}^3$ (b, black), $X_{\text{Ag}} = 0.70$; $V = 5.6 \cdot 10^4 \text{ nm}^3$ (c, blue) and $X_{\text{Ag}} = 0.46$; $V = 0.7 \cdot 10^4 \text{ nm}^3$ (d, orange). The Si signal is not shown in the EDX maps.

(HAADF-STEM) images and Energy Dispersive X-ray spectroscopy (EDX) maps. Due to the large Z-contrast difference between Au and Ag atoms, the core-shell structure of the nanorods is readily visible in the HAADF-STEM images. The different Ag-contents are most clearly seen in the EDX maps, where Au and Ag are depicted in red and green, respectively. The Si signal of the silica shell is not shown in Figure 5.1 to see the difference between the Au-core and Ag-shell more clearly.

Direct visualization of metal redistribution in individual particles with *in situ* TEM

In situ TEM was used to visualize the atomic redistribution in individual NRs with different Au-Ag ratios and volumes. To avoid variations between *in situ* TEM measurements on different samples due to *e.g.* inequalities in the heating temperature or differences in electron dose which are known to be important in *in situ* electron microscopy [219–221], we chose to compare 4 different samples in one measurement under exactly the same conditions. To achieve this, a mixture of the 4 samples with different Au-Ag ratios and particle volumes was deposited on a single SiN_x chip. The heating experiment was carried out in high vacuum with a ramp of $3 \text{ }^\circ\text{C}/\text{min}$. EDX analysis was used to map the Au and Ag metal distribution as a function of temperature.

Figure 5.2a shows the EDX maps of the mixture of Au@Ag@SiO_2 NRs at various temperatures. The EDX maps of the orange, red, grey and blue highlighted NRs in Figure 5.2a are enlarged in Figure 5.2b. We determined the Ag-fractions and particle volumes of

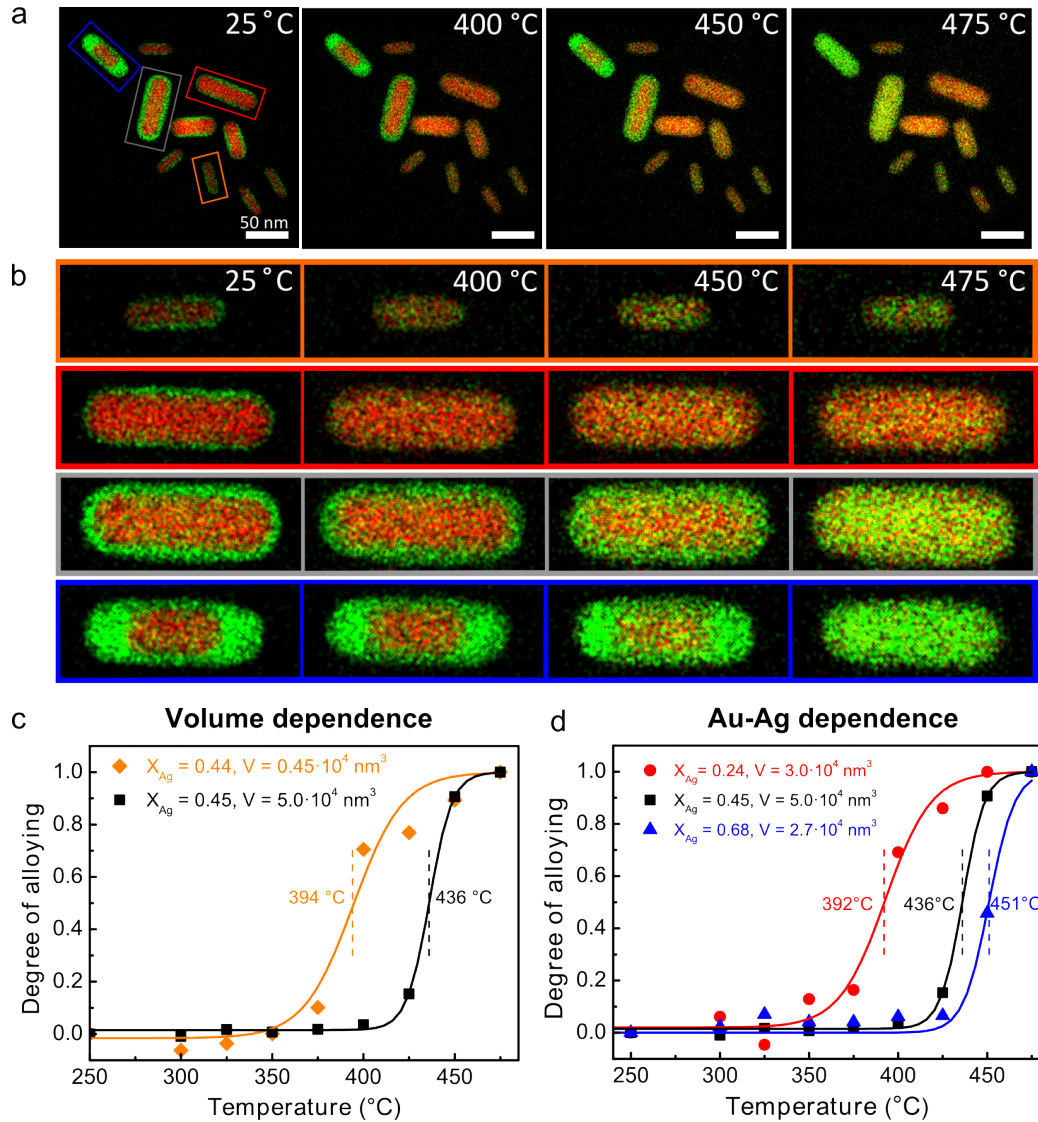


Figure 5.2: Direct visualization of atomic redistribution in individual Au@Ag@SiO₂ NRs with in situ heating TEM. (a, b) EDX maps acquired at 25, 400, 450 and 475 °C. (c) Particle volume dependence of the degree of alloying for Au@Ag@SiO₂ NRs with $V = 0.45 \cdot 10^4 \text{ nm}^3$ ($X_{Ag} = 0.44$, orange) and $V = 5.0 \cdot 10^4 \text{ nm}^3$ ($X_{Ag} = 0.45$, black). (d) The degree of alloying as a function of Ag-content with Au@Ag@SiO₂ NRs of $X_{Ag} = 0.24$ ($V = 3.0 \cdot 10^4 \text{ nm}^3$, red), $X_{Ag} = 0.45$ ($V = 5.0 \cdot 10^4 \text{ nm}^3$, black) and $X_{Ag} = 0.68$ ($V = 2.7 \cdot 10^4 \text{ nm}^3$, blue). Curves are best fit to the experimental data. The heating ramp was set to 3 °C/min.

these individual nanorods, which were slightly different from the average values in Table 5.5: $X_{Ag} = 0.44$ $V = 0.45 \cdot 10^4 \text{ nm}^3$ (orange), $X_{Ag} = 0.45$ $V = 5.0 \cdot 10^4 \text{ nm}^3$ (black) $X_{Ag} = 0.24$ $V = 3.0 \cdot 10^4 \text{ nm}^3$ (red) and $X_{Ag} = 0.68$ $V = 2.7 \cdot 10^4 \text{ nm}^3$ (blue). To precisely track the metal redistribution in these individual nanorods during the heating process, we determined the core-to-shell ratio from the core and shell diameter for each particle at each temperature (Figure 5.3). Herein, a linescan of the EDX map was taken over the length of the rod, yielding a core- and shell intensity profile. From these intensity profile we determined

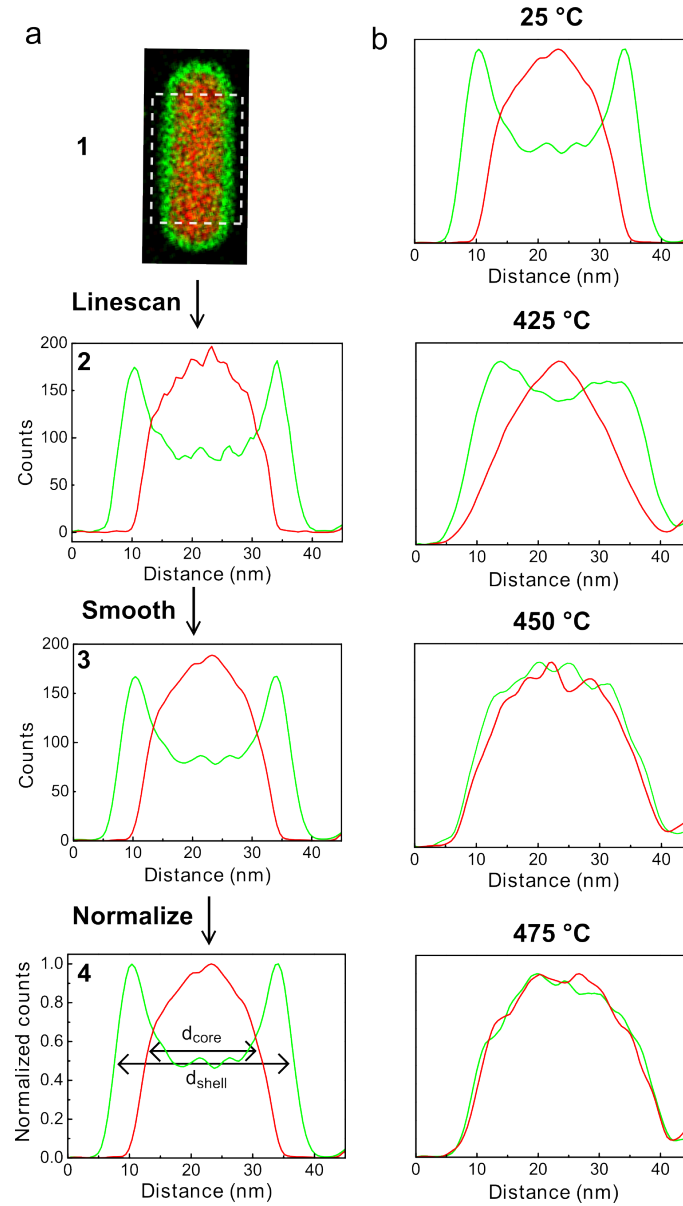


Figure 5.3: Analysis method of the EDX data. (a) Schematic representation of the analysis method, from left to right: 1) line scan of the EDX map taken over the length of the rod (dotted area), 2) smoothing of the line scan, adjacent-averaging of 10 data points, 3) normalization of maximum counts to 1, 4) determination of the core and shell diameter at a normalized count value of 0.5. (b) Normalized line scans of an Au@Ag@SiO₂ NR with $X_{\text{Ag}} = 0.45$ at 25, 425, 450 and 475 °C.

the core-to-shell diameter, at each temperature and for each particle. From the core-to-shell ratios we derived the degree of alloying at the different heating temperatures, which increases from 0 to 1 when going from a core-shell to an alloyed nanorod. In Figure 5.2c we plot the alloying curves of the black and orange highlighted single particles as a function of temperature for the 2 particles with the same Au-Ag ratio, but a factor 10 difference in particle volume. The plot in Figure 5.2d shows the individual alloying curves

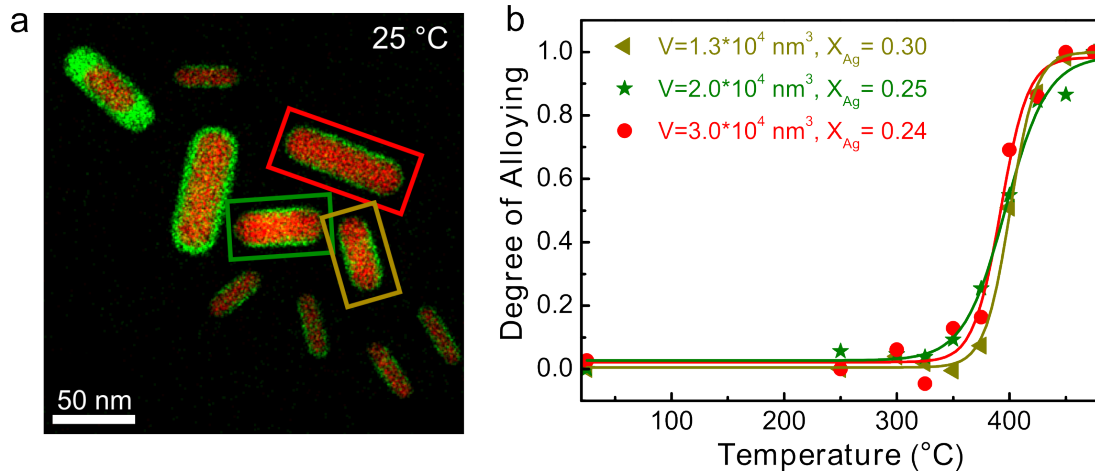


Figure 5.4: *In situ* heating of Au@Ag@SiO₂ NRs in the electron microscope. Comparison of rods with different particle volumes, but similar Au-Ag ratios: $V = 1.3$ (brown), 2.0 (green) and $3.0 \cdot 10^4$ nm³ (red) with $X_{Ag} = 0.30$, 0.25 and 0.24 , respectively. The corresponding alloying temperatures are 401 , 396 and 392 °C, showing that a volume difference of a factor 2-3 did not significantly influence the alloying temperature for Au@Ag@SiO₂ NRs with $V \geq 1 \cdot 10^4$ nm³.

of the particles in red, black and blue, which have a similar volume but different Au-Ag ratios. We defined the alloying temperature T_{Alloy} as the temperature where the degree of alloying reached 0.5 and was 392 , 394 , 436 and 451 °C for the rods with $X_{Ag} = 0.24$, $X_{Ag} = 0.44$, $X_{Ag} = 0.45$ and $X_{Ag} = 0.68$, respectively.

These *in situ* TEM measurements clearly show the impact of the particle volume and the metal composition on the atomic redistribution, where a decrease in particle volume and Ag-content led to significantly lower alloying temperatures. Lowering of the particle volume by a factor 10 (from $V = 0.45 \cdot 10^4$ nm³ to $5.0 \cdot 10^4$ nm³) resulted in a decrease in alloying temperature of 42 °C, whereas the influence of the particle volume for larger NRs with $V = 1.3$ to $3.0 \cdot 10^4$ nm³ was negligible (Figure 5.4). The considerable drop in the alloying temperature when decreasing the particle volume to $V = 0.45 \cdot 10^4$ nm³ and the diameter of the nanorod below 20 nm indicates an increased atom mobility at smaller particle dimensions. Such a size effect is in line with the previously reported particle size dependent melting of silica encapsulated AuNPs, where the melting point decreased drastically from ~ 900 to 300 °C, when decreasing the (spherical) particle diameter from 20 to 1.5 nm [5].

From EDX maps and corresponding alloying curves in Figure 5.2b and d it is clear that the atomic redistribution is also strongly influenced by the Au-Ag ratio: the Au@Ag@SiO₂ NR with the $X_{Ag} = 0.68$ alloyed at almost 50 °C higher than the one with $X_{Ag} = 0.24$. Despite the fact that the rod with $X_{Ag} = 0.68$ had a 2 times smaller volume than the rod with $X_{Ag} = 0.45$, the increase in Ag-content led to a significantly higher alloying temperature.

Ensemble averaged atomic redistribution from *in situ* EXAFS

To investigate the impact of the metal composition on the atomic redistribution for a larger number of particles, we moved from *in situ* TEM to *in situ* EXAFS and extended our study from a femtogram to milligram scale, and from single to 10^{19} particles. Additionally, *in situ* EXAFS measurements allowed dosing of gases combined with a reliable temperature control. The unconventionally fast switching between the metal absorption edges (< 1 min) at the ROCK beamline of the SOLEIL synchrotron made it possible to follow the atomic redistribution at the Au and Ag absorption edges in the same experiment. The alloying experiments were carried out under inert conditions in a He-flow, since the presence of oxygen is known to significantly change the alloying process [57].

The *in situ* EXAFS data of the atomic redistribution in the Au@Ag@SiO₂ NRs with lowest and highest Ag-content, $X_{Ag} = 0.20$ and 0.70 are shown in Figure 5.5. Figure 5.5a-d shows the normalized $\mu(E)$ spectra and $\chi(k)$ spectra acquired at the Au L₃ and Ag K absorption edges of the NRs with $X_{Ag} = 0.70$. The oxidation state of the Au and Ag atoms in the core and in the shell of the NRs before heating was determined from the XAFS spectra at room temperature (RT) and found to be predominately metallic.

The *in situ* EXAFS spectra show a clear change when heating the NRs from 30 to 500 °C. To verify if metal redistribution took place, we used the EXAFS spectra before and after thermal treatment to calculate the coordination numbers between the Au and Ag atoms: N_{Au-Au} , N_{Au-Ag} , N_{Ag-Ag} and N_{Ag-Au} . Table 5.6 lists the coordination numbers for both samples. Due to the core-shell structure of the NRs the coordination numbers between unlike atoms are low before heating. As expected, N_{Ag-Au} is lowest for core-shell particles with the highest X_{Ag} . After heating the core-shell NRs to 500 °C, N_{Ag-Au} and N_{Au-Ag} increased by a factor ≥ 6 , indicating that mixing of the two elements took place in both samples. A full overview of the EXAFS fitting parameters is given in Table 1-4.

To estimate if the NRs were fully alloyed, meaning that the Au and Ag atoms were randomly dispersed within the particles, the extent of alloying (J) was calculated following the approach developed by Hwang *et al.* [211]:

$$J_{Au} = \frac{P_{observed}}{P_{random}} = \frac{[N_{Au-Ag}/(N_{Au-Ag} + N_{Au-Au})]_{observed}}{[N_{Au-Ag}/(N_{Au-Ag} + N_{Au-Au})]_{random}} \times 100\% \quad (5.3)$$

The J -values of the two components (Au and Ag) give information on the internal distribution of the two components [211]. To calculate P_{random} the Au-Ag ratios as de-

Table 5.6: Coordination number N before and after heating the NRs to 500 °C in a 25 mL/min He-flow with a 3 °C/min ramp. Based on the coordination numbers the corresponding J -values were calculated.

	N_{Ag-Ag}	N_{Ag-Au}	N_{Au-Au}	N_{Au-Ag}	J_{Ag}	J_{Au}
$X_{Ag} = 0.20$ before heating	10.1 ± 1.8	1.1 ± 1.3	11.0 ± 0.2	0.3 ± 0.2	12	13
$X_{Ag} = 0.20$ after heating	2.5 ± 0.7	6.8 ± 1.7	9.6 ± 0.2	1.8 ± 0.1	91	79
$X_{Ag} = 0.70$ before heating	11.0 ± 0.3	0.6 ± 0.3	9.8 ± 0.2	0.3 ± 0.2	17	4
$X_{Ag} = 0.70$ after heating	7.7 ± 0.4	3.5 ± 0.2	3.1 ± 0.3	8.3 ± 0.4	104	104

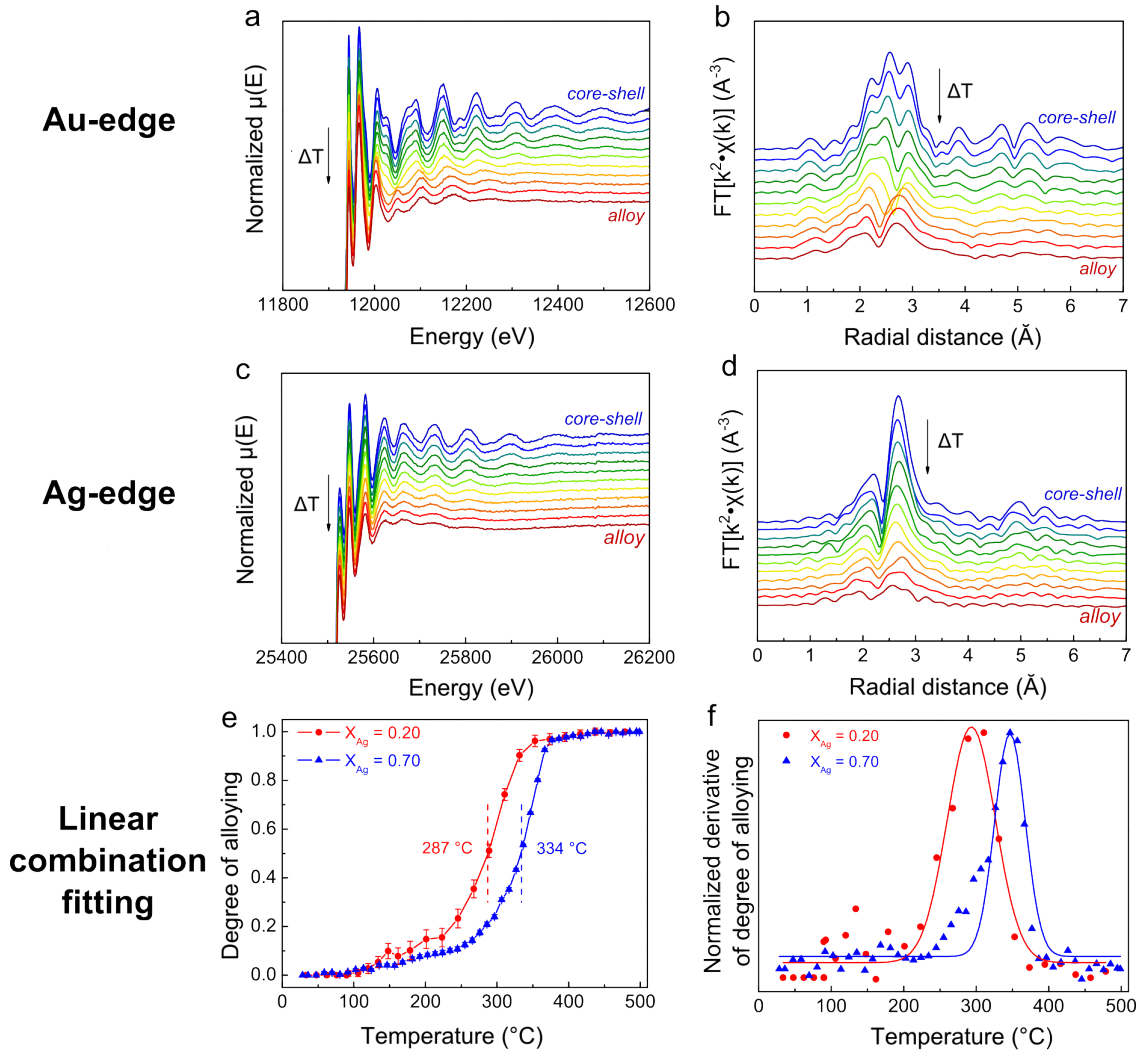


Figure 5.5: Double edge *in situ* EXAFS measurements of Au@Ag@SiO₂ NRs upon heating. Normalized $\mu(E)$ -spectra and $\text{FT}[k^2\chi(k)]$ spectra at the Au L₃-edge (a,b, $\Delta k = 3.3\text{--}14.0 \text{ \AA}^{-1}$) and Ag K-edge (c,d, $\Delta k = 3.2\text{--}12.0 \text{ \AA}^{-1}$) of the nanorods with $X_{Ag} = 0.70$, recorded every $\sim 50^\circ\text{C}$ when heating from 30 to 500 $^\circ\text{C}$. The plots in e and f show the degree of alloying and the derivative thereof as a function of temperature and were obtained by performing linear combination fitting on the normalized $\mu(E)$ -spectra at the Ag K-edge ($X_{Ag} = 0.20$, red) and Au L₃-edge ($X_{Ag} = 0.70$, blue). The EXAFS spectra were acquired during heating to 500 $^\circ\text{C}$ with 3 $^\circ\text{C}/\text{min}$ in a 25 mL/min He-flow.

terminated by EDX were used. In Table 5.6 the J -values for the two different NR samples before and after heating to 500 $^\circ\text{C}$ are given. For both alloyed samples the calculated J_{Au} and J_{Ag} -values are close to 100, indicating that the NRs are likely to have a fully alloyed structure when heating them to 500 $^\circ\text{C}$.

To deduce the evolution of the alloying process from all the spectra acquired between 30 and 500 $^\circ\text{C}$, we performed linear combination fitting on the normalized $\mu(E)$ spectra. In (E)XAFS analysis, linear combination fitting is typically used to determine and/or follow changes in the oxidation state of metal nanoparticles, but not common for following

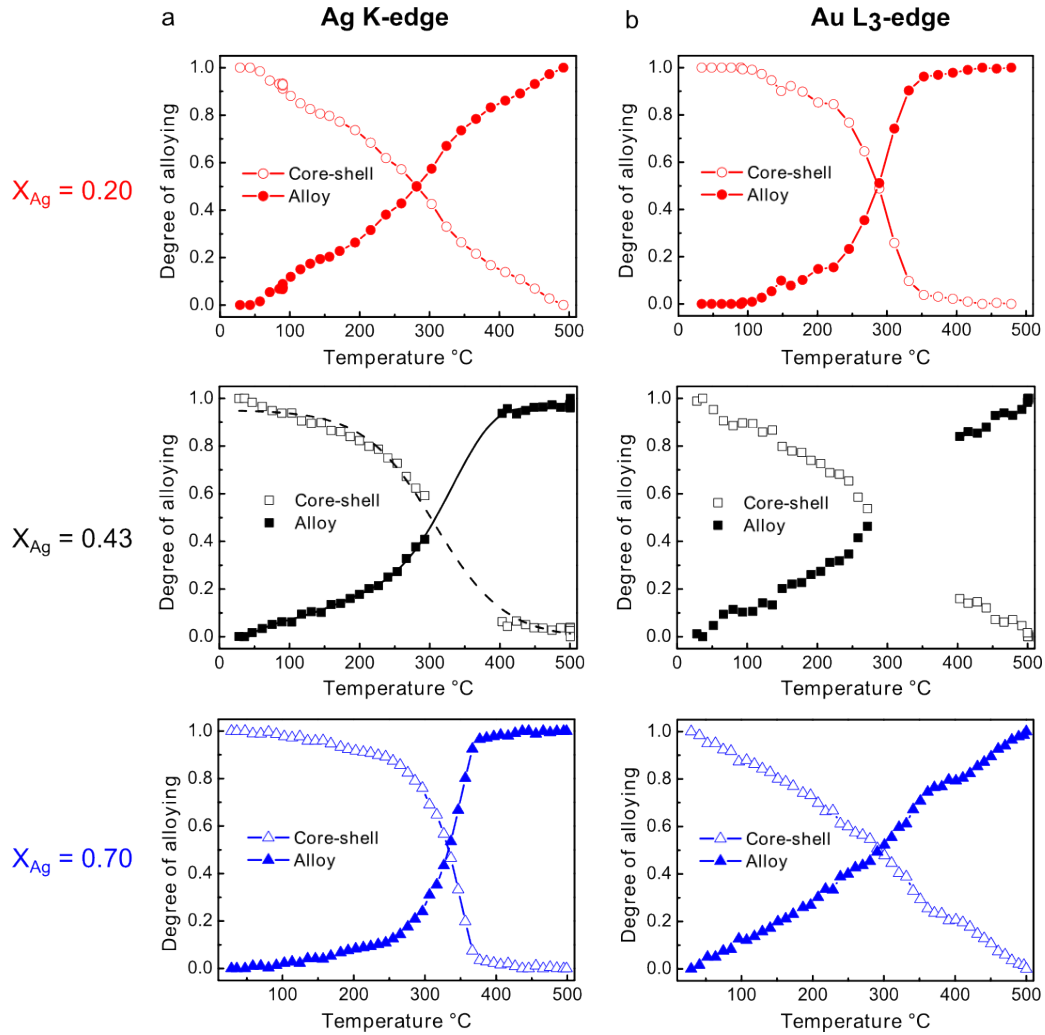


Figure 5.6: In situ EXAFS results for Au@Ag@SiO₂ NRs with $X_{Ag} = 0.20$ (a, red), 0.43 (b, black) and 0.70 (c, blue) alloying at the Ag K-edge and Au L₃-edge. The degree of alloying curves versus temperature were obtained via linear combination fitting of the XAFS-spectra. The gap in the data for the sample with $X_{Ag} = 0.43$ was caused by loss of the X-ray beam during that part of the measurement.

metal redistribution. Note that a linear combination fitting based analysis is considerably faster than calculation of the coordination numbers, which is especially important when analysing a large number of EXAFS spectra.

In our analysis, each EXAFS spectrum at a given temperature was compared to the spectrum of the initial core-shell and final alloyed state for which the spectra at 30 °C and 500 °C were taken, respectively. As shown in Figure 5.5e, the analysis was successfully applied to obtain the degree of alloying as a function of temperature. Figure 5.5e specifically shows the linear combination fitting results determined from the Ag K-edge for the $X_{Ag} = 0.20$ sample and Au L₃-edge for the $X_{Ag} = 0.70$ sample, since the change from core-shell to alloyed state is most apparent on the edge of the least abundant metal (see Figure 5.6). In addition, it is important to note that the linear combination fitting

analysis is also sensitive to changes which are not due to metal redistribution, such as damping of the EXAFS spectra due to thermal disorder with increasing temperature. This temperature contribution predominately plays a role when the change upon alloying is small, as is the case for the absorption edge of the metal which is in the majority. To demonstrate this we plot the alloying curves determined on the Au L₃ edge and the Ag K edge for the samples with $X_{Ag} = 0.20, 0.43$ and 0.70 in Figure 5.6.

From Figure 5.5e the alloying temperature determined at a degree of alloying of 0.5, was 287 and 334 °C for the sample with $X_{Ag} = 0.20$ and 0.70 , respectively. The EXAFS measurements thus confirmed the increase in alloying temperature with increasing Ag-content as observed in the *in situ* TEM, but now for a large ensemble of particles. However, it should be noted that there is a discrepancy in alloying temperatures: from the *in situ* EXAFS we obtained ~100 °C lower alloying temperatures compared to the *in situ* TEM data. This discrepancy demonstrates the need for *ex situ* measurements to establish the absolute temperature at which the metal redistribution occurs in the absence of an electron or X-ray beam.

Validation of the *in situ* data

Although electron microscopy and X-ray absorption spectroscopy enable the *in situ* observation of structural changes in metal nanoparticles, it is crucial to validate these techniques with *ex situ* measurements. In particular electron beam irradiation has been reported to induce anomalous behaviour in nanostructured materials and significantly alter the deformation behaviour, growth kinetics and structure of the nanoparticles during *in situ* studies [219–221]. To verify the dependence of the alloying temperature on the Au-Ag ratio as observed in *in situ* TEM and *in situ* EXAFS, *ex situ* measurements were carried out, heating the NRs in a furnace. Herein, we used the same heating ramp of 3 °C/min to heat to 250, 300, 325, 350, 375 and 400 °C in N₂ after which each sample was analysed with HAADF-STEM and EDX (Figure 5.7).

In every sample and for each temperature, 4 representative rods were analysed with EDX to determine their core-to-shell ratios and their compositions, which were close to the average sample compositions as given in Table 5.5. From the core-to-shell ratio the degree of alloying was calculated in the same way as described for the *in situ* TEM measurements and the degree of alloying is shown as a function of the heating temperature in Figure 5.8a. It shows that the Au@Ag@SiO₂ NRs with average $X_{Ag} = 0.17, 0.46$ and 0.72 alloy at 305, 345 and 375 °C, respectively. The EDX maps in Figure 5.7 show that all Au@Ag@SiO₂ NRs of the same composition simultaneously convert from a core-shell to alloyed state.

In Figure 5.8b an overview of the alloying temperatures versus the Ag-content for all three techniques is shown. The *ex situ* data nicely support the trends observed in the *in situ* TEM and *in situ* EXAFS measurements. In all three techniques the alloying temperature increases with an increasing Ag-content, only the absolute temperatures vary. The *ex situ* TEM measurements match the EXAFS results, but the alloying temperatures determined by *in situ* TEM are 75–90 °C too high. The relatively high alloying temperatures from the *in situ* TEM measurements could be related to an altered heat conductivity in the SiN_x chip after depositing the nanorods combined with possible carbon contamination, leading to inaccurate temperatures in the heating chip. Alternatively, the strongly

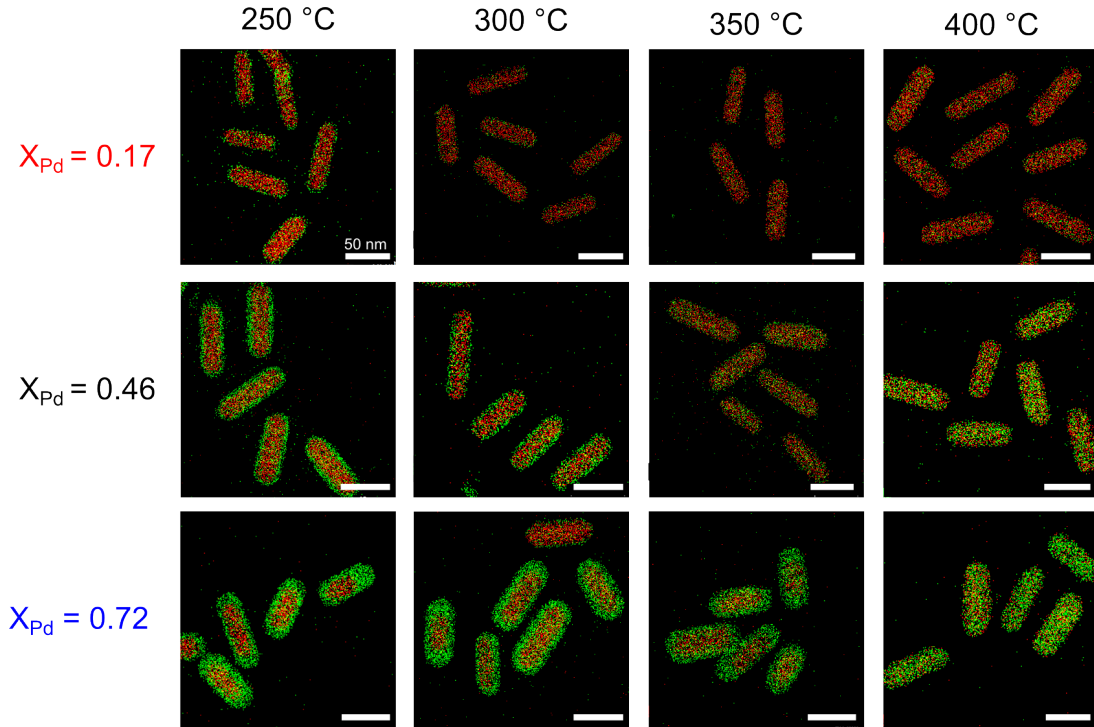


Figure 5.7: *Ex situ* TEM measurements on the alloying of Au@Ag@SiO₂ NRs. The EDX maps were acquired after heating the Au@Ag@SiO₂ NRs with $X_{Ag} = 0.17$ (top), 0.46 (middle) and 0.72 (bottom) to 250 - 400 °C.

reducing electron beam could have influenced the kinetics of the alloying process, but we did not observe significant differences in the alloying process between areas that were or were not illuminated with the electron beam prior to the heating. Thus, although care should be taken in deducing quantitative data from *in situ* TEM, it is a powerful technique in providing a qualitative insight in the metal redistribution for single nanoparticles and correctly shows the dependency of the metal redistribution on the metal composition for different nanoparticles.

For all Au-Ag compositions the observed alloying temperatures are far below the bulk melting point of Au and Ag, which points at a nanosize effect on the alloying process and enhanced atom mobilities compared to the bulk. Size effects have been observed for the melting temperatures of nanoparticles, where the melting point was significantly lowered when decreasing the nanostructure size [4, 5, 136]. Analogously, the observed lowering of the alloying temperature can be explained by a lowering in cohesive energy, which is the binding strength of the atom with its neighbours, with increasing particle surface to volume ratio [227, 228]. Since the cohesive energy is proportional to the vacancy formation energy and activation energy of diffusion, it is to be expected that the mobility of atoms and the rate of alloying increases for smaller nanostructures, leading to lower alloying temperatures. When decreasing the particle diameter below 5 nm even spontaneous alloying of bimetallic Au-Ag nanoparticles at room temperature can occur [199].

It should be noted that the observed trend between the alloying temperature and metal composition in the Au-Ag nanoparticles varies oppositely to the composition dependency

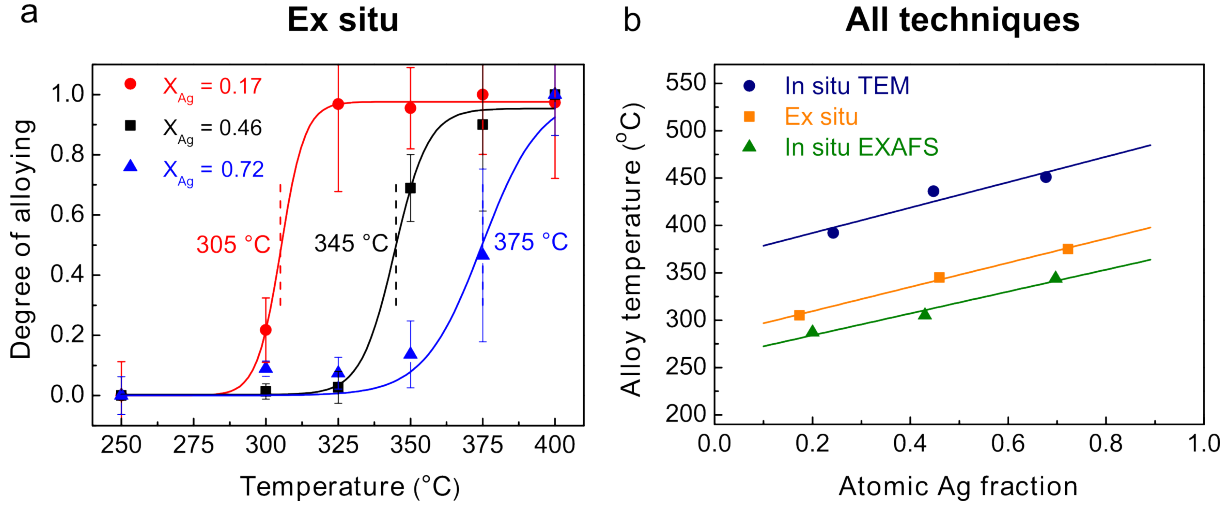


Figure 5.8: *Ex situ* TEM measurements on the alloying of Au@Ag@SiO₂ NRs. a) the degree of alloying after heating Au@Ag@SiO₂ NRs in a furnace as a function of the heating temperature. Each point is an average of 4 particles. The alloying temperatures for the Au@Ag@SiO₂ NRs with $X_{Ag} = 0.17$ (red), 0.46 (black) and 0.72 (blue) was 305, 345 and 375 °C, respectively. The samples were heated in a N₂ flow with a heating ramp of 3 °C/min. b) summary of the alloying temperature as a function of Ag fraction determined with *in situ* TEM (dark blue), *ex situ* TEM (orange) and *in situ* EXAFS (green). Curves are best fit to the experimental data.

in the melting point temperature, where $T_{melting,Ag} = 962$ and $T_{melting,Au} = 1064$ °C. A similar trend for atomic diffusion was measured in bulk Au-Ag crystals.[224] The activation energy of diffusion for both Au and Ag atoms in Au-Ag alloys was reported to increase with increasing Ag fraction going from 1.74 to 1.93 eV for Ag atoms in pure Au and Ag, and 1.81 to 2.09 eV for Au atoms in pure Au and Ag [224]. From these activation energies it follows that Ag atoms are more mobile than Au atoms, but that the diffusion of both Au and Ag atoms is slower in high Ag-content Au-Ag alloys. A possible explanation for this phenomenon can be derived from the energy of vacancy formation and atom migration, which are known to be higher in Ag compared to Au: $E(\text{vacancy formation})_{Ag} = 1.10$ eV, $E(\text{vacancy formation})_{Au} = 0.97$ eV, $E(\text{atom migration})_{Ag(in)Ag} = 0.83$ eV, $E(\text{atom migration})_{Ag(in)Au} = 0.77$ eV [224, 229, 230]. Since atomic diffusion in Au-Ag crystals is known to go *via* vacancy hopping, a lower number of vacancies and a higher energy cost for hopping into the vacancies with increasing Ag-content could explain the observed retardation of Au and Ag in high content Ag alloys. In addition to Au-Ag, similar trends of self-diffusion dependency opposite to melting temperature have been reported for *e.g.* Ag-Mn [231], TiCr [232, 233] and Tl-Pb bulk crystals [234]. In this study, we show experimental proof of this trend at the nanoscale.

Modelling atomic redistribution

We devised a simple model that can correctly describe the diffusion in Au-Ag nanoparticles as a function of temperature and composition. We numerically calculate the diffusion of Au atoms n_{Au} and Ag atoms n_{Ag} passing through a static Au-Ag interface per time step Δt according to Fick's first law:

$$n_{Ag}/\Delta t = (A/r) \cdot D_0^{Ag} e^{-Q_{Ag}/(RT)} \cdot |C_{core}^{Ag} - C_{shell}^{Ag}| \quad (5.4)$$

where A is the interface area, r the radius of the NP, D_0^{Ag} the frequency factor, Q_{Ag} the activation energy, R the gas constant, T the temperature, C_{core}^{Ag} the silver concentration of the core and C_{shell}^{Ag} the silver concentration of the shell (expressed in atoms per m^3). An analogous formula holds for the Au atoms. The rate of diffusion was calculated iteratively, where D_0 , Q and the concentration difference $C_{core} - C_{shell}$ were updated every time step. The frequency factor D_0 and activation energy for diffusion Q depend on the Au-Ag composition and have been measured experimentally in bulk crystals [224]. We corrected these composition dependent bulk D_0 and Q values for the NP size according to the model of Guisbiers *et al.* [225, 226]. Herein, the activation energy of diffusion in NPs Q_{NP} was derived from the activation energy of diffusion in the bulk Q_{Bulk} by using a so-called shape factor α_{shape} which amongst others depends on the surface-to-volume ratio of the NPs. More details on the calculation of the α_{shape} factor can be found in the experimental section. For the Au-Ag NRs used in this study, the correction of Q_{Bulk} to Q_{NP} , resulted ~ 50 °C lower alloying temperatures.

The resulting theoretical predictions for the alloying curves of the *in situ* EXAFS measurements are shown in Figure 5.9a. The theoretical predictions are in very good agreement with the experimental *in situ* EXAFS data and the alloying temperatures as

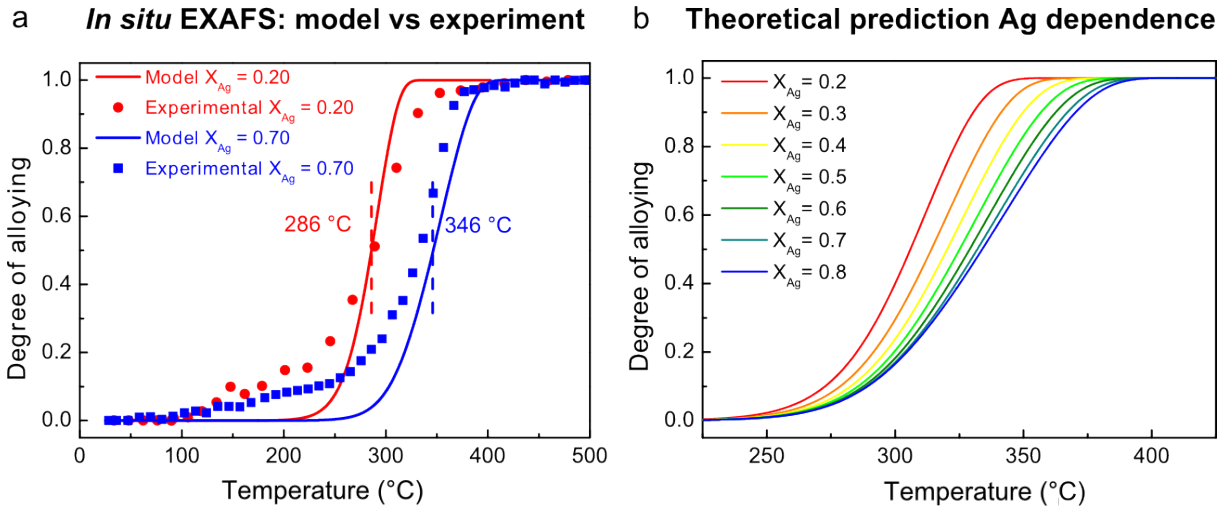


Figure 5.9: Theoretical prediction of the change in the degree of alloying as a function of heating temperature and atomic Ag fraction. (a) The theoretical prediction for the *in situ* EXAFS experiment give an alloying temperature of 286 and 346 °C for the samples with $X_{Ag} = 0.20$ and 0.70. The plot in b shows the theoretical prediction of the alloying curves for Au-Ag NRs of $V = 4 \cdot 10^4$ nm^3 and $X_{Ag} = 0.2-0.8$ (red-blue) heated with 3 °C/min.

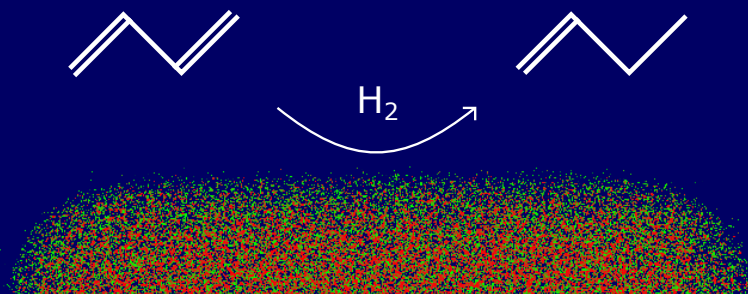
predicted by the model, 286 and 346 °C for the $X_{Ag} = 0.20$ and 0.70, match the experimental values of 287 and 334 °C closely. In Figure 5.9b we show the theoretical prediction for the alloying curves of Au-Ag NRs with $V = 4 \cdot 10^4 \text{ nm}^3$ and $X_{Ag} = 0.2-0.8$. In the calculation of these curves a heating ramp of 3 °C/min was considered, as in the experimental studies. The theoretical predictions clearly demonstrate the importance of including the dependency of the diffusion on the metal composition. We would like to stress that it is remarkable that the metal composition still plays such a crucial role in the diffusion kinetics in nanoparticles, where size and shape have generally been considered to play the most important role [198, 209, 225] and the influence of the particle composition has therefore been neglected so far.

5.4 Conclusions

We have used a multi-technique approach to precisely follow metal redistribution, a process crucial in catalysis, *in situ* and at different length scales. A combination of *in situ* TEM with *in situ* EXAFS validated with *ex situ* measurements, provided both a single particle and ensemble averaged characterization. Our well-defined model system, consisting of mesoporous silica coated, single-crystalline Au-core Ag-shell nanorods of tunable size and composition, allowed a systematic study of the nanoparticle composition on the atomic redistribution kinetics. We unambiguously showed that the atomic diffusion in Au-Ag nanoparticles strongly depends on the composition, a trend which has been observed in bulk crystals, but which has, to the best of our knowledge, not been reported for nanomaterials. Additionally, we find indications for a nanoscale effect on the alloying process, leading to lower alloying temperatures when decreasing the nanoparticle size. Finally, we show that to correctly model metal redistribution in metallic nanoparticles not only the nanoscale dimensions, but also the metal composition should be taken into account. Both our experimental approach and theoretical model are likely to apply to a wide range of bimetallic nanoparticle based materials.

Acknowledgements

The work presented in this chapter was performed in collaboration with Tom Welling (modelling), Tiago Silva (EXAFS), Jeroen van den Reijen (modelling), Camille La Fontaine (EXAFS), Xavier Carrier (EXAFS) and Catherine Louis (EXAFS). We thank Marijn van Huis for providing the *in situ* electron microscopy heating equipment, Maarten Bransen for useful discussion on the nanorod synthesis and Simone Dussi for critically reading this chapter.



Tuning the metal distribution of gold-palladium catalysts for bimetallic synergy in the selective hydrogenation of butadiene

6

Abstract

In the polymer industry, alkadiene and alkyne impurities in alkene feedstocks are problematic as they can poison polymerization catalysts. To remove these impurities, active and highly selective hydrogenation catalysts have to be used as undesired over-hydrogenation to alkanes can easily occur. Bimetallic catalysts are promising candidates to comply to these requirements and offer the opportunity to combine one selective and one active metal into one bimetallic nanoparticle (NP). Despite the numerous investigations on alloyed bimetallic catalysts, little is known about the influence of the metal distribution within the bimetallic NPs on the catalytic performance. As it is difficult to vary the metal distribution without changing other parameters in the system that influence the catalytic performance, a systematic study correlating the atomic distribution and catalytic properties of bimetallic hydrogenation catalysts is difficult to design. Here, we achieve such a study by making use of a well-defined model system consisting of colloiddally synthesized mesoporous silica coated Au-core Pd-shell nanorods (NRs) of which the metal distribution was easily tuned via thermal treatment without changing the size, shape, composition and single-crystalline structure of the NRs. We used this model system to investigate the impact of the metal distribution of AuPd catalysts in the selective hydrogenation of butadiene impurities in propene. We show that core-shell structured AuPd catalyst are about 45 times more active in hydrogenating butadiene than their fully alloyed counterparts, while maintaining an exceptionally high selectivity. Moreover, when varying the Pd-shell thickness from 1-8 atomic layers, a non-monotonic dependence of the catalytic activity on the shell thickness was observed, where the core-shell structure with 2 atomic Pd layers was most active. The results presented in this chapter show that precise tuning of the metal distribution can lead to bimetallic synergy and that it opens up an enormous, additional parameter space to tune the catalytic activity and selectivity of bimetallic catalysts.

6.1 Introduction

Light alkenes are important building blocks in the production of polymers. However, alkenes feedstocks are usually contaminated with alkadiene and alkyne impurities [235]. Trace amounts of these impurities can affect the polymerization process and poison the polymerization catalysts [236]. It is therefore essential to remove these impurities before the polymerization takes place. This is typically done by selectively hydrogenating alkynes and alkadienes to alkenes [235, 237]. Industrially relevant examples of such reactions are the selective hydrogenation of acetylene impurities in ethylene and the selective hydrogenation of 1,3-butadiene molecules in butene. In these processes the main challenge is to selectively convert the 1,3-butadiene (or acetylene) without hydrogenating the large excess of butene (or ethylene) present in the gas feed. Thus, these processes require a catalyst with an exceptionally high selectivity towards the hydrogenation of the impurities, while leaving the alkenes untouched. A selective hydrogenation catalysts should therefore preferentially adsorb the alkadiene and alkyne impurities compared to the alkenes. In addition, the hydrogenation should stop after hydrogenating the impurity to an alkene and not hydrogenate it further to an alkane. This condition is met when the catalyst has a larger activation barrier for alkene hydrogenation compared to alkene desorption [71]. Finally, the catalyst should not only be highly selective but also have a sufficiently high activity.

Pd-based materials are typically active hydrogenation catalysts as hydrogen is easily dissociated on the Pd-surface [238]. When the impurity concentration is high, Pd catalysts can be highly selective [239]. However, the unfavourable hydrogenation of alkenes becomes increasingly important when the impurity concentration is low [240], as the activation barrier for alkene hydrogenation and desorption are comparable [71]. By combining Pd with a poorly active material like Ag this problem can be suppressed [241], but not without compromising for a lower catalytic activity. Au-based catalysts on the other hand are much less active but exhibit a high selectivity even if the impurity concentration is very low, allowing full conversion of the impurities at an alkene conversion as low as 0.3 % [97, 242–245]. Considering the high activity of Pd and exceptional selectivity of Au, bimetallic Au-Pd catalysts hold great promise to combine the best of both. High Au content AuPd alloys indeed exhibit an improved activity compared to Au and improved selectivity compared to Pd [246], but the final catalytic properties are still a compromise between the monometallic catalysts, meaning that they are less active and selective compared to pure Pd and pure Au, respectively.

Although the composition, size and support effects of bimetallic hydrogenation catalysts have been investigated [99, 246, 247], the impact of the atom distribution is still largely unexplored. The ability to tune the metal distribution would offer a new way to control and optimize the catalytic performance and could lead to new catalytic properties inaccessible to alloyed and monometallic systems. For instance, the properties of core-shell NPs can be very different from their alloyed counterparts due to electronic and strain induced effects [76, 106, 248, 249]. To systematically investigate the impact of the metal distribution on the catalytic behaviour, a well-defined model system is crucial. However, a precisely tunable model system in which the metal distribution can be varied without

altering any other parameter in the system is not easily accessible via standard catalyst preparation methods.

In this work, we employ colloiddally synthesized, mesoporous silica coated Au-core Pd-shell nanorods (Au@Pd@SiO₂ NRs) with a well-defined, single-crystalline atomic structure as a model system to investigate the impact of the metal distribution on the catalytic performance of selective hydrogenation catalysts. The composition, shape and size of these core-shell nanorods could be tuned precisely [54, 104], where the typical length and diameter of the rods was around 70 and 20 nm, respectively. Via thermal treatment the metal distribution was changed from core-shell to alloy while retaining exactly the same size, shape, crystal structure and composition [57, 104]. We investigated the performance of the differently structured catalysts in the selective hydrogenation of 1,3-butadiene to butene in the excess of propene. This reaction mimics the industrial selective hydrogenation process of butadiene in excess butene, but simplifies the analysis of the reaction products [243]. First, we show that Pd-shell Au-core structures outperform the alloyed structures with the same composition by a factor 45 in activity while running at high hydrogen selectivity and less than 0.3 % propene conversion. Next, we further explored the core-shell structured catalysts and varied the Pd-shell thickness between 0 and 8 atomic layers. The core-shell structures all outperformed their monometallic counterparts and their activity exhibited a non-monotonic dependence on the Pd-shell thickness. We identified 2 atomic Pd layers as the optimal shell thickness for the core-shell structured catalysts. The work in this chapter shows the importance of tuning the atomic distribution, which opens up a large, additional parameter space in optimizing the performance of bimetallic catalysts.

6.2 Experimental

Chemicals

Chemicals used in the synthesis

All chemicals were used as received without further purification. Hexadecyltrimethylammonium bromide (CTAB, >98.0 %) and sodium oleate (NaOL, >97.0 %) were purchased from TCI America. Hydrogen tetrachloroaurate trihydrate (HAuCl₄·3H₂O) and sodium hydroxide (NaOH, 98 %) were purchased from Acros Organics. L-Ascorbic Acid (BioXtra, ≥99 %), hydrogen peroxide (H₂O₂, 30 wt% in H₂O), hydrochloric acid (HCl, 37 wt% in water), silver nitrate (AgNO₃, ≥99 %), sodium borohydride (NaBH₄, 99 %), sodium tetrachloropalladate-(II) (Na₂PdCl₄, 98 %) and tetraethyl orthosilicate (TEOS, 98 %) were purchased from Sigma-Aldrich. Ultrapure water (Millipore Milli-Q grade, MQ H₂O) with a resistivity of 18.2 MΩ was used in all of the experiments. Methanol (MeOH) was purchased from Interchema (≥99.85 %.) All glassware for the AuNR synthesis was cleaned with fresh aqua regia (HCl/HNO₃ in a 3:1 volume ratio), rinsed with large amounts of water and dried at 100 °C before usage.

Synthesis

Gold nanorod synthesis

Monodisperse AuNRs were synthesized according to the protocol of Ye *et al.* [13]. The synthesis was performed on a 500 mL scale with a growth solution containing 7.0 g CTAB, 1.24 g NaOL, 250 mL MQ H₂O and 250 mL 1.0 mM HAuCl₄, 4.8 mL AgNO₃, 2.10 mL concentrated HCl (37 wt%), 1.25 mL 64 mM ascorbic acid and 0.8 mL seed solution. The seeds were prepared from a 10 mL 0.10 M CTAB, 51 μ L 50 mM HAuCl₄ and 1.0 mL 6.0 mM NaBH₄. The subsequent rod growth was performed under static conditions in a 30 °C water bath overnight. The resulting AuNR suspensions had a longitudinal surface plasmon resonance at $\lambda(\text{LSPR})= 742\text{-}794$ nm with an extinction maximum (Ext) of 1.0 (4 \times diluted in H₂O). The rods were centrifuged at 9000 rcf (relative centrifugal force) for 45 min (Rotina 380R Hettich centrifuge), washed with H₂O and redispersed in 40 mL 5.0 mM CTAB H₂O.

Note: the use of AgNO₃ in the AuNR synthesis resulted in about 1 atom percent (atm%) Ag in the Au NRs which could not be removed by washing with etching solutions such as the H₂O₂/NH₃ in H₂O mixture used in Chapter 4.

Mesoporous silica coating

The CTAB stabilized AuNRs were coated with a 18 nm mesoporous silica shell following the method of Gorelikov *et al.* [90]. The coating was performed by diluting the as synthesized 40 mL dispersion of AuNRs in 5.0 mM CTAB H₂O to a 200 mL 1.5 mM CTAB aqueous solution to which 2.0 mL 0.10 M NaOH was added. While magnetically stirring at 300 rpm (revolutions per minute) in a 30 °C waterbath, 3 times 0.60 mL 0.90 M TEOS in ethanol (EtOH) were added with a 30 min time interval. Thereafter, the reaction mixture was left for 2 days, while stirring at 300 rpm in a 30 °C waterbath. Finally, the Au@SiO₂ NRs were centrifuged at 8000 rcf for 50 min, washed with 100 mL water, 40 mL EtOH and redispersed in 31 mL EtOH.

Etching of the silica coated AuNRs

Only for the synthesis of the high content Au@Pd@SiO₂NRs (atomic Pd fraction, $X_{Pd}= 0.32$) the Au@SiO₂ NRs were etched prior to the metal overgrowth, to create more space in the silica shell to accommodate the Pd shell. To this end, the Au@SiO₂ NRs ($L_{Au}= 70$ and $D_{Au}= 22$ nm) were dispersed in 50 mL MeOH ($\lambda_{LSPR}= 737$ nm, Ext= 1.2, 2 \times diluted in MeOH) and heated in a 60 °C water bath, while stirring at 400 rpm. Next, 1.0 mL HCl (12.1 M) and 1.0 mL H₂O₂ (20 mM in MeOH) were added. After 20 min, the reaction was quenched by adding 50 mL cold methanol and by cooling the reaction mixture in 4 °C water bath ($\lambda_{LSPR}= 667$ nm, Ext= 0.77, 2 \times diluted in MeOH). The etched Au@SiO₂ NRs were washed once with 20 mL MeOH and twice with 20 mL EtOH (centrifugation at 8500 rcf for 20 min) and were redispersed in 3.2 mL EtOH for storage. The etched Au-cores had a length of 61 ± 8 nm and a diameter of 22 ± 2 nm.

Table 6.1: Reaction parameters used in the Pd overgrowth of Au@SiO₂ NRs resulting in the Au@Pd@SiO₂ NR shown in Figure 6.1.

X_{Pd}	Au@SiO ₂ NRs in EtOH (mL)	x H ₂ O (mL)	y Na ₂ PdCl ₄ (mM)	z AA (mM)
0.042	5.0	250	1.5	6.0
0.083	5.0	200	2.25	9.0
0.21	5.0	240	5.5	22
0.34	2.9	145	8.0	32

CTAB removal

To remove the CTAB and open the mesopores of the silica coated AuNRs, we washed the NRs with 0.10 M HCl in EtOH. To 31 mL dispersion of Au@SiO₂ NRs in EtOH, 260 μ L of concentrated HCl (12.1 M) was added such that the HCl concentration in EtOH was 0.10 M. The acidified dispersion was sonicated for 30 min at room temperature (RT). Next, the Au@SiO₂ NRs were centrifuged at 8000 rcf for 35 min, washed with 20 mL EtOH and twice with 10 mL EtOH to remove the HCl. Thereafter, the rods were redispersed in 10 mL EtOH.

Thermogravimetric analysis (TGA) measurements were performed to quantify the CTAB content in the Au@SiO₂ NRs before and after the HCl-washing (see Characterization). The TGA measurements presented in Figure 6.2 were done with Au@SiO₂ NRs with $L_{Au} = 95 \pm 8$ nm, $D_{Au} = 26 \pm 2$ nm ($\lambda_{LSPR} = 795$ nm) and a ~ 18 nm thick mesoporous silica shell.

Palladium overgrowth

The Pd overgrowth was performed on a large scale similar to the procedures in Chapter 3 and 5 as large quantities of Au@Pd@SiO₂ NRs were needed for the catalysis experiments. For the synthesis of the Pd@Au@SiO₂ NRs with $X_{Pd} = 0.04, 0.08$ and 0.21 Au@SiO₂ NRs from different batches with comparable sizes and an average AR of 3.1 were used. For the Pd@Au@SiO₂ NRs with $X_{Pd} = 0.32$ the batch of etched Au@SiO₂ NRs was used.

Typically, 5.0 mL dispersion of Au@SiO₂ NRs in EtOH were centrifuged for 20 min at 10.000 rcf and redispersed in x H₂O, such that the absorption maximum of the LSPR peak was 2.0. Next, 1.0 vol% 0.10 M HCl and 1.0 vol% y mM Na₂PdCl₄ were added while stirring magnetically at high speed (800 rpm). Thereafter, 1.0 vol% of z mM ascorbic acid in H₂O was added while still stirring. The used values for x , y and z can be found in Table 6.1. The mixture was left to react for 30 min while stirring at 400 rpm. Afterwards, the Au@Pd@SiO₂ NRs were separated from the reaction mixture by centrifugation for 30 min at 4000 rcf. Next, the rods were washed with H₂O and EtOH and redispersed in 5.0 mL ethanol. The core-shell samples were *always* stored in the dark at 4 °C to prevent oxidation of the Pd-shell.

Deposition on silica support

For the catalysis experiments the Au@Pd@SiO₂ NRs were deposited on a commercial silica support: Aerosil50 (Evonik, BET surface area of 50 m²/g). Prior to the deposition

the concentration of the Au@Pd@SiO₂ NRs in ethanol dispersions was determined with Inductively Coupled Plasma Atomic Emission Spectroscopy (ICP-AES, see Characterization). Depending on the concentration, a given amount of AuPd@SiO₂ NRs in ethanol were added to 1.0 g of SiO₂ support in a 20 mL glass vial, such that the total metal loading on the SiO₂ was 0.20 wt% for the Au@Pd@SiO₂ NRs and 1.0 wt% for the Au NRs@SiO₂. The resulting mixture was sonicated for about an hour to ensure a homogeneous distribution of the NRs over the silica support. Next, 14.0 mL of toluene was added followed by a few minutes of sonication. The addition of toluene as an apolar, antisolvent ensured aggregation of the NRs onto the silica support. Thereafter, the mixture was centrifuged at 500 rcf for 5 min, resulting in a colourless supernatant and a homogeneously coloured sediment of the NRs on Aerosil50. After removal of the supernatant, the supported NRs were dried in a N₂-flow for several minutes and dried overnight at 60 °C in air. Thereafter, the samples were sieved to obtain catalysts with a grain size of 90-212 μm.

***Ex situ* heating**

The *ex situ* heating experiments were performed in a tubular oven (Thermolyne 79300 tube furnace) under a constant H₂ flow of 100 mL/min. The dispersion of Au@Pd@SiO₂ NRs with $X_{Pd}=0.08$ was dropcasted on a copper TEM grid (200 mesh copper (100), Formvar/carbon film), which was placed in a ceramic cup and transferred to a quartz tube. The tube was flushed with Argon for 1 h. Thereafter, the sample was heated with a ramp of 2 °C/min to the desired temperature, which was 250, 300, 325, 350, 375, 400 or 450 °C, where the temperature was kept constant for 60 min. The sample was cooled down in H₂. After the thermal treatment the TEM grids were analysed in the electron microscope (see Characterization).

Catalysis

The catalytic properties of the Au@Pd@SiO₂ NRs were tested for the selective hydrogenation of butadiene to butene in the presence of excess propene. Typically, 10-50 mg of the Au@Pd@SiO₂ on Aerosil50 (0.02-0.2 wt%, sieve fraction of 90-212 μm) were loaded into a Pyrex plug flow reactor (internal diameter of 4 mm). As the catalytic activity of the Au@Pd@SiO₂ NRs strongly depends on the atomic structure (core-shell or alloyed) and Pd content, the amount of metal loaded was varied such that all catalysts were active in the same temperature range. To achieve this, the catalysts (0.2 wt% metal on Aerosil50) were diluted with Aerosil50 (sieve fraction of 90-212 μm). In Table 6.2 the amount of catalyst and metal loading of the catalysts used for the metal distribution (Figure 6.5 and 6.6) and core-shell (Figure 6.7 and 6.9) experiments are listed.

Prior to the reaction, the catalysts were thermally treated in H₂ at ≥ 250 °C to ensure that the Au-Pd NRs were fully reduced to the metallic state and had smooth particle surface (see Chapter 3). The metal distribution of the Au@Pd@SiO₂ NRs was changed by reducing the Au@Pd@SiO₂ NRs at different temperatures (250-500 °C). The pretreatment was always done in 50 mL/min pure H₂, a heating ramp of 2 °C/min and kept at a constant temperature (250-500 °C) for 60 min. The pretreated catalysts were cooled down in H₂ to 30 °C. Thereafter, the gas atmosphere was changed from H₂ to a pre-mixed reaction

Table 6.2: Overview of the catalyst loadings used in the metal redistribution and core-shell catalysis experiments. Different metal loadings were obtained by diluting the Au@Pd@SiO₂ NRs on Aerosil50 (0.2 wt% metal loading) with Aerosil50 (90-212 μm).

$T_{Pretreatment}$ (°C)	Atomic Pd fraction	Catalyst loaded (mg)	Metal loading (wt%)
250	0.083	20	0.020
300	0.083	20	0.020
325	0.083	20	0.020
350	0.083	20	0.040
375	0.083	20	0.070
400	0.083	20	0.17
450	0.083	40	0.20
250	0	50	1.0
250	0.042	30	0.20
250	0.083	30	0.040
250	0.21	30	0.020
250	0.32	30	0.020
250	1.0	30	0.0065

mixture consisting of 0.3 % butadiene, 30 % propene and 20 % H₂ balanced with He to a total flow rate of 50 mL/min. The catalyst was slowly heated with 1 °C/min to 300 °C. Meanwhile, the composition of the reaction gas was analysed every 15 min with an on-line gas chromatograph.

The turnover frequencies (TOFs) were expressed in number of converted butadiene molecules per second per metal surface atom. The number of converted butadiene molecules per second were calculated from the reactant and product concentrations measured by the GC at a given temperature. The number of metallic surface atoms was calculated from the size parameters of the Au@Pd@SiO₂ NRs obtained via TEM analysis. Herein, the nanorods were approximated to have a spherocylindrical shape with a surface area of $\pi \times D \times L$ and a volume of $1/12 \times D^2 \times (3L - D)$. The density (ρ) and van der Waals radius (r_{vdW}) of the metal atoms were corrected for the metal composition of the different AuPd@SiO₂ NRs samples as follows: $\rho_{AuPd} = \rho_{Au} \times X_{Au} + \rho_{Pd} \times X_{Pd}$ and $r_{vdW} = r_{vdWAu} \times X_{Au} + r_{vdWPd} \times X_{Pd}$. For the core-shell structures we assumed that the surface layer was only composed of Pd atoms. For the alloyed structures we assumed a mix of Au and Pd surface atoms with a ratio equal to the overall X_{Pd} and X_{Au} content.

Note: all data presented in this chapter were measured by using the same propylene gas bottle with purity of ≥ 99.5 % (grade 2.5, Linde, product code 4290105). We noticed that the Au@Pd@SiO₂ NRs were more active when using higher purity propylene (≥ 99.95 %, grade 3.5, Airliquide, product code P1717S10R0A001), which is possibly related to the higher H₂O and O₂ content in the lower purity propylene feed. To make a fair comparison between different samples, it is therefore important to perform all measurements with the same quality of propylene. To avoid that impurities in the gas feed affect the catalytic activity usage of a high purity gasses is recommended.

Characterization

Characterization of the size, composition and metal distribution of Au@Pd@SiO₂ NRs and Pd@SiO₂ NPs was done on a FEI Talos F200X electron microscope operated at 200 kV in High-angle annular dark-field (HAADF-STEM) imaging mode combined with Energy Dispersive X-ray Spectroscopy (EDX). The optical properties of the nanorods in solution (H₂O, MeOH or EtOH) were analysed with Visible Near Infrared (VIS-NIR) spectroscopy on a Bruker Vertex 70 FTIR/VIS spectrophotometer. The CTAB content of the unwashed and washed MCM-48 and Au@SiO₂ NRs samples was determined with TGA analysis. The TGA measurements were performed on a PerkinElmer balance (Pyris 1). The samples (typically 10 mg) were heated in 20 mL/min O₂ to 100 °C with 5 °C and kept at 100 °C for 30 min. Thereafter, the sample was heated with 5 °C to 600 °C. Inductively Coupled Plasma Atomic Emission Spectroscopy (ICP-AES) analysis was carried out to determine the metal concentration and composition of the Au@Pd@SiO₂ NRs dispersions. The ICP-AES experiments were carried out on PerkinElmer Optical emission Spectrometer Optima 8300 equipped with a PerkinElmer S10 Autosampler. Prior to the ICP analysis 10 μL Au@Pd@SiO₂ NRs in EtOH were centrifuged at 8000 rcf for 5 min, dissolved in 500 μL aqua regia (HNO₃, Sigma Aldrich, ≥99.999 trace metal basis and HCl, Fluka, for trace analysis) and diluted with 4.50 mL MQ H₂O to 10 % aqua regia in H₂O. Thereafter, the solution was centrifuged for 5 min at 15000 rcf (to remove remainders of the silica shell). The top 4.50 mL was then used for the ICP analysis.

6.3 Results

Preparation of the Au-Pd nanorod catalysts

The Au-Pd core-shell nanorods were prepared via colloidal synthesis, which enabled a precise control over the size, shape and composition. The colloidal synthesis was carried out on a relatively large, milligram scale to obtain a sufficient amount of Au@Pd@SiO₂ NRs for the catalytic testing. To this end, the metal overgrowth was carried out in an acidified aqueous solution in which the metal overgrowth was sufficiently slow to allow a homogeneous mixing of all reagents (see Chapter 3, Figure 3.8). By varying the Pd-precursor concentration, the Pd-shell thickness of the resulting Au@Pd@SiO₂ NRs was tuned. We minimized the differences in volume between the different batches of Au@Pd@SiO₂ by performing the metal overgrowth for the low Pd content samples directly on the Au-core. For the highest Pd content Au@Pd@SiO₂ NRs, we first etched the AuNRs to a smaller core-size prior to the metal overgrowth.

In Figure 6.1 the HAADF-STEM images and EDX maps of the resulting Au@Pd@SiO₂ NRs are shown. The atomic Pd fraction (X_{Pd}) and the number of atomic Pd-shell layers were 0.04, 0.08, 0.21 and 0.32, and 1, 2, 5 and 8, respectively. The HAADF-STEM images show that the NRs were homogeneous in size and shape. The EDX maps show a 2D projection of the elemental distribution of Au, Pd and Si in red, green and blue, respectively and clearly reveal the core-shell structure of the Au-Pd nanorods. Note that there is a slightly higher Pd content at the NR tips, which could be homogenized via mild thermal treatment at 250 °C in H₂ (see Figure 6.5a). The Si signal in the EDX

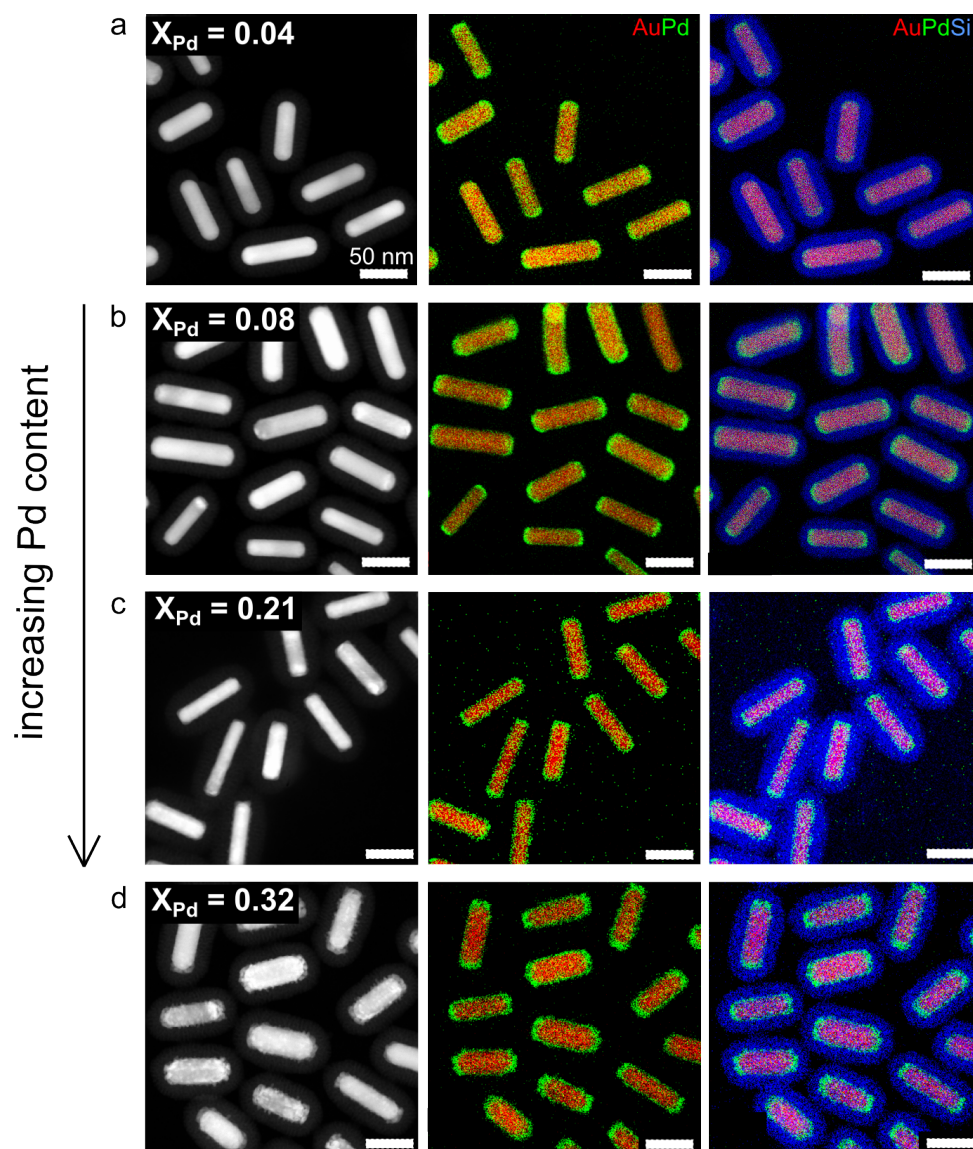


Figure 6.1: Monodisperse Au@Pd@SiO₂ NRs with increasing Pd content and Pd-shell thickness: X_{Pd} = 0.04, 0.08, 0.21 and 0.32 with 1, 2, 5, 8 atomic Pd shell layers (a-d). The left column of images are HAADF-STEM images. The middle and right column of images are EDX maps showing Au, Pd and Si in red, green and blue, respectively.

maps shows that each NR was encapsulated with a 18 nm thick mesoporous silica shell. The mesoporous silica shell protected the particles from deformation and sintering at the elevated temperatures needed in the subsequent catalytic and alloying experiments, whilst the mesopores ensured mass transport to the metal surface. We removed the organic template molecules from the mesopores by washing with an acidified ethanol solution, which removed most of the CTAB as shown in Figure 6.2. The size parameters and metal composition of the Au@Pd@SiO₂ NRs are listed in Table 6.3 and were obtained from TEM and ICP analysis. In Figure 6.3 we plotted the atomic Pd fraction as determined with ICP against the the Pd-precursor (Na₂PdCl₄) concentration present in the reaction

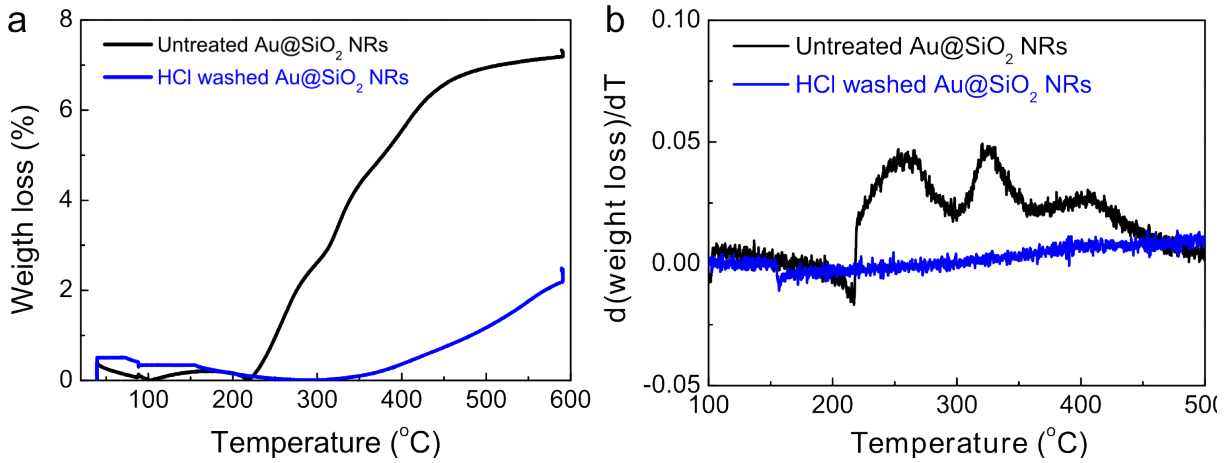


Figure 6.2: CTAB removal from the mesopores of silica coated AuNRs analyzed with TGA. a) Weight loss of untreated and 0.10 M HCl in EtOH washed Au@SiO₂ NRs. b) Derivative of the weight loss curves presented in a).

mixture during the metal overgrowth. The plot clearly shows that our colloidal synthesis approach enabled a precise control over the composition of the Au@Pd@SiO₂ NRs, and thus over the exact number of atomic shell layers.

Table 6.3: Sample details for the Au@Pd@SiO₂ NRs depicted in Figure 6.1. The average and corresponding standard deviations of the atomic Pd fraction determined with ICP, length, diameter and volume are indicated with X_{Pd} , L , D and V , respectively. The values were based on 50 measurements per sample. The $X_{Pd}=1.00$ sample is a reference sample containing spherical Pd NPs supported on silica (Aerosil300).

X_{Pd} (ICP)	Number of Pd-layers	L (nm)	D (nm)	V ($\cdot 10^4$ nm ³)
0.00	0	68 \pm 11	21 \pm 2	2.1 \pm 0.50
0.04	1	71 \pm 8	22 \pm 2	2.4 \pm 0.5
0.08	2	69 \pm 7	21 \pm 3	2.1 \pm 0.6
0.21	5	66 \pm 6	18 \pm 4	1.5 \pm 0.4
0.32	8	72 \pm 8	24 \pm 3	3.0 \pm 1.0
1.00	-	-	6.1 \pm 2.5	0.016 \pm 0.025

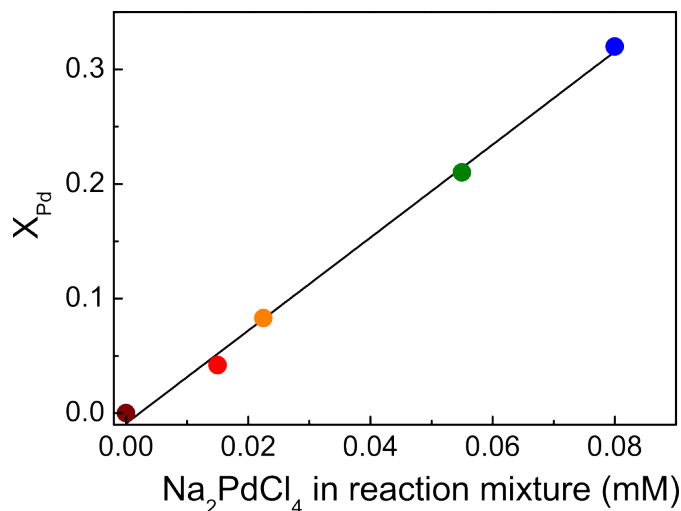


Figure 6.3: Synthesis of Au@Pd@SiO₂ NRs with a controllable atomic Pd fraction (X_{Pd}). X_{Pd} is plotted as a function of the Na_2PdCl_4 concentration present in the reaction mixture during the metal overgrowth. The Au and Pd content were determined with ICP. The brown, red, orange, green and blue points correspond to the Au@Pd@SiO₂ NRs with $X_{\text{Pd}}= 0, 0.04, 0.08, 0.21$ and 0.32 , respectively, and are shown in Figure 6.1. Note that for the sample with $X_{\text{Pd}}= 0.32$ the metal overgrowth was performed on etched Au@SiO₂ NRs. For all other samples unetched Au@SiO₂ NRs were used.

Alloying and thermal stability of the Au-Pd nanorods

Next, we investigated the alloying behaviour of the Au@Pd@SiO₂ NRs and identified the temperature range in which the metal structure changed from core-shell to alloyed. To this end, Au@Pd@SiO₂ NRs with a fixed Pd content of $X_{\text{Pd}}= 0.08$ were heated *ex situ* in H₂. In Figure 6.4a the EDX maps of the Au@Pd@SiO₂ NRs after thermal treatment are shown. From these EDX maps we analysed the core and shell diameter of 4 particles at each temperature and determined the degree of alloying (Figure 6.4b). Herein, the initial core-shell structure at 250 °C and fully alloyed structure at 450 °C had a degree of alloying of 0 and 1, respectively, where a degree of 1 corresponds to a equal core and shell diameter (see Chapter 5 for details on the data analysis). The alloying temperature was defined at a degree of alloying of 0.5 and was 382 °C for Au@Pd@SiO₂ NRs with $X_{\text{Pd}}= 0.08$, which is about 100 °C higher than the alloying temperature of Au@Ag@SiO₂ NRs with a similar composition [104]. The relatively high alloying temperature Au@Pd@SiO₂ NRs is likely due to the higher melting temperature of Pd compared to Au and Ag, which is 1555, 1064 and 962 °C for bulk crystals, respectively. The observed difference in alloying temperature between Au@Pd@SiO₂ NRs and Au@Ag@SiO₂ NRs is also in line with our *in situ* electron microscopy measurements reported in Chapter 4.

We observe in Figure 6.4c in which the aspect ratio (length/diameter) of the NRs is plotted versus the heating temperature that the Au@Pd@SiO₂ NRs did not deform upon thermal treatment. The excellent thermal stability of the Au@Pd@SiO₂ NRs is a combined effect of the stabilization by the silica shell, the relatively large particle volume, the low aspect ratio of the NRs (see Chapter 2) and the higher melting point of Pd. The high thermal stability of the AuPd@SiO₂ NRs made it therefore possible to change the

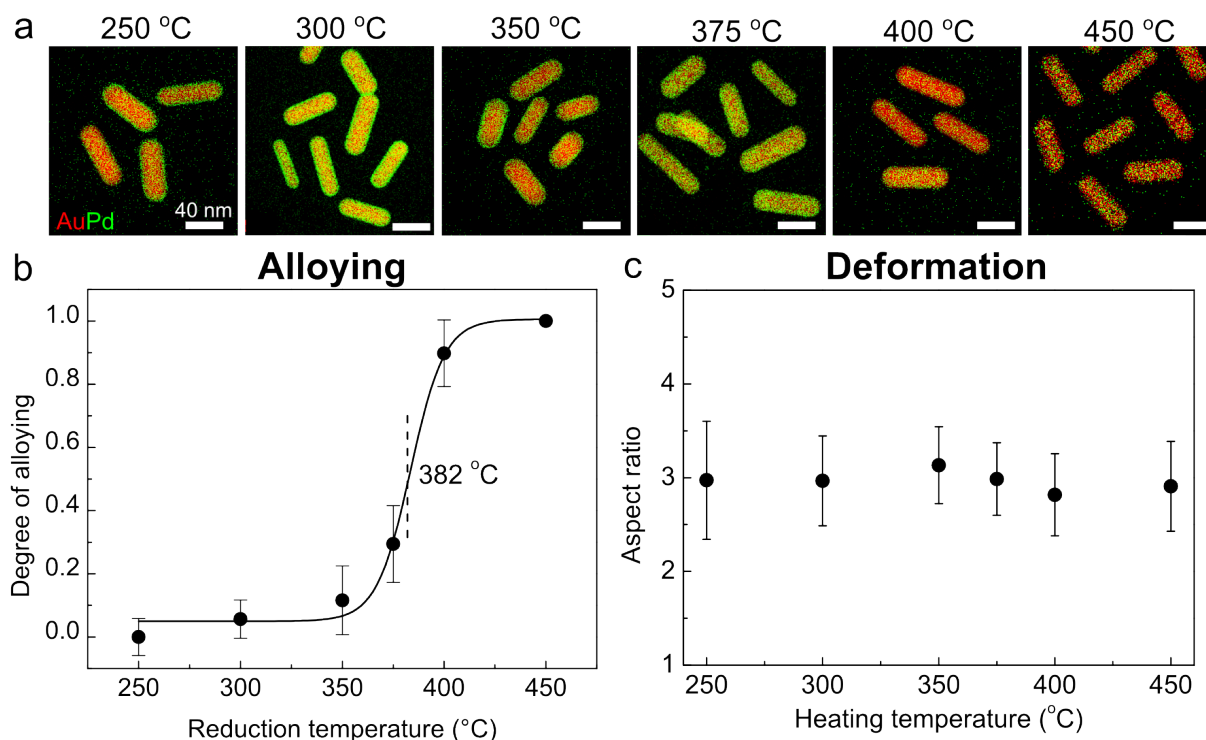


Figure 6.4: *Ex situ* TEM measurements on the alloying behaviour of Au@Pd@SiO₂ NRs with $X_{Pd} = 0.08$. a) EDX maps of the AuPd@SiO₂ NRs after they were heated at 250–450 °C for 1 h in hydrogen. The heating ramp was 2 °C/min. b) The degree of alloying deduced from the EDX maps plotted against the reduction temperature. The alloying temperature was estimated to be 382 °C at a degree of alloying of 0.5. c) The aspect ratio of the AuPd@SiO₂ NRs plotted versus the heating temperature.

metal distribution from core-shell to alloyed with full retention of the particle shape, even at temperatures as high as 450 °C.

Catalytic properties as a function of the metal distribution

We used the differently structured Au@Pd@SiO₂ NRs as displayed in Figure 6.4 to probe the catalytic activity as a function of the metal distribution in the selective hydrogenation of butadiene to butene in the presence of excess propene. To make the Au@Pd@SiO₂ NRs suitable for gas phase catalysis, the NRs were supported on a commercial silica support (Aerosil50). We used Au@Pd@SiO₂ NRs with an overall composition of $X_{Pd} = 0.08$ and a Pd-shell of 2 atomic layers.

In Figure 6.5a the EDX maps of single particles treated at 250, 350 and 450 °C are shown. Note that the treatment at 250 °C led to the formation of a Pd-shell with a homogeneous thickness over the whole particle, while the as-synthesized Au@Pd@SiO₂ NRs had a slightly higher Pd-content at the tips of the rod (Figure 6.1b). The yellow and red highlighted EDX maps were taken after treatment at 350 and 450 °C and show partial and full alloying, respectively. In Figure 6.5b we show the catalytic activity of the differently pretreated Au-Pd NRs as a function of the reaction temperature. The catalytic activity

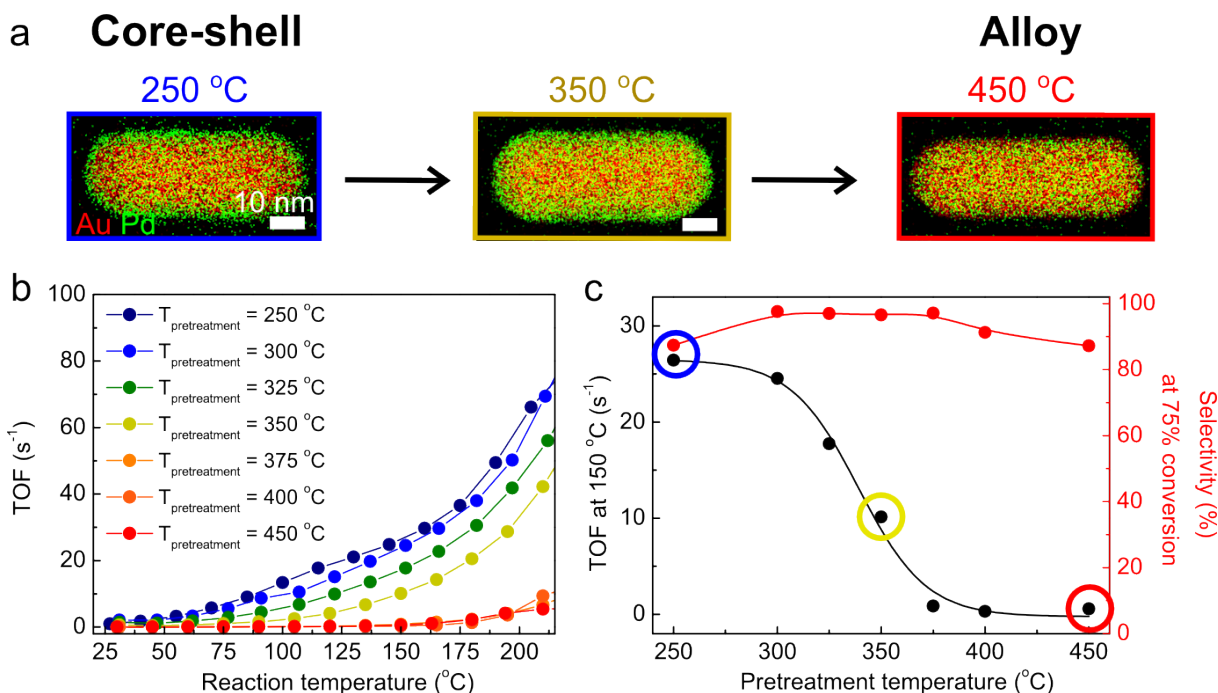


Figure 6.5: Catalytic activity of differently structured AuPd@SiO₂ NRs with $X_{Pd} = 0.08$ in the selective hydrogenation of butadiene. a) EDX maps showing the core-shell (250 °C), partially alloyed (350 °C) and alloyed (450 °C) metal distribution. b) Turnover frequency (TOF) expressed in the number of butadiene molecules converted per metal surface atom per second, of the differently structured AuPd@SiO₂ NRs as a function of the reaction temperature (30-225 °C). c) TOF and selectivity at a reaction temperature of 150 °C plotted versus the pretreatment temperature of the catalysts. For the catalytic tests 20-40 mg catalysts with a metal weight loading of 0.02-0.2 wt% was loaded (see Table 6.2). The reaction mixture consisted of 0.3 % butadiene, 30 % propene, 20 % H₂ and He to balance the flow rate to 50 mL/min.

is given as a turnover frequency (TOF) which is expressed as the number of butadiene molecules converted per second per metal surface atom. The TOFs of the Au@Pd@SiO₂ NRs pretreated below the alloying temperature (250-325 °C) are significantly higher than the NRs pretreated at and above the alloying temperature (375-450 °C). This difference in activity is more clearly visualized in Figure 6.5c where the TOF at a fixed reaction temperature of 150 °C is plotted as a function of the pretreatment temperature. The blue, yellow and red encircled points correspond to the likewise coloured EDX maps in Figure 6.5a. The TOF frequency of the core-shell structure was exceptionally high (TOF = 26 s⁻¹) and 45× higher than the alloyed structure (TOF = 0.58 s⁻¹) with the same metal composition ($X_{Pd} = 0.08$), showing the large impact of the atomic metal distribution on the catalytic activity. For the partially alloyed samples treated below the alloying temperature ($T_{Alloy} = 382$ °C, Figure 6.4) at 325-375 °C, partial mixing of Au into the Pd-shell already resulted in a strong activity drop.

The red data points in Figure 6.5c show the selectivity of the catalysts at 75 % conversion of butadiene. Herein, the selectivity was defined as the number of hydrogen molecules used for the conversion of butadiene to butene divided by the total number of consumed

Table 6.4: Summary of the catalytic activity and selectivity of AuPd@SiO₂ NRs (X_{Pd} = 0.08) with a core-shell, partially alloyed and fully alloyed metal structure. The TOF is given at a reaction temperature of 150 °C. The propane conversion and selectivity are given at a butadiene conversion of 75 %.

$T_{Pretreatment}$	Structure	TOF at 150 °C (s ⁻¹)	Propane conversion (%)	Selectivity (%)
250	core-shell	26	0.12	87
300	core-shell	24	0.024	98
325	partially alloyed	18	0.028	97
350	partially alloyed	10	0.032	97
375	partially alloyed	0.87	0.026	97
400	fully alloyed	0.31	0.085	91
450	fully alloyed	0.58	0.13	87

hydrogen molecules. In Table 6.4 we list both the propene conversion and selectivity at a butadiene conversion of 75%. Ideally, one would give the values at a butadiene conversion closer to 100% as more significant differences are expected at high conversion. However, under the conditions that we measured not all Au-Pd structures reached 100% conversion, which is why the selectivities are given at 75% conversion. Both the core-shell and (partially) alloyed structures had a very high selectivity towards butenes (87-98%), meaning that almost all the hydrogen was used to convert butadiene to butene. For all samples, less than 0.15% propene was converted to propane and no butane was observed in the product stream. The partially alloyed NRs exhibited the highest selectivity ($\geq 97\%$), whereas the selectivity dropped slightly below 90% upon alloying. Thus, in terms of selectivity and activity the core-shell structure heated at 250 and 300 °C had the most favourable properties: a TOF of 24 and 26 s⁻¹ with a selectivity of 98 and 87%, respectively.

We further investigated the selectivity of the differently structured Au-Pd@SiO₂ to the different C4-products: 1-butene, trans-2-butene, cis-2-butene and n-butane. The plot in Figure 6.6a shows the C4-product selectivity at a fixed reaction temperature of 225 °C as function of the pretreatment temperature. In Figure 6.6b-h the concentration of the C4-molecules over a reaction temperature from 30-300 °C are plotted for the Au-Pd NRs pretreated at 250-450 °C. For the core-shell structures 1-butene is the most formed product. Upon alloying an increase in the trans-2-butene and cis-butene fraction was observed. It is important to point out that for none of the AuPd NR catalysts butane formation was observed. Note that the butadiene signal goes up again above 250 °C, meaning that the catalyst deactivated, which could be due to metal redistribution or coking of the catalyst surface.

Dependence on the Pd shell thickness

From Figure 6.5 it is clear that the core-shell structure had superior catalytic properties and combined both a high selectivity and activity. We therefore further investigated the core-shell structures, and studied the influence of the shell thickness on the catalytic behaviour. Herein, NRs with 0, 1, 2, 5, 8 Pd shell layers and X_{Pd} = 0, 0.04, 0.08, 0.21, 0.32 were used and compared to a Pd reference catalyst (Figure 6.1). As it was not feasible to synthesize well-defined monometallic Pd rods, we prepared a catalyst consisting of

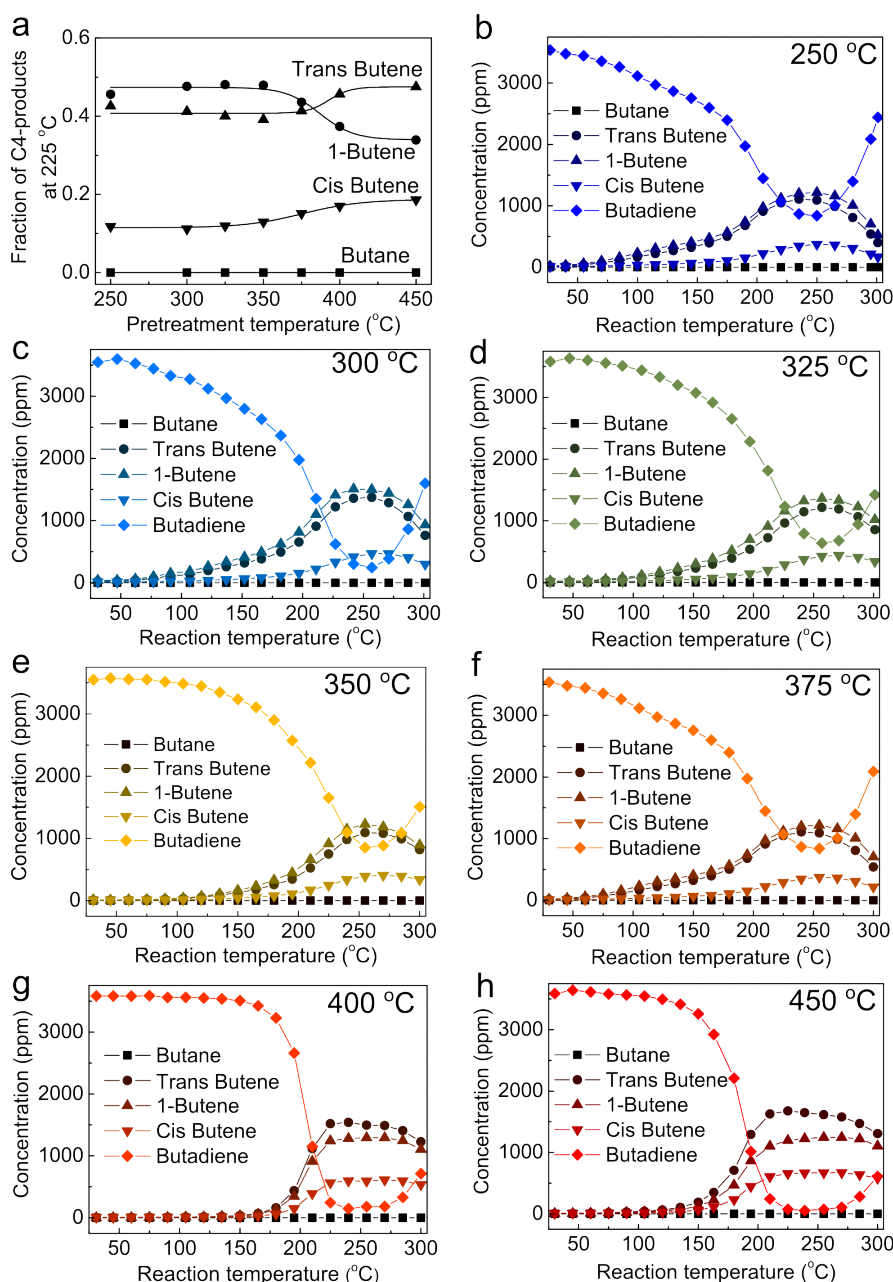


Figure 6.6: C4 product selectivity of differently structured AuPd@SiO₂ NRs with $X_{Pd} = 0.08$ in the selective hydrogenation of butadiene. a) Fraction of trans-2-butene, 1-butene and cis-2-butene at a fixed reaction temperature of 225 °C versus the pretreatment temperature of the Au@Pd@SiO₂ NRs. The lines are best fits to the experimental data. a-h) Concentration of C4 products as a function of the reaction temperature for Au@Pd@SiO₂ NRs pretreated at 250 (b), 300 (c), 325 (d), 350 (e), 375 (f), 400 (g) and 450 (h) °C in H₂. To make sure that the catalysts had similar conversions in the same temperature range the amount of AuPd@SiO₂ NRs loaded per run was varied as listed in Table 6.2. The reaction mixture consisted of 0.3 % butadiene, 30 % propene, 20 % H₂ and He to balance the flow rate to 50 mL/min.

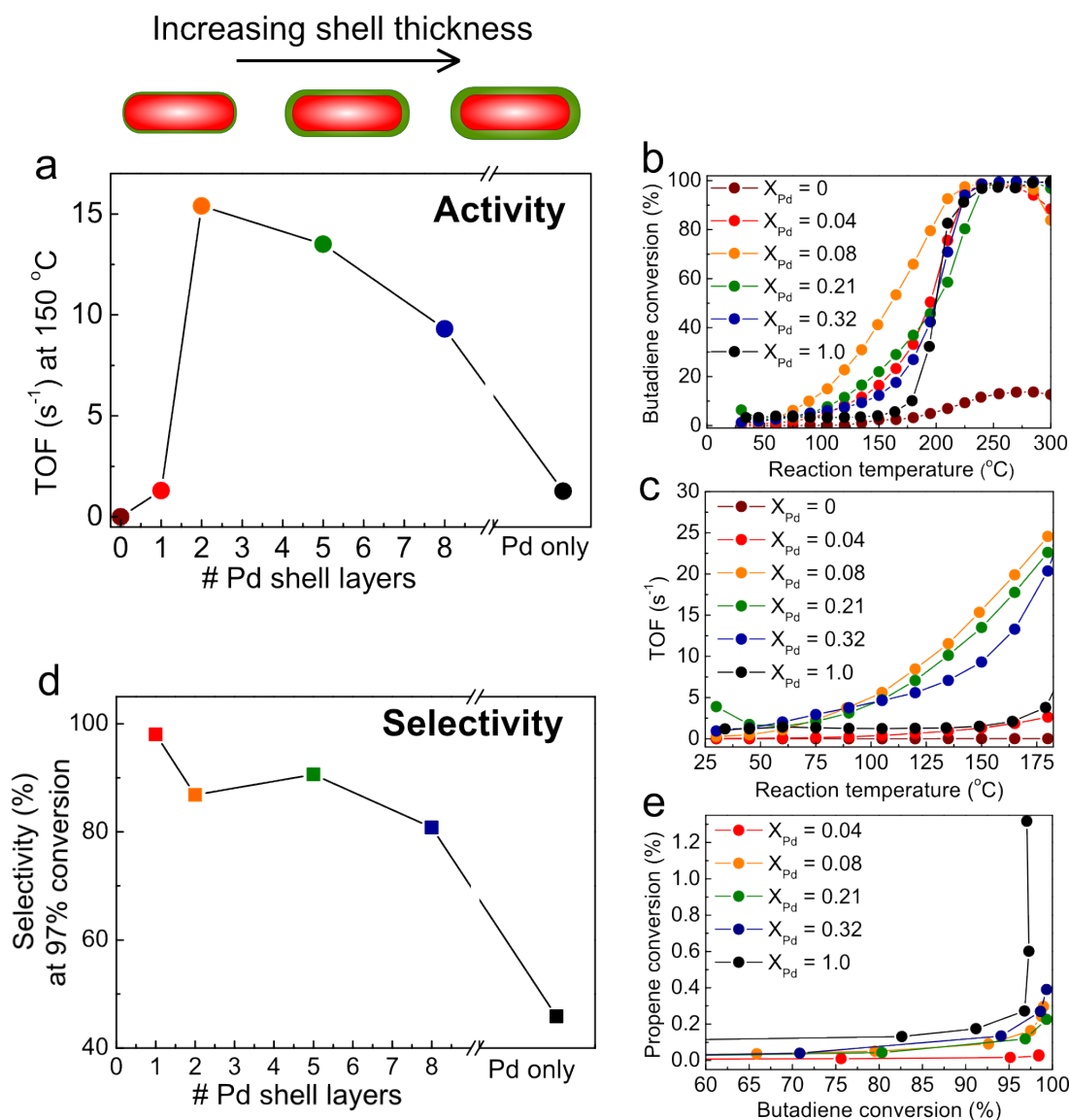


Figure 6.7: Catalytic activity and selectivity of core-shell Au@Pd@SiO₂ NRs with different Pd-shell thickness in the selective hydrogenation of butadiene. a) TOFs at a reaction temperature of 150 °C plotted versus the number of Pd-shell layers of Au@Pd@SiO₂ NRs with X_{Pd} = 0.04 (red), 0.08 (orange), 0.21 (green), 0.32 (blue) and a X_{Pd} = 1.0 Pd@SiO₂ reference catalyst (black). b) Butadiene conversion and c) TOF as a function of the reaction temperature. d) Selectivity at 97% butadiene conversion as a function of the Pd-shell thickness. e) Propene conversion plotted versus the butadiene conversion. The reaction mixture consisted of 0.3 % butadiene, 30 % propene, 20 % H₂ and He to balance the flow rate to 50 mL/min.

spherical Pd NPs with an average diameter of 6.1 nm on a silica support instead. A TEM image and XRD spectrum of the Pd reference catalyst are shown in Figure 6.8.

The catalytic performance of the bimetallic core-shell and monometallic Au and Pd catalysts are shown in Figure 6.7. In Figure 6.7a the catalytic activity (expressed as TOF) at a reaction temperature of 150 °C is plotted as a function of the number of atomic Pd-shell layers. All core-shell structures outperformed the monometallic AuNR

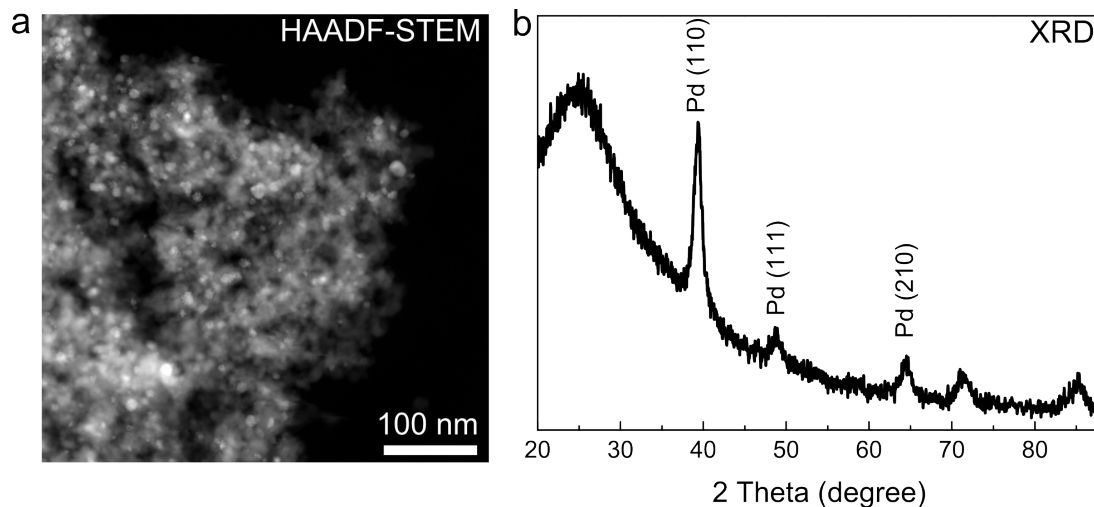


Figure 6.8: Palladium reference catalyst containing 4.8 wt% of 6.1 nm Pd nanoparticles on silica. a) HAADF-STEM image and b) XRD of the Pd@SiO₂ NP catalyst. The silica support was Aerosil300.

and Pd NPs considerably. The activity of the Au@Pd@SiO₂ NRs showed a non-monotonic dependence on the shell thickness, with an optimum at a Pd shell thickness of 2 atomic layers. Increasing the Pd thickness further caused a decrease in activity and the catalytic behaviour of the Au@Pd@SiO₂ NRs started to resemble those of pure Pd. The data in Figure 6.7a are based on the conversion plots and corresponding TOFs plotted in Figure 6.7b and c. Note that we diluted the catalysts such that they were all active in the same temperature range and had similar conversions (Figure 6.7b), which enabled a good comparison between the different catalysts. The corresponding TOFs were deliberately only calculated up to 180 °C before any of the samples had reached full conversion. From Figure 6.7c it is clear that the core-shell structures with 2, 5 and 8 layers had higher TOFs over the full temperature range compared to the NRs with only one or no Pd-shell layers, and compared to the pure Pd reference catalyst.

In Figure 6.7d the selectivity at high (97 %) butadiene conversion is plotted versus the number of Pd shell layers. We specifically chose to compare the catalysts at high conversion as selectivity of the different samples started to deviate significantly from each other (Figure 6.7e). Note that the AuNR sample is not shown as it did not reach 97 % conversion. The plot in Figure 6.7d clearly shows that all the core-shell structures exhibited a high selectivity and outperformed the pure Pd sample. Especially the core-shell NRs with 1 Pd layer had an exceptionally high selectivity of about 98 % and a propene conversion of 0.02 % at 97 % butadiene conversion. In Figure 6.7e the propene versus butadiene conversion is shown and in Table 6.5 the TOFs, propene conversion and selectivities are listed. The plot in Figure 6.7e shows that at high butadiene conversions (above 95 %) the undesired conversion of propene to propane steeply increased for the pure Pd sample, whereas the core-shell NRs reached up to full conversion without a strong increase in the propene conversion. Thus, the core-shell structures (especially with 2-8 layers) combined very high activities and selectivities, which enabled high butadiene

Table 6.5: Summary of the catalytic activity and selectivity of core-shell Au@Pd@SiO₂ NRs with X_{Pd} = 0.04 - 0.32, pure AuNRs and a pure Pd reference catalyst. The TOF is given at a reaction temperature of 150 °C. The propane conversion and selectivity are given at a butadiene conversion of 97 %.

X_{Pd}	# Pd-layers	TOF at 150 °C (s ⁻¹)	Propane conversion (%)	Selectivity (%)
0.0	0	0.016	-	-
0.04	1	1.3	0.021	98
0.08	2	16	0.15	87
0.16	5	13	0.12	90
0.32	8	9.3	0.22	84
1.0	-	1.3	1.3	45

conversions while having an very low (<0.3 %) propene conversion, which was not possible with their monometallic counterparts.

In Figure 6.9b-f we show the full overview of the catalytic data of the core-shell structures and the Pd-reference, where the butadiene, trans-2-butene, 1-butene, cis-2-butene and butane concentration are plotted as a function of the reaction temperature. In Figure 6.9a the fraction of the C4 products at a fixed reaction temperature of 225 °C is plotted versus the Pd composition of the catalyst. We chose to compare the catalysts at 225 °C as the concentrations of the reactants is high and the error in the fraction of C4 products small. The plot in Figure 6.9a shows a clear trend. For catalysts consisting of only Au or ≤ 2 Pd shell layers, 1-butene was the product which was formed the most. When increasing the shell thickness above 2 atomic Pd layers, trans-2-butene was the most formed product and its concentration increased with increasing Pd-shell thickness/content. Thus, the shell thickness also influenced the C4-selectivity.

6.4 Discussion

Particle size independent catalytic activity

The bimetallic NRs used in this study are quite large compared to the NPs in typical selective hydrogenation catalysts, containing NPs with diameter of 1-10 nm. However, when comparing the activity per surface atom of our NR based catalysts to much smaller AuPd and Au NPs as reported in literature, there are no significant differences. For instance, the TOF (at 60 °C) of spherical, alloyed AuPd NPs (X_{Pd} = 0.05) with a size of 2-3 nm is in the range of 0.001 to 0.1 s⁻¹ depending on the preparation method [99]. The TOF of our alloyed NRs (X_{Pd} = 0.08) at 60 °C is comparable: 0.04 s⁻¹. Likewise, the TOF (at 120 °C) of 3 nm Au NPs on silica is about 0.004 s⁻¹ [97, 245] and comparable to the the TOF of our AuNRs, which was 0.002 s⁻¹ at 120 °C. This indicates that the particle size is not a critical parameter, which is supported by earlier observations for pure Au [243] and Pd systems [240], where the catalytic activity was also particle size independent. Only when going to particle sizes below 2.5 nm the activity per surface atom decreases [250]. Thus, even though the NRs are much larger than the metal NPs in typical hydrogenation catalysts, the activity per surface atom is similar, which makes

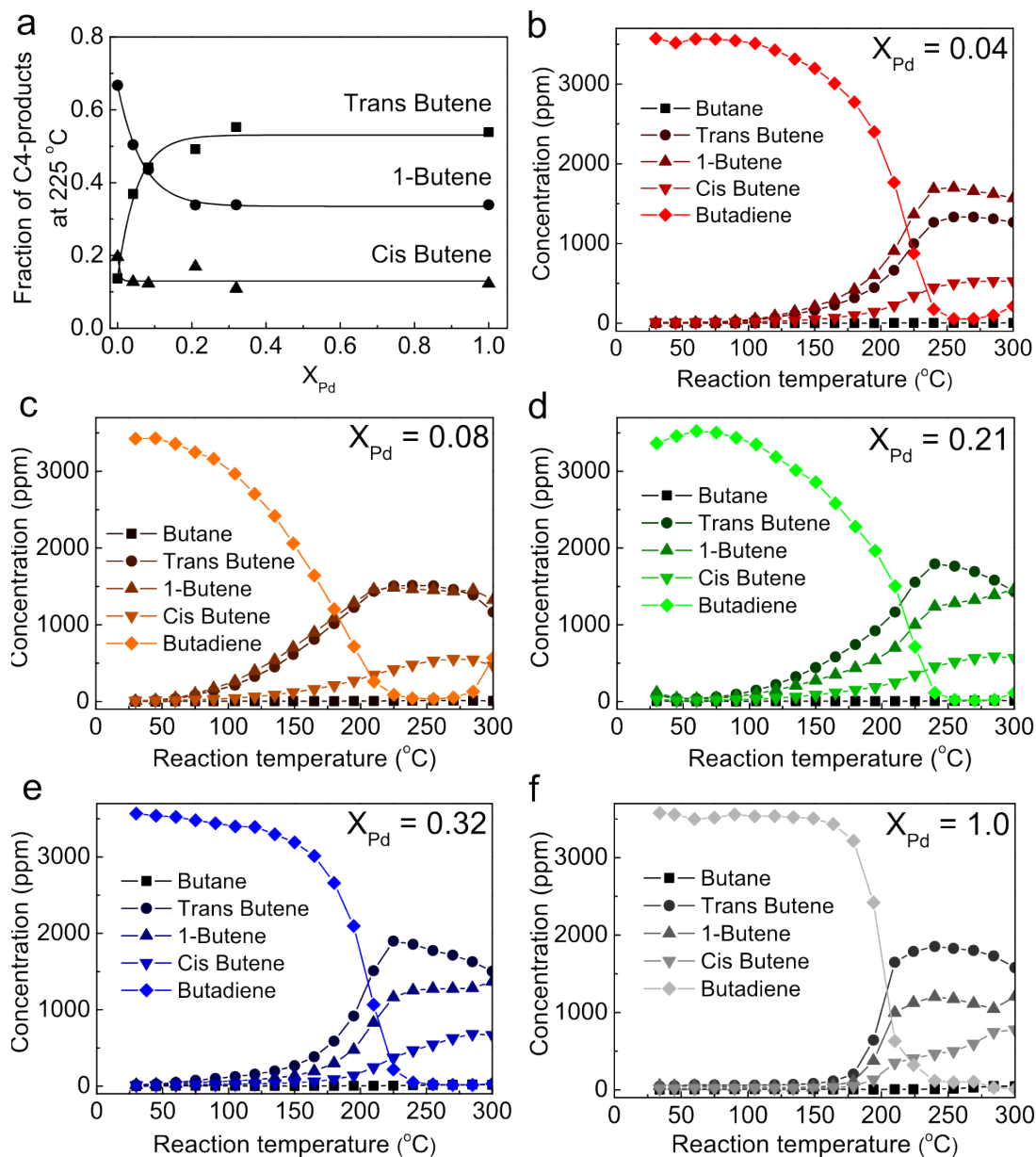


Figure 6.9: C4 product selectivity of core-shell Au@Pd@SiO₂ NRs with different Pd-shell thickness in the selective hydrogenation of butadiene. a) Fraction of trans-2-butene, 1-butene and cis-2-butene at a fixed reaction temperature of 225 °C versus the composition of the Au@Pd@SiO₂ NRs. The lines are best fits to the experimental data. b-f) Concentration of C4 products as a function of the reaction temperature for Au@Pd@SiO₂ NRs with X_{Pd} = 0.04 (b), 0.08 (c), 0.21 (d), 0.32 (e) and Pd@SiO₂ NPs with X_{Pd} = 1.0 (f). All samples were pretreated at 250 °C in H₂. The reaction mixture consisted of 0.3 % butadiene, 30 % propene, 20 % H₂ and He to balance the flow rate to 50 mL/min.

the NR based catalysts ideal model systems to bridge the gap between surface science studies performed on large, single-crystalline surfaces and more industrial, less defined nanoparticles systems.

Although the activity of Pd catalysts is not size dependent, it was reported to be very sensitive to the orientation of the surface facets [240]. Pd(110) is about one order of magnitude more active compared to Pd(111) [240, 250]. Interestingly, our NRs predominately have (110) and (100) facets, running along the length of the rods [21]. As the Pd-shell is epitaxially grown onto the Au-core (Chapter 2), the Pd-surface is mostly composed of Pd(110) and (100) facets, which could partially explain the exceptionally high activity of the Pd-shell Au-core nanorods.

The impact of the metal distribution

The plots in Figure 6.7c shows that the activity of core-shell NRs was much higher compared to the alloyed NRs of the same size and composition. When comparing the Au@Pd@SiO₂ NRs to the highest TOF reported for spherical AuPd NPs by Kolli *et al.* (0.11 s⁻¹ at 60 °C), the core-shell NRs have a ~50× higher TOF of 5 s⁻¹ at the same temperature. This shows that the metal distribution is a very important parameter vary as well and the core-shell structure is a promising alternative to alloys. It would therefore be worthwhile to realize core-shell structures in small, more spherical NPs as well.

The metal distribution also affected the selectivity (Figure 6.5c). Surprisingly, the partially alloyed structures had a higher selectivity compared to fully alloyed NRs; 97 versus 87 %, respectively. For fully mixed AuPd alloy NPs the selectivity typically increases with a decreasing Pd fraction [246, 247], which is ascribed to the absence of atomic Pd surface clusters [99]. Our data, however, show that a Pd surface diluted with a few Au atoms on an Au-core is more selective than a fully alloyed particle with 92 % of Au surface atoms. This means that it is too simplistic to only consider the outer surface layer of bimetallic nanoparticles. To understand and ultimately predict the behaviour of bimetallic catalysts, the sub-surface layers and thus the atomic structure of the entire particle, should be taken into account as well.

The C4 selectivity of Au and AuPd NRs was both structure and composition dependent. The influence of the structure is most clear from Figure 6.6a, where core-shell and alloyed structures with a fixed Pd-content make 1-butene and trans-2-butene as the main product, respectively. The composition dependence is clear from the plot in Figure 6.9a. A thick Pd shell and/or Pd content >8 % leads to preferential production of trans-2-butene, whereas pure AuNRs and core-shell structures with ≤8 % predomently make 1-butene. Such composition dependent behaviour was also observed for spherical, 3 nm Au and AuPd NPs [97, 99, 245, 246], where trans-2-butene and 1-butene are the main products for bimetallic AuPd and monometallic Au NPs, respectively.

Shell thickness dependent catalytic behaviour

The activity of the core-shell structures showed a non-monotonic dependence on the shell-thickness (Figure 6.7a), suggesting that not only the surface atoms but also the sub-surface layers determine the catalytic properties. The difference in catalytic behaviour of Pd surface atoms on Au compared to Pd surface atoms of pure Pd NPs could be related to quantum mechanical effects [106, 248] and/or due to lattice strain [249]. In this case, the latter is probably less important as the lattice mismatch between Au and Pd is only 4 %. It is more likely that the electronic properties of the shell material

are changed, as the underlying Au will cause an up-shift of the d-band centre of the Pd atoms [106]. Changes in the electronic structure of the surface atoms typically lead to different adsorption energies and thus to an altered catalytic activity as well [251]. Indirect evidence for such electronic effects can be deduced from the product selectivity as a function of the Pd content as plotted in Figure 6.9a. With increasing Pd shell thickness the product selectivity changed from 1-butene to trans-2-butene. It is known that product selectivity is related to the electronegativity of the metal, where the fraction of 1-butene increases with increasing electronegativity [252]. As thin Pd layer on Au is likely to be more electronegative, this explains why thin, ≤ 2 atomic Pd layered core-shell NRs preferentially produced 1-butene and the fraction of trans-2-butene increased with increasing shell thickness. Currently, Density Functional Theory (DFT) calculations are ongoing to study the electronic coupling between the Pd-shell and Au-core atoms in detail.

Recommendations for future work

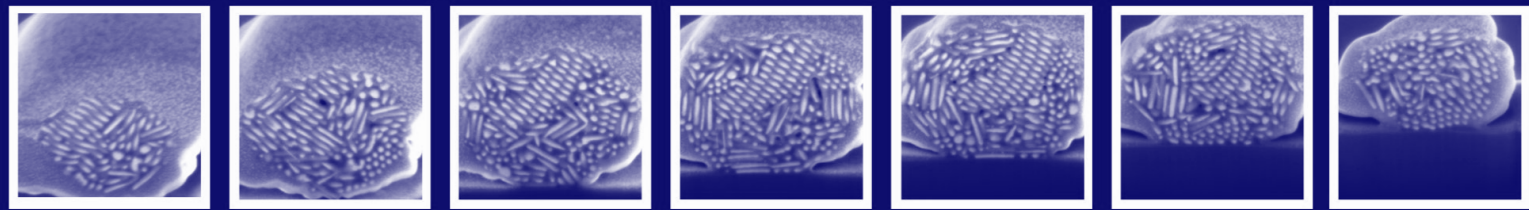
It would be worthwhile to repeat the alloy experiments presented in section 6.3.3 with higher wt% catalysts such that 100 % conversion is reached. In this way, the selectivity at full butadiene conversion can be determined since larger differences in selectivity are expected close to and at full conversion. The influence of the Pd-content on the catalytic activity and selectivity of alloyed AuPd NRs should also be investigated, despite the fact that alloyed NRs are less promising catalysts compared to the core-shell structures. We expect to see an increase in activity and decrease in selectivity when increasing the Pd content of the alloyed NRs, as observed for spherical AuPd NPs [99, 246]. Finally, the catalytic activity of the Pd-core shell and alloyed structures could be probed as a function of the partial and butadiene pressure to learn more about the reaction mechanism and the rate determining step in the selective hydrogenation of butadiene. A similar study was carried out for Au NPs by the group of C. Louis [244], but, to the best of our knowledge, it has not been carried out for bimetallic AuPd catalysts.

6.5 Conclusions

In this chapter we showed that the metal distribution of bimetallic AuPd NPs has a large impact on the catalytic properties of selective hydrogenation catalysts. By making use of a well-defined, colloidal synthesized model system consisting of precisely tunable single-crystalline AuPd core-shell and alloyed NRs, we correlate the catalysts' structural and catalytic properties in the selective hydrogenation of 1,3-butadiene to butene in the presence of excess propene. We showed that core-shell AuPd NRs are about 45 times more active compared to their alloyed counterparts, while maintaining an excellent selectivity. In addition, we demonstrated that the catalytic activity and selectivity of Au-core Pd-shell NRs is sensitive to the exact thickness of the metal shell, where a shell thickness of 2 atomic layers was found to be optimal. The observed shell-thickness dependent behaviour is most likely due to electronic effects, where a shift of the d-band center of the Pd shell-atoms could lead to altered adsorption energies of butadiene.

Acknowledgements

The work in this chapter was carried out together with Liselotte Olthof and in collaboration with Giorgio Totarella. Rolf Beerthuis is thanked for advice on the catalytic tests. Jan-Willem de Rijk is acknowledged for technical support and maintenance of the catalytic equipment. Relinde Moes van Dijk is thanked for performing the ICP-AES analysis.



3D real-space characterization of colloidal assemblies

7

Abstract

Insight in the structure of nanoparticle assemblies up to a single particle level is key to understand the collective properties of these assemblies, which critically depend on the individual particle positions and orientations. However, the characterization of large, micron sized assemblies containing small, 10-500 nanometer, sized colloids is highly challenging and cannot easily be done with the conventional light, electron or X-ray microscopy techniques. Here, we demonstrate that focused ion beam-scanning electron microscopy (FIB-SEM) tomography in combination with image processing enables quantitative real-space studies of ordered and disordered particle assemblies too large for conventional transmission electron tomography, containing particles too small for confocal microscopy. First, we demonstrate the high resolution structural analysis of spherical nanoparticle assemblies, containing small anisotropic gold nanoparticles. Herein, FIB-SEM tomography allows the characterization of assembly dimensions which are inaccessible to conventional transmission electron microscopy. Next, we show that FIB-SEM tomography is capable of characterizing much larger ordered and disordered assemblies containing silica colloids with a diameter close to the resolution limit of confocal microscopes. We determined both the position and the orientation of each individual (nano)particle in the assemblies by using recently developed particle tracking routines. Such high precision structural information is essential in the understanding and design of the collective properties of new nanoparticle based materials and processes.

7.1 Introduction

The collective properties of particle ensembles are highly structure sensitive and can deviate significantly from the properties of the single nanoparticles [11, 253, 254]. Depending on the interparticle spacing, and local and global symmetry, the plasmonic, magnetic or electronic coupling between the particles can be tuned, giving rise to altered optical, catalytic and magnetic behavior [11, 62, 83, 255, 256]. The final 3D structures of colloidal assemblies also provide insight in the assembly process and the interactions between the colloidal particles. For example, assembled structures formed in or out of equilibrium contain information on the phase behaviour or on the glass transition or aggregation, respectively, of the colloidal particles during the assembly [257–261].

Various scattering- and microscopy techniques have been used to access the structural properties of these particle assemblies. While scattering techniques can directly probe long-range periodic order averaged over macroscopic volumes [262], microscopy techniques can reveal local structures at a single particle level in real-space [263–265]. Microscopy studies therefore provide insight in the presence of defects [266, 267], which strongly influence the material properties and which are generally very hard to determine by scattering techniques, as these usually average over large numbers of particles and have a strong bias in detecting order over local disorder.

Depending on the applied radiation source - X-rays, electrons or visible light - particle assemblies can be studied at different length scales, ranging from ångströms to micrometers. X-ray microscopy techniques enable real-space imaging of the material's local structure [268, 269], where the large penetration length of X-rays makes it possible to study thick and opaque colloidal assemblies in 3D [270]. Nowadays, the spatial resolution of X-ray microscopy can be as precise as 10-30 nm with a sample thickness of 0.05-20 μm depending on the X-ray energy and the material properties of the sample [271]. However, the image acquisition can only be carried out at synchrotron facilities and irradiation damage can occur, especially in soft polymer based systems [272].

For a significantly higher resolution (0.1-0.5 nm) electron microscopy can be used to obtain real-space structural information. Scanning electron microscopy (SEM) allows imaging of the assembly's exterior and provides information on the surface structure, whereas transmission electron microscopy (TEM) and, in particular, transmission electron tomography in combination with particle fitting algorithms can reveal the positions and orientations of the particles in the interior of colloidal assemblies [265, 273–276]. Most materials science systems analysed by transmission electron tomography are investigated in STEM-HAADF imaging mode (scanning transmission electron microscopy - high angle annular dark field), where the so-called Z-contrast stems from the difference in (high-angle) scattering power of the elements constituting the sample. When there is a sufficient difference in Z-contrast between two types of colloidal particles, 3D characterization of binary systems becomes feasible as well [265]. An important limitation in the quantitative interpretation of tomography data is the fact that it is not possible to image the object of interest over the full 180° range. This so-called missing wedge problem causes artefacts in the reconstruction. In addition, the limited penetration depth of the electron beam in larger assemblies and high Z-contrast materials limits the maximum assembly size that can be quantitatively characterized to about 500 nm [274, 275, 277].

Light microscopy techniques, on the other hand, can have larger penetration depths [278]. When the sample is refractive index matched and a dye is incorporated in the particles, confocal microscopy is capable of resolving large assemblies of >500 nm colloids in 3D [264, 279, 280]. The sample thickness can be up to $300 \mu\text{m}$ for high numerical aperture (NA) objectives [281]. The particle positions of both spherical and anisotropic particles can be extracted using multiple particle fitting and tracking algorithms [282–284]. In order to improve the resolvability of the particles, image restoration techniques using the point spread function (PSF) of the microscope can be used [285]. The advent of super-resolution techniques, such as stimulated emission depletion (STED), have made it possible to image colloidal assemblies at even higher resolutions. The axial (Z -direction) resolution is still limiting but has been brought down recently below 100 nm, allowing particles sizes of 200 nm to be resolved in 3D [263, 286, 287]. However, STED microscopy requires better dyes and is sensitive to refractive index mismatch. In practice, large confocal-like volumes are not easily imaged with STED either. This means that neither X-ray nor conventional electron nor light microscopy are able to image large sample volumes of (non-index matched) materials at a nanometer resolution.

Focused ion beam - scanning electron microscopy (FIB-SEM) tomography does offer the unique opportunity for high resolution 3D real-space imaging of hundreds to thousands of cubic microns with a resolution down to a few nanometers [288]. FIB-SEM relies on a dual beam approach, using both a focused ion and electron beam. Herein, both beams usually have their own column and lens system, allowing them to operate independently. The FIB scans a focused beam of gallium ions onto the sample surface. The momentum transfer of the gallium ions results in a sputtering process called milling. Precision milling results in trenches at predetermined locations, allowing the SEM to record high resolution images of sections of the material of interest. Consecutive slices as thin as 3 nm can be milled away by the FIB, while the SEM records images in between the milling. This process is called FIB-SEM tomography. Successful examples of FIB-SEM tomography are found in many disciplines and it has been applied to *e.g.* inorganic nanomaterials [62, 289, 290], photonic crystals [291], biological tissue [292, 293] and porous geological materials [293, 294].

In this work, we demonstrate the use of FIB-SEM tomography in the 3D characterization of colloidal assemblies with nano- to micrometer sized colloidal particles. We show that for assemblies of gold nanorods, TEM tomography is limited to assemblies composed of less than 100 particles, whereas FIB-SEM tomography can be used to characterize assemblies of more than 1000 particles. In addition, we show the use of FIB-SEM tomography in the structural analysis of disordered and ordered assemblies composed of single and binary species of $\sim 0.5 \mu\text{m}$ sized silica particles. We compare this to confocal microscopy in combination with image restoration and discuss the advantages of FIB-SEM tomography.

7.2 Experimental

All chemicals were used as received without further purification. Hexadecyltrimethylammonium bromide (CTAB, >98.0%) and sodium oleate (NaOL, >97.0%) were purchased from TCI America. Hydrogen tetrachloroaurate trihydrate ($\text{HAuCl}_4 \cdot 3\text{H}_2\text{O}$) and sodium hydroxide (98%) were purchased from Acros Organics. Butylamine (99.5%), L-Ascorbic Acid (BioXtra, $\geq 99\%$), cyclohexane ($\geq 99.8\%$), dextran (average molecular weight 1,500,000–2,800,000), hydrochloric acid (HCl, 37 wt% in water), octadecyltrimethoxysilane (OTMS, 90%), silver nitrate (AgNO_3 , $\geq 99\%$), sodium borohydride (NaBH_4 , 99%), sodium silicate solution ($\geq 27\%$ SiO_2 basis, Purum $\geq 10\%$ NaOH), tetraethyl orthosilicate (TEOS, 98%), sodium dodecyl sulfate (SDS $\geq 99\%$), sodium citrate tribasic dehydrate, polyvinylpyrrolidone (PVP, $M_w=10,000 \text{ g mol}^{-1}$), rhodamine B isothiocyanate (RITC, mixed isomers), (3-aminopropyl)triethoxysilane (APTES, 99%), Igepal CO-520, ammonium hydroxide solution (ACS reagent, 28.0–30.0% NH_3 basis) and *N,N*-dimethylformamide (DMF) were purchased from Sigma-Aldrich. Absolute ethanol was purchased from Merck. Ultrapure water (Millipore Milli-Q grade) with a resistivity of 18.2 $\text{M}\Omega$ was used in all of the experiments. All glassware for the AuNR and gold core synthesis was cleaned with fresh aqua regia (HCl/ HNO_3 in a 3:1 volume ratio), rinsed with large amounts of water and dried at 100 °C before use.

Synthesis of silica coated gold nanorod assemblies

The preparation of the gold nanorod based assemblies consisted of four steps: colloidal synthesis of high aspect ratio AuNRs (I), silica coating (II), OTMS coating (III) and self-assembly into spherical ensembles (IV).

The synthesis of high aspect ratio AuNRs was done according to the procedure by Ye *et al.* [13]. The growth mixture consisted of CTAB (7.0 g), sodium oleate (1.23 g), Milli-Q (MQ) H_2O (250 mL), AgNO_3 (9.6 mL, 10 mM), HAuCl_4 (250 mL, 1.0 mM), HCl (37 wt%, 4.8 mL), ascorbic acid (1.25 mL, 0.064 M) and gold seeds (0.40 mL). The seed solution was prepared by adding an icecold NaBH_4 in H_2O solution (1.0 mL, 0.0060 M) to a mix of CTAB (10 mL, 0.10 M) and HAuCl_4 aqueous solution (51 μL , 50 mM). The resulting rods were centrifuged for 25 min at 8,000 g, washed with water and re-dispersed in 30 mL 5.0 mM CTAB water ($\lambda_{LSPR} = 1250 \text{ nm}$, Ext = 4.8, $\sim 40 \text{ mg L}^{-1}$). The resulting AuNRs had a length of 119 nm (11% PDI, TEM) and diameter of 16 nm (13% PDI, TEM).

The thin silica coating was carried out as follows: to the AuNRs (1.0 mL, $\lambda_{LSPR} = 1250 \text{ nm}$, Ext = 4.8) sodium silicate (0.15 mL, 0.54 wt% SiO_2 , 0.12 M) was added while stirring vigorously. The mixture was stirred for 45 minutes at room temperature after which the rods were washed with water and ethanol, and re-dispersed in ethanol (200 μL , $[\text{Au}] \approx 200 \text{ mg L}^{-1}$).

To disperse the rods in an apolar solvent like cyclohexane the silica shell was made hydrophobic by coating it with octadecyltrimethoxysilane (OTMS). To this end, the silica-coated AuNR dispersion (750 μL) was diluted with ethanol (1.75 mL) to which OTMS (250 μL) and butylamine (125 μL) were added. The mixture was sonicated for 2 h at 30–40 °C. Thereafter, the reaction mixture was centrifuged at low speed (100 rcf for 5 min),

washed with toluene, centrifuged at 7,000 rcf for 10 min, washed twice with cyclohexane (2.0 mL) and redispersed in cyclohexane (250 μL , $[\text{Au}] \approx 600 \text{ mg L}^{-1}$).

The spherical $\text{SiO}_2\text{@AuNR}$ supraparticles were made *via* emulsification of an apolar particle dispersion in a larger polar phase [283]. The polar phase consisted of dextran (400 mg) and sodium dodecyl sulfate (SDS) (50 mg) dissolved in H_2O (10 mL). The apolar phase consisted of cyclohexane (200 μL) containing OTMS-functionalised silica-coated AuNRs ($[\text{Au}] \approx 600 \text{ mg L}^{-1}$). The emulsification was done by shortly pre-mixing the apolar and polar phase in a vortex shaker after which it was placed in a sonication bath for 1 minute. Afterwards, the vial was covered with parafilm containing several small holes and the cyclohexane droplets in the emulsion were slowly dried overnight by shaking in an orbital shaker (IKA KS260 basic). The resulting particles assemblies were collected with centrifugation (500 rcf for 15 min), washed with H_2O (8 and 2 mL), and redispersed in H_2O (500 μL).

Synthesis of colloidal silica assemblies

Monodisperse 531 nm core-shell silica colloids with gold and fluorescent cores were synthesized. 15 nm gold cores were grown using the inverse sodium citrate reduction method [295, 296]: HAuCl_4 (3.4 mL, 25 mM) was added to a boiling solution of sodium citrate in water (345 mL, 1.0 mM) under constant vigorous stirring. After 15 minutes, water (155 mL) and sodium citrate solution (5 mL, 2.2 mM) were added to the obtained deep red solution. After reheating and boiling for an additional 10 minutes the solution was cooled down to 90 $^\circ\text{C}$. Growth of the seeds to 30 nm was performed in four steps using a kinetically controlled seeded growth procedure [297]: for every growth step sodium citrate (1.7 mL, 120 mM) and HAuCl_4 (1.7 mL, 50 mM) were added followed by 60 minutes stirring at 90 $^\circ\text{C}$. 100 mL of the obtained solution of gold nanoparticles was functionalized with polyvinylpyrrolidone (PVP) [296, 298] by the addition of PVP (5 mL, 10 mM, $M_w = 10,000 \text{ g mol}^{-1}$) and 16 hours stirring. The functionalized particles were transferred to ethanol by centrifugation (10 min, 15,000 g) followed by redispersion in ethanol (100 mL).

Fluorescent rhodamine B labeled cores with a diameter of $\sim 45 \text{ nm}$ were synthesized using a reverse micro-emulsion method [299]. Rhodamine B isothiocyanate (RITC) was coupled to (3-aminopropyl)triethoxysilane (APTES) prior to the synthesis by mixing RITC (6.0 mg), absolute ethanol (500 μL) and APTES (12.0 μL) and stirring for 5 hours. The reverse micro emulsion was prepared by mixing cyclohexane (50 mL), Igepal CO-520 (6.5 mL), tetraethyl orthosilicate (TEOS, 400 μL) and fluorophore-APTES complex (50 μL). Particle growth was initiated by the addition of ammonia (750 μL) and after homogenization the solution was stored for 24 hours. The cyclohexane was removed by rotary evaporation under reduced pressure and the obtained pink viscous liquid was diluted in dimethylformamide (10 mL) and ethanol (10 mL) to obtain a clear pink solution.

Next, in two separate reactions, the gold and fluorescent cores were coated with a non-fluorescent silica to obtain a total diameter of $\sim 200 \text{ nm}$ using a seeded growth procedure based on the Stöber method [300]. After cleaning *via* repeated centrifugation and redispersion in ethanol, the weight fractions of both solutions were determined, which were used to prepare a 1 to 100 (gold to fluorescent core) mixture in ethanol. Further

silica growth was performed to obtain particles with a total diameter 531 nm ($<2\%$ polydispersity index (PDI), 100 particles, transmission electron microscopy), after cleaning by repeated centrifugation and redispersion in ethanol to remove small silica spheres caused by secondary nucleation.

396 nm monodisperse core-shell silica colloids with a fluorescent core were synthesized in the following way. First, using a reverse microemulsion method, a silica core of about ~ 50 nm was synthesized [299]. Next, using the seeded Stöber growth method [300], a fluorescein isothiocyanate doped silica shell was grown around the core to a diameter of ~ 200 nm, followed by two silica shells without dye, arriving at a total diameter of 396 nm (1% PDI, static light scattering).

For the assembly of a colloidal crystal of the 531 nm silica particles, an adaption at elevated temperature of the method by Jiang *et al.* [301] was used to speed up the evaporation process. A cover glass (#1.5H) was placed under a small angle of $\sim 5^\circ$ in a particle in ethanol dispersion (8 mL, 1 v%) inside a 20 mL vial. Together with a 100 mL beaker filled with ethanol the vial was placed in a 50°C preheated oven (RS-IF-203 Incufridge, Revolutionary Science) and covered with a large beaker placed upside down. After 16 hours the cover glass was removed from the dispersion and a crystal had formed on the cover glass. Any particles sticking to the back of the cover glass were removed by wiping it with an ethanol soaked tissue.

Transmission electron tomography

The transmission electron microscopy (TEM) tomography was performed on a FEI Talos F200X operated at 200 kV in STEM-HAADF (scanning transmission electron microscopy - high angle annular dark field) imaging mode. A droplet of aqueous dispersion containing the AuNR assemblies was dried on a special tomography copper grid with parallel bars and a R2/2 Quantifoil film (Electron Microscopy Sciences). The tomography grid was placed in a high tilt holder (Fischione, FP90997/19 tomography holder). The sample was tilted from -70° to $+70^\circ$ with a tilt step of 2° . The tilt images were recorded with 2048×2048 pixels per image, 0.24 nm per pixel, a dwell time per pixel of $1.40 \mu\text{s}$ and a total frame time of 6.37 s. The camera length of the HAADF-STEM detector was set to 160 mm. The probe current was 40 pA. Data processing, comprising alignment of the tilt-images *via* cross-correlation and subsequent reconstruction using a simultaneous iterative reconstruction technique (SIRT) algorithm (100 iterations), was carried out in TomoJ (version 2.31) [302].

FIB-SEM tomography

The AuNR assemblies dispersion was drop casted on silicon wafer, which was placed on top of an aluminium SEM stub and connected with a conductive carbon tape. The colloidal crystal and binary glass were first infiltrated with a resin to fill the air pockets between the particles. To this end, the colloidal crystal and binary glass were embedded in resin (Lowicryl HM20) and cured overnight in an oven at 65°C . The cover glasses with the colloidal crystal and the binary glass were attached on an aluminum SEM stub with carbon tape. To prevent charging of the samples under the electron beam, a conductive

pathway was created by bridging the top of the cover glass and the stub with a strip of carbon tape. Additionally, the colloidal crystal and binary glass were coated with a 5 nm thick layer of platinum, using a Cressington HQ280 sputter coater.

The FIB-SEM tomography of the AuNR assembly was performed in a Helios Nanolab G3 UC FIB-SEM (Thermo Fisher Scientific) under high-vacuum conditions (10^{-6} mbar). *In situ* Pt deposition (~ 100 nm thick) was accomplished across an AuNR supraparticle by ion beam induced deposition prior to the tomography routine. Subsequently, the FIB (30 kV, 7.7 pA) milled 160 consecutive slices with a width of $2.5 \mu\text{m}$ and a nominal slice thickness of 3 nm. The SEM (2 kV, 100 pA) recorded images in SE and BSE mode (Ultra-High Resolution mode) with a scan resolution of 2304×2048 pixels per image, 0.324×0.411 nm per pixel and dwell time $3 \mu\text{s}$ per pixel.

FIB-SEM tomography of the colloidal crystal was performed in a Scios FIB-SEM (Thermo Fisher Scientific). Standard preparation procedures (Pt deposition, milling of trenches and polishing of the cross section to be imaged) were performed manually prior to the execution of the tomography routine. The FIB (30 kV, 300 pA) milled 212 consecutive slices with a width of $22 \mu\text{m}$, a calculated depth of $20 \mu\text{m}$ and a nominal slice thickness of 50 nm. The SEM (3.5 kV, 100 pA) recorded images (3072×2048 pixels, pixel size 10 nm, dwell time $6 \mu\text{s}$) with the T1 detector in BSE mode.

FIB-SEM tomography of the binary glass was also performed in a Scios FIB-SEM (Thermo Fisher Scientific). Again, standard preparation procedures were performed manually. Following, the FIB (30 kV, 300 pA) milled 100 consecutive slices with a width of $35 \mu\text{m}$, a calculated depth of $15 \mu\text{m}$ and a nominal slice thickness of 50 nm. The SEM (3.5 kV, 100 pA) recorded images (3072×2048 pixels, pixel size 9.4 nm, dwell time $6 \mu\text{s}$) with the T1 detector in BSE mode.

Confocal microscopy

For confocal microscopy imaging, the binary glass was index matched with a glycerol/*n*-butanol mixture ($n_D^{23} = 1.44$). A Leica TCS SP8 confocal microscope equipped with a super continuum white light laser (SuperK, NKT Photonics), a HyD detector and a $100\times/1.4$ NA confocal objective was used to image the glass. The sample was sequentially scanned with the pinhole set to 1 airy unit to, first, image the rhodamine B dyed particles with the excitation laser set to 550 nm and the detection range from 565 to 687 nm and, second, the FITC dyed particles with the excitation laser set to 488 nm and the detection range from 498 to 590 nm. The voxel size was $31 \times 31 \times 50 \text{ nm}^3$ ($X \times Y \times Z$).

Deconvolution

The confocal image stack was deconvoluted with a theoretical point spread function using the classic maximum likelihood estimation restoration method in the Huygens software (17.04, Scientific Volume Imaging) to a final signal-to-noise ratio of 20.

Particle identification

To find the positions and orientations of the rods we used the algorithm as described by Besseling *et al.* [283] We coloured the rods depending on their orientation with $c_{\text{red}} = |n_x|$, $c_{\text{green}} = 1/2 - n_y/2$ and $c_{\text{blue}} = 1/2 - n_z/2$ where n_x, n_y and n_z are the components of the normalized orientation vector \mathbf{n} along the length of the rod.

To determine the positions of the spherical particles in the FIB-SEM datasets we used a new algorithm of which we will give short description here. A schematic overview of the main steps in the gradient based tracking method is given in ref [303].

After alignment and an initial filtering step the images were blurred with a Gaussian blur (typically with $d = 1.0$ pixels) to remove noise. Next, the gradients of the image were calculated in the x, y and z directions resulting in 3 bitmaps (G_x, G_y, G_z) containing both negative as well as positive values. We also produced a kernel from an ideal image containing a single particle with the same dimensions as the particles that we want to locate and blurred this by the same amount. We then calculated its gradients in 3D (K_x, K_y, K_z) and the convolution (by FFT) of the gradient images with the kernel $G_x * K_x + G_y * K_y + G_z * K_z$, this final image can be seen as Hough transform [304] and produces a sharp peak at the location of each particle. We then found all local maxima in this image brighter than a predetermined threshold and fitted their position with a quadratic function to obtain sub-pixel accuracy. For the binary sample we used several (typically 10) kernels for particles with an increasing diameter and searched for a maximum in the resulting 4D dataset (x, y, z and diameter). The distribution of sizes was fitted with two Gaussians and the intersection of the two (475 nm) was chosen to distinguish the small and large particles in the assembly.

The positions of the particles in the confocal data sets were determined after image restoration using an extension to 3D [264] of a classic 2D tracking algorithm [282].

7.3 Results

FIB-SEM tomography for particle assemblies

We applied FIB-SEM tomography to three 3D assemblies: a $<1 \mu\text{m}^3$ sized nanoparticle (NP) assembly, consisting of silica coated gold nanorods (AuNRs , $L_{\text{Au}} = 119 \text{ nm}$ (11% PDI), $D_{\text{Au}} = 16 \text{ nm}$ (13% PDI)), a much larger $\sim 1000 \mu\text{m}^3$ sized assembly composed of large spherical silica colloids ($d = 531 \text{ nm}$, $<2\%$ PDI) and a similarly sized assembly composed of a binary glass of the same spheres mixed with smaller silica spheres ($d = 396 \text{ nm}$, 1% PDI). In Figure 7.1 we depict the general approach in which FIB-SEM tomography is used in the 3D characterization of particle assemblies. The characterization can be divided in three stages: (1) acquisition of the tomography series, (2) alignment of the 2D image stack and (3) fitting of the positions and orientations of the particles in 3D.

We used two different ways of sample preparation depending on the type and size of the particle assembly. For the large colloidal assemblies consisting of the 531 nm silica spheres, the assembly was embedded in a resin, to preserve the assembly structure during the milling process by the FIB. This is essential to correctly determine the initial particle coordinates and orientations. Thereafter, a conductive platinum layer was sputter coated

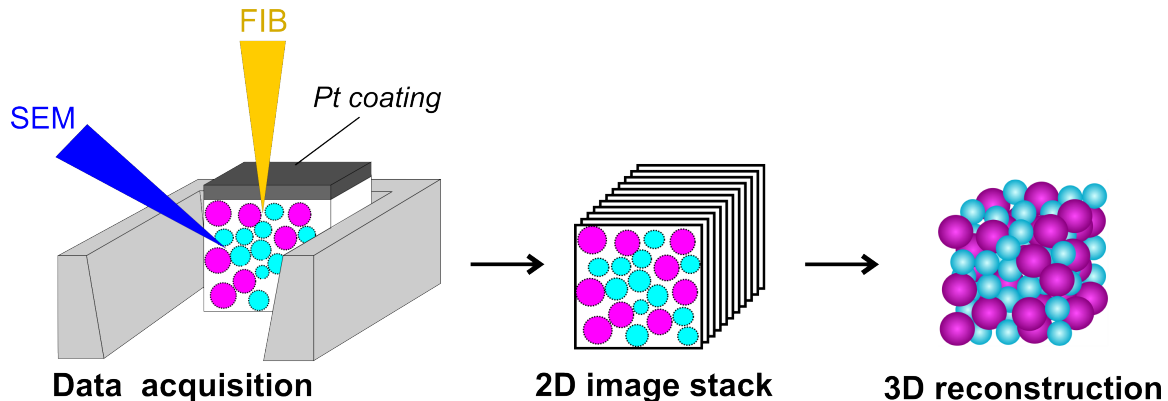


Figure 7.1: 3D characterization of colloidal assemblies with FIB-SEM tomography. Left: the tomography data acquisition, obtained by iteratively removing a slice of the assembly with the FIB beam (yellow) and imaging of the assembly with the electron beam (dark blue). Middle: the obtained stack of 2D images acquired at different Z -depths. Right: 3D reconstruction of the particle coordinates from the 2D image stack.

on top of the ensemble at the region of interest to prevent charging during FIB-milling and/or SEM-imaging. The small spherical AuNR nanoparticle assemblies, called supraparticles, were not embedded in a resin, but the selected supraparticle was only covered with a Pt-coating, which prevented both charging and deformation of the spherical assembly shape during the milling process. In the tomography data acquisition the slice thickness was varied for the different colloidal particle sizes and was chosen such that at least 6 slices through each individual particle were obtained. Thereafter, the SEM images were aligned and the coordinates and orientation of the individual particles determined. For particle identification of the nanorod assemblies we used the rod-tracking code developed by Besseling *et al.* [283]. For the micron sized colloidal assemblies we used a more recent analysis method in which the particles are identified with gradient tracking. The gradient based tracking approach is a more general method in comparison to the rod-tracking code which can only be applied to rod-like particles [283].

High resolution 3D imaging of gold nanorod assemblies

For the FIB-SEM tomography on nanoparticle based assemblies, we prepared ~ 200 nm to $2 \mu\text{m}$ large spherical supraparticles of silica coated gold nanorods ($L_{Au} = 119$ nm (11% PDI), $D_{Au} = 16$ nm (13% PDI)). This type of nanoparticle system is particularly interesting for Raman spectroscopy (see Chapter 8), where the Raman enhancement depends on the overlap between the surface plasmons of the individual gold particles and thus on the precise position and orientation of the nanorods [62]. To obtain the AuNR assemblies, we first synthesized colloidal gold nanorods [13] coated with a 3 nm thin silica shell, functionalized with a hydrophobic coating [305]. Subsequently, the rods were assembled in spherical clusters by using a solvent evaporation method [273] that we recently also applied to rod-like particles [283] (see Experimental section for more synthesis details).

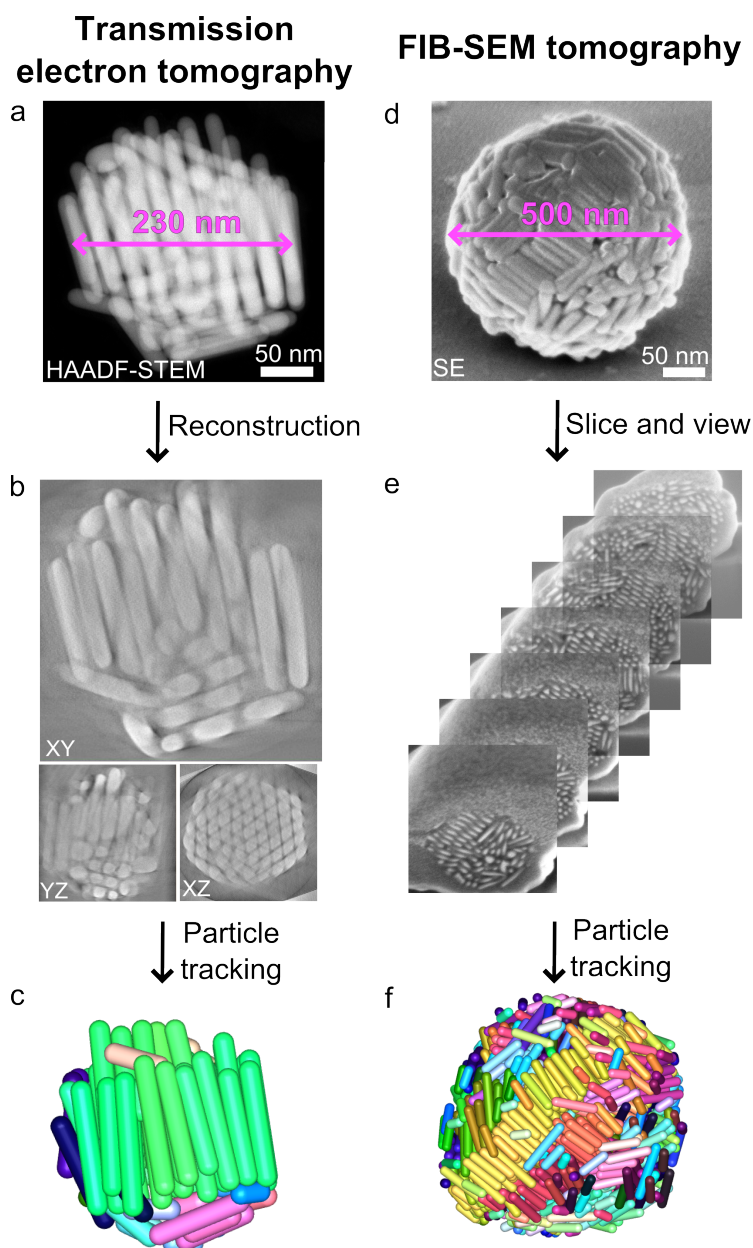


Figure 7.2: 3D characterization of differently sized silica coated gold nanorod assemblies with transmission electron and FIB-SEM tomography. Left: transmission electron tomography of a small AuNRs@SiO₂ ($L_{Au} = 119$ nm (11% PDI), $D_{Au} = 16$ nm (13% PDI)) assembly with $d = 230$ nm, consisting of 96 nanorods: a) Single HAADF-STEM image, acquired at 0° tilt, b) XY, YZ and XZ orthoslices of the assembly's interior, after reconstruction of the tilt series, c) tracking of the position and orientation of the nanorods in 3D, where the rods are coloured according to their orientation. Right: FIB-SEM tomography of a larger AuNRs@SiO₂ assembly with $d = 500$ nm, consisting of 1279 nanorods: d) SE-image of the exterior of the AuNRs@SiO₂ assembly, e) SE images acquired while milling into the interior of the assembly with the FIB, f) 3D representation of the tracked AuNRs in the assembly.

We applied both transmission electron tomography and FIB-SEM tomography to obtain the 3D structure of the AuNR assemblies. In Figure 7.2 we show the transmission electron and FIB-SEM tomography results for the characterization of a small and a larger AuNR supraparticle, of which the spherical shape is usually well suited for transmission electron tomography [273, 275, 276]. Figure 7.2a-c shows the tilt series, reconstruction and 3D model of a 230 nm assembly obtained *via* transmission electron tomography. In the 3D model the rods are colour-coded based on their orientation, showing that the rods are preferentially ordered in the same direction. For this relatively small assembly the positions and orientations of all 96 rods could successfully be obtained from the 3D reconstruction. The transmission electron tomography tilt series, reconstruction and 3D model of the tracked AuNR assembly can be viewed in Movie S1-S3, respectively.

Due to the limited penetration depth of the electron beam caused by the high Z -contrast of the Au atoms, transmission electron tomography can only be applied to small particle assemblies for this type of systems. To illustrate this we performed transmission electron tomography on a larger, 340 nm ensemble composed of the same AuNRs as the assembly shown in Figure 7.2a-c. In Figure 7.3 we show that the 340 nm assembly was too large to obtain a high quality reconstruction. To access the full structural properties of larger and/or denser assemblies, we applied FIB-SEM tomography. In Figure 7.2d-f we show the secondary electron (SE) image of the exterior, part of the FIB-SEM tomography series of the interior and the 3D reconstruction of a 500 nm AuNR supraparticle, consisting of the same AuNRs as the assembly in Figure 7.2a-c. In order to reliably distinguish the individual NRs, the lowest possible Z step size of 3 nm had to be used, such that at least 6 slices per rod were obtained. The tomography series consisted of 160 XY -slices (2304×2048 pixels), spaced 3 nm apart resulting in a voxel size $X \times Y \times Z$ of $0.3244 \times 0.411 \times 3 \text{ nm}^3$. The total imaged volume was $0.300 \mu\text{m}^3$. The particles coordinates and orientations were determined by making use of a rod fitting algorithm [283]. From the FIB-SEM tomography data set in Figure 7.2e we obtained the positions and orientations of 1279 rods. The complete FIB-SEM tomography series and 3D model of the tracked AuNR assembly can be found in Movie S4 and S5, respectively.

FIB-SEM tomography of a colloidal crystal

To demonstrate the feasibility of FIB-SEM tomography to also analyze much larger colloidal assemblies containing micron sized particles, we prepared a colloidal crystal of monodisperse silica spheres ($d = 531 \text{ nm}$, $<2\%$ PDI). About one percent of the particles had a 30 nm gold core, whereas the other 99 percent had a 45 nm fluorescently (rhodamine B isothiocyanate, RITC) labeled core to also enable characterization with confocal microscopy. The crystal was grown by controlled vertical deposition at elevated temperature onto a glass slide [301], resulting in a thickness of $\sim 11 \mu\text{m}$ (which corresponds to ~ 25 layers).

In Figure 7.4a we show a slice from the FIB-SEM tomogram with a pixel size in X and Y of 10.5 nm, recorded with a milling step size in Z of 50.0 nm. The total sampled volume was $2610 \mu\text{m}^3$. The inset in Figure 7.4a shows a gold core in one of the silica particles, demonstrating the possibility of investigating multiple length scales in hierarchical assemblies using FIB-SEM tomography. From the full data stack we cropped

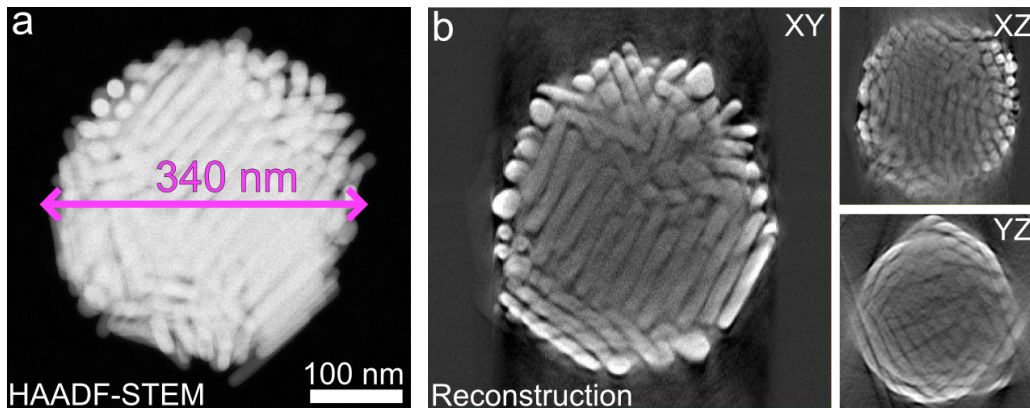


Figure 7.3: Transmission electron tomography result for AuNR assembly with $d = 340$ nm, which is too large for a reliable reconstruction. a) 0° tilt image, acquired in HAADF-STEM mode. b) XY , XZ and YZ views of the 3D reconstruction. The tilt series was acquired from -70 to $+70^\circ$ with a tilt step of 2° .

a volume of $1000 \mu\text{m}^3$ (dashed cyan rectangle in Figure 7.4a) for reconstruction, see Figure 7.4b. Using a gradient tracking algorithm the particle coordinates were obtained, as we show in Figure 7.4c where the particles positions are depicted by the cyan circles. In Movie S6 and S7 the full FIB-SEM tomography series and corresponding 3D model, respectively, are shown.

To obtain insight into the structure of the crystal, we calculated the local bond orientational order of every particle in the assembly [303, 306]. In Figure 7.4d we show a computer rendering of the particle assembly, where the particles are coloured according to their local symmetry (see ref. [303] for details). Although the majority of the particles have local face-centered cubic (FCC) symmetry, the particles at the bottom of the reconstructed volume are packed locally with hexagonal close-packed (HCP) symmetry. Moreover, a slanted stacking fault runs through the crystal, also with local HCP symmetry. When the radial distribution function $g(r)$ is calculated from the reconstructed coordinates (8912 particles), a good agreement with the FCC structure is found (see Figure 7.4e). There is however a double peak at $r/d \approx 1$, which is absent in close packed crystals grown in bulk or by gravity [307]. From the ratio of the r/d values of the two peaks in Figure 7.4e it follows that the difference is close to 4%. This is in good agreement with previous work on colloidal crystals grown using the vertical deposition method, where the same $\sim 4\%$ of shrinkage in the growth direction in the hexagonal (111) planes has been measured with X-ray diffraction and confocal microscopy [308].

Characterization of a binary colloidal glass

FIB-SEM tomography can also be used to obtain real-space information of binary particle systems. Here we intentionally made a binary glassy sample as it is more difficult to retrieve the particle coordinates from the microscopy data in comparison to a crystalline structure. To demonstrate this, we mixed the previously used 531 nm RITC labeled silica colloids with smaller 396 nm (1% PDI) silica particles, which had a fluorescently

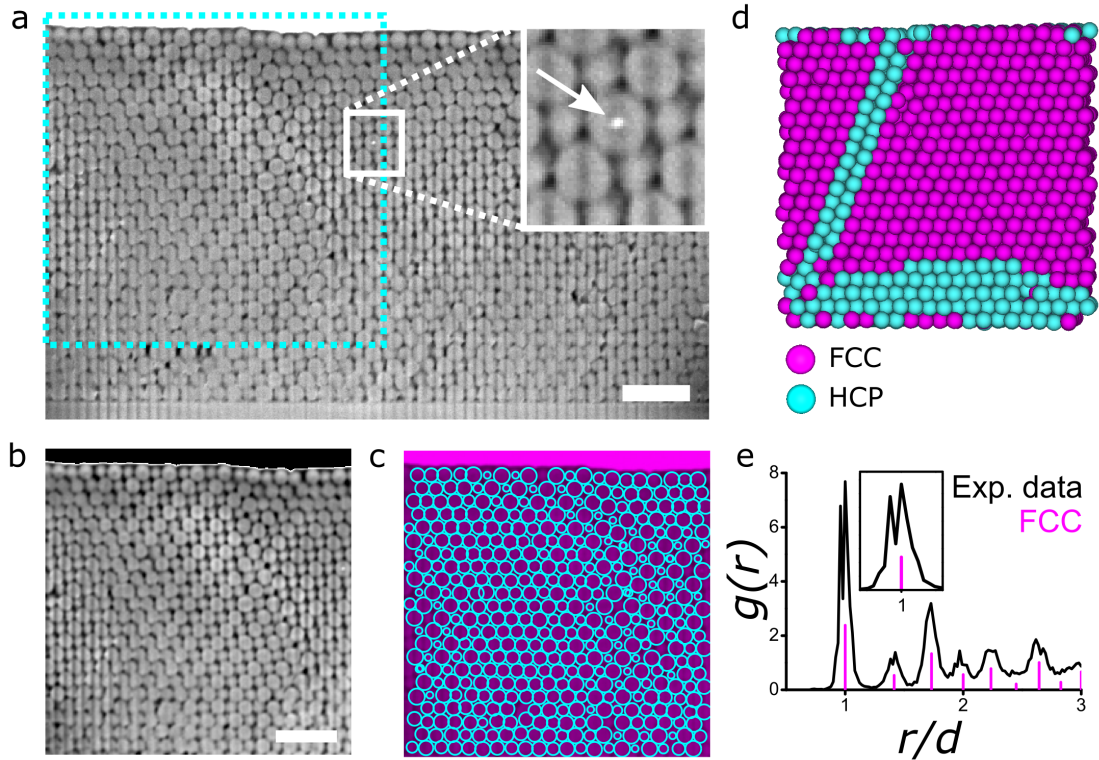


Figure 7.4: FIB-SEM tomography on a crystal of silica colloids ($d = 531 \text{ nm}$, $<2\%$ PDI). a) Slice from FIB-SEM tomogram with a total volume of $2610 \mu\text{m}^3$. Arrow in inset points at the gold core of a particle. b) Zoom-in of the dashed cyan rectangle in the (a). c) Overlay of (b) with cyan circles indicating identified particles. d) Cut-through of computer rendering of coordinates from the reconstruction in (c) with colours of particles assigned to local symmetry of particles as calculated with bond orientational order parameters showing that the crystal structure is majorly FCC (magenta) with a horizontal stacking fault at the bottom and a slanted stacking fault running through the structure, both with HCP symmetry (cyan). The reconstructed volume is $1000 \mu\text{m}^3$, with 8891 particles. e) Radial distribution function $g(r)$ calculated from coordinates of the rendering partly shown in (d) (black), compared to the peaks of an ideal FCC crystal (magenta). The inset shows the double peak in the $g(r)$ at $r/d \approx 1$, due to the shrinkage in the growth direction of the crystal. The scale bars are $2 \mu\text{m}$.

(fluorescein isothiocyanate, FITC) labeled core of $\sim 200 \text{ nm}$. For comparison, the particles were imaged with both confocal laser scanning microscopy and FIB-SEM tomography.

For confocal microscopy, the particles were drop casted from an ethanol dispersion on a cover glass and refractive index matched with a mixture of glycerol and n -butanol ($n_D^{23} = 1.44$). Image stacks of the two differently labelled particles were imaged sequentially, as shown in Figure 7.5a, spanning a volume of $\sim 1200 \mu\text{m}^3$. Figure 7.5b shows the stacks after image restoration, which involves deconvolution of the data with the microscope point spread function using the Huygens (SVI) deconvolution software. The deconvoluted confocal data stack of the binary glass can be viewed in Movie S8. Using a classical particle tracking routine [282] extended to 3D data sets [264], we identified the coordinates of both species in the assembly. A fragment of a computer rendering of the

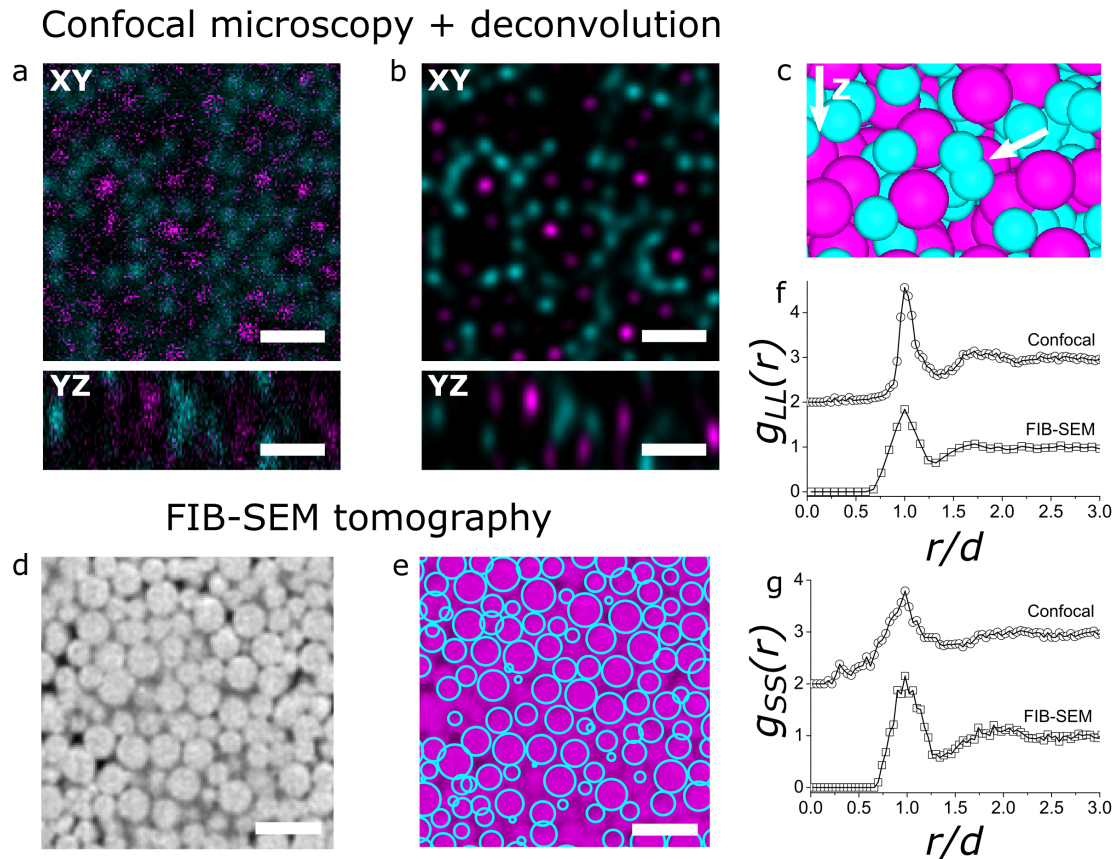


Figure 7.5: Binary glass characterized by confocal microscopy, in combination with image restoration, and FIB-SEM tomography. a) XY and YZ slices from a two channel confocal microscopy image stack of a binary glass of 396 nm (1% PDI) fluorescein (cyan, S) and 531 nm (<2% PDI) rhodamine (magenta, L) labeled core-shell silica colloids, with a total volume of $\sim 1200 \mu\text{m}^3$. b) Same slices after deconvolution of the image stack. c) Fragment of computer rendering of coordinates identified from the image stack in b). The arrow points at two overlapping particles, where the particle tracking algorithm misidentified two particles with a small separation in the axial direction. d) Fragment of FIB-SEM tomogram of the same binary glass with a total volume of $\sim 500 \mu\text{m}^3$. e) Overlay of d) with cyan circles indicating identified particles. Partial radial distribution functions $g_{LL}(r)$ (f) and $g_{SS}(r)$ (g) from the coordinates obtained through confocal microscopy and image restoration, and FIB-SEM tomography. The scale bars are $1 \mu\text{m}$.

coordinates is shown in Figure 7.5c (the full set of coordinates can be viewed in Movie S9), from which the partial radial distribution functions of the large ($g_{LL}(r)$, 4192 particles) and small particles ($g_{SS}(r)$, 6544 particles) were calculated (Figure 7.5f,g).

For FIB-SEM tomography, the particles were embedded in a resin after dropcasting. A stack with a total volume of $\sim 1000 \mu\text{m}^3$ was recorded with a FIB milling step size of 50 nm. From this stack, a volume of $\sim 500 \mu\text{m}^3$ was cropped for particle identification (Figure 7.5d). The coordinates of the particles were obtained using a gradient tracking algorithm, where the particle sizes were fitted for every particle (Figure 7.5e). This resulted in a distribution of sizes with two peaks where the population was divided into

small and large species using a threshold diameter of 475 nm. From the coordinates of the different particles, the partial radial distribution functions $g_{LL}(r)$ (2448 particles) and $g_{SS}(r)$ (2817 particles) were calculated, as shown in Figure 7.5f and g, respectively. Movie S10 and S11 show the FIB-SEM tomography series and the corresponding 3D model of the binary glass.

When comparing the partial radial distribution functions of the large ($g_{LL}(r)$) and small spheres ($g_{SS}(r)$) acquired using the two techniques, an agreement was found for the peak positions in the $g_{LL}(r)$, although the $g_{LL}(r)$ from FIB-SEM had a broader first peak (Figure 7.5f). The functions of the smaller particles $g_{SS}(r)$, however, disagreed to a higher extent (Figure 7.5g). The radial distribution function calculated from the coordinates obtained by confocal microscopy had a lower first peak and was non-zero at values smaller than the smallest distance the particles can be apart (~ 390 nm). This points at overlapping particles due to mis-identification of the smaller particles positioned relatively close to each other in the axial direction of the confocal microscope, as reported in Ref. [309]. An example of such overlapping particles in the computer rendering of the coordinates is shown in Figure 7.5c. These types of errors were absent in the confocal $g_{LL}(r)$, indicating that for the small particles, the limit of the (axial) resolving power of the confocal microscope was approached. FIB-SEM tomography, on the other hand, does have sufficient resolving power to identify the positions of the smaller particles correctly.

7.4 Discussion

Data acquisition

During the FIB-SEM data acquisition it is crucial that the colloidal particles are imaged in their original positions and orientations within the ensemble. Depending on the type of assembly various changes in the ensemble structure can occur during the tomography. Supraparticles, especially composed of NPs, are prone to deform to a more flat, non-spherical structure during FIB exposure and should therefore be encapsulated in a Pt coating before tomography. On the other hand, in the image acquisition of the assemblies composed of the micron sized colloids we noticed that particles could "fall off" during the milling process, when the particles are no longer supported by their neighbors. This can cause a shift in the apparent position of the particles in the 3D reconstruction. To prevent this, it is advisable to embed the particle assembly in a resin prior to the image acquisition.

When imaging porous assemblies with FIB-SEM, so-called curtaining effects are likely to arise due to the different (material) densities. Curtaining occurs when the milling speed in the region of interest is inhomogeneous, resulting in different slice thicknesses in the milling direction. Such inhomogeneities in slice thickness complicate or even prohibit a quantitative reconstruction of the correct assembly structure in 3D. We observed these curtaining effects when milling the relatively porous and thick colloidal crystal and binary glass, but not for the densely packed and thin AuNR assemblies. The curtaining during the data acquisition can successfully be suppressed by embedding the colloidal assemblies in a resin beforehand. In this way, the pores in between the particles are filled, making the milling speeds more homogeneous. The remaining curtaining "stripes" can be filtered out

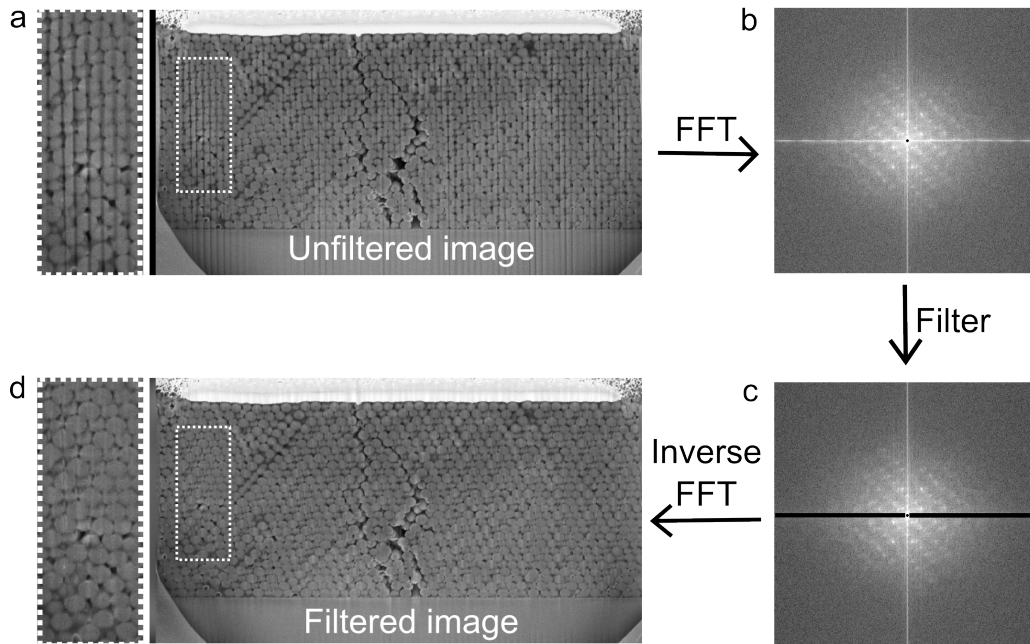


Figure 7.6: The FFT filtering procedure to remove curtaining stripes. a) Unfiltered image of colloidal crystal consisting of silica spheres ($d = 531$ nm). b) FFT of the image in a. c) Filtered FFT. d) The filtered image without curtaining stripes, after performing an inverse FFT of c.

during the data processing by using fast Fourier transform (FFT) filtering. Herein, one calculates the FFT of the acquired image, removes the lines in the FFT patterns caused by the curtaining and performs an inverse FFT to obtain the filtered image (Figure 7.6). The curtaining effect can also be suppressed using advanced acquisition methods and image processing [310].

Another difficulty encountered during acquisition is the accumulation of charge in the sample due to the scanning electron beam, resulting in white areas in the SEM images. Although the samples were connected to the SEM stub with conductive carbon tape and sputter coated with Pt to prevent the build-up of charge, charging still occurred. One way to reduce this effect was to acquire the SEM images at a lower beam current, and compensate for the signal reduction by integrating multiple images. Instead of modifying the acquisition parameters, the effects of charging can also be suppressed by image processing [310].

Determining particle coordinates and orientations

There are several advantages in using the gradient based particle tracking algorithm used in this work. First, it is not limited to the recognition of spherical particles only, but can also be applied to different (anisotropic) shapes [276], and therefore to a wide variety of particle assemblies. Second, it enables the determination of the particle orientation for each *individual* particle. The ability to exactly determine the orientation and position of each NP and all interparticle distances is crucial in, for instance, calculating the assembly's collective plasmonic properties. Previously, only average orientations of several

particles per assembly volume could be obtained [62]. With our particle specific analysis method it now becomes feasible to directly compare the theoretical and experimental behavior of plasmonic particle assemblies and to predict their performance for *e.g.* Raman spectroscopy, which is strongly influenced by the exact particle locations and the presence of so-called hot-spots, where locally electromagnetic fields can non-linearly enhance each other (see Chapter 8).

When the contrast between the particles and their surroundings is low, tracking is more difficult. For the spherical AuNR assembly in Figure 7.2, the contrast between the Au of the NRs and the Pt of the protective coating was very low. Particles in or close to the Pt coating were prone to misidentification and difficult to distinguish from real particles. Reliable tracking was therefore only possible for the layers below the particle layer that was closest to the Pt coating.

Comparing the real-space microscopy techniques

We studied the AuNRs assemblies with both transmission electron tomography and FIB-SEM tomography. Which method is to be preferred predominately depends on the size and Z-contrast of the individual nanoparticles, and the size of the total ensemble. Generally, the spatial resolution of the transmission electron microscope is superior to the resolution of the electron beam used in FIB-SEM tomography. More importantly, the resolution in the Z-direction for the current generation of high-end Ga-based FIB-SEM microscopes is limited to 3 nm, which is the minimum slice thickness that can be milled with the FIB. Since a minimum of about 6 slices per nanoparticle is required to reliably determine its position and orientation, FIB-SEM tomography is presently only suited for assemblies consisting of ≥ 18 nm particles. Although the accuracy of the tracking is generally higher than the resolution of the FIB-SEM images [282, 283], for now transmission electron tomography is still the preferred analysis technique for small nanoparticle assemblies.

However, for assemblies with a thickness larger than 300 nm and/or composed of high Z-contrast materials, transmission electron tomography is no longer applicable. When imaging such assemblies with transmission electron tomography, the intensity of the particles in the interior is underestimated with respect to the particles at the exterior of the assembly. This is caused by partial absorption and scattering of the incoming electron beam before reaching the inside of the particle ensemble. Likewise, the electrons that are scattered from the inside of the assembly have to penetrate a considerable amount of material before reaching the detector. This results in thickness dependent, non-linear damping of the recorded intensities, which is called a cupping artefact [311]. In the reconstruction the cupping artifact hampers a quantitative 3D structural analysis of the particle ensembles interior. An example of the cupping artifact is for example already visible in the reconstruction of the 340 nm AuNR assembly in Figure 7.3. Apart from post reconstruction methods to correct for the cupping effect, an alternative method to study the interior of nanoparticle assemblies larger than 300 nm is to perform microtomy prior to the transmission electron tomography measurement. Herein, one embeds the particle assemblies in a resin and cuts the sample with a diamond knife to slices as thin as 50 nm, after which electron tomography can be performed on a single slice. However, this method does not allow the continuous spatial analysis of a full particle assembly. Thus, to

characterize a complete nanoparticle ensemble larger than 300 nm, FIB-SEM tomography is indispensable.

We also compared FIB-SEM tomography to confocal microscopy for particle ensembles consisting of particles with a size close to the resolution limit of conventional confocal microscopy. For the binary glass (Figure 7.5), we observed that the large spheres could still be resolved with confocal microscopy, but the smaller ($d = 396$ nm) particles could not. The overlapping particles shown in Figure 7.5c indicate that the limit of the resolving power of the confocal microscope was reached. Despite the fact that more advanced particle fitting algorithms have been developed to increase the accuracy of particles position determination, these algorithms do not significantly lower the size limit of the smallest particles that can be imaged with confocal microscopy [280, 309, 312, 313]. By using STED one could improve both the axial and lateral resolutions significantly (even to below 100 nm), but this technique is complicated in large sample volumes and sensitive to refractive index mismatches. FIB-SEM tomography, however, is capable of quantitatively characterizing (binary) assemblies of particles too small for confocal microscopy, without the need of refractive index matching or the incorporation of dyes in the particles.

Possible future applications of FIB-SEM tomography on colloidal systems

In this study, the assemblies were composed of particles similar in size and composition. However, the high resolution of FIB-SEM tomography would also allow the study of mixed assemblies with particle sizes ranging from 20 to 1000 nm. Either by size or by the difference in material density, different particles types can be distinguished within a mixed assembly. For example, in the case of the micron size colloidal crystal, a fraction of the silica spheres contained a much smaller (30 nm), higher density gold core instead of a silica core. The gold core could be identified in the FIB-SEM image series due to its higher Z-contrast and smaller particle size (Figure 7.4a (inset)). In future research, FIB-SEM could thus be applied to fully characterize heterogeneous assemblies, *e.g.* photonic crystals composed of particles with strongly scattering cores.

The imaging method described in this work can also be applied to study low density colloidal dispersions. To do so, the colloidal dispersions would have to be arrested prior to the imaging process. This can be done either by cryogenic quenching [314] or chemical arrest by the polymerization of the continuous fluid phase. The latter technique enables a controlled timing of the arrest and would therefore allow the study of the different stages in assembly processes. Structural analysis of particle dispersions is also relevant in measuring for example the interparticle interactions, through the calculation of the radial distribution function [315]. The high resolution of the FIB-SEM microscope would make it possible to start investigating interparticle interactions between nanoparticles, too small to be imaged with confocal microscopy.

It is worth noting that FIB-SEM tomography also allows the analysis of the porosity of particle assemblies. Where in previous studies the porosity of geological materials was analysed by counting the voxels of the pores after a thresholding step, the particle tracking used here allows for the calculation of the total particle volume from the particle coordinates and sizes, and therefore the total pore volume. In addition, one could analyse

the pore size distribution by fitting the largest possible sphere in each pore and plot the distribution of radii to obtain an estimate of the pore size distribution [316].

7.5 Conclusions

We have demonstrated a general approach using FIB-SEM tomography for the 3D real-space characterization of colloidal particle assemblies. We showed that this technique combines high resolution imaging with large sampling volumes, allowing the precise characterization of assemblies too large for conventional electron tomography, and containing particles too small to resolve with confocal microscopy. To this end, we first demonstrated the use of FIB-SEM tomography for high resolution imaging of nanorod assemblies. In contrast to conventional electron tomography, the position and orientation of the individual nanorods in assemblies larger than 300 nm could still be obtained. Next, we applied FIB-SEM tomography for the imaging of a colloidal crystal and a binary glass consisting of fluorescently labeled sub-micron silica spheres for large sampling volumes ($\geq 1000 \mu\text{m}^3$). While FIB-SEM tomography was able to identify all particles in the binary glass, conventional confocal microscopy could not resolve all particles in the axial direction. Additionally, FIB-SEM tomography does not require the incorporation of dye in the particles or refractive index matching. For the data analysis we used a recently developed gradient based tracking algorithm, which can be used for different particle shapes and materials. In combination with such a data analysis methodology, we have shown that FIB-SEM tomography is applicable to a broad range of materials, and particle sizes and shapes, bridging and extending several other quantitative imaging techniques.

Acknowledgements

The work in this chapter was performed in collaboration with Ernest van der Wee (silica assemblies and confocal analysis), Matthijs de Winter (FIB-SEM acquisition), Michiel Hermes (particle tracking), Yang Liu (FIB-SEM acquisition), Jantina Fokkema (silica assemblies), Maarten Bransen (gold nanorod assemblies), Marijn van Huis and Hans Gerritsen. J. Fermie is acknowledged for the help with FIB-SEM sample preparation and H. Meeldijk for EM support. We thank T.-S. Deng for useful discussion on the AuNR synthesis and self-assembly.

Supplementary movies

Movies S1-S11 can be viewed via this link:

<https://pubs.rsc.org/en/content/articlelanding/2019/nr/c8nr09753d!divAbstract>

8.1 Introduction

Nowadays surface enhanced Raman spectroscopy (SERS) is used in the detection of trace amounts of molecules and applied in many fields ranging from in single-molecule spectroscopy [64] and catalysis [65, 317, 318], to applications in biomedicine [64], forensic research [41] and even art history [66]. SERS relies on the use of plasmonic nanoparticles (NPs) which can strongly enhance the Raman signal of scattering molecules close to the plasmonic NP surface. The SERS performance is very sensitive to the plasmonic properties of the metal NPs. Small changes in local field enhancements around the NP surface can already induce a large increase in the Raman signal, as the latter scales with the field enhancements to the 4th power [45–47]. The SERS performance of a plasmonic nanoparticle can therefore be tuned via the particle shape, morphology and metal composition [49, 50, 52, 53].

Rod shaped particles are particularly promising candidates for sensing applications. As explained in the introduction of this thesis, gold nanorods (AuNRs) exhibit superior plasmonic properties compared to spheres as they have enhanced and highly tunable plasmonic properties due their longitudinal surface plasmon resonance in the visible and near-infrared. By bringing the NRs in close proximity, the localized surface plasmons of the individual NRs overlap, which gives rise to plasmonic hotspots in between the NRs. The strength of the local field enhancement in these hotspots can be tuned via the interparticle spacing and the orientation of the NRs [58, 319–321]. As the local field enhancement at the tips of the NRs are largest, a tip-to-tip geometry renders the highest field enhancements.

There are several ways to create nanostructures with interparticle plasmonic hotspots. One can connect the NPs particles via molecular linkers [46, 319, 322] or via self-assembly [53, 59–62]. The self-assembly of AuNRs was shown to result in colloidal crystals giving enhancements of the Raman signal on the order of 10^5 - 10^6 [59, 62]. However, the problem with these larger AuNR assemblies is that the Raman signal can become severely hampered by the limited porosity of these colloidal assemblies due to the small interparticle distances between the NRs. This makes that the probe molecules can only access outer particle layers, whereas the highest local field enhancements exist in the interior of the NR assembly [59, 60]. The main problem here is that on the one hand the particles in the assembly should be as close as possible to ensure strong interparticle hotspots, whereas on the other hand sufficient porosity is required for the probe molecules to reach the hotspots in the interior of the assembly. Additionally, a good wetting of the probe molecules on the assembly surfaces is needed, such that uptake of the probe molecules into the assembly can occur due to capillary interactions. Infiltrating the structure with mesoporous silica after the assembly process, was observed to increase the porosity and the SERS performance [62], which shows that further improvement of plasmonic particle ensembles for sensing will require a precise tuning of the assembly's porosity, wetting and interparticle distances.

Here, we do this by coating the AuNRs with a silica shell of which the thickness and porosity was controlled, before assembling them into larger ensembles. In the self-assembly processes we used a solvent evaporation method in which an aqueous dispersion of silica coated gold nanorods (Au@SiO₂ NRs) was emulsified in a larger apolar phase

(hexadecane). Upon evaporation of the water phase, the silica coated AuNRs assembled into spherical clusters, called supraparticles. The size of these supraparticles could be tuned via the droplet size of the water phase. The porosity of the supraparticles and coupling between the AuNRs was set via the porosity and thickness of the silica shells, respectively. By assembling thin (3 nm) and thicker mesoporous (18, 35 nm) silica coated NRs, supraparticles with a different degree of interparticle coupling could be obtained. We probed the performance of these supraparticles in Raman spectroscopy and demonstrate a general method to correlate the SERS properties of plasmonic particle assemblies to their structural properties by performing Raman spectroscopy and FIB-SEM analysis on the same assemblies. We find that more open structures consisting of 3 nm thin silica coated AuNRs give significantly higher Raman signals compared to supraparticles of 18 nm and 35 nm thick mesoporous silica coated AuNRs and discuss the parameters to be tuned in further optimizing AuNR supraparticles for sensing applications.

8.2 Experimental

Synthesis

Chemicals

All chemicals were used as received without further purification. Hexadecyltrimethylammonium bromide (CTAB, >98.0 %) and sodium oleate (NaOL, >97.0 %) were purchased from TCI America. Hydrogen tetrachloroaurate trihydrate ($\text{HAuCl}_4 \cdot 3\text{H}_2\text{O}$) and sodium hydroxide (98 %) were purchased from Acros Organics. L-Ascorbic Acid (BioXtra, ≥ 99 %), hydrochloric acid (HCl, 37 wt% in water), silver nitrate (AgNO_3 , ≥ 99 %), sodium borohydride (NaBH_4 , 99 %), sodium silicate solution (≥ 27 % SiO_2 basis, Purum ≥ 10 % NaOH), tetraethyl orthosilicate (TEOS, 98 %), decane (≥ 99.5 %), pyridine (≥ 99 %) and crystal violet (CV, ≥ 90 %) were purchased from Sigma-Aldrich. Absolute ethanol and hexadecane (≥ 99.0 %) were purchased from Merck. SPAN80 was purchased from Fluka. Ultrapure water (Millipore Milli-Q grade) with a resistivity of 18.2 M Ω was used in all of the experiments. All glassware for the AuNR synthesis was cleaned with fresh aqua regia (HCl/ HNO_3 in a 3:1 volume ratio), rinsed with large amounts of water and dried at 100 °C before use.

Gold nanorod synthesis

The gold nanorod synthesis was performed according to the procedure of Ye *et al.* [13]. The seed solution consisted of 10 mL 0.10 M CTAB and 51 μL 50 mM HAuCl_4 to which 1.0 mL 0.0060 M NaBH_4 was added while stirring vigorously for 2 min. For the growth solution 7.0 g CTAB and 1.24 g NaOL were dissolved in 250 mL MQ H_2O . Next, 250 mL 1.0 mM HAuCl_4 , 7.2 mL 10 mM AgNO_3 , 3.0 mL HCl (37 wt%, 12.1 M), 1.25 mL 0.064 M ascorbic acid and 0.80 mL seed solution were added, while stirring at 350 rpm (revolutions per minute) in a 30 °C waterbath. The reaction mixture was left unstirred overnight. Thereafter, the rods were washed with 120 mL H_2O via centrifugation at 8000 ref (relative centrifugal force) for 30 min and stored in 36 mL 5.0 mM CTAB water. The

resulting rods had an average length (L_{Au}) and standard deviation of 95 ± 8 nm, diameter (D_{Au}) of 17 ± 2 nm and aspect ratio (AR_{Au}) of 5.5 ± 0.76 nm.

Thin silica coating

Tuning the shell thickness via the reaction time: For the thin silica coated AuNRs 2.0 mL AuNRs in 5.0 mM CTAB H₂O were used ($\lambda_{LSPR}= 964$ nm, Ext= 1.42 when diluted 40 \times in H₂O), centrifuged at 9000 rcf for 10 min, redispersed in 22 mL MQ H₂O and transferred to a 40 mL glass vial. While vigorously stirring at room temperature (RT), 3.5 mL sodium silicate (0.54 wt% SiO₂, ~ 0.12 M sodium silicate) was added. After 5 minutes stirring, the reaction vial was placed in a 60 °C waterbath. After 15 min, 30 min, 1 h, 2 h and 4 h part of the reaction mixture was removed from the reaction vial, washed 2 times with 6 mL H₂O, 2 times with 6 mL EtOH and redispersed in 2.0 mL EtOH for storage.

Tuning the shell thickness via the reaction temperature: For the thin silica coated AuNRs 2.0 mL AuNRs in 5.0 mM CTAB H₂O were used ($\lambda_{LSPR}= 964$ nm, Ext= 1.42 when diluted 40 \times in H₂O), centrifuged at 9000 rcf for 10 min and redispersed in 22 mL MQ H₂O. While vigorously stirring at RT, 3.5 mL sodium silicate (0.54 wt% SiO₂, ~ 0.12 M sodium silicate) was added. After 5 minutes stirring, the reaction mixture was divided in 3 batches, which were placed in a 20, 40 or 60 °C waterbath. After 2 h, the reaction mixtures were removed from the reaction vial, washed 2 times with 6 mL H₂O, 2 times with 6 mL EtOH and redispersed in 2.0 mL EtOH for storage.

Stability of the silica shell: It should be noted that all silica coatings described in this section and in particular the thin silica shell grown at low temperatures (20-40 °C) were unstable in water and had the tendency to dissolve [323, 324], leading to aggregation of the gold nanorods. The silica coated rods should therefore always be stored in ethanol. To strengthen the thin silica shell, we dispersed 1.0 mL SiO₂@AuNRs in 10 mL MeOH and heated them at 60 °C for 2 h. Thereafter, the Au@SiO₂ NRs were washed 2 times with and redispersed in 1.0 mL EtOH.

Mesoporous silica coating with 2.5 nm pores

For the mesoporous silica coating we used the procedure of Gorelikov *et al.*[90], which typically yields AuNRs with a 15-20 nm coating containing 2.5 nm wide mesopores. The silica coating was performed on a 10 mL scale. 2.0 mL of the stored AuNRs in 5.0 mM CTAB water were used, to which 1.0 mL 5.0 mM aqueous CTAB solution, 7.0 mL MQ H₂O and 100 μ L 0.10 M NaOH were added. While magnetically stirring at 300 rpm in a 30 °C waterbath, 3 times 30 μ L 0.90 M TEOS in EtOH were added with a 45 min time interval. The Au@SiO₂ NRs were centrifuged at 8000 rcf for 30 min, washed with water and ethanol and redispersed in 2.0 mL EtOH for storage.

Mesoporous silica coating with increased porosity

The pore size of the mesopores in the silica shells was increased by adding a mixture of decane and toluene, which swells the CTAB micelles. We modified the protocol of Gorelikov *et al.* [90] in the following way. To 2.0 mL of the stored AuNRs in 5.0 mM CTAB water, 2.0 mL ethylene glycol and 6.0 mL 5.0 mM CTAB water were added. Next, 100 μL 0.10 M NaOH and 101 μL decane were added. The mixture was stirred at ~ 300 rpm for 2 h in a 70 °C waterbath. Thereafter, 12.8 μL toluene was added. After 2 h of stirring, 3 times 30 μL 0.90 M TEOS in EtOH were added with a 45 min time interval between the additions. The reaction mixture was left overnight at 50 °C. The rods were washed with 8 mL H₂O, 8 mL EtOH and redispersed in 2.0 mL EtOH for storage. Note that the addition of ethylene glycol is crucial to obtain a homogeneous shell growth [325].

Removal of the CTAB from the mesopores

To remove the CTAB and open the mesopores of the silica coated AuNRs, we washed the NRs with 0.10 M HCl in EtOH. To 2.0 mL dispersion of Au@SiO₂ NRs in EtOH, 17 μL of concentrated HCl (12.1 M) was added such that the HCl concentration in EtOH was 0.10 M. The acidified dispersion was sonicated for 30 min at RT. Next, the Au@SiO₂ NRs were centrifuged at 8000 rcf for 15 min, washed 3 times with 2 mL EtOH to remove the HCl. Thereafter, the rods were redispersed in 1.0 mL EtOH and stored in the dark at 4 °C.

Stöber silica coating

To increase the shell thickness of the thin silica coated AuNRs a subsequent growth step was carried out. To 10 mL dispersion (8 mL EtOH, 2 mL H₂O) of 3 nm silica coated AuNRs (Ext= 4.0 when 4 \times diluted in EtOH), 40 μL of a 0.10 M NaOH solution was added, immediately followed by the addition of 100 μL 0.045 mM TEOS in EtOH was added. The reaction was left overnight and washed twice with 10 mL H₂O (7000 rcf \times 15 min) and redispersed in 10 mL EtOH for storage.

Self-assembly

The self-assembly of the silica coated AuNRs into spherical clusters was done via a water in oil emulsion, which is different from the oil in water method described by de Nijs *et al.* used in Chapter 7 [273, 303]. Typically, 300 μL of the silica coated gold nanorods as stored in ethanol were centrifuged at 8000 rcf for 5 min and redispersed in 100 μL MQ H₂O. This aqueous rod suspension was then added to a 40 mL glass vial containing 5.0 mL hexadecane with 1 wt% SPAN80. The mixture was emulsified by mixing for 2 min with a Turrax mixer (IKA T25 digital, Ultra Turrax) of which the speed was set to 6000, 10000 or 180000 rpm depending on the desired droplet size. Afterwards, the vial was covered with teflon tape. With a needle a hole was made in the teflon tape after which the vial was placed in a vortex shaker (IKA KS 260 basic). The emulsion was left to dry for 1-1.5 day while shaking at 300 rpm. The resulting supraparticles were centrifuged at 300-1000 rcf for 5 min and redispersed in 1.0 mL toluene or hexane.

Raman measurements

The sample preparation for the Raman measurements with the supraparticles was done as schematically shown in Figure 8.6. First, the supraparticles were drop-cased on a silicon wafer. Next, the silicon wafer was placed in an ethanol solution containing $1.0 \mu\text{M}$ crystal violet (CV) in EtOH solution for 1 h. Thereafter, the wafer was dried and placed on a glass microscope slide. With scotch tape a copper 200 mesh TEM finder grid was placed on top of the silicon wafer (the copper grid did not contain a polymer film). The glass slide was mounted on a Renishaw Raman microscope equipped with a RL532C50 and RL633nm HeNe laser giving 532 and 633 nm light, respectively, with a maximum power of ~ 12.5 mW. For the Raman measurements a $50\times$ air objective with $\text{NA} = 0.75$ and a laser spot size of about $1 \mu\text{m}$ was used. Typically, a laser power of 0.5% (~ 0.07 mW), exposure time of 1 s and 1 accumulation were used. The step size in the 2D Raman mapping experiments was $0.2 \mu\text{m}$.

The pyridine Raman measurements were carried out as follows: $10 \mu\text{L}$ of the Au@SiO₂ NRs were dried on a silicon wafer, which was placed on a glass microscope slide. Next, $20 \mu\text{L}$ of a 10 mM pyridine in H₂O solution and a glass slide were put on top. For the measurements, a laser power of 10% (~ 0.13 mW), exposure time of 10 s and 1 accumulation were used.

Characterization

The individual silica coated AuNRs and their assemblies were analysed with TEM (transmission electron microscope) on a FEI Talos F200X or FEI Tecnai 20FEG operated at 200 kV. The Tecnai20FEG microscope was equipped with a secondary electron detector enabling the analysis of the surface structure of the supraparticles. The supraparticles used for Raman spectroscopy were characterized with SEM (scanning electron microscope) on a Helios Nanolab G3 UC FIB-SEM (Thermo Fisher Scientific) microscope. The optical properties of the silica coated AuNRs in ethanol and AuNR supraparticles in toluene were measured using a Bruker Vertex 70 FTIR/VIS spectrophotometer.

8.3 Results

Tuning the silica shell thickness and porosity

To regulate the degree of coupling between the AuNRs, we tuned the silica shell thickness of the individual NRs. The synthesis of thin, homogeneous silica shells around AuNRs is particularly challenging, as the ligand (CTAB) concentration should be very low to prevent irregular and mesoporous shell growth. Due to the low surfactant concentration the AuNRs are prone to aggregation. We therefore first developed a suitable synthesis protocol to tune the shell thickness by modifying the synthesis method of Li *et al.* [326]. The most important differences are that we did not use a coupling agent as it is not necessary for the silica shell growth on CTAB stabilized AuNRs and avoided high temperatures ($90 \text{ }^\circ\text{C}$) as this leads to aggregation of the NRs.

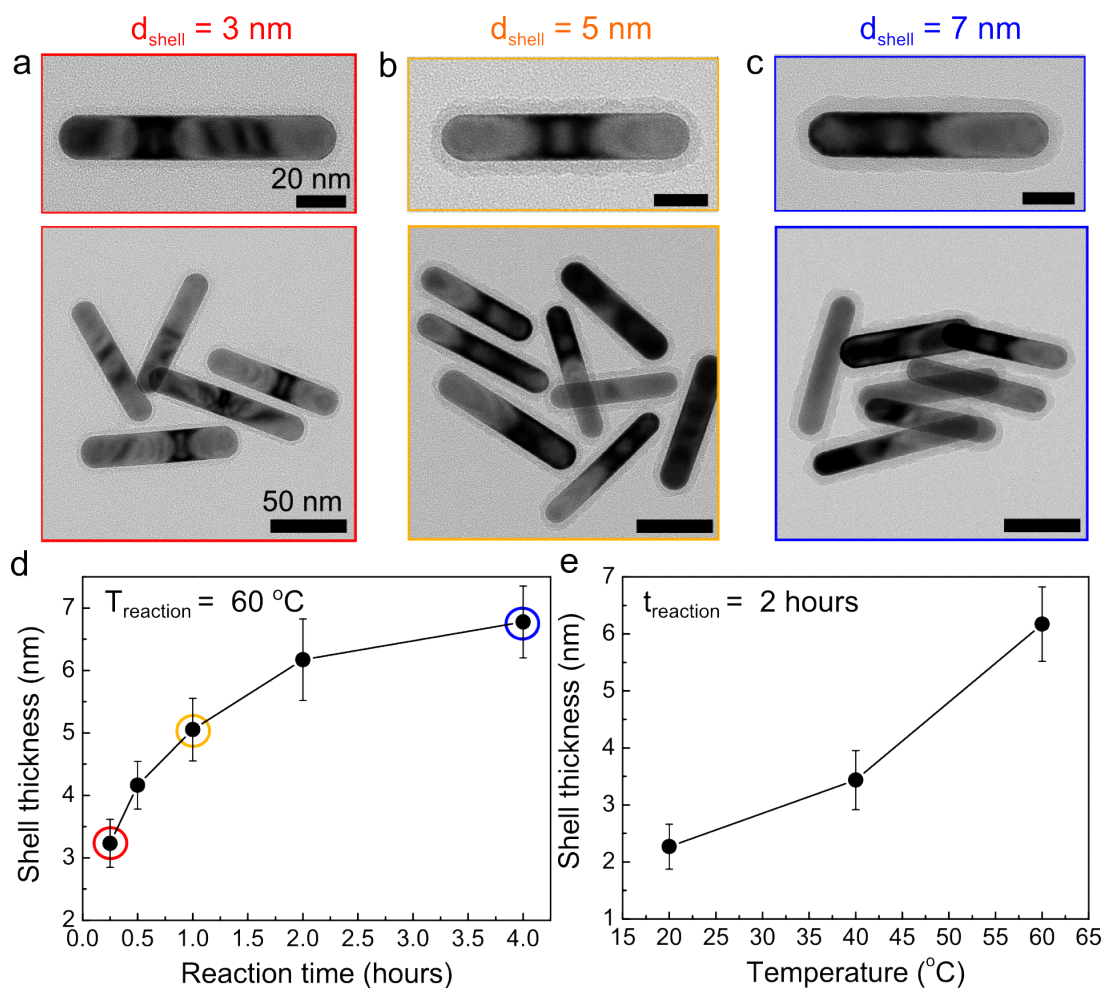


Figure 8.1: Tuning of the silica shell thickness around AuNRs via the reaction time and temperature. 3 nm (a, red), 5 nm (b, orange) and 7 nm (c, blue) thick silica shells were obtained when coating the AuNRs for 15 min, 1 h, and 4 hours at 60 °C, respectively. d) The silica shell thickness plotted as a function of the reaction time at fixed reaction temperature of 60 °C. e) Plot of the silica shell thickness as a function of the reaction temperature with a fixed reaction time of 2 h.

Figure 8.1 shows that we could control the silica shell thickness via the reaction time and temperature. In Figure 8.1a, b and c the transmission electron microscopy images of thin silica coated AuNRs grown at 60 °C for 15 min, 1 h and 4 h with a shell thickness of 3, 5 and 7 nm are shown, respectively. Note that the electron microscopy images in Figure 8.1a-c show that the silica shell became more rough when increasing the shell thickness. In Figure 8.1d, the relation between the silica shell thickness and reaction time is illustrated more clearly, where the shell thickness could be varied between 3 and 7 nm. The plot in Figure 8.1e shows that the shell thickness could also be adjusted via the reaction temperature. Herein, the reaction time was kept constant (2 h) and the temperature varied between 20 and 60 °C. We observed that the silica coatings grown at higher temperatures (60 °C) were more stable in water and are therefore more suitable

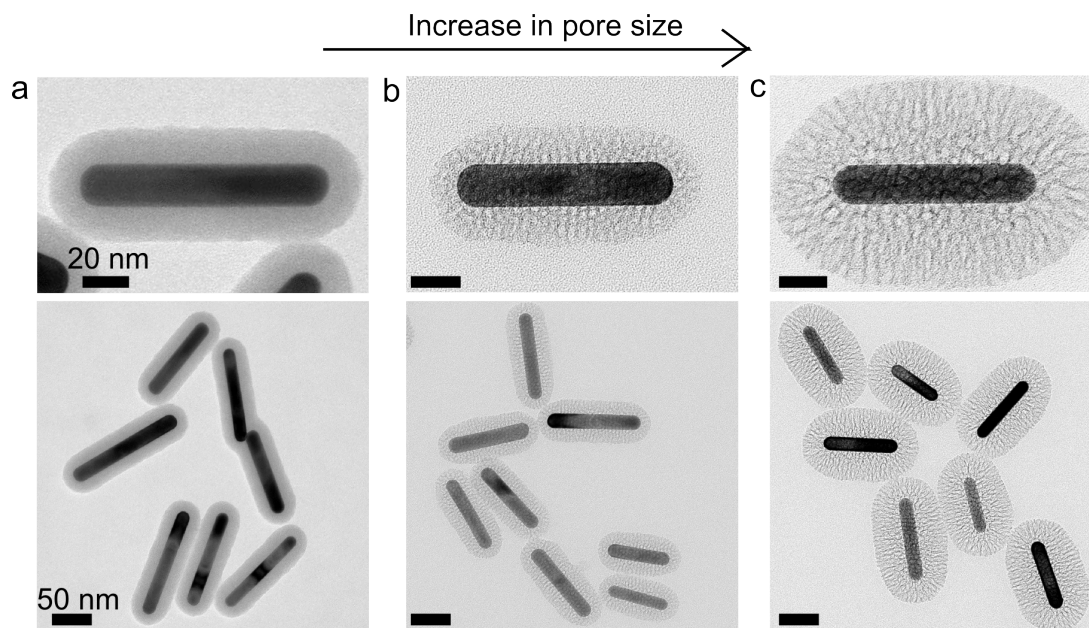


Figure 8.2: Varying the pore size of silica shells around AuNRs. a) Non-porous, Stöber silica coated AuNRs with a shell thickness of 16 nm. b) Mesoporous, 18 nm thick silica coated AuNRs with pores of about 2.5 nm. c) Mesoporous silica coated AuNRs with 4-5 nm wide pores and a shell thickness of 35 nm.

for the subsequent self-assembly experiments. Probably the same stability could also be achieved by an increased temperature annealing step [324].

Apart from the silica shell thickness, the porosity of the silica shells could be controlled. In Figure 8.2 electron microscopy images of AuNRs coated with a non-mesoporous and mesoporous silica shells with a pore size of 2.5 and 4-5 nm are shown. In the synthesis of the non-mesoporous shells (Figure 8.2a), the AuNRs were first coated with a thin silica layer (Figure 8.1). After washing, an additional growth step was carried out to increase the thickness of the non-mesoporous shell. To grow mesoporous silica shells CTAB was added to the reaction mixture. Above the critical micelle concentration (~ 1 mM) CTAB forms micelles, which functioned as template for the mesopore formation in the silica shell growth [90]. The resulting mesoporous silica coated AuNRs are shown in Figure 8.2b. The mesopores had a diameter (d_{pore}) of about 2.5 nm (see Chapter 2).

To create larger pores we modified the procedure of ref. [90] and added a mixture of toluene and decane to swell the CTAB micelles, similar to the method described by Zhang *et al.* for the growth of mesoporous shells around iron oxide NPs [327]. The resulting particles are shown in Figure 8.2c. One can readily see from the electron microscopy images that the pore size was significantly larger than that of the Au@SiO₂ NRs in Figure 8.2b. From the electron microscopy measurements we estimated the pore size to be between 4 and 5 nm. To analyse the pore size more precisely one could consider to perform Raman measurements in which the Au@SiO₂ NRs are exposed to differently sized probe molecules [141] or perform nitrogen physisorption measurements.

Note that although the same amount of silica precursor and the same AuNR concentration were used, the porous silica shells in Figure 8.2c have a thicker shell compared to

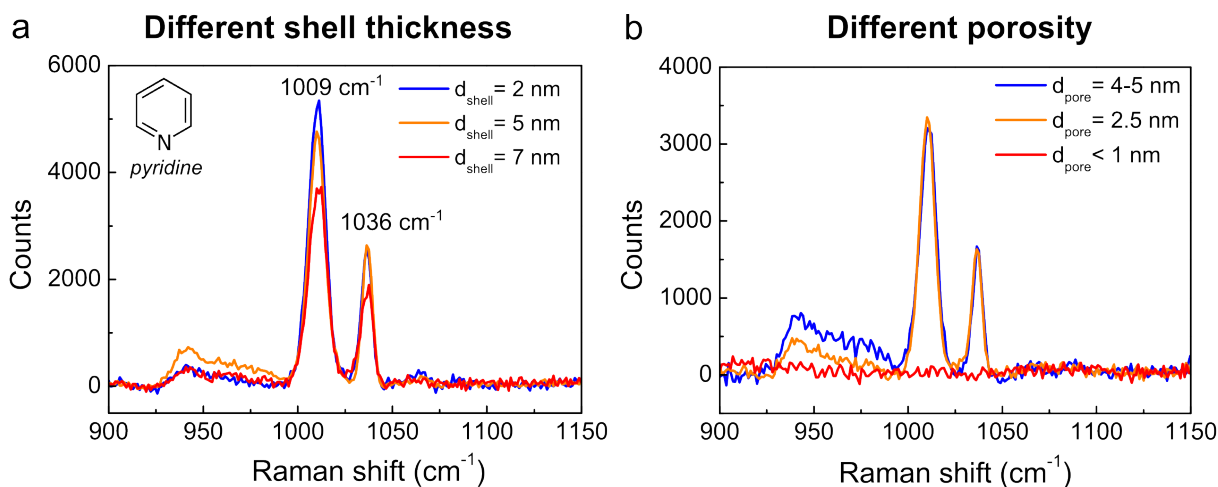


Figure 8.3: Probing the accessibility of silica coated AuNRs with different shell thickness and porosity. a) Raman spectra of pyridine (10 mM in H₂O) recorded in the presence of Au@SiO₂ NRs with a non-mesoporous shell thickness (d_{shell}) of 2 (blue), 5 (orange) and 7 nm (red). b) Raman spectra of pyridine recorded in the presence of Au@SiO₂ NRs with non-mesoporous and mesoporous shells with a pore size (d_{pore}) of <1 (red), 2.5 (orange) and 4-5 nm (blue) and d_{shell} = 16, 18 and 35 nm, respectively. The Au@SiO₂ NRs were dried on a silicon wafer before exposing them to the pyridine solution. Each spectrum in the plot is an average of 5 Raman spectra recorded on different spots in the sample with a 50× air objective (NA= 0.75), laser power of 1.3 mW and measurement time of 10 s.

those in Figure 8.2b. This is most likely due to the higher reaction temperature used for the Au@SiO₂ NRs in Figure 8.2c: 60 instead of 30 °C. Additionally, we noticed that the pore size could be controlled via the toluene/decane ratio [325, 327].

To remove the CTAB-template from the mesopores, the Au@SiO₂ NRs were washed with an acidified ethanol solution (0.10 M HCl). In Chapter 6 we already showed that this is an effective way to remove the CTAB from the pores. Here, we verified the accessibility of the silica coated AuNRs in an additional way. The differently coated nanorods deposited on a silicon wafer were exposed to a dilute aqueous (10 mM) pyridine solution and analysed with Raman spectroscopy. A Raman signal should only be visible if the pyridine binds to the Au surface [326]. Thus, the detection of a Raman signal from pyridine is related to the accessibility of the Au-surface and therefore to the porosity of the silica shell. In Figure 8.3a the Raman spectra of pyridine recorded on thin silica coated AuNRs synthesized at 20, 40 and 60 °C and shell thickness (d_{shell}) of 2, 4 and 7 nm are shown, respectively. In Figure 8.3b the Raman spectra of pyridine recorded on silica coatings with different porosity (Figure 8.2) with pore size (d_{pore}) < 1 nm, 2.5 nm and 4-5 nm after HCl washing are shown. As significant variations in the signal intensity were observed the average of 5 spectra taken at different places in the sample are shown for each sample. The intensity differences were probably due an inhomogeneous distribution of the dried NRs on the silicon wafer. The plots in Figure 8.3 reveal that all Au@SiO₂ NRs were accessible for pyridine, except the Stöber coated ($d_{pore} < 1$ nm) shells. Furthermore, some variation in the intensity of the pyridine signal can be observed. In Figure 8.3a the signal decreased slightly with an increasing shell thickness, implying a decrease in the accessibility of the Au-

surface. It should, however, be noted that the measurements presented in Figure 8.3 are not quantitative. To quantitatively compare the accessible surface area of the differently coated AuNRs it is better to average over more than 5 spectra and to control the number of particles in the laser spot in every measurement. Furthermore, one should control the interparticle distance e.g. via controlled drying to avoid interparticle hotspots [328], which strongly amplify the Raman signal and make that it is no longer proportional to the accessible Au surface area.

Self-assembly of silica coated gold nanorods in spherical supraparticles

Next, we assembled the silica coated AuNRs into spherical supraparticles. To do so, a solvent evaporation method was used similar to the one of de Nijs *et al.* (see also Chapter 7) [273, 303], but now with a water in oil instead of an oil in water emulsion. For the original oil in water method the Au@SiO₂ NRs first had to be functionalized with a hydrophobic coating to be able to disperse them in the oil phase. However, hydrophobic coated Au@SiO₂ NRs are not compatible with SERS measurements of polar analyte solutions as the accessibility of the AuNRs for the probe molecules is severely hampered due to low wetting. Furthermore, when using a water in oil system no additional functionalization step is required and the Au@SiO₂ NRs can readily be dispersed in the water phase. In this study, the oil phase consisted of hexadecane with 1.0 wt% SPAN80. The latter functioned as a surfactant and prevented the water droplets from coalescence.

In Figure 8.4a the assembly process is schematically depicted. First, an aqueous dispersion of the Au@SiO₂ NRs was dispersed in a larger oil phase. Subsequent drying of the water phase, caused shrinkage of the water droplets and led to the formation of spherical supraparticles. In Figure 8.4b and c electron microscopy images of Au@SiO₂ NRs ($L_{Au} = 95 \pm 8$ nm, $D_{Au} = 17 \pm 2$ nm, $d_{shell} = 18$ nm and $d_{pore} = 2.5$ nm) before and after self-assembly are shown. The NRs are randomly oriented in the spherical clusters, which is due to their relatively low aspect ratio ($AR_{Au} = 5.5$, $AR_{Au+SiO_2} \sim 2.5$). Higher aspect ratio rods tend to organize in a more ordered way where the rods have the same orientation (see Chapter 7) [303].

In Figure 8.4d, we show the plasmonic properties of the single and supraparticles with different sizes. The average size of the supraparticles was set via the droplet size of the water droplets in the oil phase, which was varied by emulsifying the water and oil at different mixing speeds. In Figure 8.4 the size distribution of supraparticles with an average size of 380, 480 and 960 nm prepared from emulsions mixed at 6000, 10000 and 18000 rpm, respectively, are shown. From the graph it is clear that the size distributions were rather broad, which allows studying of the SERS performance of differently sized supraparticle in the subsequent Raman measurements.

We used this method to synthesize supraparticles consisting of differently coated AuNRs. By using Au@SiO₂NRs with a small and large shell thickness (3, 18 and 35 nm), supraparticles with strong and weak interparticle hotspots were synthesized, respectively. In Figure 8.5 the resulting supraparticles are shown. In Figure 8.5b and c supraparticles synthesized from 3 nm thick silica coated AuNRs (Figure 8.5a) with interparticle hotspots are shown. The supraparticles in Figure 8.5e-f and Figure 8.5h-i were obtained

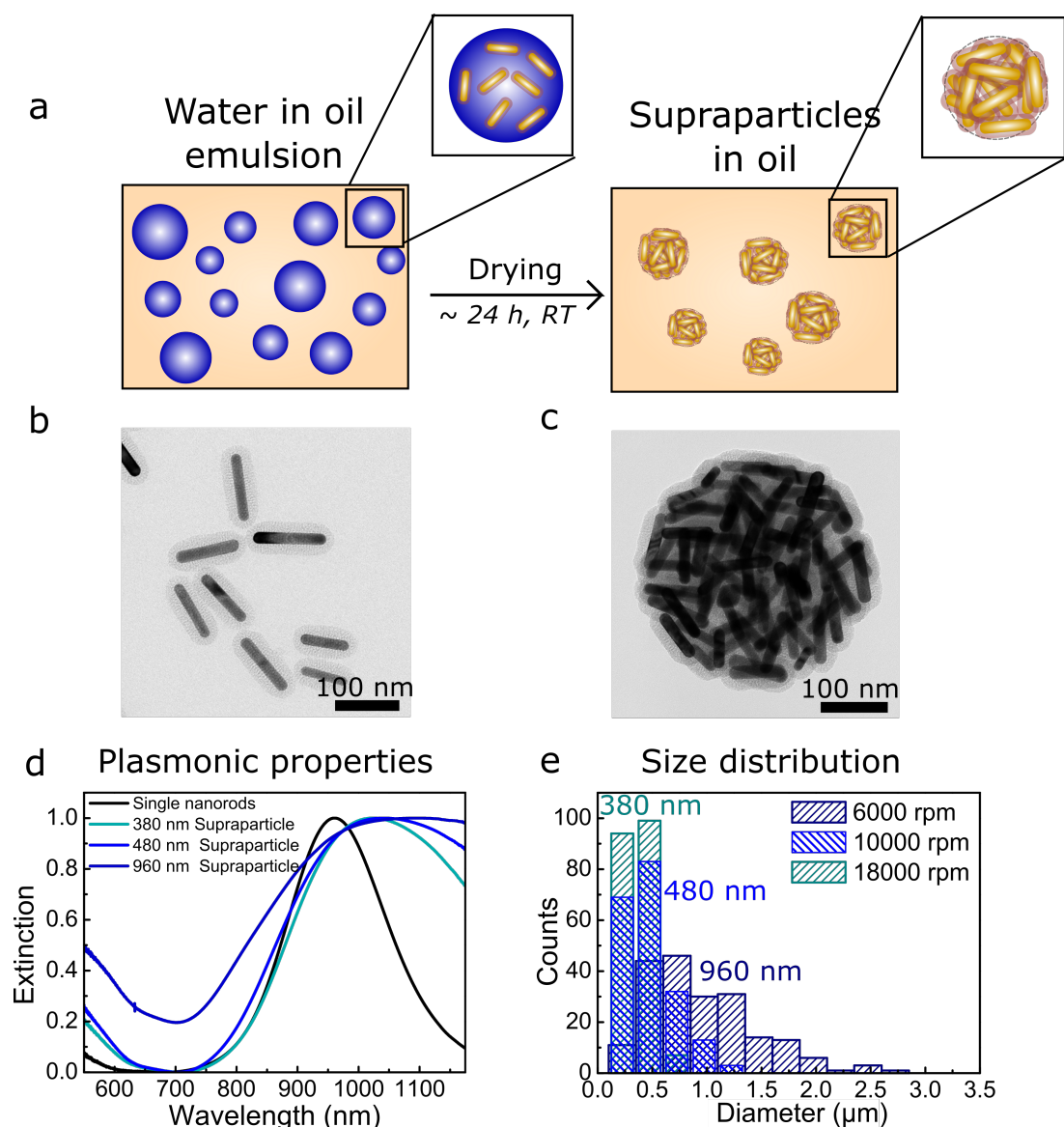


Figure 8.4: Self-assembly of silica coated AuNRs into spherical supraparticles. a) Schematic representation of the assembly process: an aqueous dispersion of Au@SiO₂ NRs was added to a larger oil phase consisting of hexadecane with 1 wt% SPAN80. After emulsification, the water droplets were slowly dried at room temperature (RT) for about 1 day. Upon drying, spherical supraparticles of Au@SiO₂ NRs were formed. b) TEM image of 18 nm thick mesoporous silica coated AuNRs before and c) after self-assembly. d) VIS-NIR spectra of the single Au@SiO₂ NRs (black) and self-assembled as supraparticles with an average assembly size of 380, 480 and 960 nm. e) Histogram of the diameters of the supraparticles prepared by using different mixing speeds in the emulsification process (6000-18000 rpm).

by assembling 18 nm (Figure 8.5d) and 35 nm (Figure 8.5g) thick mesoporous silica coated AuNRs, respectively. The lower magnification TEM images show that the mesoporous silica coated AuNRs all assembled into spherical clusters, whereas the assembly of the thin coated AuNRs also resulted in the formation of non-spherical clusters.

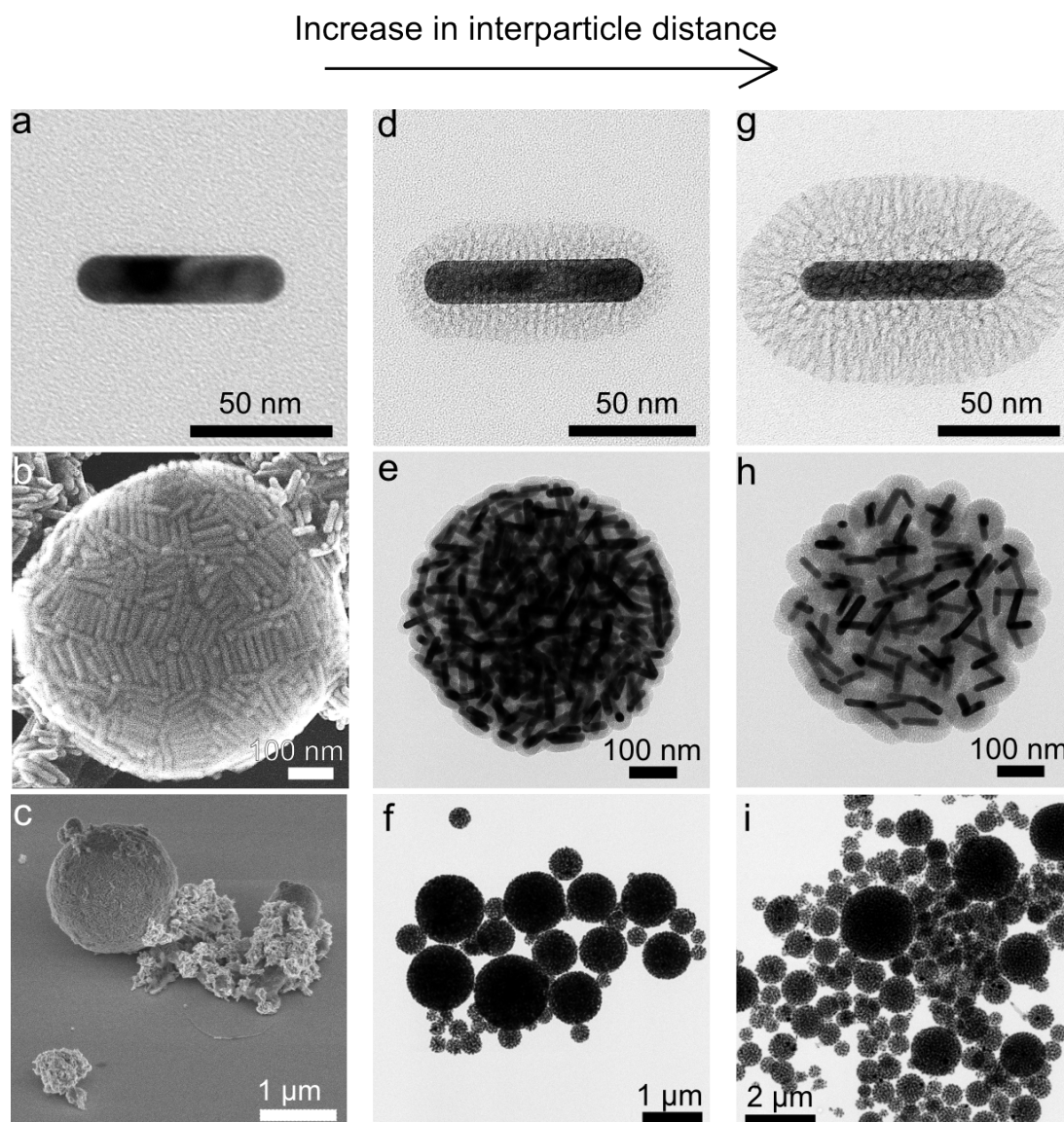


Figure 8.5: Self-assembly of differently silica coated AuNRs into spherical supraparticles. Electron microscopy images of a 2 nm thin (a-c), 18 nm mesoporous (d-f) and 35 nm mesoporous (g-i) silica coated AuNRs before (a,d,g) and after self assembly into supraparticles (b, c, e, f, h, i). All images were recorded in bright mode in the TEM, except b and c, which were recorded by making use of the secondary electron detector in the TEM and SEM, respectively.

Correlative Raman spectroscopy and electron microscopy of gold nanorod supraparticles

The supraparticles presented in Figure 8.5 were studied in Raman spectroscopy to investigate the influence of interparticle plasmonic hotspots on the SERS performance. To do so, we developed a method to probe both the SERS performance as well as the structural properties of the same supraparticle in the electron microscope. The procedure is schematically outlined in Figure 8.6. Crystal violet (CV) was used as a probe molecule (Figure 8.6a) to compare our supraparticles to the AuNR colloidal crystals reported by

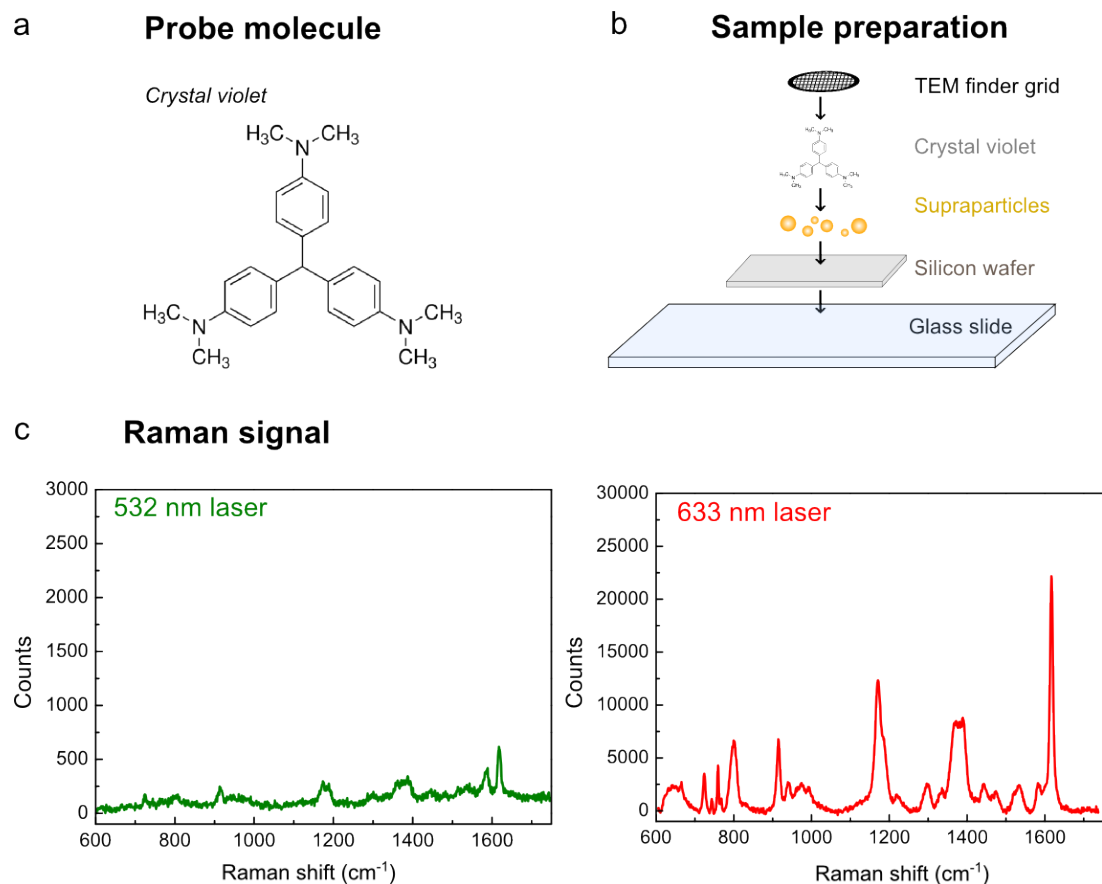


Figure 8.6: Experimental approach for Raman and subsequent electron microscopy measurements on the same supraparticles. a) Structural formula of the probe molecule, crystal violet, used for the Raman microscopy measurements. b) Schematic overview of the sample preparation for the Raman measurements. c) Raman signal of crystal violet on a supraparticle consisting of thin silica coated AuNRs, recorded with a 532 nm and 633 nm laser (0.07 mW). A 50 \times air objective with NA= 0.75 and a laser spot size of about 1 μ m was used. Note that the scale of the left and right graph is from 0-3000 and from 0-30000.

Marzán *et al.* [59, 62]. In Figure 8.6b a schematic overview of the sample preparation is depicted. First, the supraparticles were dropcasted on a silicon wafer. After drying, the supraparticles exposed to a 1.0 μ M CV in ethanol solution. Next, the silicon wafer was placed on a microscope glass slide and a TEM finder grid was placed on top, enabling a correlative Raman and electron microscopy study. For the Raman measurements a 633 nm laser was used, which gave a $\sim 5\times$ higher Raman signal compared to a 532 nm laser (Figure 8.6c). The large difference is due to the fact that 633 nm laser light matches an absorption band of crystal violet and therefore leads to surface enhanced resonant Raman scattering [59], which is known to increase Raman signals up to a factor 6 [329].

In Figure 8.7 the 2D Raman measurements and corresponding FIB-SEM images of a 1.4 μ m large supraparticle consisting of 18 nm mesoporous silica coated AuNR supraparticle, and a 1.3 and 0.9 μ m large supraparticle consisting of 3 nm microporous Au@SiO₂ NRs are shown. The 2D Raman maps were derived by taking the intensity of the Ra-

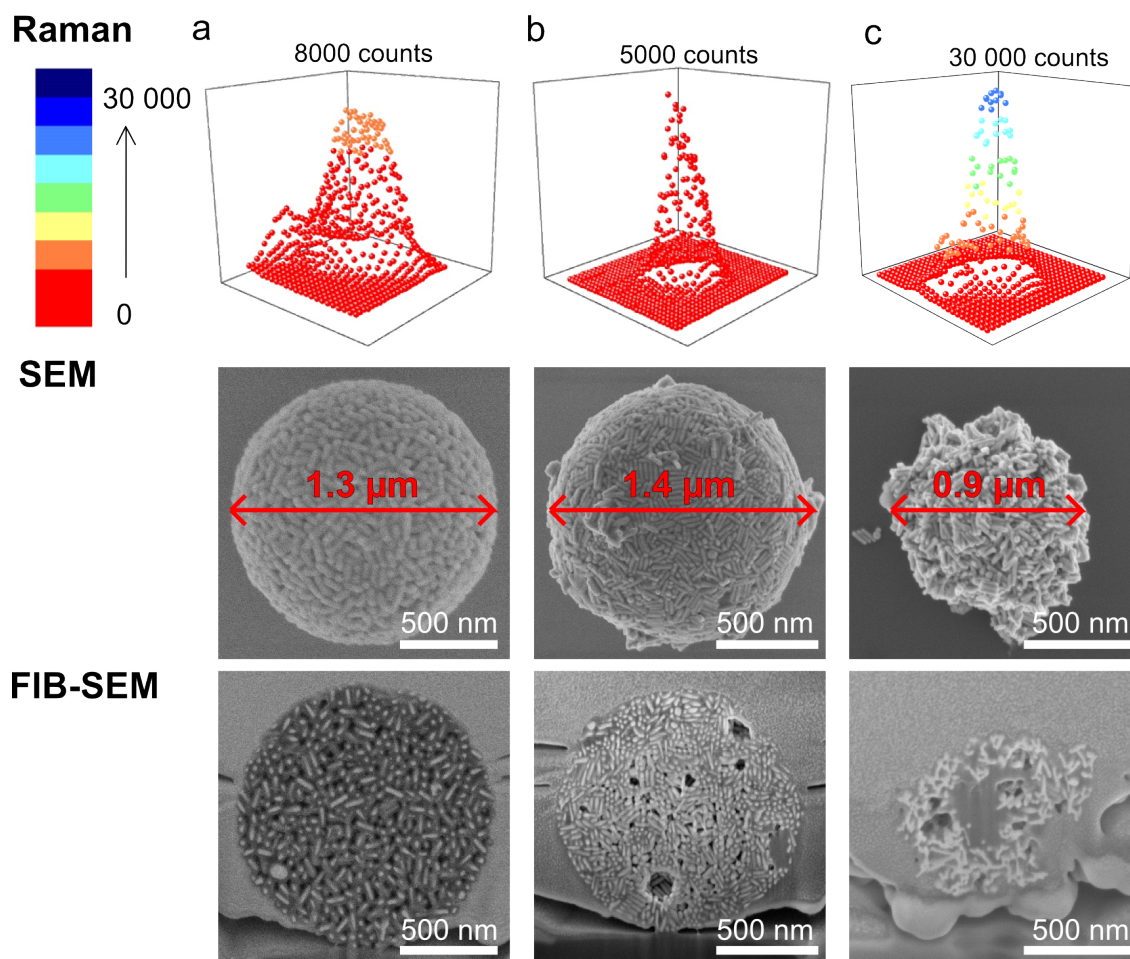


Figure 8.7: Raman spectroscopy and FIB-SEM results of supraparticles containing 18 nm thick mesoporous silica (a) and 3 nm thin microporous silica (b-c) coated AuNRs. Top: 2D Raman measurements showing the intensity of the Raman signal of crystal violet at 1617 cm^{-1} . Middle: SEM images of the corresponding supraparticles. Bottom: the same supraparticles as above but now sliced with FIB-SEM showing the interior of the supraparticles. The Raman measurements were recorded with a 633 nm laser, 0.07 mW laser power, $50\times$ air objective (NA=0.75, spotsize $\sim 1\text{ }\mu\text{m}$). The 2D maps were a collection of spectra recorded as a function of the x and y position with a stepsize of $0.2\text{ }\mu\text{m}$.

man signal at a Raman shift of 1617 cm^{-1} and plotting it as a function of the x and y sample position. Next, the corresponding supraparticles were imaged in the electron microscope. The exterior of the particles is shown in the SEM images. The interior was imaged after embedding the supraparticle in a protective Pt coating and removing part of the supraparticle with a FIB-beam.

The Raman results in Figure 8.7 show that all structures were Raman active and successfully enhanced the Raman signal of crystal violet. The thin microporous silica coated supraparticle with a disordered structure gave the largest enhancement and a maximum intensity of 30 000 counts at 1617 cm^{-1} . Despite the smaller assembly size, the less spherical assembly exhibited a better Raman performance compared to the spherical, $1.3\text{ }\mu\text{m}$ supraparticle composed of the same particles. The FIB-SEM analysis shows that the main

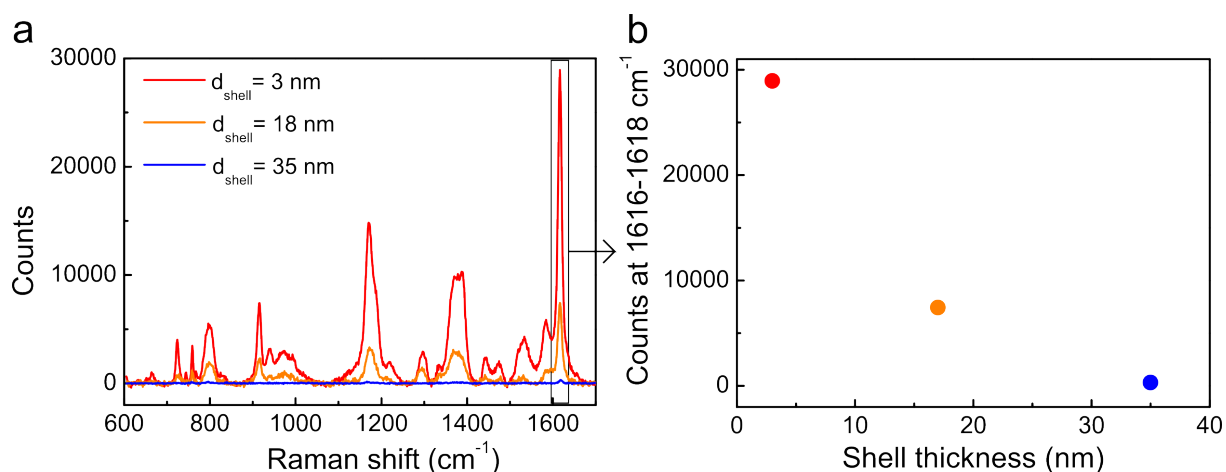


Figure 8.8: SERS performance of supraparticles containing Au@SiO₂ NRs with a different silica shell thickness. a) Raman spectra of crystal violet on supraparticles consisting of Au@SiO₂ NRs with $d_{shell} = 3$ (red), 18 (orange) and 35 nm (blue) and $d_{pore} = <1, 2.5$ and 4-5 nm, respectively. b) The maximum intensity between 1616 and 1618 cm⁻¹ as a function of the shell thickness. The Raman measurements were recorded with a 633 nm laser, 0.07 mW laser power, 50 \times air objective (NA= 0.75, spotsize ~ 1 μ m).

difference between these supraparticles is the assembly structure, where the assembly in Figure 8.7c has a more open and disordered structure, whereas the Au@SiO₂NRs are more closely packed in the assembly in Figure 8.7b. The latter structure is less porous, which could hamper the diffusion of crystal violet into the assembly and thus explain the relatively low Raman signal. The porosity of the supraparticle in Figure 8.7a consisting of mesoporous silica coated AuNRs is high, which could explain why this supraparticles still exhibits a rather high Raman signal, despite the much larger interparticle spacing (~ 36 nm).

To further investigate the influence of the interparticle distance on the SERS performance of the supraparticles, we compared the the SERS signal of CV on supraparticles consisting of Au@SiO₂ NRs with a 3, 18 or 35 nm thick mesoporous silica shell. The resulting Raman spectra are shown in Figure 8.8a. In Figure 8.8b the maximum intensity between 1616 and 1618 cm⁻¹ is plotted as a function of the silica shell thickness. The shell thickness clearly influenced the Raman performance of the Au@SiO₂NRs, where thinner silica shells/smaller interparticle distances led to a steep increase of the Raman signal.

8.4 Discussion

Optimizing the individual nanorods for self-assembly and SERS

In section 8.3.1 we demonstrated a method for the synthesis of 2-7 nm thick shells around AuNRs in which the shell thickness was controlled via the reaction time and reaction temperature. The advantage of our method is that it is simple and only comprises an aqueous AuNR dispersion to which a diluted sodium silicate solution is added. It is likely that this method can be extended to differently shaped CTAB/CTAC stabilized gold nanoparticles such as triangles [14], bipyramids and decahedra [19] and therefore enables the coating of differently shaped plasmonic NPs for SERS and self-assembly. Such thin silica coated plasmonic NPs would also be suitable materials to use for Shell-Isolated Nanoparticle-Enhanced Raman Spectroscopy (SHINERS) in monitoring catalytic reactions *in situ* [65, 317, 318, 326]. For this purpose the silica shell should be closed and made pinhole free, to prevent the gold surface from affecting the catalytic process. The Raman measurements with pyridine in Figure 8.3a showed that the thin silica coatings were not completely closed and part of the gold surface was still accessible. In order to make the particles suitable for SHINERS applications one could grow a thin Stöber layer as we did in Figure 8.2a, or by giving the silica shell a thermal treatment to condensate the silica and decrease the porosity of the shell.

For self-assembly applications the stability of the thin shell can be problematic, especially when doing the self-assembly in water. The high solubility of the silica shell is most likely related to the limited thickness of the shell and the low degree of condensation of the silica. It is known that the solubility of small silica nanoparticles synthesized with sodium silicate in water is particle size dependent, where the solubility increases with decreasing particle size [323]. In addition, the solubility depends on reaction temperature used during the synthesis [323]. Silica particles synthesized at 25 °C are considerably less stable in water compared to those grown at 60 °C, which is ascribed to a lower degree of condensation [323]. This is in line with our results, as we observed that the silica shell stability could significantly be improved by coating the AuNRs at 60 instead of 20 °C or when condensating the silica in MeOH at 60 °C after the synthesis.

To optimize the silica coated AuNRs for SERS, the ability to tune the LSPR via their aspect ratio (AR) should be exploited. Ideally, the LSPR is tuned to the wavelength of the laser light used in the Raman measurements [330]. The AuNRs described in this chapter had a relatively high AR ($AR_{Au} = 5.5$) with a LSPR at $\lambda_{LSPR} = 960$ nm (Figure 8.4d), which is much higher compared to the 633 nm laser light used in the Raman measurements. The wavelength of the laser was optimal for the probe molecule used (crystal violet, Figure 8.6c), whereas the high AR of the rods was chosen to induce a more ordered arrangement of the NRs during the self-assembly (see Chapter 7) [303]. To match the LSPR of the NRs with the laser light one could etch the rods to lower ARs as demonstrated in Chapter 3 or by synthesizing lower AR rods as shown in Chapter 2. This will induce an overlap of the LSPR with the laser light and therefore increase the SERS performance of the Au@SiO₂ NRs and their assemblies.

Controlling the self-assembly of silica coated AuNRs into supraparticles

In general we found that the thin coated AuNRs were more prone to aggregation during the assembly, leading to the formation of non-spherical, unordered supraparticles (Figure 8.5c). The tendency of the thin coated AuNRs to aggregate can be ascribed to different factors. Firstly, the thin silica layer was prone to dissolution in water, resulting in partially uncoated AuNRs which aggregated during the assembly process. As mentioned previously, this problem can be solved by growing the thin silica shell at higher temperatures (60 °C) or giving the silica shell a thermal treatment in methanol to strengthen it. Secondly, the thin shell allowed the AuNRs to approach each other closely, which can give rise to van der Waals attractions between the NRs. Such van der Waals attractions were also found to be important in the self-assembly of much smaller (11 nm, FeO/CoFe₂O₄) NPs into supraparticles [331].

Strong attractions between colloidal particles could prevent the self-assembly into ordered structures. To assess if attractions played a role in our assembly experiments we estimated the van der Waals interaction between two nanorods. Herein, the Au NRs were approximated as cylinders with radius $R = 8.7$ nm and length $L = 95.7$ nm. The attraction due to van der Waals forces between two parallel NRs was estimated by using the following formula [332, 333]:

$$U_{vdW}(z) = -\frac{3}{8\pi} A_H \frac{(\pi R^2)^2 L}{z^5}$$

where z is the separation between the two cylinder axis and A_H is the Hamaker constant, for which values between 20 and 73 $k_B T$ have been reported for gold in water [332]. We use the latter value to estimate the upper bound of this interaction when the two NRs are in contact, that is $U_{vdW}(z = 2R + 2h) = -7k_B T$, where $h = 3$ nm is the silica shell thickness. The van der Waals attractive interactions can be balanced by the electrostatic repulsion between the silica shells. The electrostatic repulsion depends on the conductivity of the solvent and the charge of the silica shells. This means that the effective interaction can be tuned via the thickness and charge of the silica shells around the Au-cores. Although $-7 k_B T$ is significant, it is possible that in our experiments the van der Waals forces between the gold cores were completely screened and attractions did not play a crucial role in the self-assembly. This is supported by the lack of clear evidence for a strong preference for side-to-side arrangement (that is extremely favourable for attractive rods) in the electron microscopy images.

Not only the interparticle interactions can influence the assembly process, the drying rate of the water droplets can determine the structure and morphology of the resulting supraparticles as well. Recently, it was shown that for 244 nm large polystyrene the drying rate was critical for the final structure [334]. Too fast drying (2-4 h) rendered non-spherical, unordered ensembles, whereas slow drying rates (1-40 days) resulted in smooth, crystalline supraparticles [334]. Alternatively, much smaller 6 and 11 nm FeO/CoFe₂O₄ NPs could be dried at elevated temperature within 5 h and still assemble in crystalline supraparticles [273, 331]. In our case, the particle size is in between the small FeO/CoFe₂O₄ NPs and the 244 nm polystyrene spheres. This means that the translational and rotational diffusion time of the NRs is shorter than that of the polystyrene spheres and longer

than that of the FeO/CoFe₂O₄ NPs. We therefore chose an intermediated drying time of 1-1.5 days at room temperature during the self-assembly of the Au@SiO₂ NRs. Drying for several days could potentially render more ordered assemblies but is not necessarily better as the silica shell slowly dissolves in water, resulting in unstable AuNRs over time, which can result in the formation of unordered aggregates.

The emulsion based assembly method described in this chapter has several advantages over template directed methods. Firstly, the emulsion method allows control over the assembly size via the size of the water droplets in the emulsion and the concentration of the NRs dispersed in the droplets. We prepared the emulsion via mixing with a Turrax mixer. Depending on the mixing speed a different average assembly size was obtained (Figure 8.4e). The size and monodispersity can further be improved by using microfluidics, which is a promising way to precisely set the droplet size and make monodisperse supraparticles [334, 335]. Secondly, our emulsion based assembly method yields well-dispersed supraparticles in solution, which enables easy deposition and also allows further modification of the supraparticles via wet chemical methods, e.g. coating them with a protective layer or specific functionality to make them suitable for biomedical applications [336].

Towards quantitative Raman measurements

We compared the SERS performance of the supraparticles to previous studies on AuNR assemblies. The disordered, 0.94 μm supraparticle consisting of thin silica coated AuNRs amplified the Raman signal of crystal violet to 30 000 counts at 1617 cm^{-1} (Figure 8.7c), which is significantly higher compared to assemblies of uncoated AuNRs [59, 61] and comparable AuNRs crystals infiltrated with mesoporous silica [62], which had a signal of 700-1300 and 25 000 counts at 1618-1632 cm^{-1} , respectively. It should be noted that the colloidal crystals in ref [62] contained considerably more AuNRs and had a height of about 1.4-2.0 μm , which means that more particles were in the laser spot when performing the Raman measurements compared to the supraparticles depicted in Figure 8.7. The measurement conditions were slightly different: in refs [59, 61, 62] a 100 \times objective with N.A.= 0.85, 633 nm laser, 0.15 mW and 0.1-0.5 s integration time were used, and in our measurements a 50 \times objective with N.A.= 0.75, 633 nm laser, 0.07 mW and 1.0 s integration time. Although this complicates a quantitative comparison, we can conclude that the supraparticles are able to give similar SERS performance even though they consist of considerably less particles. In addition, there are still plenty of parameters which can be tuned to further optimize the SERS performance of the AuNR supraparticles. One could play with the porosity, aspect ratio and shell thickness of the individual NRs and/or co-assemble a second particle species with high porosity to create binary structures with interparticle hotspots and a high enough porosity for the probe molecules.

In Figure 8.8 we showed that the Raman signal of crystal violet decreased with increasing silica shell thickness, and thus with increasing interparticle distance. The fact that the Au@SiO₂ NRs with $d_{shell}=18$ nm still enhanced the Raman signal more strongly compared to the rods with $d_{shell}=35$ nm could indicate that the Au@SiO₂NRs with $d_{shell}=18$ nm are not fully decoupled and that there is still some overlap of the surface plasmons of the individual NRs. For dimers of AuNRs, the plasmonic coupling was found

to exponentially decay for interparticle separations (d_{gap}) of 0.1-1 times the rod length (L) and complete decoupling of the rods when $d_{gap} = 3 L$ [321]. This means that even for the 18 nm thick coated NRs with a $d_{gap} \sim 36$ nm ($0.4 L$), plasmonic coupling can still occur, which could explain why the Raman signal is higher for the supraparticles consisting of Au@SiO₂ NRs with $d_{shell} = 18$ nm compared to $d_{shell} = 35$ nm. Previously, a similar dependence of the SERS performance on the interparticle distance has been observed for dimers of Ag spheres coated with silica shells of a different thickness. However, in that case the enhancement factor already dropped drastically at $d_{gap} \sim 10-15$ nm [337].

It is worthwhile to point out that the experimental approach described in this chapter would also allow for a direct comparison between experimental measurements and theoretical predictions of the SERS performance of plasmonic particle assemblies. One can first determine the Raman performance followed by a detailed structural analysis with FIB-SEM tomography to render all particle coordinates, interparticle distances and pore volumes (see also Chapter 7) [303]. The particle coordinates can be used as input for calculations to compute the strength of the interparticle hotspots and the theoretical SERS performance [59].

8.5 Conclusions

In this chapter we demonstrated an alternative approach to obtain gold nanorod based assemblies suitable for sensing applications. To tune the properties of the assemblies, the AuNRs were coated with a silica layer prior to the assembly process. By modifying the silica shell (thickness and pore size) the interparticle distance and porosity in the final assembly were adjusted. The self-assembly was carried via an emulsion based solvent evaporation method, yielding spherical assemblies in solution of which the size could be varied via the droplet size of the water in oil emulsion. To correlate the SERS properties of the supraparticles to their structural properties we developed a method to analyse the same particle in Raman spectroscopy and electron microscopy. We showed that both the silica shell thickness as well as the accessibility of the ensemble for the probe molecules are important in the SERS performance of AuNR assemblies, where a more open, porous assembly consisting of 3 nm thin silica coated AuNRs showed the best Raman performance. All together, our work demonstrates that gold nanorod supraparticles are promising materials for sensing and that there is still a wide parameter space to explore in further optimizing these assemblies for SERS applications.

Acknowledgements

We thank Maarten Bransen and Inge Clemens for their help in the synthesis of the non-porous and mesoporous silica coatings, respectively. Matthijs de Winter is thanked for the FIB-SEM imaging. Simone Dussi is acknowledged for useful discussion regarding the interparticle interactions.

References

- [1] E. Roduner, *Size matters: why nanomaterials are different*. Chem. Soc. Rev., 35:583–592, 2006.
- [2] C. Louis and O. Pluchery. *Gold Nanoparticles for Physics, Chemistry, and Biology*. Imperial College Press, 2012.
- [3] M. Haruta, N. Yamada, T. Kobayashi, and S. Iijima, *Gold catalysts prepared by coprecipitation for low-temperature oxidation of hydrogen and of carbon monoxide*. Journal of Catalysis, 115(2):301 – 309, 1989.
- [4] P. Buffat and J.-P. Borel, *Size effect on the melting temperature of gold particles*. Phys. Rev. A, 13:2287–2298, 1976.
- [5] K. Dick, T. Dhanasekaran, Z. Zhang, and D. Meisel, *Size-Dependent Melting of Silica-Encapsulated Gold Nanoparticles*. J. Am. Chem. Soc., 124(10):2312–2317, 2002.
- [6] C. de Mello Donega. *Nanoparticles Workhorses of Nanoscience*. Springer-Verlag Berlin Heidelberg, 2014.
- [7] A. McNaughy. *IUPAC compendium of chemical terminology*. Blackwell Science Inc. (Hoboken), 2nd edition edition, 1997.
- [8] R. Brown, *A brief account of microscopical observations made in the months of june, july and august 1827, on the particles contained in the pollen of plants; and on the general existence of active molecules in organic and inorganic bodies*. The Philosophical Magazine, 4(21):161–173, 1828.
- [9] A. Einstein, *Über die von der molekularkinetischen theorie der wärme geforderte bewegung von in ruhenden flüssigkeiten suspendierten teilchen*. Annalen der Physik, 322(8):549–560, 1905.
- [10] J. Perrin, *Mouvement brownien et réalité moléculaire*. Annales de chimie et de physique, 18, 1909.
- [11] M. A. Boles, M. Engel, and D. V. Talapin, *Self-Assembly of Colloidal Nanocrystals: From Intricate Structures to Functional Materials*. Chem. Rev., 116(18):11220, 2016.
- [12] T. K. Sau and C. J. Murphy, *Room temperature, high-yield synthesis of multiple shapes of gold nanoparticles in aqueous solution*. Journal of the American Chemical Society, 126(28):8648–8649, 2004.
- [13] X. Ye, C. Zheng, J. Chen, Y. Gao, and C. B. Murray, *Using binary surfactant mixtures to simultaneously improve the dimensional tunability and monodispersity in the seeded growth of gold nanorods*. Nano Lett., 13:765–771, 2013.
- [14] L. Scarabelli, M. Coronado-Puchau, J. J. Giner-Casares, J. Langer, and L. M. Liz-Marzán, *Monodisperse gold nanotriangles: Size control, large-scale self-assembly, and performance in surface-enhanced raman scattering*. ACS Nano, 8(6):5833–5842, 2014.
- [15] Y. Xia, K. D. Gilroy, H.-C. Peng, and X. Xia, *Seed-mediated growth of colloidal metal nanocrystals*. Angewandte Chemie International Edition, 56(1):60–95, 2017.
- [16] N. R. Jana, L. Gearheart, and C. J. Murphy, *Wet chemical synthesis of silver nanorods and nanowires of controllable aspect ratio*. Chem. Commun., pages 617–618, 2001.

- [17] Y. Xiong, H. Cai, B. J. Wiley, J. Wang, M. J. Kim, and Y. Xia, *Synthesis and mechanistic study of palladium nanobars and nanorods*. *Journal of the American Chemical Society*, 129(12):3665–3675, 2007.
- [18] N. R. Jana, L. Gearheart, and C. J. Murphy, *Seed-mediated growth approach for shape-controlled synthesis of spheroidal and rod-like gold nanoparticles using a surfactant template*. *Advanced Materials*, 13(18):1389–1393, 2001.
- [19] A. Sánchez-Iglesias, N. Winckelmans, T. Altantzis, S. Bals, M. Grzelczak, and L. M. Liz-Marzán, *High-yield seeded growth of monodisperse pentatwinned gold nanoparticles through thermally induced seed twinning*. *Journal of the American Chemical Society*, 139(1):107–110, 2017.
- [20] B. Nikoobakht and M. A. El-Sayed, *Preparation and growth mechanism of gold nanorods (nrs) using seed-mediated growth method*. *Chemistry of Materials*, 15(10):1957–1962, 2003.
- [21] B. Goris, S. Bals, W. Van den Broek, E. Carbó-Argibay, S. Gómez-Graña, L. M. Liz-Marzán, and G. Van Tendeloo, *Atomic-scale determination of surface facets in gold nanorods*. *Nature Materials*, 11:930–935, 2012.
- [22] W. Tong, M. J. Walsh, P. Mulvaney, J. Etheridge, and A. M. Funston, *Control of symmetry breaking size and aspect ratio in gold nanorods: Underlying role of silver nitrate*. *The Journal of Physical Chemistry C*, 121(6):3549–3559, 2017.
- [23] C. J. Orendorff and C. J. Murphy, *Quantitation of metal content in the silver-assisted growth of gold nanorods*. *The Journal of Physical Chemistry B*, 110(9):3990–3994, 2006.
- [24] S. R. Jackson, J. R. McBride, S. J. Rosenthal, and D. W. Wright, *Where’s the silver? imaging trace silver coverage on the surface of gold nanorods*. *Journal of the American Chemical Society*, 136(14):5261–5263, 2014.
- [25] M. Liu and P. Guyot-Sionnest, *Mechanism of silver(i)-assisted growth of gold nanorods and bipyramids*. *The Journal of Physical Chemistry B*, 109(47):22192–22200, 2005.
- [26] F. Hubert, F. Testard, and O. Spalla, *Cetyltrimethylammonium bromide silver bromide complex as the capping agent of gold nanorods*. *Langmuir*, 24(17):9219–9222, 2008.
- [27] G. Wulff, *Zur frage der geschwindigkeit des wachstums und der auflösung der krystallflagen*. *Zeitschrift für Krystallographie und Mineralogie*, 34, 1901.
- [28] A. Wieckowski and E. R. Savinova. *Catalysis and Electrocatalysis at Nanoparticle Surfaces*. Taylor & Francis e-Library, 2003.
- [29] L. Marks, P. Ajayan, and J. Dundurs, *Quasi-melting of small particles*. *Ultramicroscopy*, 20(1):77 – 82, 1986.
- [30] A. S. Barnard, N. P. Young, A. I. Kirkland, M. A. van Huis, and H. Xu, *Nanogold: A quantitative phase map*. *ACS Nano*, 3(6):1431–1436, 2009.
- [31] M. Faraday, *On the color of colloidal gold*. *Philos. Trans. R. Soc. London*, 147(145), 1857.
- [32] G. Mie, *Beiträge zur optik trüber medien, speziell kolloidaler metallösungen*. *Annalen der Physik*, 330(3):377–445, 1908.
- [33] J. M. Sanz, D. Ortiz, R. Alcaraz de la Osa, J. M. Saiz, F. González, A. S. Brown, M. Lo-surdo, H. O. Everitt, and F. Moreno, *Uv plasmonic behavior of various metal nanoparticles in the near- and far-field regimes: Geometry and substrate effects*. *The Journal of Physical Chemistry C*, 117(38):19606–19615, 2013.

- [34] P. B. Johnson and R. W. Christy, *Optical constants of the noble metals*. Phys. Rev. B, 6:4370–4379, 1972.
- [35] E. D. Palik. *Handbook of Optical Constants of Solids*. Academic Press: San Diego, 1998.
- [36] J. A. Scholl, A. L. Koh, and J. A. Dionne, *Quantum plasmon resonances of individual metallic nanoparticles*. Nature, 483:421–427, 2012.
- [37] R. Gans, *Über die form ultramikroskopischer silberteilchen*. Annalen der Physik, 352(10):270–284, 1915.
- [38] V. Myroshnychenko, J. Rodriguez-Fernandez, I. Pastoriza-Santos, A. M. Funston, C. Novo, P. Mulvaney, L. M. Liz-Marzan, and F. J. Garcia de Abajo, *Modelling the optical response of gold nanoparticles*. Chem. Soc. Rev., 37:1792–1805, 2008.
- [39] C. V. Raman and K. S. Krishnan, *Polarisation of scattered light-quanta*. Nature, 122:169, 1928.
- [40] Y. Wang, B. Yan, and L. Chen, *Sers tags: Novel optical nanoprobess for bioanalysis*. Chemical Reviews, 113(3):1391–1428, 2013.
- [41] C. Muehlethaler, M. Leona, and J. R. Lombardi, *Review of surface enhanced raman scattering applications in forensic science*. Analytical Chemistry, 88(1):152–169, 2016.
- [42] M. Fleischmann, P. Hendra, and A. McQuillan, *Raman spectra of pyridine adsorbed at a silver electrode*. Chemical Physics Letters, 26(2):163 – 166, 1974.
- [43] D. L. Jeanmaire and R. P. V. Duyne, *Surface raman spectroelectrochemistry: Part i. heterocyclic, aromatic, and aliphatic amines adsorbed on the anodized silver electrode*. Journal of Electroanalytical Chemistry and Interfacial Electrochemistry, 84(1):1 – 20, 1977.
- [44] M. G. Albrecht and J. A. Creighton, *Anomalously intense raman spectra of pyridine at a silver electrode*. Journal of the American Chemical Society, 99(15):5215–5217, 1977.
- [45] N. Félidj, J. Aubard, G. Lévi, J. R. Krenn, M. Salerno, G. Schider, B. Lamprecht, A. Leitner, and F. R. Aussenegg, *Controlling the optical response of regular arrays of gold particles for surface-enhanced raman scattering*. Phys. Rev. B, 65:075419, Feb 2002.
- [46] A. Lee, G. F. S. Andrade, A. Ahmed, M. L. Souza, N. Coombs, E. Tumarkin, K. Liu, R. Gordon, A. G. Brolo, and E. Kumacheva, *Probing dynamic generation of hot-spots in self-assembled chains of gold nanorods by surface-enhanced raman scattering*. Journal of the American Chemical Society, 133(19):7563–7570, 2011.
- [47] G. C. Schatz, M. A. Young, and R. P. Van Duyne. *Electromagnetic Mechanism of SERS*. Springer Berlin Heidelberg, Berlin, Heidelberg, 2006.
- [48] S. Yi, L. Sun, S. C. Lenaghan, Y. Wang, X. Chong, Z. Zhang, and M. Zhang, *One-step synthesis of dendritic gold nanoflowers with high surface-enhanced raman scattering (sers) properties*. RSC Adv., 3:10139–10144, 2013.
- [49] M. N. Sanz-Ortiz, K. Sentosun, S. Bals, and L. M. Liz-Marzán, *Templated growth of surface enhanced raman scattering-active branched gold nanoparticles within radial mesoporous silica shells*. ACS Nano, 9(10):10489–10497, 2015.
- [50] R. Contreras-Caceres, C. Dawson, P. Formanek, D. Fischer, F. Simon, A. Janke, P. Uhlmann, and M. Stamm, *Polymers as templates for au and au@ag bimetallic nanorods: Uv-vis and surface enhanced raman spectroscopy*. Chemistry of Materials, 25(2):158–169, 2013.

- [51] S. Nie and S. R. Emory, *Probing single molecules and single nanoparticles by surface-enhanced raman scattering*. *Science*, 275(5303):1102–1106, 1997.
- [52] Y. Yang, J. Liu, Z.-W. Fu, and D. Qin, *Galvanic replacement-free deposition of Au on Ag for core-shell nanocubes with enhanced chemical stability and SERS activity*. *Journal of the American Chemical Society*, 136(23):8153–8156, 2014.
- [53] S. Gómez-Graña, B. Goris, T. Altantzis, C. Fernández-López, E. Carbó-Argibay, A. Guerrero-Martínez, N. Almora-Barrios, N. López, I. Pastoriza-Santos, J. Pérez-Juste, S. Bals, G. Van Tendeloo, and L. M. Liz-Marzán, *Au@Ag nanoparticles: Halides stabilize 100 facets*. *The Journal of Physical Chemistry Letters*, 4(13):2209–2216, 2013.
- [54] T. S. Deng, J. E. S. Van Der Hoeven, A. O. Yalcin, H. W. Zandbergen, M. A. Van Huis, and A. Van Blaaderen, *Oxidative etching and metal overgrowth of gold nanorods within mesoporous silica shells*. *Chem. Mater.*, 27:7196–7230, 2015.
- [55] M. Rycenga, C. M. Cobley, J. Zeng, W. Li, C. H. Moran, Q. Zhang, D. Qin, and Y. Xia, *Controlling the synthesis and assembly of silver nanostructures for plasmonic applications*. *Chemical Reviews*, 111(6):3669–3712, 2011.
- [56] C. Gao, Y. Hu, M. Wang, M. Chi, and Y. Yin, *Fully Alloyed Ag/Au Nanospheres: Combining the Plasmonic Property of Ag with the Stability of Au*. *J. Am. Chem. Soc.*, 136(20):7474–7479, 2014.
- [57] W. Albrecht, J. E. S. Van Der Hoeven, T. S. Deng, P. E. De Jongh, and A. Van Blaaderen, *Fully Alloyed Metal Nanorods with Highly Tunable Properties*. *Nanoscale*, 9:2845–2851, 2017.
- [58] M. Moskovits, *Surface-enhanced raman spectroscopy: a brief retrospective*. *Journal of Raman Spectroscopy*, 36(6-7):485–496, 2005.
- [59] C. Hamon, S. M. Novikov, L. Scarabelli, D. M. Solís, T. Altantzis, S. Bals, J. M. Taboada, F. Obelleiro, and L. M. Liz-Marzán, *Collective plasmonic properties in few-layer gold nanorod supercrystals*. *ACS Photonics*, 2(10):1482–1488, 2015.
- [60] R. A. Alvarez-Puebla, A. Agarwal, P. Manna, B. P. Khanal, P. Aldeanueva-Potel, E. Carbó-Argibay, N. Pazos-Pérez, L. Vigdeman, E. R. Zubarev, N. A. Kotov, and L. M. Liz-Marzán, *Gold nanorods 3d-supercrystals as surface enhanced raman scattering spectroscopy substrates for the rapid detection of scrambled prions*. *Proceedings of the National Academy of Sciences*, 108(20):8157–8161, 2011.
- [61] C. Hamon, S. Novikov, L. Scarabelli, L. Basabe-Desmonts, and L. M. Liz-Marzán, *Hierarchical self-assembly of gold nanoparticles into patterned plasmonic nanostructures*. *ACS Nano*, 8(10):10694–10703, 2014.
- [62] C. Hamon, M. N. Sanz-Ortiz, E. Modin, E. H. Hill, L. Scarabelli, A. Chuvilin, and L. M. Liz-Marzán, *Hierarchical organization and molecular diffusion in gold nanorod/silica supercrystal nanocomposites*. *Nanoscale*, 8:7914, 2016.
- [63] S. Wintzheimer, T. Granath, M. Oppmann, T. Kister, T. Thai, T. Kraus, N. Vogel, and K. Mandel, *Supraparticles: Functionality from uniform structural motifs*. *ACS Nano*, 12(6):5093–5120, 2018.
- [64] X.-M. Qian and S. M. Nie, *Single-molecule and single-nanoparticle sers: from fundamental mechanisms to biomedical applications*. *Chem. Soc. Rev.*, 37:912–920, 2008.

- [65] T. Hartman and B. M. Weckhuysen, *Thermally stable TiO₂- and SiO₂-shell-isolated au nanoparticles for in situ plasmon-enhanced raman spectroscopy of hydrogenation catalysts*. Chemistry – A European Journal, 24(15):3733–3741, 2018.
- [66] F. Casadio, M. Leona, J. R. Lombardi, and R. Van Duyne, *Identification of organic colorants in fibers, paints, and glazes by surface enhanced raman spectroscopy*. Accounts of Chemical Research, 43(6):782–791, 2010.
- [67] P. Sabatier, *Hydrogénations et deshydrogénations par catalyse*. Ber. Dtsch. Chem. Ges., 44:1984, 1911.
- [68] A. Balandin. *Modern state of the multiplet theor of heterogeneous catalysis*. volume 19 of *Advances in Catalysis*, pages 1 – 210. Academic Press, 1969.
- [69] C. T. Campbell and J. R. V. Sellers, *Enthalpies and entropies of adsorption on well-defined oxide surfaces: Experimental measurements*. Chemical Reviews, 113(6):4106–4135, 2013.
- [70] J. K. Nørskov, F. Abild-Pedersen, F. Studt, and T. Bligaard, *Density functional theory in surface chemistry and catalysis*. Proceedings of the National Academy of Sciences, 108:937–943, 2011.
- [71] F. Studt, F. Abild-Pedersen, T. Bligaard, R. Z. Sørensen, C. H. Christensen, and J. K. Nørskov, *Identification of non-precious metal alloy catalysts for selective hydrogenation of acetylene*. Science, 320(5881):1320–1322, 2008.
- [72] R. D. Ramsier, Q. Gao, H. Neergaard Waltenburg, and J. T. Yates, *Thermal dissociation of no on pd surfaces: The influence of step sites*. The Journal of Chemical Physics, 100(9):6837–6845, 1994.
- [73] R. Kose, W. A. Brown, and D. A. King, *Energetics and kinetics of step-terrace adsorbate distribution: C₂H₂ on Pt211*. Journal of the American Chemical Society, 121(20):4845–4851, 1999.
- [74] M. Turner, V. B. Golovko, O. P. H. Vaughan, P. Abdulkin, A. Berenguer-Murcia, M. S. Tikhov, B. F. G. Johnson, and R. M. Lambert, *Selective oxidation with dioxygen by gold nanoparticle catalysts derived from 55-atom clusters*. Nature, 454:981–984, 2008.
- [75] Q. Zhang, L. Han, H. Jing, D. A. Blom, Y. Lin, H. L. Xin, and H. Wang, *Facet control of gold nanorods*. ACS Nano, 10(2):2960–2974, 2016.
- [76] X. Wang, S.-I. Choi, L. T. Roling, M. Luo, C. Ma, L. Zhang, M. Chi, J. Liu, Z. Xie, J. A. Herron, M. Mavrikakis, and Y. Xia, *Palladium–platinum core-shell icosahedra with substantially enhanced activity and durability towards oxygen reduction*. Nature Communications, 6:7594, 2015.
- [77] K. Zhou and Y. Li, *Catalysis based on nanocrystals with well-defined facets*. Angewandte Chemie International Edition, 51(3):602–613, 2012.
- [78] S. Xie, S.-I. Choi, X. Xia, and Y. Xia, *Catalysis on faceted noble-metal nanocrystals: both shape and size matter*. Current Opinion in Chemical Engineering, 2(2):142 – 150, 2013. Nanotechnology / Separation engineering.
- [79] C. T. Campbell and J. R. V. Sellers, *Electronic perturbations*. Nature Chemistry, 4:597, 2013.
- [80] X. Y. Liu, A. Wang, T. Zhang, and C.-Y. Mou, *Catalysis by gold: New insights into the support effect*. Nano Today, 8(4):403 – 416, 2013.

- [81] C. Hernández Mejía, T. W. van Deelen, and K. P. de Jong, *Thermal dissociation of no on pd surfaces: The influence of step sites*. The Journal of Chemical Physics, 9:4459, 2018.
- [82] M. Cargnello, V. V. T. Doan-Nguyen, T. R. Gordon, R. E. Diaz, E. A. Stach, R. J. Gorte, P. Fornasiero, and C. B. Murray, *Control of metal nanocrystal size reveals metal-support interface role for ceria catalysts*. Science, 341(6147):771–773, 2013.
- [83] Y. Kang, X. Ye, J. Chen, L. Qi, R. E. Diaz, V. Doan-Nguyen, G. Xing, C. R. Kagan, J. Li, R. J. Gorte, E. A. Stach, and C. B. Murray, *Engineering catalytic contacts and thermal stability: Gold/iron oxide binary nanocrystal superlattices for co oxidation*. J. Am. Chem. Soc., 135(4):1499, 2013.
- [84] D. Widmann and R. J. Behm, *Active oxygen on a Au/TiO₂ catalyst: Formation, stability, and CO oxidation activity*. Angewandte Chemie International Edition, 50(43):10241–10245, 2011.
- [85] R. Bliem, J. van der Hoeven, A. Zavodny, O. Gamba, J. Pavelec, P. E. de Jongh, M. Schmid, U. Diebold, and G. S. Parkinson, *An atomic-scale view of CO and H₂ oxidation on a Pt/Fe₃O₄ model catalyst*. Angewandte Chemie, 127(47):14205–14208, 2015.
- [86] K. D. Gilroy, A. Ruditskiy, H.-C. Peng, D. Qin, and Y. Xia, *Bimetallic nanocrystals: Syntheses, properties, and applications*. Chemical Reviews, 116(18):10414–10472, 2016.
- [87] E. V. Shevchenko, D. V. Talapin, C. B. Murray, and S. O’Brien, *Structural characterization of self-assembled multifunctional binary nanoparticle superlattices*. Journal of the American Chemical Society, 128(11):3620–3637, 2006.
- [88] M. Cargnello, P. Fornasiero, and R. J. Gorte, *Playing with structures at the nanoscale: Designing catalysts by manipulation of clusters and nanocrystals as building blocks*. ChemPhysChem, 14(17):3869–3877, 2013.
- [89] S. H. Joo, J. Y. Park, C.-K. Tsung, Y. Yamada, P. Yang, and G. A. Somorjai, *Thermally stable Pt/mesoporous silica core-shell nanocatalysts for high-temperature reactions*. Nat. Mater., 8(2):126–131, 2009.
- [90] I. Gorelikov and N. Matsuura, *Supporting Information Single-Step Coating of Mesoporous Silica on CTAB- Capped Nanoparticles*. Nano Lett., 8:369–373, 2008.
- [91] Gergely-F *Thermal stability of mesoporous silica-coated gold nanorods with different aspect ratios*. Materials Chemistry and Physics, 148(3):909 – 913, 2014.
- [92] S. M. Ansar, F. S. Ameer, W. Hu, S. Zou, C. U. Pittman, and D. Zhang, *Removal of molecular adsorbates on gold nanoparticles using sodium borohydride in water*. Nano Letters, 13(3):1226–1229, 2013.
- [93] B. Donoeva and P. E. de Jongh, *Colloidal Au catalyst preparation: Selective removal of polyvinylpyrrolidone from active au sites*. ChemCatChem, 10(5):989–997, 2018.
- [94] G. J. Hutchings, *Heterogeneous gold catalysis*. ACS Central Science, 4(9):1095–1101, 2018.
- [95] B. G. Donoeva, D. S. Ovoshchnikov, and V. B. Golovko, *Establishing a Au nanoparticle size effect in the oxidation of cyclohexene using gradually changing au catalysts*. ACS Catalysis, 3(12):2986–2991, 2013.
- [96] B. Donoeva, N. Masoud, and P. E. de Jongh, *Carbon support surface effects in the gold-catalyzed oxidation of 5-hydroxymethylfurfural*. ACS Catalysis, 7(7):4581–4591, 2017.
- [97] N. Masoud, L. Delannoy, C. Calers, and J. J. Gallet, *Silica-Supported Au-Ag Catalysts for the Selective Hydrogenation of Butadiene*. Chem. Cat. Chem., 9:2418–2425, 2017.

- [98] J.-H. Liu Wang, A.-Q., Chin, Y.-S., Lin, H.-P. and Mou, C.-Y., *Synergistic Effect in an Au-Au Alloy Nanocatalyst: CO Oxidation*. J. Phys. Chem. B, 109:40–43, 2005.
- [99] N. E. Kolli, L. Delannoy, and C. Louis, *Bimetallic au–pd catalysts for selective hydrogenation of butadiene: Influence of the preparation method on catalytic properties*. Journal of Catalysis, 297:79 – 92, 2013.
- [100] H. Liao, A. Fisher, and Z. J. Xu, *Surface Segregation in Bimetallic Nanoparticles: A Critical Issue in Electrocatalyst Engineering*. Small, 11(27):3221–3246, 2015.
- [101] M. Ahmadi, F. Behafarid, C. Cui, P. Strasser, and B. R. Cuenya, *Long-Range Segregation Phenomena in Shape-Selected Bimetallic Nanoparticles: Chemical State Effects*. ACS Nano, 7(10):9195–9204, 2013.
- [102] B. Zugic, L. Wang, C. Heine, D. N. Zakharov, B. A. J. Lechner, E. A. Stach, J. Biener, M. Salmeron, R. J. Madix, and C. M. Friend, *Dynamic restructuring drives catalytic activity on nanoporous gold-silver alloy catalysts*. Nat. Mater., 16:558–565, 2016.
- [103] P. Destro, T. M. Kokumai, A. Scarpellini, L. Pasquale, L. Manna, M. Colombo, and D. Zanchet, *The crucial role of the support in the transformations of bimetallic nanoparticles and catalytic performance*. ACS Catal., 8(2):1031–1037, 2018.
- [104] J. E. S. van der Hoeven, T. A. J. Welling, T. A. G. Silva, J. E. van den Reijen, C. La Fontaine, X. Carrier, C. Louis, A. van Blaaderen, and P. E. de Jongh, *In situ observation of atomic redistribution in alloying gold-silver nanorods*. ACS Nano, 12(8):8467–8476, 2018.
- [105] F. Tao, M. E. Grass, Y. Zhang, D. R. Butcher, J. R. Renzas, Z. Liu, J. Y. Chung, B. S. Mun, M. Salmeron, and G. A. Somorjai, *Reaction-driven restructuring of Rh-Pd and Pt-Pd core-shell nanoparticles*. Science, 322:932–934, 2008.
- [106] T. Bligaard and J. Nørskov, *Ligand effects in heterogeneous catalysis and electrochemistry*. Electrochimica Acta, 52(18):5512 – 5516, 2007. Surface Imaging/Spectroscopy at Solid/Liquid Interface (ISSIS).
- [107] S. Mukherjee, F. Libisch, N. Large, O. Neumann, L. V. Brown, J. Cheng, J. B. Lassiter, E. A. Carter, P. Nordlander, and N. J. Halas, *Hot electrons do the impossible: Plasmon-induced dissociation of H₂ on Au*. Nano Letters, 13(1):240–247, 2013.
- [108] S. Linic, U. Aslam, C. Boerigter, and M. Morabito, *Photochemical transformations on plasmonic metal nanoparticles*. Nat. Mater., 14(6):567–576, 2015.
- [109] M. J. Kale, T. Avanesian, and P. Christopher, *Direct photocatalysis by plasmonic nanostructures*. ACS Catalysis, 4(1):116–128, 2014.
- [110] W. Ni, X. Kou, Z. Yang, and J. Wang, *Tailoring longitudinal surface plasmon wavelengths, scattering and absorption cross sections of gold nanorods*. ACS Nano, 2(4):677–686, 2008.
- [111] P. Zijlstra, J. W. M. Chon, and M. Gu, *Five-Dimensional Optical Recording Mediated by Surface Plasmons in Gold Nanorods*. Nature, 459(7245):410–413, 2009.
- [112] P. Zijlstra, J. W. M. Chon, and M. Gu, *Effect of heat accumulation on the dynamic range of a gold nanorod doped polymer nanocomposite for optical laser writing and patterning*. Opt. Express, 15:12151–12160, 2007.
- [113] A. B. Taylor, J. Kim, and J. W. M. Chon, *Detuned surface plasmon resonance scattering of gold nanorods for continuous wave multilayered optical recording and readout*. Opt. Express, 20(5):5069–5081, Feb 2012.

- [114] L. C. Kennedy, L. R. Bickford, N. A. Lewinski, A. J. Coughlin, Y. Hu, E. S. Day, J. L. West, and R. A. Drezek, *A New Era for Cancer Treatment: Gold-Nanoparticle-Mediated Thermal Therapies*. *Small*, 7:169–183, 2011.
- [115] X. Huang, I. H. El-Sayed, W. Qian, and M. A. El-Sayed, *Cancer cell imaging and photothermal therapy in the near-infrared region by using gold nanorods*. *Journal of the American Chemical Society*, 128(6):2115–2120, 2006.
- [116] Z. Zhang, L. Wang, J. Wang, X. Jiang, X. Li, Z. Hu, Y. Ji, X. Wu, and C. Chen, *Mesoporous silica-coated gold nanorods as a light-mediated multifunctional theranostic platform for cancer treatment*. *Advanced Materials*, 24(11):1418–1423, 2012.
- [117] B. Li, T. Gu, T. Ming, J. Wang, P. Wang, J. Wang, and J. C. Yu, *(gold core)@(ceria shell) nanostructures for plasmon-enhanced catalytic reactions under visible light*. *ACS Nano*, 8(8):8152–8162, 2014.
- [118] Z. Zheng, T. Tachikawa, and T. Majima, *Single-particle study of Pt modified Au nanorods for plasmon-enhanced hydrogen generation in visible to near-infrared region*. *Journal of the American Chemical Society*, 136(19):6870–6873, 2014.
- [119] H. Petrova, J. Perez Juste, I. Pastoriza-Santos, G. V. Hartland, L. M. Liz-Marzán, and P. Mulvaney, *On the temperature stability of gold nanorods: comparison between thermal and ultrafast laser-induced heating*. *Phys. Chem. Chem. Phys.*, 8:814–821, 2006.
- [120] C. van Kats. *Anisotropic Model Colloids*. PhD thesis, Utrecht University, 2008. available at www.colloids.nl.
- [121] W. Albrecht, A. van de Glind, H. Yoshida, Y. Isozaki, A. Imhof, A. van Blaaderen, P. E. de Jongh, K. P. de Jong, J. Zečević, and S. Takeda, *Impact of the electron beam on the thermal stability of gold nanorods studied by environmental transmission electron microscopy*. *Ultramicroscopy*, 193:97 – 103, 2018.
- [122] A. B. Taylor, A. M. Siddiquee, and J. W. M. Chon, *Below melting point photothermal reshaping of single gold nanorods driven by surface diffusion*. *ACS Nano*, 8(12):12071–12079, 2014.
- [123] W. Albrecht, T.-S. Deng, B. Goris, M. A. van Huis, S. Bals, and A. van Blaaderen, *Single particle deformation and analysis of silica-coated gold nanorods before and after femtosecond laser pulse excitation*. *Nano Letters*, 16(3):1818–1825, 2016.
- [124] Y. Khalavka, C. Ohm, L. Sun, F. Banhart, and C. Sönnichsen, *Enhanced thermal stability of gold and silver nanorods by thin surface layers*. *The Journal of Physical Chemistry C*, 111(35):12886–12889, 2007.
- [125] Y.-S. Chen, W. Frey, S. Kim, K. Homan, P. Kruizinga, K. Sokolov, and S. Emelianov, *Enhanced thermal stability of silica-coated gold nanorods for photoacoustic imaging and image-guided therapy*. *Opt. Express*, 18(9):8867–8878, Apr 2010.
- [126] N. A. Joy, B. K. Janiszewski, S. Novak, T. W. Johnson, S.-H. Oh, A. Raghunathan, J. Hartley, and M. A. Carpenter, *Thermal stability of gold nanorods for high-temperature plasmonic sensing*. *The Journal of Physical Chemistry C*, 117(22):11718–11724, 2013.
- [127] R. Zou, Q. Zhang, Q. Zhao, F. Peng, H. Wang, H. Yu, and J. Yang, *Thermal stability of gold nanorods in an aqueous solution*. *Colloids and Surfaces A: Physicochemical and Engineering Aspects*, 372(1):177 – 181, 2010.
- [128] M. B. Mohamed, K. Z. Ismail, S. Link, and M. A. El-Sayed, *Thermal reshaping of gold nanorods in micelles*. *The Journal of Physical Chemistry B*, 102(47):9370–9374, 1998.

- [129] S. H. Joo, J. Y. Park, C.-K. Tsung, Y. Yamada, P. Yang, and G. A. Somorjai, *Thermally stable pt/mesoporous silica core-shell nanocatalysts for high-temperature reactions*. *Nature Materials*, 8:126 – 131, 2008.
- [130] J. Chen, R. Zhang, L. Han, B. Tu, and D. Zhao, *One-pot synthesis of thermally stable gold@mesoporous silica core-shell nanospheres with catalytic activity*. *Nano Research*, 6(12):871–879, Dec 2013.
- [131] Y. Wang, S. Teitel, and C. Dellago, *Surface-driven bulk reorganization of gold nanorods*. *Nano Letters*, 5(11):2174–2178, 2005.
- [132] G. Opletal, G. Grochola, Y. H. Chui, I. K. Snook, and S. P. Russo, *Stability and transformations of heated gold nanorods*. *The Journal of Physical Chemistry C*, 115(11):4375–4380, 2011.
- [133] H. Katz-Boon, M. Walsh, C. Dwyer, P. Mulvaney, A. M. Funston, and J. Etheridge, *Stability of crystal facets in gold nanorods*. *Nano Letters*, 15(3):1635–1641, 2015.
- [134] C. J. Johnson, E. Dujardin, S. A. Davis, C. J. Murphy, and S. Mann, *Growth and form of gold nanorods prepared by seed-mediated, surfactant-directed synthesis*. *J. Mater. Chem.*, 12:1765–1770, 2002.
- [135] W. J. Kennedy, S. Izor, B. D. Anderson, G. Frank, V. Varshney, and G. J. Ehlert, *Thermal reshaping dynamics of gold nanorods: Influence of size, shape, and local environment*. *ACS Applied Materials & Interfaces*, 10(50):43865–43873, 2018.
- [136] T. Castro, R. Reifengerger, E. Choi, and R. P. Andres, *Size-dependent melting temperature of individual nanometer-sized metallic clusters*. *Phys. Rev. B*, 42:8548–8556, Nov 1990.
- [137] T. Besseling. *Self-Assembly of Colloidal Spheres and Rods in External Fields*. PhD thesis, Utrecht University, 2014. available at www.colloids.nl.
- [138] M. R. K. Ali, B. Snyder, and M. A. El-Sayed, *Synthesis and optical properties of small au nanorods using a seedless growth technique*. *Langmuir*, 28(25):9807–9815, 2012.
- [139] P. Zijlstra, C. Bullen, J. W. M. Chon, and M. Gu, *High-temperature seedless synthesis of gold nanorods*. *The Journal of Physical Chemistry B*, 110(39):19315–19318, 2006. PMID: 17004786.
- [140] J. Zhang, C. Xi, C. Feng, H. Xia, D. Wang, and X. Tao, *High yield seedless synthesis of high-quality gold nanocrystals with various shapes*. *Langmuir*, 30(9):2480–2489, 2014.
- [141] Z. Gao, N. D. Burrows, N. A. Valley, G. C. Schatz, C. J. Murphy, and C. L. Haynes, *In solution sers sensing using mesoporous silica-coated gold nanorods*. *Analyst*, 141:5088–5095, 2016.
- [142] W. Albrecht. *Plasmonics and Thermal Stability of Anisotropic Nanoparticles: Heating and Fs-Laser Excitation*. PhD thesis, Utrecht University, 2017. available at www.colloids.nl.
- [143] A. Van Blaaderen and A. Vrij, *Synthesis and characterization of colloidal dispersions of fluorescent, monodisperse silica spheres*. *Langmuir*, 8(12):2921–2931, 1992.
- [144] R. Kumar, H.-T. Chen, J. L. V. Escoto, V. S.-Y. Lin, and M. Pruski, *Template removal and thermal stability of organically functionalized mesoporous silica nanoparticles*. *Chemistry of Materials*, 18(18):4319–4327, 2006.
- [145] L. Zhang, M. D’Acunzi, M. Kappl, A. Imhof, A. v. Blaaderen, H.-J. Butt, R. Graf, and D. Vollmer, *Tuning the mechanical properties of silica microcapsules*. *Phys. Chem. Chem. Phys.*, 12:15392–15398, 2010.

- [146] C.-Y. Chen, S. L. Burkett, H.-X. Li, and M. E. Davis, *Studies on mesoporous materials II. Synthesis mechanism of MCM-41*. *Microporous Materials*, 2(1):27–34, 1993.
- [147] H. Chen, L. Shao, Q. Li, and J. Wang, *Gold nanorods and their plasmonic properties*. *Chem. Soc. Rev.*, 42:2679–2724, 2013.
- [148] M. B. Cortie and A. M. McDonagh, *Synthesis and optical properties of hybrid and alloy plasmonic nanoparticles*. *Chemical Reviews*, 111(6):3713–3735, 2011.
- [149] K. Q. Sun, Y. C. Hong, G. R. Zhang, and B. G. Xu, *Synergy between Pt and Au in Pt-on-Au Nanostructures for Chemoselective Hydrogenation Catalysis*. *ACS Catal.*, 1:1336–1346, 2011.
- [150] J. W. Hong, D. Kim, Y. W. Lee, M. Kim, S. W. Kang, and S. W. Han, *Atomic-Distribution-Dependent Electrocatalytic Activity of Au-Pd Bimetallic Nanocrystals*. *Ang. Chem. Int. Ed.*, 50(38):8876–8880, 2011.
- [151] S. Sarina, H. Zhu, E. Jaatinen, Q. Xiao, H. Liu, J. Jia, C. Chen, and J. Zhao, *Enhancing catalytic performance of palladium in gold and palladium alloy nanoparticles for organic synthesis reactions through visible light irradiation at ambient temperatures*. *Journal of the American Chemical Society*, 135(15):5793–5801, 2013.
- [152] J. Huang, Y. Zhu, M. Lin, Q. Wang, L. Zhao, Y. Yang, K. X. Yao, and Y. Han, *Site-specific growth of au-pd alloy horns on au nanorods: A platform for highly sensitive monitoring of catalytic reactions by surface enhancement raman spectroscopy*. *Journal of the American Chemical Society*, 135(23):8552–8561, 2013.
- [153] S. Rodal-Cedeira, V. Montes-García, L. Polavarapu, D. M. Solís, H. Heidari, A. La Porta, M. Angiola, A. Martucci, J. M. Taboada, F. Obelleiro, S. Bals, J. Pérez-Juste, and I. Pastoriza-Santos, *Plasmonic Au@Pd nanorods with boosted refractive index susceptibility and SERS efficiency: A multifunctional platform for hydrogen sensing and monitoring of catalytic reactions*. *Chemistry of Materials*, 28(24):9169–9180, 2016.
- [154] C.-Y. Chiu and M. H. Huang, *Polyhedral au-pd core-shell nanocrystals as highly spectrally responsive and reusable hydrogen sensors in aqueous solution*. *Angewandte Chemie International Edition*, 52(48):12709–12713, 2013.
- [155] Z. Zheng, T. Tachikawa, and T. Majima, *Plasmon-enhanced formic acid dehydrogenation using anisotropic pd-au nanorods studied at the single-particle level*. *Journal of the American Chemical Society*, 137(2):948–957, 2015.
- [156] F. Wang, C. Li, H. Chen, R. Jiang, L.-D. Sun, Q. Li, J. Wang, J. C. Yu, and C.-H. Yan, *Plasmonic Harvesting of Light Energy for Suzuki Coupling Reactions*. *J. Am. Chem. Soc.*, 135(15):5588–5601, 2013.
- [157] H. Chen, F. Wang, K. Li, K. C. Woo, J. Wang, Q. Li, L.-D. Sun, X. Zhang, H.-Q. Lin, and C.-H. Yan, *Plasmonic percolation: Plasmon-manifested dielectric-to-metal transition*. *ACS Nano*, 6(8):7162–7171, 2012.
- [158] S. E. Habas, H. Lee, V. Radmilovic, G. A. Somorjai, and P. Yang, *Shaping binary metal nanocrystals through epitaxial seeded growth*. *Nature Materials*, 6:692–697, 2007.
- [159] Y. Okuno, K. Nishioka, A. Kiya, N. Nakashima, A. Ishibashi, and Y. Niidome, *Uniform and controllable preparation of Au-Ag core-shell nanorods using anisotropic silver shell formation on gold nanorods*. *Nanoscale*, 2:1489–1493, 2010.

- [160] B. Goris, A. De Backer, S. Van Aert, S. Gómez-Graña, L. M. Liz-Marzán, G. Van Tendeloo, and S. Bals, *Three-dimensional elemental mapping at the atomic scale in bimetallic nanocrystals*. *Nano Letters*, 13(9):4236–4241, 2013.
- [161] F.-R. Fan, D.-Y. Liu, Y.-F. Wu, S. Duan, Z.-X. Xie, Z.-Y. Jiang, and Z.-Q. Tian, *Epitaxial growth of heterogeneous metal nanocrystals: From gold nano-octahedra to palladium and silver nanocubes*. *Journal of the American Chemical Society*, 130(22):6949–6951, 2008.
- [162] E. Bauer and J. H. van der Merwe, *Structure and growth of crystalline superlattices: From monolayer to superlattice*. *Phys. Rev. B*, 33:3657–3671, Mar 1986.
- [163] X. Xia, Y. Wang, A. Ruditskiy, and Y. Xia, *25th anniversary article: Galvanic replacement: A simple and versatile route to hollow nanostructures with tunable and well-controlled properties*. *Advanced Materials*, 25(44):6313–6333, 2013.
- [164] B. Goris, L. Polavarapu, S. Bals, G. Van Tendeloo, and L. M. Liz-Marzán, *Monitoring galvanic replacement through three-dimensional morphological and chemical mapping*. *Nano Letters*, 14(6):3220–3226, 2014.
- [165] F. Wang, S. Cheng, Z. Bao, and J. Wang, *Anisotropic overgrowth of metal heterostructures induced by a site-selective silica coating*. *Angewandte Chemie International Edition*, 52(39):10344–10348, 2013.
- [166] M. Grzelczak, J. Pérez-Juste, B. Rodríguez-González, and L. M. Liz-Marzán, *Influence of silver ions on the growth mode of platinum on gold nanorods*. *J. Mater. Chem.*, 16:3946–3951, 2006.
- [167] Q. Cai, Z.-S. Luo, W.-Q. Pang, Y.-W. Fan, X.-H. Chen, and F.-Z. Cui, *Dilute solution routes to various controllable morphologies of mcm-41 silica with a basic medium*. *Chemistry of Materials*, 13(2):258–263, 2001.
- [168] S. M. Foiles, M. I. Baskes, and M. S. Daw, *Embedded-atom-method functions for the fcc metals Cu, Ag, Au, Ni, Pd, Pt and their alloys*. *Phys. Rev. B*, 33:7983–7991, 1986.
- [169] W. Tyson and W. Miller, *Surface free energies of solid metals: Estimation from liquid surface tension measurements*. *Surface Science*, 62(1):267 – 276, 1977.
- [170] C. Kittel. *Introduction to Solid State Physics, 8th ed.* John Wiley and Sons, 2005.
- [171] D. R. Lide. *CRC Handbook of Chemistry and Physics, Internet Version*. CRC Press, Boca Raton, 2005.
- [172] P. Vanýsek. *CRC Handbook of Chemistry and Physics, 93rd Edition*. CRC Press, Taylor and Francis group, 2012.
- [173] G. Berhault, M. Bausach, L. Bisson, L. Becerra, C. Thomazeau, and D. Uzio, *Seed-mediated synthesis of pd nanocrystals: factors influencing a kinetic- or thermodynamic-controlled growth regime*. *The Journal of Physical Chemistry C*, 111(16):5915–5925, 2007.
- [174] B. N. Khlebtsov, V. A. Khanadeev, J. Ye, G. B. Sukhorukov, and N. G. Khlebtsov, *Overgrowth of gold nanorods by using a binary surfactant mixture*. *Langmuir*, 30(6):1696–1703, 2014.
- [175] J. E. S. van der Hoeven, L. A. Olthof, G. Totarella, A. van Blaaderen, and P. E. de Jongh, *Correlating the structural and catalytic properties of bimetallic Au-Pd nanorods*. to be published.
- [176] G. G. Li, D. A. Blom, S. Pandey, R. J. Koch, S. T. Mixture, S. R. Phillpot, and H. Wang, *Overcoming the interfacial lattice mismatch: Geometry control of gold-nickel bimetallic heteronanostructures*. *Particle & Particle Systems Characterization*, 35(5):1700361, 2017.

- [177] L. Vigderman, B. P. Khanal, and E. R. Zubarev, *Functional Gold Nanorods: Synthesis, Self-Assembly, and Sensing Applications*. Adv. Mater., 24(36):4811–4841, 2012.
- [178] D. I. Enache, J. K. Edwards, P. Landon, B. Solsona-Espriu, A. F. Carley, A. A. Herzing, M. Watanabe, C. J. Kiely, D. W. Knight, and G. J. Hutchings, *Solvent-free oxidation of primary alcohols to aldehydes using Au-Pd/TiO₂ catalysts*. Science, 311(5759):362–365, 2006.
- [179] P. C. Chen, G. Liu, Y. Zhou, K. A. Brown, N. Chernyak, J. L. Hedrick, S. He, Z. Xie, Q. Y. Lin, V. P. Dravid, S. A. O’Neill-Slawecki, and C. A. Mirkin, *Tip-Directed Synthesis of Multimetallic Nanoparticles*. J. Am. Chem. Soc., 137(28):9167–9173, 2015.
- [180] A. Wittstock, V. Zielasek, J. Biener, C. M. Friend, and M. Bäumer, *Nanoporous Gold Catalysts for Selective Gas-Phase Oxidative Coupling of Methanol at Low Temperature*. Science, 327(January):319–322, 2010.
- [181] J. Edwards, B. Solsona, P. Landon, A. Carley, A. Herzing, C. Kiely, and G. Hutchings, *Direct synthesis of hydrogen peroxide from H₂ and O₂ using TiO₂ supported Au-Pd catalysts*. J. Catal., 236(1):69–79, 2005.
- [182] X. Liu, A. Wang, X. Yang, T. Zhang, C. Y. Mou, D. S. Su, and J. Li, *Synthesis of Thermally Stable and Highly Active Bimetallic Au-Ag Nanoparticles on Inert Supports*. Chem. Mater., 21(2):410–418, 2009.
- [183] A. Cao and G. G. Veser, *Exceptional high-temperature stability through distillation-like self-stabilization in bimetallic nanoparticles*. Nat. Mater., 9(1):75–81, 2010.
- [184] H. M. Bok, K. L. Shuford, S. G. Kim, S. K. Kim, and S. Park, *Multiple Surface Plasmon Modes for Gold/Silver Alloy Nanorods*. Langmuir, 25(9):5266–5270, 2009.
- [185] J. Huang, Y. Zhu, C. Liu, Y. Zhao, Z. Liu, M. N. Hedhili, A. Fratolocchi, and Y. Han, *Fabricating a Homogeneously Alloyed AuAg Shell on Au Nanorods to Achieve Strong, Stable, and Tunable Surface Plasmon Resonances*. Small, 11(39):5214–5221, 2015.
- [186] J. Crespo, J. M. López-de Luzuriaga, M. Monge, M. E. Olmos, M. Rodríguez-Castillo, B. Cormary, K. Soulantica, M. Sestu, and A. Falqui, *The spontaneous formation and plasmonic properties of ultrathin gold-silver nanorods and nanowires stabilized in oleic acid*. Chem. Commun., 51(93):16691–16694, 2015.
- [187] Q. Liu, Z. Yan, N. L. Henderson, J. C. Bauer, D. W. Goodman, J. D. Batteas, and R. E. Schaak, *Synthesis of CuPt Nanorod Catalysts with Tunable Lengths*. J. Am. Chem. Soc., 131(16):5720–5721, 2009.
- [188] Y. Lu, Y. Jiang, and W. Chen, *PtPd porous nanorods with enhanced electrocatalytic activity and durability for oxygen reduction reaction*. Nano Energy, 2(5):836–844, 2013.
- [189] C. Wang, S. Peng, R. Chan, and S. Sun, *Synthesis of AuAg Alloy Nanoparticles from Core/Shell-Structured Ag/Au*. Small, 5(5):567–570, 2009.
- [190] H. Petrova, J. Perez Juste, I. Pastoriza-Santos, G. V. Hartland, L. M. Liz-Marzán, and P. Mulvaney, *On the temperature stability of gold nanorods: comparison between thermal and ultrafast laser-induced heating*. Phys. Chem. Chem. Phys., 8:814–821, 2006.
- [191] C.-Y. Chen, H.-X. Li, and M. E. Davis, *Studies on mesoporous materials: I. synthesis and characterization of MCM-41*. Microporous Materials, 2(1):17 – 26, 1993.
- [192] D. Rioux, S. Vallières, S. Besner, P. Muñoz, E. Mazur, and M. Meunier, *An Analytic Model for the Dielectric Function of Au, Ag, and their Alloys*. Adv. Opt. Mater., 2(2):176–182, 2014.

- [193] S. Link, Z. L. Wang, and M. A. El-Sayed, *Alloy Formation of Gold-Silver Nanoparticles and the Dependence of the Plasmon Absorption on Their Composition*. *J. Phys. Chem. B*, 103(18):3529–3533, 1999.
- [194] E. A. Coronado and G. C. Schatz, *Surface plasmon broadening for arbitrary shape nanoparticles: A geometrical probability approach*. *J. Chem. Phys.*, 119:3926–3934, 2003.
- [195] M. S. Shore, J. Wang, A. C. Johnston-Peck, A. L. Oldenburg, and J. B. Tracy, *Synthesis of Au(Core)/Ag(Shell) Nanoparticles and their Conversion to AuAg Alloy Nanoparticles*. *Small*, 7(2):230–234, 2011.
- [196] L. J. Lewis, P. Jensen, and J.-L. Barrat, *Melting, freezing, and coalescence of gold nanoclusters*. *Phys. Rev. B*, 56:2248–2257, 1997.
- [197] C. Burda, X. Chen, R. Narayanan, and M. A. El-Sayed, *Chemistry and Properties of Nanocrystals of Different Shapes*. *Chem. Rev.*, 105:1025–1102, 2005.
- [198] G. Guisbiers, R. Mendoza-Cruz, L. Bazán-Díaz, J. J. Velázquez-Salazar, R. Mendoza-Perez, J. A. Robledo-Torres, J. L. Rodriguez-Lopez, J. M. Montejano-Carrizales, R. L. Whetten, and M. José-Yacamán, *Electrum, the Gold-Silver Alloy, From the Bulk Scale to the Nanoscale: Synthesis, Properties, and Segregation Rules*. *ACS Nano*, 10(1):188–198, 2016.
- [199] T. Shibata, B. A. Bunker, Z. Zhang, D. Meisel, C. F. Vardeman, and J. D. Gezelter, *Size-dependent spontaneous alloying of Au-Ag nanoparticles*. *J. Am. Chem. Soc.*, 124:11989–11996, 2002.
- [200] E. Gergely-Fülöp, D. Zámbo, and A. Deák, *Thermal stability of mesoporous silica-coated gold nanorods with different aspect ratios*. *Mater. Chem. Phys.*, 148:909–913, 2014.
- [201] J. Hu, W. Cai, H. Zeng, C. Li, and F. Sun, *Substrate dependent surface plasmon resonance evolution of Ag nanoparticles treated in atmospheres*. *J. Phys. Condens. Matter*, 18(23):5415–5423, 2006.
- [202] E. Ringe, C. J. DeSantis, S. M. Collins, M. Duchamp, R. E. Dunin-Borkowski, S. E. Skrabalak, and P. A. Midgley, *Resonances of nanoparticles with poor plasmonic metal tips*. *Sci. Rep.*, 5:17431, 2015.
- [203] Z. Zhang, J. Wang, X. Nie, T. Wen, Y. Ji, X. Wu, Y. Zhao, and C. Chen, *Near Infrared Laser-Induced Targeted Cancer Therapy Using Thermoresponsive Polymer Encapsulated Gold Nanorods*. *J. Am. Chem. Soc.*, 136(20):7317–7326, 2014.
- [204] d. A. Dorleta Jimenez, S.-M. Ana Belén, and L.-M. Luis M., *Modern applications of plasmonic nanoparticles: From energy to health*. *Adv. Opt. Mater.*, 3(5):602–617, 2015.
- [205] R. Ferrando, J. Jellinek, and R. L. Johnston, *Nanoalloys: From Theory to Applications of Alloy Clusters and Nanoparticles*. *Chem. Rev.*, 108(3):845–910, 2008.
- [206] A. K. Singh and Q. Xu, *Synergistic Catalysis over Bimetallic Alloy Nanoparticles*. *Chem. Cat. Chem.*, 5(3):652–676, 2013.
- [207] X. Liu, A. Wang, X. Yang, T. Zhang, C. Y. Mou, D. S. Su, and J. Li, *Synthesis of Thermally Stable and Highly Active Bimetallic Au-Ag Nanoparticles on Inert Supports*. *Chem. Mater.*, 21(2):410–418, 2009.
- [208] C. S. Bonifacio, S. Carenco, C. H. Wu, S. D. House, H. Bluhm, and J. C. Yang, *Thermal stability of core-shell nanoparticles: A combined in situ study by xps and tem*. *Chem. Mater.*, 27(20):6960–6968, 2015.

- [209] M. Lasserus, M. Schnedlitz, D. Knez, R. Messner, A. Schiffmann, F. Lackner, A. W. Hauser, F. Hofer, and W. E. Ernst, *Thermally Induced Alloying Processes in a Bimetallic System at the Nanoscale: AgAu sub-5 nm Core-Shell Particles Studied at Atomic Resolution*. *Nanoscale*, 10:2017–2024, 2018.
- [210] S. Pramanik, S. Chattopadhyay, J. K. Das, U. Manju, and G. De, *Extremely fast Au-Ag alloy-dealloy associated reversible plasmonic modifications in SiO_2 films*. *J. Mater. Chem. C*, 4:3571–3580, 2016.
- [211] B. J. Hwang, L. S. Sarma, J. M. Chen, C. H. Chen, S. C. Shih, G. R. Wang, D. G. Liu, J. F. Lee, and M. T. Tang, *Structural Models and Atomic Distribution of Bimetallic Nanoparticles as Investigated by X-ray Absorption Spectroscopy*. *J. Am. Chem. Soc.*, 127(13):11140–11145, 2005.
- [212] Y. Ding, F. Fan, Z. Tian, and Z. Wang, *Atomic Structure of Au-Pd Bimetallic Alloyed Nanoparticles*. *J. Am. Chem. Soc.*, 132(35):12480–12486, 2010.
- [213] A. Sandoval, A. Aguilar, C. Louis, A. Traverse, and R. Zanella, *Bimetallic Au-Ag/TiO₂ Catalyst Prepared by Deposition-Precipitation: High Activity and Stability in CO Oxidation*. *J. Catal.*, 281(1):40–49, 2011.
- [214] F. Tao and M. Salmeron, *In situ studies of chemistry and structure of materials in reactive environments*. *Science*, 331:171–174, 2011.
- [215] H. L. Xin, S. Alayoglu, R. Tao, A. Genc, C. M. Wang, L. Kovarik, E. A. Stach, L. W. Wang, M. Salmeron, G. A. Somorjai, and H. Zheng, *Revealing the Atomic Restructuring of Pt-Co Nanoparticles*. *Nano Lett.*, 14(6):3203–3207, 2014.
- [216] C. Hølse, C. F. Elkjær, A. Nierhoff, J. Sehested, I. Chorkendorff, S. Helveg, and J. H. Nielsen, *Dynamic Behavior of CuZn Nanoparticles Under Oxidizing and Reducing Conditions*. *J. Phys. Chem. C*, 119(5):2804–2812, 2015.
- [217] S. Carenco, C. H. Wu, A. Shavorskiy, S. Alayoglu, G. A. Somorjai, H. Bluhm, and M. Salmeron, *Synthesis and Structural Evolution of Nickel-Cobalt Nanoparticles Under H_2 and CO_2* . *Small*, 11(25):3045–3053, 2015.
- [218] J. H. Hodak, A. Henglein, M. Giersig, and G. V. Hartland, *Laser-induced inter-diffusion in AuAg core-shell nanoparticles*. *J. Phys. Chem. B*, 104(49):11708–11718, 2000.
- [219] R. Sarkar, C. Rentenberger, and J. Rajagopalan, *Electron Beam Induced Artifacts During In Situ TEM Deformation of Nanostructured Metals*. *Sci. Rep.*, 5:1–11, 2015.
- [220] T. J. Woehl, J. E. Evans, I. Arslan, W. D. Ristenpart, and N. D. Browning, *Direct In Situ Determination of the Mechanisms Controlling Nanoparticle Nucleation and Growth*. *ACS Nano*, 6(10):8599–8610, 2012.
- [221] R. Van Den Berg, C. F. Elkjaer, C. J. Gommers, I. Chorkendorff, J. Sehested, P. E. De Jongh, K. P. De Jong, and S. Helveg, *Revealing the Formation of Copper Nanoparticles from a Homogeneous Solid Precursor by Electron Microscopy*. *J. Am. Chem. Soc.*, 138(10):3433–3442, 2016.
- [222] A. I. Frenkel, *Applications of extended x-ray absorption fine-structure spectroscopy to studies of bimetallic nanoparticle catalysts*. *Chem. Soc. Rev.*, 41:8163–8178, 2012.
- [223] B. Ravel and M. Newville, *ATHENA, ARTEMIS, HEPHAESTUS: Data Analysis for X-Ray Absorption Spectroscopy using IFEFFIT*. *J. Synchrotron Rad.*, 12(4):537–541, Jul 2005.

- [224] W. Mallard, A. B. Gardner, R. Bass, and L. Slifkin, *Self-Diffusion in Silver-Gold Solid Solutions*. Phys. Rev., 129(2):617–625, 1963.
- [225] G. Guisbiers and L. Buchailot, *Modeling the Melting Enthalpy of Nanomaterials*. J. Phys. Chem. C, 113(9):3566–3568, 2009.
- [226] G. Guisbiers, *Size-Dependent Materials Properties Toward a Universal Equation*. Nanoscale Res. Lett., 5(7):1132–1136, 2010.
- [227] C. C. Yang and S. Li, *Investigation of cohesive energy effects on size-dependent physical and chemical properties of nanocrystals*. Phys. Rev. B, 75:165413, Apr 2007.
- [228] K. K. Nanda, S. N. Sahu, and S. N. Behera, *Liquid-drop model for the size-dependent melting of low-dimensional systems*. Phys. Rev. A, 66:013208, Jul 2002.
- [229] M. Doyama and J. S. Koehler, *Quenching and annealing of lattice vacancies in pure silver*. Phys. Rev., 127:21–31, Jul 1962.
- [230] R. O. Simmons and R. W. Balluffi, *Measurement of equilibrium concentrations of lattice vacancies in gold*. Phys. Rev., 125:862–872, Feb 1962.
- [231] W. Hagel and J. Westbrook, *Silver diffusion in the intermetallic compound agmg*. Trans. TMS-AIME, 221:951, 1961.
- [232] A. J. Mortlocks and D. H. Tomlin, *The atomic diffusion of chromium in the titanium-chromium system*. Philo. Mag., 4(41):628–643, 1959.
- [233] R. Peart and D. Tomlin, *Diffusion of solute elements in beta-titanium*. Acta Metall., 10(2):123 – 134, 1962.
- [234] H. Resing and N. Nachtmeh, *Self-diffusion of lead, thallium and bismuth in the solid lead-thallium system*. J. Phys. Chem. Sol., 21(1):40 – 56, 1962.
- [235] M. L. Derrien. *Chapter 18 selective hydrogenation applied to the refining of petrochemical raw materials produced by steam cracking*. In L. Cerveny, editor, *Catalytic Hydrogenation*, volume 27 of *Studies in Surface Science and Catalysis*, pages 613 – 666. Elsevier, 1986.
- [236] J. H. Paul and R. L. Banks, *Purification of olefin-rich feed prior to polymerization*. US Patent, US2837587A, 1954.
- [237] B. M. Collins, *Selective hydrogenation of highly unsaturated hydrocarbons in the presence of less unsaturated hydrocarbons*. US Patent, US4126645A, 1976.
- [238] W.-Y. Yu, G. M. Mullen, and C. B. Mullins, *Hydrogen adsorption and absorption with pd-au bimetallic surfaces*. The Journal of Physical Chemistry C, 117(38):19535–19543, 2013.
- [239] Árpád Molnár, A. Sárkány, and M. Varga, *Hydrogenation of carbon-carbon multiple bonds: chemo-, regio- and stereo-selectivity*. Journal of Molecular Catalysis A: Chemical, 173(1):185 – 221, 2001. Catalysis with Supported Palladium Metal at the Turn of the 21st Century.
- [240] J. Silvestre-Albero, G. Rupprechter, and H.-J. Freund, *From pd nanoparticles to single crystals: 1,3-butadiene hydrogenation on well-defined model catalysts*. Chem. Commun., pages 80–82, 2006.
- [241] C. Thahn, B. Didillon, P. Sarrazin, and C. Cameron, *Selective hydrogenation catalyst and a process using that catalyst*. US Patent, US6054409A, 1996.
- [242] L. McEwan, M. Juliusa, S. Roberts, and J. C. Q. Fletcher, *A review of the use of gold catalysts in selective hydrogenation reactions*. Gold Bulletin, 43(4):298–306, Dec 2010.

- [243] A. Hugon, L. Delannoy, and C. Louis, *Supported gold catalysts for selective hydrogenation of 1,3-butadiene in the presence of an excess of alkenes*. Gold Bulletin, 41(2):127–138, Jun 2008.
- [244] A. Hugon, L. Delannoy, and C. Louis, *Influence of the reactant concentration in selective hydrogenation of 1,3-butadiene over supported gold catalysts under alkene rich conditions: A consideration of reaction mechanism*. Gold Bulletin, 42(4):310–320, Dec 2009.
- [245] N. Masoud, L. Delannoy, H. Schaink, A. van der Eerden, J. W. de Rijk, T. A. G. Silva, D. Banerjee, J. D. Meeldijk, K. P. de Jong, C. Louis, and P. E. de Jongh, *Superior stability of Au/SiO₂ compared to Au/TiO₂ catalysts for the selective hydrogenation of butadiene*. ACS Catalysis, 7(9):5594–5603, 2017.
- [246] A. Hugon, L. Delannoy, J.-M. Krafft, and C. Louis, *Selective hydrogenation of 1,3-butadiene in the presence of an excess of alkenes over supported bimetallic gold palladium catalysts*. The Journal of Physical Chemistry C, 114(24):10823–10835, 2010.
- [247] H. Miura, M. Terasaka, K. Oki, and T. Matsuda. *Preparation of Egg-Shell Type Pd-Ag and Pd-Au Catalysts by Selective Deposition and Hydrogenation of 1,3-Butadiene*, volume 75 of *Studies in Surface Science and Catalysis*. Elsevier, 1993.
- [248] Y.-J. Zhang, S.-B. Li, S. Duan, B.-A. Lu, J. Yang, R. Panneerselvam, C.-Y. Li, P.-P. Fang, Z.-Y. Zhou, D. L. Phillips, J.-F. Li, and Z.-Q. Tian, *Probing the electronic structure of heterogeneous metal interfaces by transition metal shelled gold nanoparticle-enhanced raman spectroscopy*. The Journal of Physical Chemistry C, 120(37):20684–20691, 2016.
- [249] L. Bu, N. Zhang, S. Guo, X. Zhang, J. Li, J. Yao, T. Wu, G. Lu, J.-Y. Ma, D. Su, and X. Huang, *Biaxially strained PtPb/Pt core/shell nanoplate boosts oxygen reduction catalysis*. Science, 354(6318):1410–1414, 2016.
- [250] J. C. Bertolini, P. Delichere, B. C. Khanra, J. Massardier, C. Noupa, and B. Tardy, *Electronic properties of supported pd aggregates in relation with their reactivity for 1,3-butadiene hydrogenation*. Catalysis Letters, 6(2):215–223, Mar 1990.
- [251] A. Borgna, B. Morawek, J. Massardier, and A. Renouprez, *New supported palladium-chromium catalysts: characterization and catalytic properties*. Journal of Catalysis, 128(1):99 – 112, 1991.
- [252] R. Moyes, P. Wells, J. Grant, and N. Salman, *Electronic effects in butadiene hydrogenation catalysed by the transition metals*. Applied Catalysis A: General, 229(1):251 – 259, 2002.
- [253] Z. Nie, A. Petukhova, and E. Kumacheva, *Properties and emerging applications of self-assembled structures made from inorganic nanoparticles*. Nat. Nanotech., 5:15, 2010.
- [254] M. Grzelczak, J. Vermant, E. M. Furst, and L. M. Liz-Marzán, *Directed Self-Assembly of Nanoparticles*. ACS Nano, 4(7):3591, 2010.
- [255] N. Vogel, S. Utech, G. T. England, T. Shirman, K. R. Phillips, N. Koay, I. B. Burgess, M. Kolle, D. A. Weitz, and J. Aizenberg, *Color from hierarchy: Diverse optical properties of micron-sized spherical colloidal assemblies*. Proc. Natl. Acad. Sci. USA, 112(35):10845, 2015.
- [256] F. Montanarella, T. Altantzis, D. Zanaga, F. T. Rabouw, S. Bals, P. Baesjou, D. Vanmaekelbergh, and A. van Blaaderen, *Composite supraparticles with tunable light emission*. ACS Nano, 11(9):9136, 2017.
- [257] V. J. Anderson and H. N. W. Lekkerkerker, *Insights into Phase Transition Kinetics from Colloid Science*. Nature, 416(6883):811, 2002.

- [258] U. Gasser, E. R. Weeks, A. Schofield, P. N. Pusey, and D. A. Weitz, *Real-Space Imaging of Nucleation and Growth in Colloidal Crystallization*. *Science*, 292(5515):258, 2001.
- [259] A. D. Dinsmore and D. A. Weitz, *Direct imaging of three-dimensional structure and topology of colloidal gels*. *J. Phys. Condens. Matter*, 14(33):7581, 2002.
- [260] F. Montanarella, J. J. Geuchies, T. Dasgupta, P. T. Prins, C. van Overbeek, R. Dattani, P. Baesjou, M. Dijkstra, A. V. Petukhov, A. van Blaaderen, and D. Vanmaekelbergh, *Crystallization of nanocrystals in spherical confinement probed by in situ x-ray scattering*. *Nano Lett.*, 18(6):3675, 2018.
- [261] A. Kuijk, D. V. Byelov, A. V. Petukhov, A. van Blaaderen, and A. Imhof, *Phase Behavior of Colloidal Silica Rods*. *Faraday Discuss.*, 159:181, 2012.
- [262] A. V. Petukhov, J.-M. Meijer, and G. J. Vroege, *Particle shape effects in colloidal crystals and colloidal liquid crystals: Small-angle x-ray scattering studies with microradian resolution*. *Curr. Opin. Colloid Interface Sci.*, 20(4):272, 2015.
- [263] B. Harke, C. K. Ullal, J. Keller, and S. W. Hell, *Three-Dimensional Nanoscopy of Colloidal Crystals*. *Nano Lett.*, 8(5):1309, 2008.
- [264] A. van Blaaderen and P. Wiltzius, *Real-space structure of colloidal hard-sphere glasses*. *Science*, 270(5239):1177, 1995.
- [265] H. Friedrich, C. J. Gommers, K. Overgaag, J. D. Meeldijk, W. H. Evers, B. de Nijs, M. P. Boneschanscher, P. E. de Jongh, A. J. Verkleij, K. P. de Jong, A. van Blaaderen, and D. Vanmaekelbergh, *Quantitative Structural Analysis of Binary Nanocrystal Superlattices by Electron Tomography*. *Nano Lett.*, 9(7):2719, 2009.
- [266] R. J. D. Tilley. *Defects in solids*. John Wiley & Sons, Inc., 2008.
- [267] A. M. Alsayed, M. F. Islam, J. Zhang, P. J. Collings, and A. G. Yodh, *Chemistry: Premelting at Defects within Bulk Colloidal Crystals*. *Science*, 309(5738):1207, 2005.
- [268] T. A. Waigh and C. Rau, *X-ray and neutron imaging with colloids*. *Curr. Opin. Colloid Interface Sci.*, 17(1):13, 2012.
- [269] D. V. Byelov, J.-M. Meijer, I. Snigireva, A. Snigirev, L. Rossi, E. van den Pol, A. Kuijk, A. Philippe, A. Imhof, A. van Blaaderen, G. J. Vroege, and A. V. Petukhov, *In Situ Hard X-Ray Microscopy of Self-Assembly in Colloidal Suspensions*. *RSC Adv.*, 3(36):15670, 2013.
- [270] J. Hilhorst, M. M. van Schooneveld, J. Wang, E. de Smit, T. Tyliczszak, J. Raabe, A. P. Hitchcock, M. Obst, F. M. F. de Groot, and A. V. Petukhov, *Three-dimensional structure and defects in colloidal photonic crystals revealed by tomographic scanning transmission x-ray microscopy*. *Langmuir*, 28(7):3614, 2012.
- [271] F. M. F. de Groot, E. de Smit, M. M. van Schooneveld, L. R. Aramburo, and B. M. Weckhuysen, *In situ scanning transmission x-ray microscopy of catalytic solids and related nanomaterials*. *ChemPhysChem*, 11(5):951, 2010.
- [272] J. Wang, C. Morin, L. Li, A. P. Hitchcock, A. Scholl, and A. Doran, *Radiation damage in soft x-ray microscopy*. *J. Electron. Spectrosc. Relat. Phenom.*, 170(1):25, 2009.
- [273] B. de Nijs, S. Dussi, F. Smalenburg, J. D. Meeldijk, D. J. Groenendijk, L. Filion, A. Imhof, A. van Blaaderen, and M. Dijkstra, *Entropy-Driven Formation of Large Icosahedral Colloidal Clusters by Spherical Confinement*. *Nat. Mater.*, 14(1):56, 2015.

- [274] D. Zanaga, F. Bleichrodt, T. Altantzis, N. Winckelmans, W. J. Palenstijn, J. Sijbers, B. de Nijs, M. A. van Huis, A. Sanchez-Iglesias, L. M. Liz-Marzán, A. van Blaaderen, K. J. Batenburg, S. Bals, and G. Van Tendeloo, *Quantitative 3d analysis of huge nanoparticle assemblies*. *Nanoscale*, 8:292, 2016.
- [275] T. Altantzis, D. Zanaga, and S. Bals, *Advanced electron tomography of nanoparticle assemblies*. *EPL*, 119(3):38001, 2017.
- [276] D. Wang, M. Hermes, R. Kotni, Y. Wu, N. Tasios, Y. Liu, B. de Nijs, E. B. van der Wee, C. B. Murray, and A. van Blaaderen, *Interplay between spherical confinement and particle shape on the self-assembly of rounded cubes*. *Nat. Commun.*, 9(2228):2041, 2018.
- [277] T. Altantzis, B. Goris, A. Sánchez-Iglesias, M. Grzelczak, L. M. Liz-Marzán, and S. Bals, *Quantitative structure determination of large three-dimensional nanoparticle assemblies*. *Part. Part. Syst. Char.*, 30(1):84–88, 2013.
- [278] M. S. Elliot and W. C. K. Poon, *Conventional Optical Microscopy of Colloidal Suspensions*. *Adv. Colloid Interface Sci.*, 92(1-3):133, 2001.
- [279] V. Prasad, D. Semwogerere, and E. R. Weeks, *Confocal microscopy of colloids*. *J. of Phys. Condens. Matter*, 19(11):113102, 2007.
- [280] B. D. Leahy, N. Y. C. Lin, and I. Cohen, *Quantitative light microscopy of dense suspensions: Colloid science at the next decimal place*. *Curr. Opin. Colloid Interface Sci.*, 34:32, 2018.
- [281] N. Martini, J. Bewersdorf, and S. W. Hell, *A new high-aperture glycerol immersion objective lens and its application to 3d-fluorescence microscopy*. *J. Microsc.*, 206(2):146, 2002.
- [282] J. C. Crocker and D. G. Grier, *Methods of digital video microscopy for colloidal studies*. *J. Colloid Interface Sci.*, 179(1):298, 1996.
- [283] T. H. Besseling, M. Hermes, A. Kuijk, B. de Nijs, T. S. Deng, M. Dijkstra, A. Imhof, and A. van Blaaderen, *Determination of the Positions and Orientations of Concentrated Rod-Like Colloids from 3D Microscopy Data*. *J. Phys. Condens. Matter*, 27(19):194109, 2015.
- [284] U. Dassanayake, S. Fraden, and A. van Blaaderen, *Structure of electrorheological fluids*. *J. Chem. Phys.*, 112(8):3851, 2000.
- [285] J. B. de Monvel, S. Le Calvez, and M. Ulfendahl, *Image restoration for confocal microscopy: Improving the limits of deconvolution, with application to the visualization of the mammalian hearing organ*. *Biophys. J.*, 80(5):2455, 2001.
- [286] S. W. Hell, *Far-Field Optical Nanoscopy*. *Science*, 316(5828):1153, 2007.
- [287] G. Vicidomini, P. Bianchini, and A. Diaspro, *STED Super-Resolved Microscopy*. *Nat. Methods*, 15(3):173, 2018.
- [288] M. Cantoni and L. Holzer, *Advances in 3d focused ion beam tomography*. *MRS Bulletin*, 39(4):354, 2014.
- [289] C. R. Perrey, C. B. Carter, J. R. Michael, P. G. Kotula, E. A. Stach, and V. R. Radmilovic, *Using the fib to characterize nanoparticle materials*. *J. Microsc.*, 214(3):222, 2004.
- [290] D. A. M. de Winter, F. Meirer, and B. M. Weckhuysen, *Fib-sem tomography probes the mesoscale pore space of an individual catalytic cracking particle*. *ACS Catal.*, 6(5):3158, 2016.

- [291] J. W. Galusha, M. R. Jorgensen, and M. H. Bartl, *Diamond-structured titania photonic-bandgap crystals from biological templates*. *Adv. Mater.*, 22(1):107, 2009.
- [292] K. Narayan and S. Subramaniam, *Focused ion beams in biology*. *Nat. Methods*, 12(11):1021, 2015.
- [293] D. A. M. de Winter, C. T. W. M. Schneijdenberg, M. N. Lebbink, B. Lich, A. J. Verkleij, M. R. Drury, and B. M. Humbel, *Tomography of insulating biological and geological materials using focused ion beam (fib) sectioning and low-kv bse imaging*. *J. Microsc.*, 233(3):372, 2009.
- [294] Y. Liu, H. E. King, M. A. van Huis, M. R. Drury, and O. Plümper, *Nano-tomography of porous geological materials using focused ion beam-scanning electron microscopy*. *Minerals*, 6(4):1, 2016.
- [295] I. Ojea-Jiménez, N. G. Bastús, and V. Puentes, *Influence of the sequence of the reagents addition in the citrate-mediated synthesis of gold nanoparticles*. *J. Phys. Chem. C*, 115(32):15752, 2011.
- [296] J. Fokkema, J. Fermie, N. Liv, D. J. van den Heuvel, T. O. M. Konings, G. A. Blab, A. Meijerink, J. Klumperman, and H. C. Gerritsen, *Fluorescently labelled silica coated gold nanoparticles as fiducial markers for correlative light and electron microscopy*. *Sci. Rep.*, 8:13625, 2018.
- [297] N. G. Bastús, J. Comenge, and V. Puentes, *Kinetically controlled seeded growth synthesis of citrate-stabilized gold nanoparticles of up to 200 nm: Size focusing versus ostwald ripening*. *Langmuir*, 27(17):11098, 2011.
- [298] C. Graf, D. L. J. Vossen, A. Imhof, and A. van Blaaderen, *A general method to coat colloidal particles with silica*. *Langmuir*, 19:6693, 2003.
- [299] K. Osseo-Asare and F. J. Arriagada, *Preparation of SiO₂ nanoparticles in a non-ionic reverse micellar system*. *Colloids and Surf.*, 50:321, 1990.
- [300] H. Giesche, *Synthesis of monodispersed silica powders i. particle properties and reaction kinetics*. *J. Eur. Ceram. Soc.*, 14(3):189, 1994.
- [301] P. Jiang, J. F. Bertone, K. S. Hwang, and V. L. Colvin, *Single-crystal colloidal multilayers of controlled thickness*. *Chem. Mat.*, 11(8):2132, 1999.
- [302] C. Messaoudi, T. Boudier, C. Sanchez Sorzano, and S. Marco, *Tomoj: Tomography software for three-dimensional reconstruction in transmission electron microscopy*. *BMC Bioinform.*, 8:288, 2007.
- [303] J. E. S. van der Hoeven, E. B. van der Wee, D. A. M. de Winter, M. Hermes, Y. Liu, J. Fokkema, M. Bransen, M. van Huis, H. Gerritsen, P. E. de Jongh, and A. van Blaaderen, *Bridging the gap: 3d real-space characterization of colloidal assemblies via fib-sem tomography*. *Nanoscale*, 2019. accepted.
- [304] J. Illingworth and J. Kittler, *A survey of the hough transform*. *Comput. Gr. Image Process.*, 44(1):87, 1988.
- [305] B. Liu, T. H. Besseling, M. Hermes, A. F. Demirörs, A. Imhof, and A. van Blaaderen, *Switching plastic crystals of colloidal rods with electric fields*. *Nat. Comm.*, 5:3092, 2014.
- [306] W. Lechner and C. Dellago, *Accurate determination of crystal structures based on averaged local bond order parameters*. *J. Chem. Phys.*, 129(11):114707, 2008.

- [307] J. P. Hoogenboom, P. Vergeer, and A. van Blaaderen, *A real-space analysis of colloidal crystallization in a gravitational field at a flat bottom wall*. J. Chem. Phys., 119(6):3371, 2003.
- [308] J. H. J. Thijssen. *Characterization of Photonic Colloidal Crystals in Real and Reciprocal Space*. PhD thesis, Utrecht University, 2007.
- [309] M. Leocmach and H. Tanaka, *A novel particle tracking method with individual particle size measurement and its application to ordering in glassy hard sphere colloids*. Soft Matter, 9:1447, 2013.
- [310] T. H. Loeber, B. Laegel, S. Wolff, S. Schuff, F. Balle, T. Beck, D. Eifler, J. H. Fitschen, and G. Steidl, *Reducing curtaining effects in fib/sem applications by a goniometer stage and an image processing method*. J. Vac. Sci. Technol. B, 35(6):06GK01, 2017.
- [311] W. V. den Broek, A. Rosenauer, B. Goris, G. Martinez, S. Bals, S. V. Aert, and D. V. Dyck, *Correction of non-linear thickness effects in haadf stem electron tomography*. Ultramicroscopy, 116:8, 2012.
- [312] M. Jenkins and S. Egelhaaf, *Confocal microscopy of colloidal particles: Towards reliable, optimum coordinates*. Adv. Colloid Interface Sci., 136(1):65, 2008.
- [313] K. E. Jensen and N. Nakamura, *Note: An iterative algorithm to improve colloidal particle locating*. Rev. Sci. Instrum., 87(6):066103, 2016.
- [314] N. A. Elbers, J. E. S. van der Hoeven, D. A. M. de Winter, C. T. W. M. Schneijdenberg, M. N. van der Linden, L. Filion, and A. van Blaaderen, *Repulsive van der waals forces enable pickering emulsions with non-touching colloids*. Soft Matter, 12:7265, 2016.
- [315] C. R. Iacovella, R. E. Rogers, S. C. Glotzer, and M. J. Solomon, *Pair interaction potentials of colloids by extrapolation of confocal microscopy measurements of collective suspension structure*. J. Chem. Phys., 133(16):164903, 2010.
- [316] B. Münch and L. Holzer, *Contradicting geometrical concepts in pore size analysis attained with electron microscopy and mercury intrusion*. J. Am. Ceram. Soc., 91(12):4059–4067, 2008.
- [317] H. Zhang, C. Wang, H.-L. Sun, G. Fu, S. Chen, Y. J. Zhang, B. H. Chen, J. R. Anema, Z. L. Yang, and Z. Q. Tian, *In situ dynamic tracking of heterogeneous nanocatalytic processes by shell-isolated nanoparticle-enhanced raman spectroscopy*. Nature Communications, 8:15447, 2017.
- [318] T. Hartman, C. S. Wondergem, N. Kumar, A. van den Berg, and B. M. Weckhuysen, *Surface- and tip-enhanced raman spectroscopy in catalysis*. The Journal of Physical Chemistry Letters, 7(8):1570–1584, 2016.
- [319] C. Sönnichsen, B. M. Reinhard, J. Liphardt, and A. P. Alivisatos, *A molecular ruler based on plasmon coupling of single gold and silver nanoparticles*. Nature Biotechnology, 23:741–745, 2005.
- [320] K. D. Alexander, K. Skinner, S. Zhang, H. Wei, and R. Lopez, *Tunable sers in gold nanorod dimers through strain control on an elastomeric substrate*. Nano Letters, 10(11):4488–4493, 2010.
- [321] A. M. Funston, C. Novo, T. J. Davis, and P. Mulvaney, *Plasmon coupling of gold nanorods at short distances and in different geometries*. Nano Letters, 9(4):1651–1658, 2009.
- [322] N. Gandra, A. Abbas, L. Tian, and S. Singamaneni, *Plasmonic planet–satellite analogues: Hierarchical self-assembly of gold nanostructures*. Nano Letters, 12(5):2645–2651, 2012.

- [323] G. B. Alexander, W. M. Heston, and R. K. Iler, *The solubility of amorphous silica in water*. The Journal of Physical Chemistry, 58(6):453–455, 1954.
- [324] P. A. Bazula, P. M. Arnal, C. Galeano, B. Zibrowius, W. Schmidt, and F. Schüth, *Highly microporous monodisperse silica spheres synthesized by the stöber process*. Microporous and Mesoporous Materials, 200:317 – 325, 2014.
- [325] J. L. Clemens. *Visualising the local pore-structure of mesoporous silica shells around gold nanorods*, 2018. Bachelor thesis.
- [326] J. F. Li, X. D. Tian, S. B. Li, J. R. Anema, Z. L. Yang, Y. Ding, Y. F. Wu, Y. M. Zeng, Q. Z. Chen, B. Ren, Z. L. Wang, and Z. Q. Tian, *Surface analysis using shell-isolated nanoparticle-enhanced raman spectroscopy*. Nature Protocols, 8:52–65, 2012.
- [327] J. Zhang, X. Li, J. M. Rosenholm, and H. chen Gu, *Synthesis and characterization of pore size-tunable magnetic mesoporous silica nanoparticles*. Journal of Colloid and Interface Science, 361(1):16 – 24, 2011.
- [328] J. J. Penninkhof, A. Moroz, A. van Blaaderen, and A. Polman, *Optical properties of spherical and oblate spheroidal gold shell colloids*. The Journal of Physical Chemistry C, 112(11):4146–4150, 2008.
- [329] A. Królikowska, *Surface-enhanced resonance raman scattering (serrs) as a tool for the studies of electron transfer proteins attached to biomimetic surfaces: Case of cytochrome c*. Electrochimica Acta, 111:952 – 995, 2013.
- [330] N. Pazos-Perez, L. Guerrini, and R. A. Alvarez-Puebla, *Plasmon tunability of gold nanostars at the tip apexes*. ACS Omega, 3(12):17173–17179, 2018.
- [331] F. Montanarella, J. J. Geuchies, T. Dasgupta, P. T. Prins, C. van Overbeek, R. Dattani, P. Baesjou, M. Dijkstra, A. V. Petukhov, A. van Blaaderen, and D. Vanmaekelbergh, *Crystallization of nanocrystals in spherical confinement probed by in situ x-ray scattering*. Nano Letters, 18(6):3675–3681, 2018.
- [332] V. Parsegian. *Van der Waals forces: a handbook for biologists, chemists, engineers, and physicists*. Cambridge University Press, 2006.
- [333] Y. Nagaoka, T. Wang, J. Lynch, D. LaMontagne, and Y. Cao, *Binary assembly of colloidal semiconductor nanorods with spherical metal nanoparticles*. Small, 8:843, 2012.
- [334] J. Wang, C. F. Mbah, T. Przybilla, B. Apeleo Zubiri, E. Spiecker, M. Engel, and N. Vogel, *Lasing supraparticles self-assembled from nanocrystals*. Nature Communications, 9(1):5259, 2018.
- [335] F. Montanarella, D. Urbonas, L. Chadwick, P. G. Moerman, P. J. Baesjou, R. F. Mahrt, A. van Blaaderen, T. Stöferle, and D. Vanmaekelbergh, *Lasing supraparticles self-assembled from nanocrystals*. ACS Nano, 12(12):12788–12794, 2018.
- [336] O. Chen and *et al.*, *Magneto-fluorescent core-shell supernanoparticles*. Nature Communications, 5:5093, 2014.
- [337] M. Shanthil, R. Thomas, R. S. Swathi, and K. George Thomas, *Ag@SiO₂ core-shell nanostructures: Distance-dependent plasmon coupling and sers investigation*. The Journal of Physical Chemistry Letters, 3(11):1459–1464, 2012.

Summary

This thesis is titled *Gold based nanorods: tuning the structure for catalysis and sensing* and describes the use of gold nanorods as model systems in addressing fundamental questions regarding the thermal stability, alloying, catalytic behaviour and self-assembly of mono- and bimetallic nanoparticles. Gold nanorods are particularly suitable for such model studies as the size and shape of the nanorods can be tuned precisely and they have a single-crystalline atomic structure with well-defined surface facets. Furthermore, gold nanorods exhibit very interesting plasmonic properties resulting in beautiful colours ranging from purple, blue, green to brown, which makes them valuable materials for optical applications and sensing. In **Chapter 1**, we give a general introduction to gold nanoparticles, explain how the colours of the nanorods are related to their plasmonic properties and discuss general concepts in colloid synthesis, sensing and catalysis related to the work discussed in the rest of the thesis.

In **Chapter 2** we start with discussing the synthesis of monometallic nanorods using colloidal synthesis. The rod growth was achieved via a seed mediated growth process in which small gold seeds were prepared in a separate solution before adding them to a larger amount of growth solution for subsequent rod growth. By tuning the seed concentration and the reaction rate, the size and aspect ratio (length over diameter) of the nanorods were tuned precisely. The nanorods described in this thesis typically had a length of 40-120 nm and a diameter 10-40 nm. After the rod growth, the nanorods were coated with a protective silica shell containing mesopores of about 2.5 nm. This is large enough to allow a good mass transport from and to the gold surface which is essential for e.g. catalysis applications (Chapter 6). We investigated the shape stability of these silica coated nanorods as a function of their particle volume and aspect ratio and found that the rods deformed more severely when having a smaller particle volume and/or higher aspect ratio. For all samples the mesoporous silica coating had a stabilizing effect and helped to retain the anisotropic rod shape up to higher temperatures compared to uncoated nanorods. For this reason, silica coated gold nanorods were used for the work described in the rest of this thesis.

In **Chapter 3** we describe how to extend the synthesis from monometallic- to bimetallic core-shell nanorods. To achieve this, we developed a stepwise synthesis protocol to grow a silver (Ag), palladium (Pd), platinum (Pt) shell around the gold (Au) cores within the mesoporous silica shells. Via the metal-precursor concentration the shell thickness and thus the metal composition of the core-shell nanorods was tuned precisely. We observed a different behaviour depending on the type of shell metal. Whereas Ag always formed a smooth epitaxial metal shell, Pd and Pt shells were typically rough. By thermally treating the core-shell rods below the alloying temperature, the rough shell was transformed into a smooth epitaxial shell. Another important achievement described in Chapter 3 is the scaling up of the core-shell nanorod synthesis from micro- to milligrams and from millilitre to litre scale. To achieve this, the reaction speed of the metal overgrowth was decreased by lowering the pH such that all reactants were homogeneously mixed before they reacted, enabling a large scale synthesis of monodisperse core-shell nanorods. The scaling up of the

synthesis was crucial for the work in described in Chapter 5 and 6 where large quantities of nanorods were needed for the X-ray absorption and catalysis experiments.

In **Chapter 4** we present a method to alloy the core-shell nanorods of Chapter 3 via thermal treatment without losing the anisotropic shape of the nanorods. The mesoporous silica shell was key in preventing the nanorods from deforming to a more spherical shape. We demonstrate that the alloyed nanorods have tunable plasmonic properties and an improved chemical stability compared to their core-shell counterparts, as the Ag-shell of the latter is prone to oxidation, leading to (partial) loss of the plasmonic properties. We showed that we can alloy Ag, Pd, Pt shells with Au, but our method should also be applicable to nanoparticles with different compositions as long as the metals are miscible.

In **Chapter 5** we zoom in on the alloying behaviour of Au-core Ag-shell nanorods. The main objective was to investigate the influence of the particle volume and metal composition on the alloying temperature. To answer this question we made use of a combination of advanced characterization techniques to study the alloying on a single particle level and averaged over many particles. First, we investigated the alloying process for single particles with *in situ* electron microscopy, where a mix of particles with different volumes and compositions was slowly heated in the electron microscope. We observed that nanorods with a larger particle volume and higher silver content alloyed at higher temperatures, and we verified this trend for many more particles by carrying out *in situ* X-ray microscopy measurements and *ex situ* oven measurements. All techniques unanimously showed that the alloying temperature increased as a function of the particle volume and silver content. Based on our results we devised a theoretical model with which the alloying temperature of bimetallic nanoparticles of a given size and composition can be predicted.

In the work described in **Chapter 6** we made use of the fact that we can control the metal distribution of the nanorods varying from core-shell to alloy, and used this to study the effect of the metal distribution on the catalytic performance of Au-Pd nanorods in the selective hydrogenation of butadiene to butene in excess propene. This reaction is analogous to the industrial process for the the removal of trace amounts of butadiene from butene streams prior to the polymerization. Here, the main challenge is to hydrogenate the butadiene and not the excess of butene/propene. Gold is a very selective catalyst for this type of reactions, but not very active, whereas palladium is very active but not selective. Combining these two metals in a bimetallic nanoparticle renders a catalyst with both a high activity and selectivity. In chapter 6 we find that not only the ratio in which the 2 metals are mixed matters, but also the way in which the metals are arranged. Core-shell structures were found to be exceptionally active while maintaining a good selectivity and outperformed their alloyed and monometallic counterparts. Furthermore, the catalytic performance of the core-shell nanorods turned out to be very sensitive for the exact shell thickness, where 2 atomic Pd layers gave the highest activity. The work in this chapter shows that that precise tuning of the metal distribution can lead to bimetallic synergy and that it opens up a large, additional parameter space to tune the catalytic activity and selectivity of bimetallic catalysts.

In the previous chapters we looked at single nanoparticles. For the study described in **Chapter 7** we moved on to assemblies of nanoparticles and used a state of the art electron microscopy technique called focussed ion beam scanning electron microscopy

(FIB-SEM) to analyse these nanoparticle ensembles in 3D. In FIB-SEM the high imaging resolution of the electron beam is combined with the large sampling volume accessible with the FIB beam. We show that we can obtain the coordinates and orientations of the individual nanoparticles in the ensemble with FIB-SEM tomography and compare these results to those of conventional techniques measured on the same particle systems. We demonstrate that FIB-SEM tomography enabled the analysis of particle assemblies too thick for conventional electron tomography consisting of particles too small to be resolved with confocal microscopy, including also particles systems that cannot be index matched.

In **Chapter 8** the usage of gold nanorod assemblies for Raman spectroscopy is discussed. By bringing the nanoparticles in close proximity, hotspots can arise in between the nanoparticles. These hotspots can be used to enhance the Raman signal of molecules. In this study, we investigated spherical assemblies of gold nanorods, called supraparticles, for surface enhanced Raman spectroscopy. By tuning the thickness and porosity of the silica shell around the nanoparticles, the interparticle distances between the nanorods and porosity of the supraparticles could be tuned. We found that the Raman signal increased with decreasing interparticle distances, as long as the porosity of the assembly remains sufficient, and provide recommendations for further optimization of plasmonic supraparticles for sensing applications.

All together, the work in this thesis shows that we can understand and design the properties of nanoparticles by playing with their structure in new ways. By first developing methods to control and characterize the structure of the individual mono- and bimetallic rods, and their assemblies, we obtained well-defined model systems for catalysis and plasmonics. A clear example of this is described in Chapter 6, where our ability to tune the structure of bimetallic nanoparticles enabled us to discover the large impact of metal distribution on the properties of bimetallic catalysts. Although the work described in this thesis comprises fundamental research, it also contains important clues for applications, such as in the design of better catalysts via bimetallics or the assembly of nanoparticles into larger clusters for sensing. An idea for the future design of metal catalysts would be to use layered, core-shell structured catalysts as an alternative to conventional monometallic and alloyed catalysts. By coating a thin layer of an expensive, active metal on top of a cheap metal, one could for instance make better and more cost-effective catalysts.

Samenvatting voor iedereen

Beste lezer, wat fijn dat je wilt weten waar mijn promotieonderzoek over gaat. In deze samenvatting ga ik mijn best doen aan de hand van een aantal vragen zo helder mogelijk uit te leggen waar ik vier jaar aan gewerkt heb en waarom goudnanostaafjes zo fascinerend zijn.

Waarom zijn nanodeeltjes bijzonder?

Voordat we kunnen begrijpen waarom goudnanostaafjes, de hoofdrolspelers in dit proefschrift, interessant zijn, moeten we eerst begrijpen waarom nanodeeltjes in algemene zin hele speciale materialen zijn. We noemen iets een nanodeeltje als de grootte van het deeltje in de orde van 1-100 nanometer (nm) is. Hierbij is 1 nm gelijk aan 0.000000001 meter, wat ongeveer 100 000 keer dunner is dan de dikte van een menselijke haar. Nanodeeltjes bestaan typisch uit enkele duizenden atomen. Omdat nanodeeltjes zo klein zijn wijken hun eigenschappen sterk af van de gebruikelijke materiaal eigenschappen. Bijvoorbeeld, goud is een niet reactief, edel metaal wat om deze reden veel gebruikt wordt voor het maken van sieraden. Echter, wanneer je goud in hele kleine nanodeeltjes onderverdeelt gaat het zich heel anders gedragen. De goudnanodeeltjes worden minder edel, veranderen van kleur en beginnen te smelten bij lagere temperaturen. Wanneer je goudnanodeeltjes heel klein maakt (≤ 1 nm) kunnen ze zelfs al smelten bij kamertemperatuur, terwijl hun smeltpunt normaliter 1064 °C is.

In het algemeen zijn de eigenschappen van nanodeeltjes zeer gevoelig voor het precieze aantal atomen dat ze bevatten en dus voor de grootte van de nanodeeltjes. Je zou dit grootteafhankelijke gedrag met het groepsgedrag van mensen kunnen vergelijken. Mensen gedragen zich immers anders wanneer ze met slechts een paar personen zijn dan wanneer ze met tientallen of honderden personen samen zijn. Het groepsgedrag verandert niet alleen met het aantal mensen, maar is ook afhankelijk van het type mens. Dit is bij nanodeeltjes net zo, naast hun grootte (het aantal atomen waaruit ze bestaan) is ook hun samenstelling van belang voor de uiteindelijke eigenschappen. Door bijvoorbeeld twee verschillende typen metaalatomen in één nanodeeltje samen te brengen kun je van een monometallisch naar een bimetallisch deeltje gaan, welke weer hele andere eigenschappen kan hebben. Tot slot heeft ook de vorm van het nanodeeltje invloed op de eigenschappen. Tegenwoordig kunnen we nanodeeltjes met allerlei verschillende vormen maken; kubussen, sterren, driehoeken etc. Afhankelijk van zijn vorm heeft het nanodeeltje andere eigenschappen, zo kan de kleur bijvoorbeeld verschillend zijn. Een goed voorbeeld hiervan is te zien in de foto in figuur 1.1 van de introductie. Wanneer je van korte naar lange nanostaafjes gaat, verandert de kleur van de oplossing met staafjes van paars, naar blauw, groen en bruin.

Kunnen we nanodeeltjes zien?

Een belangrijke stap in het begrijpen van het gedrag van nanodeeltjes is het zichtbaar maken van deze materialen, zodat we beter kunnen begrijpen hoe de structurele eigen-

schappen van de deeltjes samenhangen met hun functionele eigenschappen. Omdat nanodeeltjes zo klein zijn lukt dit niet met het blote oog en hebben we hier een speciale microscoop voor nodig. Waar een fotocamera met een macrolens geschikt is voor het fotograferen van millimeter (0.001 m) grote objecten en een lichtmicroscoop wordt gebruikt voor micrometer (0.000001 m) grote objecten, gebruiken we een elektronenmicroscoop om nanometer (0.000000001 m) grote deeltjes te "zien". Hiervoor wordt in een elektronenmicroscoop een bundel van elektronen gebruikt in plaats van zichtbaar licht zoals bij een fotocamera of lichtmicroscoop.

De plaatjes van de nanostaafjes die in deze thesis staan zijn allemaal gemaakt met een elektronenmicroscoop. Wanneer je door het proefschrift bladert zie je dat de nanostaafjes soms als een donker staafje op een lichte achtergrond en soms als een licht staafje op een donkere achtergrond worden weergegeven. In het eerste geval is een detector gebruikt die de elektronen heeft opgevangen die door het sample zijn doorgelaten (transmissie). Het staafje houdt hierbij een deel van de elektronen tegen, waardoor er op die plek minder elektronen op de detector vallen en het staafje te zien is als een donker object. Wanneer je echter naar de elektronen kijkt die worden afgebogen door het staafje, dan komen er juist veel 'verstrooide' elektronen van de plek waar het goudstaafje is. Hierdoor zie je het staafje als een licht object op een donkere achtergrond. We noemen deze manieren van beeldvorming ook wel licht- en donkerveldelektronenmicroscopie.

Afgezien van de zwart-wit plaatjes, staan er in deze thesis ook veel gekleurde elektronenmicroscopieplaatjes. Dit soort plaatjes zijn verkregen door de Röntgenstraling die van het nanodeeltje komt op te vangen. Deze Röntgenstraling ontstaat wanneer het nanodeeltje door de elektronenbundel belicht wordt. Omdat iedere atoomsoort Röntgenstraling met een andere energie uitstraalt, kunnen we precies vaststellen waar een bepaald type atoom zich in het nanodeeltje bevindt en een gekleurd plaatje verkrijgen waarbij iedere pixel de kleur krijgt van het atoomsoort dat daar voorkomt.

Waar worden goudnanodeeltjes voor gebruikt?

Goud nanodeeltjes worden in een breed scala van toepassingen gebruikt. Een van die toepassingen is katalyse, waarbij de nanodeeltjes worden gebruikt als katalysator. Een katalysator is een materiaal dat een chemische reactie versnelt zonder dat het daarbij zelf wordt opgebruikt. Metaal nanodeeltjes zijn in staat om als katalysator te fungeren, omdat ze relatief veel oppervlakte atomen hebben ten opzichte van hun volume. Dat betekent dat er relatief veel atomen zijn die geen naburige metaal-atomen hebben en daardoor meer geneigd zijn om bindingen aan te gaan met moleculen uit hun omgeving. Tijdens een katalytisch proces wordt hier gebruik van gemaakt: de reactantmoleculen adsorberen op het oppervlak van het nanodeeltje, reageren met elkaar, waarna de producten het oppervlak weer verlaten door te desorberen. Zoals hierboven besproken, is goud normaliter een weinig reactief metaal en derhalve een slechte katalysator. Echter, goudnanodeeltjes zijn wel in staat om reacties te versnellen vanwege hun hoge oppervlakte tot volume verhouding. Goud nanodeeltjes zijn bijvoorbeeld heel goed in het omzetten van giftige CO moleculen naar CO₂, in selectieve oxidatie (reacties met zuurstof) en in selectieve hydrogenatie reacties (reacties met waterstof).

Naast hun katalytische eigenschappen, hebben goudnanodeeltjes ook hele interessante optische eigenschappen. Zo werden in de Romeinse tijd en in de Middeleeuwen goudnanodeeltjes al gebruikt om glas te kleuren. De rode kleur van glas-in-loodramen in vele kerken is bijvoorbeeld afkomstig van goudnanodeeltjes. De kleur van goudnanodeeltjes is afkomstig van hun "surface plasmon resonance", ofwel oppervlakteplasmonresonantie. Zo'n oppervlakteplasmonresonantie ontstaat wanneer de gouddeeltjes belicht worden met licht van een golflengte waarop de vrije elektronen in het staafje collectief gaan oscilleren. Je zou de collectieve oscillatie van de elektronen kunnen vergelijken met een "wave" die door een stadion met mensen gaat. Gezamenlijk vormen de mensen een golfbeweging, gelijk aan de elektronen die in een nanodeeltje resoneren. De plasmon eigenschappen van goudnanodeeltjes kunnen worden gebruikt voor biomedische toepassingen bijvoorbeeld om selectief via fothermische therapiën kankercellen te vernietigen, of voor Raman spectroscopie. De laatst genoemde is een techniek die onder andere gebruikt wordt in forensisch onderzoek, omdat er zeer specifiek moleculen gedetecteerd en gekarakteriseerd mee kunnen worden.

Wat staat er in dit proefschrift?

Mijn proefschrift gaat over goudnanostaafjes. Deze staafjes hebben we gebruikt als modelsystemen voor katalyse, zelfordening en detectie van moleculen ("sensing"). Het proefschrift is als volgt opgebouwd: hij begint met het maken van monometallische nanostaafjes (hoofdstuk 2), wat vervolgens uitgebreid wordt naar bimetallische core-shell staafjes (hoofdstuk 3), gelegerde staafjes (hoofdstukken 4-6) en tot slot naar verzamelingen van goudnanostaafjes (hoofdstukken 7, 8). Hieronder leg ik in meer detail uit wat er in de verschillende hoofdstukken te lezen is.

Hoofdstuk 1: Dit hoofdstuk dient als inleiding om de verschillende onderwerpen die in het proefschrift aan bod komen te bespreken en bevat de benodigde achtergrond kennis over de synthese en de optische en katalytische eigenschappen van goudnanodeeltjes om de rest van het proefschrift beter te kunnen begrijpen.

Hoofdstuk 2: In dit hoofdstuk bespreken we het maken, ofwel synthetiseren van de goud nanostaafjes in een waterige oplossing. Belangrijke ingrediënten in de synthese zijn een goudzout (HAuCl_4), een speciaal soort zeepmoleculen (cetrimoniumbromide, CTAB) en een molecuul dat het goudzout naar metallisch goud kan omzetten door elektronen af te staan aan de goudionen. In dit geval gebruiken we daar ascorbinezuur voor, wat beter bekend is als vitamine C. In het synthese proces binden de CTAB moleculen aan het oppervlak van de groeiende gouddeeltjes, waardoor voorkomen wordt dat de gouddeeltjes samenklonteren en ervoor zorgt dat de gouddeeltjes in één richting harder groeien dan in de andere richting. Dit komt onder andere doordat de CTAB moleculen het oppervlak langs de lengte van de staaf beter afschermen dan het oppervlak aan de punt van het staafje. In hoofdstuk 2 beschrijven we de synthese parameters die gevarieerd kunnen worden om de grootte en verhouding tussen de lengte en diameter (= aspect ratio) in te stellen, waarbij staafjes verkregen kunnen worden met een lengte van ~ 40 - 120 nm en een diameter van ~ 10 - 40 nm. Om de stabiliteit van deze goudstaafjes te vergroten, is ieder deeltje vervolgens ingepakt in een poreus, beschermend schilletje. Dit schilletje is

gemaakt van silica, een materiaal wat ook het voornaamste bestandsdeel van glas is. In dit glazen schilletje bevinden zich poriën van ongeveer 2.5 nm groot, wat groot genoeg is voor de diffusie van moleculen van en naar het goud oppervlak. Dit is bijvoorbeeld erg belangrijk wanneer de goudstaafjes voor katalyse gebruikt worden. Vervolgens hebben we de thermische stabiliteit van de kleine, grote, korte en lange goudstaafjes gecoat met poreus silica bestudeerd. Dit hebben we gedaan door de staafjes te verhitten in de oven en te bestuderen hoe de staafjes vervormen. Hierbij bleken kleine en uitgerekte (hoge aspect ratio) staafjes verreweg het minst stabiel. Dit betekent dat ze bij relatief lage temperaturen al vervormden naar een bolvormig deeltje en hun staafjesvorm verloren. We hebben hierbij geobserveerd dat de poreuze silicaschil de stabiliteit van de staafjes sterk vergroot. De silicaschil voorkomt dat de goudstaafjes samenklonteren en helpt om de staafvorm te behouden bij hoge temperaturen, hetgeen eigenlijk niet de evenwichtsvorm is van deze metaalstaafjes. Gezien de sterk verbeterde thermische stabiliteit, hebben we in de rest van de thesis silica gecoate deeltjes gebruikt.

Hoofdstuk 3: In dit hoofdstuk wordt beschreven hoe er van monometallische bimetallische nanostaafjes gemaakt kunnen worden. Dit hebben we gedaan door een zilver, palladium of platina schil om de goudstaafjes heen te laten groeien waardoor core-shell (kern-schil) deeltjes ontstaan. De dikte van deze metaalschil en dus de samenstelling van het staafje konden precies ingesteld worden door de hoeveelheid zilver-, palladium- of platinazout in de synthese te variëren. Het groeigedrag van zilver, palladium en platina verschilden van elkaar. Waar zilver als een gladde schil om het goud heen groeide, waren palladium- en platinaschillen juist ruw. Door de deeltjes te verwarmen, konden de ruwe schillen glad gemaakt worden. Een belangrijke vooruitgang die we in dit hoofdstuk beschrijven is hoe de synthese van 1 milliliter naar 1 liter reactiemengsels kon worden opgeschaald, zodat genoeg staafjes gemaakt konden worden voor de deeltjesversneller- en katalyse-experimenten die beschreven worden in hoofdstuk 5 en 6. Door de reactiesnelheid waarmee de metaalschil om het goud groeit te verlengen van enkele seconden naar enkele minuten, konden de reactanten netjes gemengd worden voordat de reactie plaatsvond, resulterend in staafjes met allemaal vrijwel dezelfde grootte en samenstelling.

Hoofdstuk 4: In dit hoofdstuk wordt beschreven hoe de core-shell deeltjes uit hoofdstuk 3 gelegeerd kunnen worden. Door de staafjes in de oven te verwarmen werden de atomen in de kern en schil met elkaar vermengd. Het bijzondere is dat het mengen van de metalen gebeurde zonder dat de staafjes sterk van vorm veranderden. Men zou kunnen verwachten dat de mobiliteit van de metaalatomen die vereist is voor het legeren er ook voor zou zorgen dat de deeltjes vervormen naar een bolvormige evenwichtsstructuur. Dit gebeurt echter niet omdat de deeltjes ingepakt zitten in een extra, poreus schilletje, die de vorm van de nanostaafjes voldoende stabiliseerde. In dit hoofdstuk laten we zien dat core-shell deeltjes met een zilver-, palladium- en platinaschil succesvol gelegeerd kunnen worden met goud, maar in principe is onze methode ook geschikt voor core-shell deeltjes met andere metaalsamenstellingen.

Hoofdstuk 5: In hoofdstuk 5 zoomen we verder in op het legeringsproces van goud-kern zilver-schil nanostaafjes. Hierbij staat de vraag centraal wat de invloed van de deeltjesgrootte en de metaalsamenstelling op het legeringsproces is. Om deze vraag te beantwoorden maakten we gebruik van verschillende geavanceerde analyse technieken: *in situ* elektronenmicroscopie, *in situ* Röntgenabsorptiespectroscopie en *ex situ* oven metin-

gen. In de *in situ* elektronenmicroscopie metingen hebben we gekeken naar individuele goud-zilver nanostaafjes met verschillende afmetingen en metaalsamenstellingen. Door deeltjes langzaam te verwarmen in de elektronenmicroscopie konden we precies waarnemen bij welke temperatuur de staafjes legerden. De legeringstemperatuur bleek hierbij veel hoger voor deeltjes met een groter volume en/of meer zilver. Deze trend hebben we vervolgens bevestigd voor een heel groot aantal deeltjes ($\sim 10^{19}$) die werden bestudeerd met Röntgenabsorptiespectroscopie. Deze metingen moesten verricht worden in een deeltjesversneller, een grote cirkelvormige meetfaciliteit waar hoge energie Röntgenstraling opgewekt wordt voor Röntgenabsorptiespectroscopie. Tot slot hebben we ook *ex situ* oven metingen gedaan, waarbij de staafjes verwarmd werden in de oven en na afloop bekeken werden in de elektronenmicroscopie. Alle technieken lieten dezelfde trend zien: hoe meer zilver in het staafje en hoe groter het staafje, hoe hoger de temperatuur waarop je de staafjes moet verhitten om ze te laten legeren. Met behulp van een theoretisch model kunnen we nu zelfs de legeringstemperatuur van bimetallische nanodeeltjes voorspellen als functie van hun grootte en metaalsamenstelling.

Hoofdstuk 6: Met de kennis uit de voorgaande hoofdstukken was het mogelijk om gecontroleerd de atomen te positioneren in de nanodeeltjes. In hoofdstuk 6 hebben we uitgezocht wat het effect van de metaaldistributie is op de katalytische eigenschappen van bimetallische nanodeeltjes. Hierbij hebben we de katalytische eigenschappen van goud-palladium nanostaafjes in de selectieve hydrogenatie van butadiëen naar buteen bestudeerd. Butadiëen is een molecuul met 4 koolstofatomen en 2 dubbele bindingen, waarvan er 1 dubbele binding selectief verwijderd moet worden door de butadiëen met waterstof te laten reageren. Het molecuul dat daarbij ontstaat, buteen, is een belangrijke grondstof om polymeren van te maken. Goud is een goede katalysator om zeer selectief butadiëen naar buteen te hydrogeneren maar is katalytisch weinig actief, terwijl palladium juist een heel actieve maar onselectieve katalysator is en een deel van het buteen omzet naar butaan. Door gebruik te maken van een bimetallisch deeltje combineer je de goede selectiviteit van het goud met de hoge activiteit van het palladium. Wij laten in dit hoofdstuk zien dat niet alleen de verhouding waarin je de 2 metalen mengt maar vooral de manier waarop je de goud en palladium atomen in het deeltje rangschikt zeer belangrijk is voor de uiteindelijke activiteit en selectiviteit. We vinden hierbij dat palladium-schil goud-kern nanodeeltjes zeer actief zijn terwijl ze een goede selectiviteit behouden en dat ook de precieze palladium-schil dikte de katalytische eigenschappen sterk beïnvloedt.

Hoofdstuk 7: Waar in voorgaande hoofdstukken naar enkele deeltjes gekeken is, hebben we in hoofdstuk 7 naar verzamelingen van nanodeeltjes gekeken en bestudeerd hoe die in 3D gekarakteriseerd kunnen worden. We hebben hierbij gebruik gemaakt van een relatief nieuwe, geavanceerde elektronenmicroscopie techniek genaamd gefocusseerde-ionenbundel-scannende-elektronenmicroscopie (FIB-SEM). Hierbij gebruik je een ionenbundel om telkens een klein plakje van het sample af te schieten met een gerichte versnelde atomenbundel, terwijl je tussendoor een elektronenbundel gebruikt om plaatjes te maken van het sample. Je zou dit kunnen vergelijken met kaasschaven op de nanoschaal, waarbij je telkens een plakje afschaaft en een foto van de overgebleven kaas neemt. Met behulp van FIB-SEM tomografie is het gelukt om clusters van nanodeeltjes in 3D te karakteriseren en de positie en oriëntatie van ieder individueel nanodeeltje in cluster te bepalen. Deze resultaten hebben we vergeleken met die van meer conventionele technieken zoals

elektronentomografie en confocalmicroscopie (= een vorm van lichtmicroscopie). We laten zien dat FIB-SEM tomografie zeer geschikt is, ook voor samples die te ondoorzichtig zijn voor conventionele elektronentomografie en te klein voor confocalmicroscopie.

Hoofdstuk 8: In het laatste hoofdstuk, bespreken we het gebruik van verzamelingen van goudstaafjes voor Ramanspectroscopie. We noemen deze ronde clusters van goudstaafjes ook wel supradeeltjes ("supraparticles") en gebruiken ze om het Ramansignaal van moleculen te versterken. Door de nanostaafjes in een cluster dicht bij elkaar te pakken ontstaan zogeheten hotspots tussen de staafjes. Als een molecuul in zo'n hotspot komt wordt het Ramansignaal van het molecuul daar drastisch versterkt. Door de goudstaafjes met silicaschillen van verschillende dikten te coaten konden we de afstand tussen de deeltjes instellen en daarmee de sterkte van de hotspots. We vonden hierbij dat supradeeltjes die bestaan uit goudstaafjes met een dunne silicalaag die elkaar dicht kunnen naderen, het beste het Ramansignaal van moleculen kunnen versterken, mits het supradeeltje voldoende poreus is.

Wat was een heel verrassende bevinding?

De bevindingen uit hoofdstuk 6 vind ik heel verrassend. In de katalyse wordt vaak aangenomen dat de oppervlakte atomen van een nanodeeltje bepalend zijn voor de katalytische eigenschappen en dat die alleen bij heel kleine (<5 nm) goud nanodeeltjes katalytisch actief zijn. Onze resultaten laten echter zien dat dit een onjuiste aanname is: de onderliggende, sub-oppervlakte lagen doen er net zo goed toe en grotere gouddeeltjes kunnen voor bepaalde reacties nog steeds erg actief zijn. Om het gedrag van een bimetallische katalysator te begrijpen, is het beter om naar de metaaldistributie van het gehele nanodeeltje te kijken en niet alleen naar de oppervlakte atomen. Zo laten we zien dat je door met de distributie van de verschillende metalen te spelen nieuwe katalytische eigenschappen kunt verkrijgen die niet met de afzonderlijke metalen te maken zijn. Hoewel het onderzoek in hoofdstuk 6 fundamenteel is kan het wel degelijk bijdragen aan de ontwikkeling van de betere, duurzame industriële katalysatoren. Door bijvoorbeeld een dun laagje van een duur, maar actief metaal op een goedkoper metaal af te zetten in plaats van een massief deeltje van het dure metaal te gebruiken, zou je een nieuwe katalysator kunnen maken die goedkoper en actiever is.

Acknowledgements

A PhD is not just a job. It is more like a journey in which you set out to investigate something which is yet unknown, or at least partially unknown. On this journey I learned that failing experiments are not a personal failure, but simply part of the game when working on something new. This makes the PhD both challenging and very exciting. Although doing a PhD is to a certain extent an individual journey, I was never alone. Thanks to the support of many fantastic people this thesis came about and I could finish my travel.

First I would like to thank my promotors, *Petra* and *Alfons*, for guiding me. Having a shared PhD student in 2 different groups certainly demanded a lot of flexibility from both of you. I want to thank you for the freedom and trust you gave me during the past years. You provided the opportunities to learn many techniques, to work on different topics with different people and let me go to many useful conferences. *Petra*, I want to thank you for being such a good and kind mentor, both as a scientist in guiding the research as well as in advising me when other issues came on my path. Your clever ideas and sharp eye for detail certainly made a difference. *Alfons*, thank you for being such an enthusiastic, open-minded scientist and supervisor, for your impressive literature knowledge and for your endless stream of creative ideas when I did not see how to continue. A big thanks to both of you!

Next, I would like to thank all staff members of SCM and ICC for creating such nice and well-organized research groups. In particular I would like to thank *Baira Donoeva* for the pleasant catalysis related discussions, *Marijn van Huis* for sharing his electron microscopy knowledge and *Marjolein Dijkstra* and *René van Roij* for initiating some nice sport events (Pheidippides runs). *Frank de Groot*, *Bert Weckhuysen*, *Andries Meijerink*, *Xavier Carrier* and *Andrea Baldi*, thank you for being part of the reading committee and for the time you spent in reading this thesis.

I had the pleasure to work together with several scientists in France. *Catherine Louis* and *Xavier Carrier* thank you for your pleasant company on the beam trips at SOLEIL and your help in making the work into a nice publication. *Tiago da Silva*, many thanks to you for your effort and clever tricks in analysing the data. *Camille la Fontaine*, thank you for all your technical support in conducting the EXAFS measurements.

When working in a lab, the help of skilled technicians in keeping all equipment running properly is indispensable. *Hans and Chris*, thank you for keeping the electron microscopes in such a good shape and for always being available to help. *Hans*, I am very grateful to you for teaching me so much about many different electron microscopy techniques. Apart from being one of the most skilled electron microscopist I know, you are also a very kind and pleasant person to talk to. I hope you will inspire many more generations of PhD students to become better electron microscopist. *Peter*, no matter what type of technical problem arose, your presence was often enough to spontaneously make the machines behave nicely again. *Relinde*, you take great care of the SCM lab, now together with *Elleke*, and also performed many ICP measurements for me. Thank you for your support and positive attitude. *Dave*, it is nice to have such a good BHV'er and fist aid

person among us. Thank you for helping out. *Jan-Willem*, you helped me a lot in keeping the butadiene setup running and you also always showed interest in my research. To both *Ad's*, you did a great job after the fire and made sure the equipment was relocated and running again as fast as possible. Furthermore, I also want to mention *Ramon, Herrick, Denny, Oscar, Fouad and Marjan* for their technical support whenever needed.

Both groups also have very well-organized and kind secretaries taking care all sorts of administrative issues. *Marion, Hester, Diane, Linda, Dymph and Ilonka*, thank you for your help. *Dymph*, a special thanks to you for making sure that everything went smoothly in the last few months.

During my PhD I was lucky to work with 5 talented students. *Marc, Naomi, Inge, Maarten and Liselotte* thank you for your enthusiasm and effort. *Maarten*, it was clear from the start that you were a very motivated and creative student, curious to learn as much as possible about gold nanorods and their self-assembly. The beautiful supraparticles shown in Chapter 7 were synthesized by you. *Liselotte*, although you started your project in the final phase of my PhD it nevertheless turned out to be very successful and was the basis of Chapter 6. *Inge*, I very much appreciated your independent and hard work on the analysis of mesoporous silica shells with electron tomography, unfortunately it did not make it into this thesis.

Being part of 2 groups means that you don't contribute for the full 100% to each group and that you rely on the many colleagues that take on responsibilities in maintaining the equipment, organizing the lab cleaning, initiating social events, etc. *A big thanks to all my colleagues of ICC and SCM* for doing this so well and for creating such a nice group. It is not possible to name everyone here, so apologies to those not mentioned.

Rolf, you are a fantastic colleague and "buurman" to have. You were always willing to help, think along and give advise. Thank you for your support the past years, the nice dinners and bike rides. I am very happy that you are willing to be my paranimf. *Giorgio*, you taught me a lot about gas phase catalysis, explained all sorts of technical details and helped out when the hydrogenation setup was misbehaving. Thank you for your hard work, the nice collaboration and your super happy attitude. *Marisol*, it is nice to have such a kind colleague and friend. I very much enjoyed the lunch breaks and tasty (but rather spicy...) dinners. *Petra Keijzer*, "overbuurvrouw", thank you for your friendship, the nice coffee breaks and the social activities outside of work. *Carlos*, it was really fun to work together. Thank you for involving me in your project, your joyful company during the TEM measurements (often accompanied by *Lennart*) and your funny jokes. I hope you are going to win the lottery soon so I can come to work in your lab. *Johan*, whenever you brought your home-baked cookies it made my day. I also very much appreciated your and *Guusje's* plant collection.

To my dear friend *Nazila*, it was clear for me from the first day at ICC that you are an extremely kind person. I very much enjoyed being your neighbour, having food breaks together and eating the tasty Iranian food you cooked. Thank you for the many nice discussions, not only the scientific but also all the non-scientific ones. *JX*, you are a very fun and social person, who is always eager to go for beers or play some pool. Thanks for bringing, sometimes forcing, me along. *Jeroen*, your clever remarks during one of the stability meetings led to a good theoretical model to describe the experimental trends that I observed, which eventually made it to a nice publication. *Lisette*, doing the tomography

on your beautiful copper catalysts was not only fun but also motivated me to improve my microscopy skills. I am very happy that you let me be part of your project, thank you.

Katherina and Stano, we had a lot of nice lunch breaks together. Thank you for also initiating enjoyable activities outside work. *Donglong, Lee, Kang and Xinwei*, "the weekend crew", whenever I had to pass by to check or switch on/off my catalysis experiment I would be sure to find one of you in the DDW, which I very much appreciated. *Nynke*, you are a very open and social girl. Thank you for your "gezelligheid" in and outside the office.

It was great to have so many sporty colleagues. To the members of the "ICC cycling group", *Ramon, Rolf, Jogchum, Wouter, Jeroen, Joris, Frank and Suzanne*, thank you for the nice and tiring bike rides after work, and a special thanks to *Ramon* for your navigator skills. To the "SCM biking buddies" including *Ernest, Nina, Henriëtte, Chris, Pepijn, and Michele* (adopted from FCC), it was great to go biking with you and have dinner out afterwards.

From day one of my PhD I was lucky to be part of the "gezelligste" office of the Ornstein lab with wonderful people: *Nina, Wessel, Henriëtte, Pepijn, Anna and Erik*. *Nina*, since my master project you have been a mentor to me and a perfect example of a good, careful and honest researcher. I am very lucky to have learned from the best. Thank you for your good advise and your support. *Wessel*, you were in many aspects an extraordinary office mate. Thank you for the lengthy philosophical discussions, for feeding me with all sorts of delicious home baked cakes/cookies/chocolates, thinking along when experimental problems arose and for making taking care of others your priority. *Henriëtte*, I really liked the chats with you, the nice bike rides and your funny, slightly mean jokes. *Pepijn*, I am lucky to have such a loyal and enthusiastic friend as you from the beginning of our studies. It is great that we are now defending our theses at the same time. *Erik*, "het jonkie van OL12", thank you for being such an enthusiastic and friendly office mate, for the nice cookies and delicious teas. *Anna*, I have always been impressed by you and I am very grateful to have had you as my office mate. You are an exceptionally warm, caring and intelligent lady. Thank you for the many fun and encouraging conversations, the late night dinners in the lab, the shared love for cats and chocolate, and for all our failed attempts to give the plants in our office a decent life.

Tiansong, I could not have wished for a better person to teach me about the synthesis of gold and bimetallic nanorods. Thank you for sharing your knowledge so freely and for the nice collaboration. I very much enjoyed working with you. *Ernest*, thank you for the pleasant collaboration on Chapter 7 and the nice bike rides together. *Wiebke*, thank you for the many collaborations and for sharing your insights on the optical properties of gold nanorods. You also organized some very nice trips to Cardiff, France and Berlin, which I really enjoyed. *Tom*, I always liked to collaborate and speak with you, as you are not only clever but also very friendly. *Da*, thank you for teaching me more about electron tomography and self-assembly. *Matthijs* and *Yang*, both of you are very skilled microscopists. Thank you for the many FIB-SEM sessions. *Stijn*, you are a very knowledgeable and relaxed colleague. Thank you for the many lunch breaks and the nice chats. *Naveed* and *Rama*, thanks for your always "sunny" mood in the lab. *Giulia, Guido, Carmine, Doug, Toni, Sid*, thanks for the enjoyable board game nights.

To the "upstairs neighbours" from CMI: *Monty, Maryam, Marlou, Tim, Christa and Anne*, thank you for your happy company in the Ornstein. *Monty*, our travel to the MRS in Boston together with *Kanako* was certainly one of the trips I enjoyed the most. Thank you for being such a great guy with a very good sense of humour and great cooking (and eating) skills. *Christa*, it was really nice to share our experiences on being a shared PhD student. *Anne*, I am so happy that we got to know each other at the EMAT school in Antwerp. From that moment on you have become a very good and caring friend, and member of our cooking club with Pepijn. Thank you so much for your continuous, super strong support.

Sanne, Laurien, Tamara, dankjulliewel voor jullie interesse, de gezellige etentjes en het biertjes drinken buiten het werk. *Tanja*, het lijkt voor onze vriendschap niets uit te maken hoe ver we uit elkaar wonen en dat we elkaar niet vaak zien. Ook vanaf afstand ben jij belangrijk geweest tijdens mijn PhD en ik vind het fantastisch dat je bij mijn promotie aanwezig zult zijn.

Tot slot wil ik mijn lieve familie bedanken voor hun onvoorwaardelijke steun. Mijn broers, *Tom* en *Lucas*, en mijn zus, *Julie*, dankjulliewel voor jullie support en voor alle gezelligheid buiten het werk. *Cynthia*, dankjewel voor het controleren van de Nederlandse samenvatting. *Pap en mam*, jullie zijn onmisbaar geweest tijdens mijn promotietraject en waren altijd geïnteresseerd. Lieve *pap*, dankjewel voor je wijze adviezen wanneer ik even niet wist hoe ik een situatie aan moest pakken. Lieve *mam*, het is heel bijzonder dat jij mijn onderzoek inhoudelijk zo goed begreep zonder ooit een plaatje of data plot te hoeven zien. Jij hebt me regelmatig met je scherpe vragen aan het denken gezet. Het feit dat je dit kan laat niet alleen zien dat je je enorm interesseerde voor mijn onderzoek, maar ook dat je heel intelligent bent. Dankjewel voor alle fijne gesprekken, alle krantenknipsels over wetenschap die je altijd bewaarde en je fantastische steun.

Dearest *Simone*, I am incredibly lucky to have you on my side. You are never too tired to listen and give me your advise. Your support made all the difference. Un grazie enorme per tutto, caro Simo!

List of publications

This thesis is partially based on the following publications:

- J.E.S. van der Hoeven / W. Albrecht, T.-S. Deng, P.E. de Jongh, A. van Blaaderen, Synthesis and thermal stability of silica coated gold nanorods, *in preparation* (Chapter 2)
- T.-S. Deng, J.E.S. van der Hoeven, A.O. Yalcin, H.W. Zandbergen, M.A. van Huis, A. van Blaaderen, Oxidative etching and metal overgrowth of gold nanorods within silica shells, *Chemistry of Materials*, 2015, 27, 7196-7203 (Chapter 3)
- J.E.S. van der Hoeven / T.-S. Deng, W. Albrecht, M.A. van Huis, P.E. de Jongh, A. van Blaaderen, Synthesis of bimetallic core-shell nanorods, *in preparation* (Chapter 3)
- W. Albrecht / J.E.S. van der Hoeven, T.-S. Deng, P.E. de Jongh, A. van Blaaderen, Fully alloyed metal nanorods with highly tunable properties, *Nanoscale*, 2017, 9, 2845-2851 (Chapter 4)
- J.E.S. van der Hoeven, T.A.J. Welling, T.A.G. Silva, J.E. van den Reijen, C. La Fontaine, X. Carrier, C. Louis, A. van Blaaderen, P.E. de Jongh, In situ observation of atomic redistribution in alloying gold-silver nanorods, *ACS Nano*, 2018, 12, 8467-8476 (Chapter 5)
- J.E.S. van der Hoeven, L.A. Olthof, G. Totarella, A. van Blaaderen, P.E. de Jongh, Tuning the metal distribution of Au-Pd catalysts for bimetallic synergy in the selective hydrogenation of butadiene, *in preparation* (Chapter 6)
- J.E.S. van der Hoeven / E.B. van der Wee, D.A.M. de Winter, M. Hermes, Y. Liu, J. Fokkema, M. Bransen, M.A. van Huis, H.C. Gerritsen, P.E. de Jongh, A. van Blaaderen, Bridging the Gap: 3D Real-Space Characterization of Colloidal Assemblies via FIB-SEM Tomography, *Nanoscale*, 2019, 11, 5304-5316 (Chapter 7)
- J.E.S. van der Hoeven, M. Bransen, D.A.M. de Winter, J.L. Clemens, P.E. de Jongh, A. van Blaaderen, Gold nanorod supraparticles for surface enhanced Raman spectroscopy, *in preparation* (Chapter 8)

Other publications by the author:

- C.E. Pompe, D.L. van Uunen, L.I. van der Wal, J.E.S. van der Hoeven, K.P. de Jong, P.E. de Jongh, Stability of Mesocellular Foam Supported Copper Catalysts for Methanol Synthesis, *Catalysis Today*, 2019, *in press*
- J.C. Everts, S. Samin, N.A. Elbers, J.E.S. van der Hoeven, A. van Blaaderen, R. van Roij, Colloid-oil-water-interface interactions in the presence of multiple salts:

- charge regulation and dynamics, *Physical Chemistry Chemical Physics*, 2017, 19, 14345-14357
- B. Arndt, R. Bliem, O. Gamba, J.E.S. van der Hoeven, H. Noei, U. Diebold, G.S. Parkinson, A. Stierle, Atomic structure and stability of magnetite Fe_3O_4 (001): An X-ray view, *Surface Science*, 2016, 653, 76-81
 - R. Bliem, J.E.S. van der Hoeven, J. Hulva, J. Pavelec, O. Gamba, P.E. de Jongh, M. Schmid, P. Blaha, U. Diebold, G.S. Parkinson, Dual role of CO in the stability of subnano Pt clusters at the Fe_3O_4 (001) surface, *Proceedings of the National Academy of Sciences*, 2016, 113, 8921-8926
 - N.A. Elbers, J.E.S. van der Hoeven, D.A.M. de Winter, C.T.W.M. Schneijdenberg, M.N. van der Linden, L. Filion, A. van Blaaderen, Repulsive van der Waals forces enable Pickering emulsions with non-touching colloids, *Soft Matter*, 2016, 12, 7265-7272
 - R. Bliem, J.E.S. van der Hoeven, A. Zavodny, O. Gamba, J. Pavelec P.E. de Jongh, M. Schmid, U. Diebold, G.S. Parkinson, An Atomic-Scale View of CO and H_2 Oxidation on a Pt/ Fe_3O_4 Model Catalyst, *Angewandte Chemie*, 2015, 127, 14205-14208
 - M.N. van der Linden, J.C.P. Stiefelhagen, G. Heessels-Gürboğa, J.E.S. van der Hoeven, N.A. Elbers, M. Dijkstra, A. van Blaaderen, Charging of poly(methyl methacrylate)(PMMA) colloids in cyclohexyl bromide: Locking, size dependence, and particle mixtures, *Langmuir*, 2014, 31, 65-75

Oral and poster presentations

Oral presentations:

- The 16th European Microscopy Congress, 2016, Lyon, France
- MRS Fall Meeting, 2017, Boston, United States of America
- MRS Fall Meeting, 2017, Boston, United States of America
- NWO CHAINS, 2017, Veldhoven, Netherlands
- NWO Physics@Veldhoven, 2018, Veldhoven, Netherlands
- The Netherlands' Catalysis and Chemistry Conference, 2018, Noordwijkerhout, Netherlands
- World Gold Conference, 2018, Paris, France
- World Gold Conference, 2018, Paris, France
- Debye Lunch Lecture, 2019, Utrecht, Netherlands
- The Netherlands' Catalysis and Chemistry Conference, 2019, Noordwijkerhout, Netherlands

Poster presentations:

- EMAT workshop on transmission electron microscopy, 2015, Antwerp, Belgium
- World Gold Conference, 2015, Cardiff, United Kingdom
- NWO Physics@Veldhoven, 2016, Veldhoven, Netherlands
- The Netherlands' Catalysis and Chemistry Conference, 2016, Noordwijkerhout, Netherlands
- NWO Physics@Veldhoven, 2017, Veldhoven, Netherlands
- The Netherlands' Catalysis and Chemistry Conference, 2017, Noordwijkerhout, Netherlands

About the author

Jessi van der Hoeven was born on the 25th of July, 1991 in Haarlem, the Netherlands. After completing high school (Gymnasium, VWO level) in 2009, she started studying Chemistry at Utrecht University. She obtained her bachelor's degree *cum laude* and performed her bachelor research project on "Gold silver catalysts" under the supervision of Prof. K.P. de Jong in the Inorganic Chemistry and Catalysis group (Chemistry department). In 2012 she started her masters in "Nanomaterials: Chemistry and Physics" and performed her master research project on "Colloids near oil water interfaces" in the Soft Condensed Matter and Biophysics group (Physics department) under the supervision of Prof. A. van Blaaderen. Additionally, she did a 6 months research project at the Technische Universität Wien in the Institute of Applied Physics in the group of Prof. U. Diebold and Prof. G.S. Parkinson on "Single atom catalysts". She graduated *cum laude* in 2014. During her master she wrote a proposal to obtain a PhD position within the Debye institute, which was granted. In December 2014 she started her PhD project in the Inorganic Chemistry and Catalysis group and Soft Condensed Matter and Biophysics group under the supervision of Prof. P.E. de Jongh and Prof. A. van Blaaderen. Both her master- and PhD work have been published in peer-reviewed journals and were presented on national and international conferences. During her PhD, she wrote two proposals for electron microscopy (EUSMI) and X-ray spectroscopy measurement time (SOLEIL), which were both granted. Jessi taught Chemistry to high school students at the "Stichting Studiebegeleiding Leiden" from 2011 to 2014. In her free time, she likes to cook and go hiking, speed skating and biking. Best achievement so far was a 1500 km bike ride from Hilversum (the Netherlands) to Krakau (Poland) within 14 days.

